Characterization and Modelling of the Regional *In Situ* Stress Field of Continental Australia

Scott D. Reynolds, B.Sc (Hons)

National Centre for Petroleum Geology and Geophysics
Adelaide University

This thesis is submitted in fulfilment of the
requirements for the degree of Doctor of Philosophy
in the Faculty of Science, Adelaide University

July 2001

ADELAIDE
UNIVERSITY
AUSTRALIA

Table of Contents

Abstract

The Indo-Australian plate (IAP) is unique when compared to most other plates in that the maximum *in situ* horizontal stress (σ_{Hmax}) orientation is not uniform and does not parallel the direction of absolute plate velocity. Consequently, the Australian continent provides an ideal setting to study the interaction between tectonic forces and the *in situ* stress field. The focus of this thesis is on (1) improving current knowledge of the *in situ* stress field of the Australian continent, largely through the compilation of new data in the Bowen, Sydney and Perth Basins, and (2) the analysis of the origin of the Australian stress field in terms of plate boundary forces.

New *in situ* stress data based on hydraulic fracturing and overcoring measurements have been compiled for the Bowen and Sydney Basins. The Bowen Basin displays a consistent north-northeast σ_{Hmax} orientation. In contrast, the Sydney Basin displays a variable σ_{Hmax} orientation as a result of local sources of stress. The Bowen Basin is relatively aseismic compared to the Sydney Basin, which is relatively seismically active. A correlation exists between the *in situ* stress measurements and the levels of seismicity in the two basins, despite the shallow depth at which the hydraulic fracturing and overcoring data were obtained. Mohr-Coulomb analysis of the propensity for failure indicates that 41% of the new *in situ* stress data are indicative of failure in the Sydney Basin, compared with only 13% in the Bowen Basin. This difference in propensity for seismicity in the two basins based on *in situ* stress data is further emphasised when the pre-existing structural grains of the two areas are considered.

The mean orientation of σ_{Hmax} inferred from borehole breakout data in the Perth Basin is approximately east-west. This orientation is consistent with σ_{Hmax} orientations from both deeper earthquake focal mechanisms and shallower hydraulic fracturing and overcoring data from the adjacent Yilgarn Craton. Hence the regional east-west σ_{Hmax} orientation is consistent across different stress indicators, depths and geological provinces. This robust east-west σ_{Hmax} orientation is almost orthogonal to the direction of absolute plate velocity and thus this region is of particular significance to our understanding of the *in situ* stress field of Australia. Anomalous north-south σ_{Hmax} orientations identified in a number of wells in the Perth Basin can be attributed to local structural effects.

In order to compare observed *in situ* stresses with those based on modelling, the regional stress field throughout continental Australia has been defined using two different methods:

stress province definition and stress trajectory mapping. These techniques have been applied to a greatly increased Australian stress database comprising both existing stress analyses and the new analyses presented here. In general there is broad agreement between the two techniques, which reveal continental scale rotation of the stress field across Australia. Stress orientations in Australia vary from east-west in the western and southern parts of the continent (Perth region, Carnarvon and Cooper Basins) rotating to northeast-southwest across the northern margin (New Guinea, Bonaparte and Canning Basins) and northwest-southeast through southeastern Australia (Otway and Gippsland Basins). The central (Amadeus Basin) and northeastern (Bowen Basin) parts of Australia are characterised by a north-northeast to south-southwest stress field.

The tectonic forces controlling the present day regional intraplate stress field in continental Australia have been evaluated through finite element analysis of the intraplate stresses in the IAP. Constraints for the modelling are provided by the 'observed' regional stress field based on the stress province definition. This observed dataset is greatly improved compared to that used in previous modelling efforts. A weighted 'basis-set' method has been employed to quantitatively assess the misfit between the observed and predicted intraplate stresses, providing an efficient means to evaluate a very large number of boundary and potential energy force combinations acting on the plate.

The modelling results indicate that the major features of the regional stress field in continental Australia can be explained in terms of a geologically plausible array of plate boundary and potential energy forces. These results indicate that modelling of the Australian intraplate stress field is inherently non-unique such that a large number of different boundary force combinations can produce a very similar predicted stress fields. Nevertheless a number of fundamental conclusions can be made about the tectonic settings along the principal plate boundary segments including the following:

(1) Compressional forces act along the Himalayan and Papua New Guinea boundaries to produce stress focussing normal to those boundaries and stress rotation between them.
(2) The observed stress field in the Bowen Basin requires compressional forces along the Solomon and New Hebrides subduction zones.
(3) East-west compression in eastern Australia requires moderate compression acting along the Tonga-Kermadec subduction zone.
(4) Modelling stresses in southeastern Australian requires compressional forces along the New Zealand, Puysegur Trench and Macquarie Ridge boundary segments.

Declaration

This work contains no material which has been accepted for the award of any other degree or diploma in any university or other tertiary institution and, to the best of my knowledge and belief, contains no material previously published or written by another person, except where due reference has been made in the text.

I give consent to this copy of my thesis, when deposited in the University Library, being available for loan and photocopying.

.....

Scott D. Reynolds

Acknowledgments

Thanks to Richard Hillis for being such a great supervisor, who gave this project direction and drive especially in the initial stages. I'm very grateful for having such a concerned and interested supervisor. Your enthusiasm for this project was always encouraging. Thanks also to Richard and Peter Brooker for providing many opportunities to demonstrate in practicals to the undergraduates.

Thanks to Jim Enever who provided the initial data for this project in eastern Australia and for the valuable experience of participating in a hydraulic fracturing experiment in the Hunter Valley. Thanks also for your hospitality while I was in Melbourne.

I am indebted to David Coblentz for assistance with modelling of the Australian stress field and for use and modification of your finite element modelling code. The modelling could not have occurred without your help. I am very grateful to David, Christine and Kai for their hospitality while I was in America. You made the stay in El Paso bearable. Thanks also to Randy Keller for organising my participation in the LARSE II experiment in Los Angles.

Special thanks to my family, Mum, Dad, Simon and Kate, for your support and encouragement. Thanks for putting up with the minimal information I provided about my work over the last three years.

To all the friends I have made over these years, hopefully our paths will cross again. To Sandra McLaren, thanks for being a special friend who was always there to listen to my problems, for reading over a first draft of this thesis and for your continual words of encouragement and advice. Thanks to Jerry Meyer and Trevor Dhu who always kept things interesting and who were always there to provide help with my programming problems, of which there were many. Thanks to everyone who made Friday such a fun day and exciting night. To Scotty, Narelle, Jack, Bruce, Paul, Miles, Rolf, Kristy, Pete, Mark, Aaron, Johnny Nej, Max, Pete C, Rosalie, Tom and Ainslie thankyou all for being a part of my life over the last few years.

Finally I would like to thank the staff at the National Centre for Petroleum Geology and Geophysics and the Department of Geology and Geophysics for their assistance. In particular I am very grateful to Maureen, Gerald, Barbara, Yvonne, Yvette and Sherry, for their support.

Chapter 1

Introduction

1.1 Project Rationale

Knowledge of the *in situ* stress field in the earth's crust is very important in a range of disciplines such as civil and mining engineering, geology, geophysics and energy development. Some of the activities requiring knowledge of the *in situ* stress field include (Amadei and Stephansson, 1997):

- stability of underground excavations (tunnels, mines, caverns, shafts, stopes);
- slope stability;
- borehole stability in both vertical and deviated wells;
- induced hydraulic fracturing and fracture propagation;
- fluid flow and fault reactivation;
- storage and extraction of gas and oil from the subsurface;
- earthquake prediction;
- plate tectonics, and;
- neotectonics.

In 1986 the World Stress Map (WSM) project was initiated in an effort to compile and interpret data on the orientation and magnitude of the *in situ* tectonic stress field in the earth's lithosphere (Zoback, 1992). The Australian continent was poorly represented in the WSM database when compared to other continental areas such as North America and Europe (Figures 1.1 & 1.2). The Australian Stress Map (ASM) project was commenced in 1996 in order to improve our limited understanding of the *in situ* stress field of Australia. This PhD project was undertaken under the auspices of the ASM project. Since 1998 the author has maintained the ASM database and developed the ASM website (Appendix A; www.ncpgg.adelaide.edu.au/asm). The ASM project has increased the number of reliable *in situ* stress measurements for the Australian continent to 322. The new *in situ* stress indicators for the Bowen, Sydney and Perth Basins were determined within, and comprise part of this thesis.

The *in situ* stress information in the WSM database indicates that in most continental areas such as Western Europe, South America and stable North America, the maximum *in situ* horizontal stress (σ_{Hmax}) orientation broadly parallels the direction of absolute plate velocity

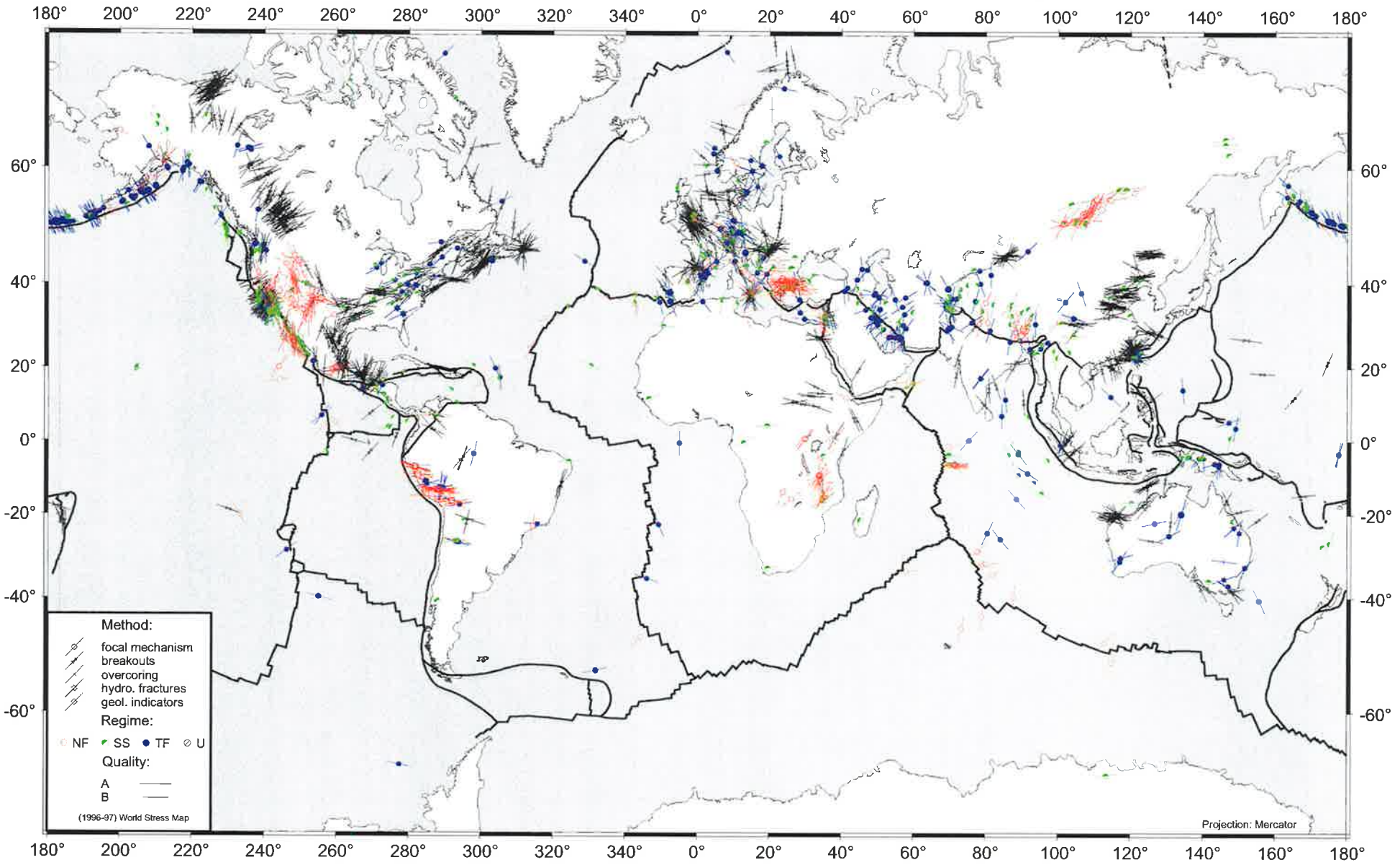

Figure 1.1 WSM 1997 release showing the small amount of stress data in Australia compared to the rest of the world (Müller *et al.*, 1997).

(Zoback *et al.*, 1989; Richardson, 1992; Gölke and Coblentz, 1996; Figure 1.3). This observation has led many investigators to conclude that plate boundary forces are the principal control on the first-order character of the intraplate stress field (Zoback *et al.*, 1989; Richardson, 1992; Gölke and Coblentz, 1996). In contrast to most other plates, σ_{Hmax} orientations in the Australian continent are not uniform and do not parallel the north-northeast direction of absolute plate velocity (Figure 1.3). Hence, an initial evaluation of the origin of the Australian intraplate stress field might suggest that plate boundary forces do not exert a similar control on the intraplate stress field of continental Australia. However, the results of finite element modelling of the *in situ* stress field of the Indo-Australian plate (IAP) has shown that the plate boundary forces indeed play a major role in determining the first-order stress field in continental Australia (Cloetingh and Wortel, 1986; Coblentz *et al.*, 1995; Coblentz *et al.*, 1998). These studies have demonstrated that the complexity in the Australian stress field can be accounted for by recognition of the heterogeneous convergent northeastern boundary of the IAP. Nevertheless, these previous studies failed to completely account for the stress field in large portions of central and eastern Australia and were based on a very incomplete 'observed' *in situ* stress dataset.

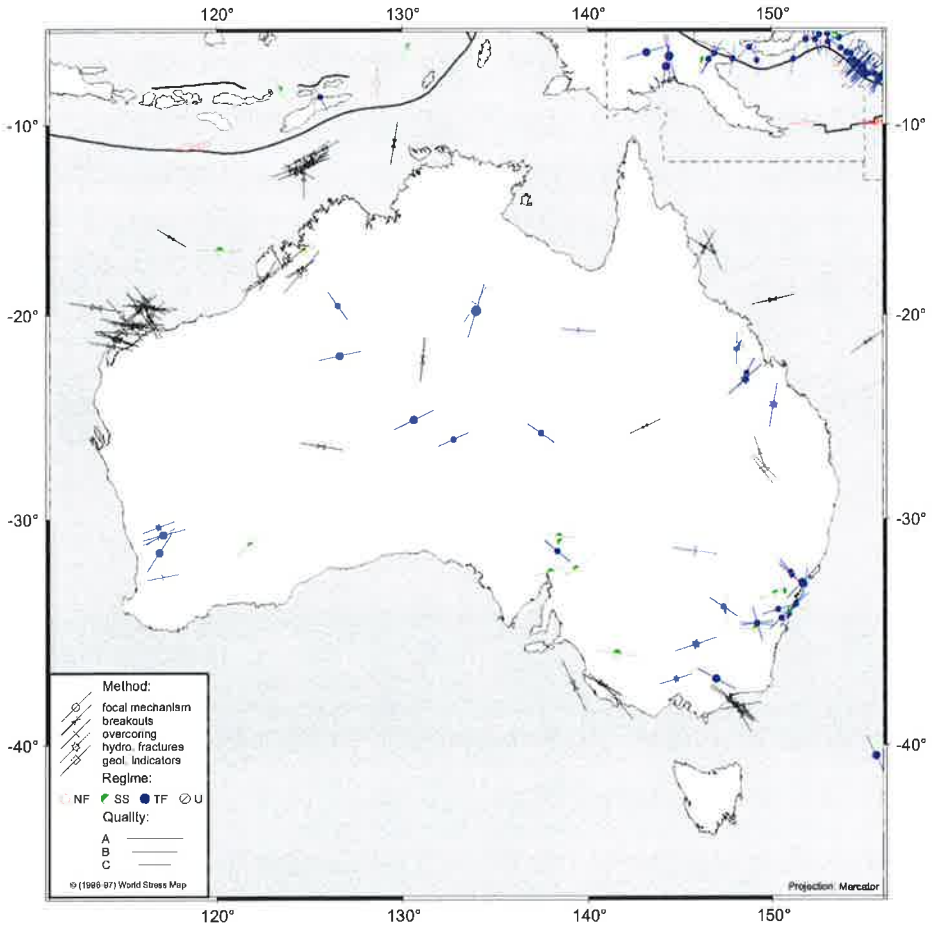

Figure 1.2 Stress map of Australia from the WSM 1997 release showing the poor data coverage over Australia (Müller *et al.*, 1997). This map does not include New Guinea, which is included in the ASM database.

The aims of this thesis are (1) to improve knowledge of the *in situ* stress field of the Bowen, Sydney and Perth Basin areas of Australia, which are poorly represented in the ASM database (2) to evaluate and define the regional *in situ* stress field of continental Australia using the new *in situ* stress measurements presented for the Bowen, Sydney and Perth Basins in this thesis and the additional stress measurements available in the ASM database and (3) to use the regional *in situ* stress field to constrain new finite element models of the plate boundary and topographic forces acting on the IAP.

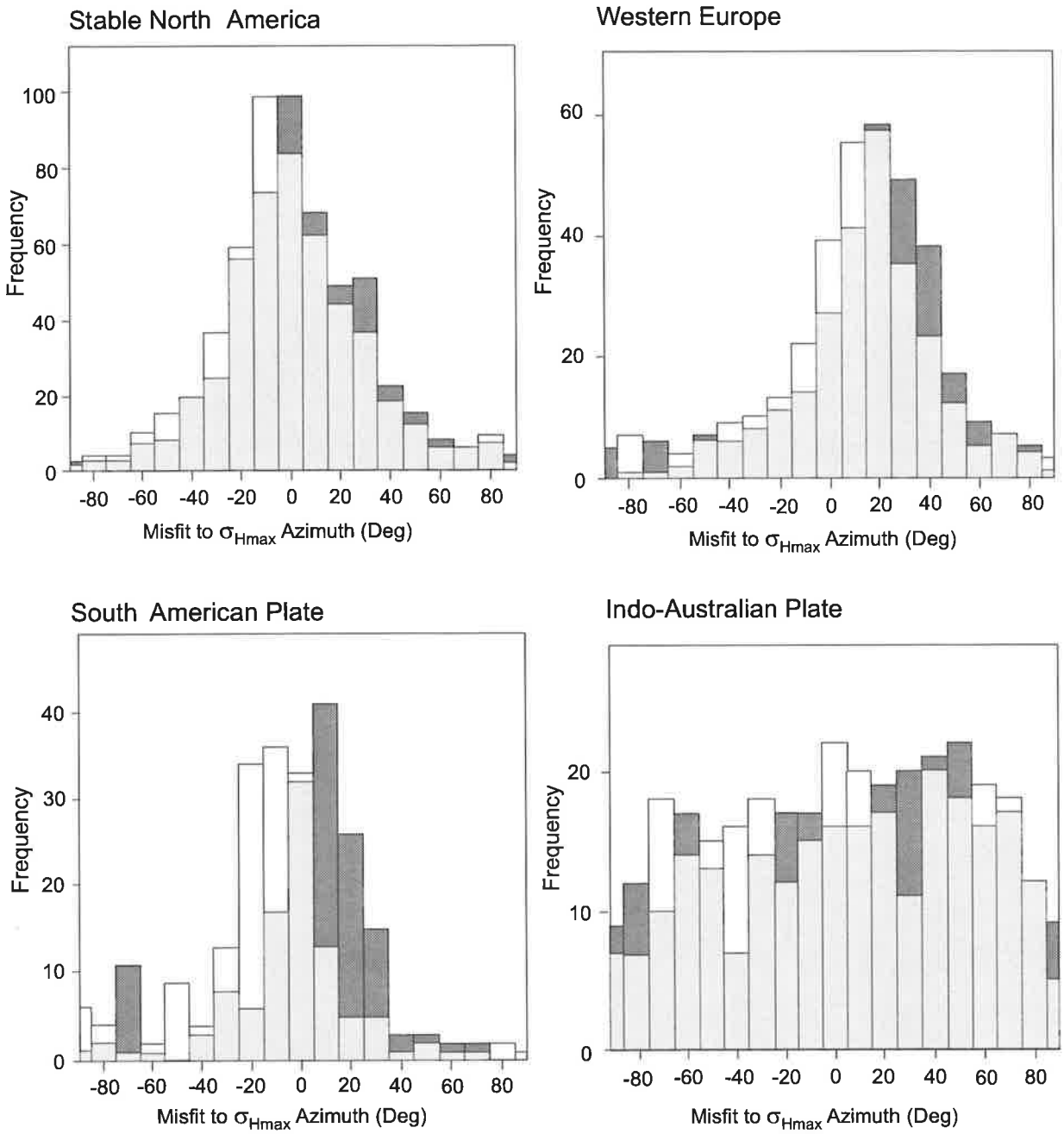

Figure1.3 Histograms of the angular difference between the observed σ_{Hmax} azimuth and ridge push torque and absolute velocity azimuths for stable North America, Western Europe, the South America plate and the Indo-Australian Plate. The darkest shading is for absolute velocity directions, the white histograms are for ridge torque directions and the grey shading is used where the two histograms over-lap. From Richardson (1992).

1.2 Determining the *In Situ* Stress Field

Rock stress cannot be measured directly and can only be inferred by disturbing the rock. Also, rock stress cannot be inferred accurately due to the complex nature of rocks and rock masses (Amadei and Stephansson, 1997). Under good conditions where the rock is linearly elastic, homogenous and continuous, it is generally possible to determine rock stresses with an error of ±10-20% for their magnitude and an error of ±10-20° for their orientation (Amadei and Stephansson, 1997). In poor quality rock (weathered, weak, soft or heavily fractured) the measurement of rock stresses is extremely difficult.

In situ stress data for the Australian continent are compiled within the ASM database, which is a subset of the WSM database. Three versions of the WSM database have been released, Zoback (1992), which included 95 reliable measurements for the Australian continent, Müller *et al.* (1997) and Müller *et al.* (2000). In addition, there have been two published releases of the ASM database, Hillis *et al.* (1998) with 206 measurements and Hillis and Reynolds (2000) with 319 measurements. The majority of the data added to the ASM database between Hillis *et al.* (1998) and Hillis and Reynolds (2000) are presented in this thesis.

A number of different methods are available to determine the *in situ* stress field indirectly in the rock mass. These methods include earthquake focal mechanisms, hydraulic fracturing, overcoring, borehole breakouts, drilling induced tensile fractures and geological indicators. All of these methods, except geological indicators, will be discussed and utilized in this thesis.

Each stress measurement technique has advantages and limitations. The hydraulic fracturing technique is one of the most popular *in situ* stress determination techniques available, as it provides information on both the orientation and magnitude of the *in situ* stress field. However, hydraulic fracturing measurements are commonly undertaken at shallow depths in association with engineering work and hence, the information obtained may not be representative of the tectonic stress field at depth (Zoback and Zoback, 1980). Similar limitations also inhibit the overcoring technique. In contrast, earthquake focal mechanisms provide *in situ* stress information from a much greater depth range (many kilometres). They also provide important information on the relative stress magnitudes of the principal stresses. Nonetheless, earthquake focal mechanisms also have their limitations. The earthquake may have resulted from slip along a pre-existing plane of weakness (McKenzie, 1969a) or may represent deformation due to the complex interaction of active faults, and hence the

information provided would not relate directly to the tectonic *in situ* stress field (Zoback, 1992).

Analysis of borehole breakouts and drilling induced tensile fractures from petroleum wells provides the majority of the *in situ* stress measurements for the ASM database. These measurement techniques are applied at depths intermediate to those of the shallower engineering type measurements (hydraulic fracturing and overcoring) and the deeper earthquake focal mechanisms. The major limitation associated with borehole breakouts and drilling induced tensile fractures is the lack of absolute or relative stress magnitude information such as that provided by the other three techniques. Thus, approximately half of the *in situ* stress indicators in the ASM database provide no information on the stress regime.

1.3 Modelling the *In Situ* Stress Field

Finite element modelling of the *in situ* stress field can be performed at a variety of scales, from broad-scale tectonic forces to the perturbations of the stress field around a fault (e.g. Richardson and Reding, 1991; Saucier *et al.*, 1992; Stefanick and Jurdy, 1992; Coblentz and Sandiford, 1994; Homberg *et al.*, 1997; Meijer *et al.*, 1997). This thesis will examine the broad-scale tectonic forces, such as plate boundary and potential energy forces, which influence the regional *in situ* stress field of continental Australia. Examination of the forces acting along the plate boundaries provides valuable information on the dynamics of plate tectonics (Richardson, 1992).

Numerical modelling of the stress field has traditionally been conducted with two-dimensional plane models (e.g. Bird and Piper 1980; Bott, 1991; Bird and Kong, 1994). However, thin-plate modelling of this kind cannot handle regional or global problems. Various other numerical modelling techniques have been developed (e.g. Richardson *et al.*, 1979; Kong and Bird, 1995; Peltzer and Saucier, 1996). The finite element modelling approach that is used in this thesis treats the IAP as a thin elastic shell consisting of many small planar-triangle elements (e.g. Richardson *et al.*, 1979; Richardson and Reding, 1991; Coblentz and Richardson, 1996).

A number of finite element modelling studies have been conducted on the IAP, including Cloetingh and Wortel (1986), Coblentz *et al.* (1995) and Coblentz *et al.* (1998). Modelling work by Cloetingh and Wortel (1986) demonstrated the important effect boundary forces have

on the intraplate stress field of the IAP. Nevertheless, they failed to explain why the ridge push force does not appear to dominate the intraplate stress field of the IAP, as is the case in most other plates. Further modelling work by Coblentz *et al.* (1995) and Coblentz *et al.* (1998) established that the torque arising from the ridge push force is the principal contributor to the first-order intraplate stress field. The modelling work of Cloetingh and Wortel (1986) predicted high intraplate stress magnitudes (of the order of hundreds of megapascals) throughout much of the IAP. In comparison, Coblentz *et al.* (1995) and Coblentz *et al.* (1998) produced models with significantly lower tectonic stress magnitudes. Their models primarily differed in the applied forces along the northern margin and the Tonga-Kermadec segment. Cloetingh and Wortel (1986) suggested that subduction forces acting along the northern and eastern plate margins produce significant tension in the IAP. However, this contradicts the *in situ* stress data, which suggests the Australian continent is dominated by a compressive stress regime (Denham *et al.*, 1979). Also, modelling results from Coblentz *et al.* (1998) showed that tensional stresses produced by subduction zones increased stress focussing along the collisional boundaries with a corresponding increase in the predicted stress magnitude but with little reorientation of predicted σ_{Hmax} orientations.

Previous finite element modelling studies of the IAP (Cloetingh and Wortel, 1986; Coblentz *et al.*, 1995; Coblentz *et al.*, 1998) have all accounted for the broad rotation in the stress field present across northwestern Australia. However, these studies cannot explain the observed stress field in other areas of the Australian continent. The present study builds on the previous modelling work in three main ways. Firstly, whereas previous studies relied on a *qualitative* assessment of the fit between predicted and observed stresses, here a *quantitative* assessment is employed. Previous *qualitative* studies failed to develop a satisfactory model of the entire continental Australian intraplate stress field, particularly in areas of eastern Australia. This *quantitative* assessment between the observed and predicted stress field has allowed the determination of the optimal boundary force combination for the current observed stress field. Secondly, the observed stress field used in the present study is considerably more refined than those used in previous investigations due to the significant increase in the amount of *in situ* stress data. Finally, the present study employs a 'basis-set' approach to computing the predicted intraplate stress field. This method allows rapid evaluation of a very large number of models (millions of boundary force combinations) and provides a quantitative assessment of the fit between the observed and predicted stress fields.

Once the regional *in situ* stress trend throughout the IAP has been defined and modelled using the broad-scale tectonic forces, it is possible to identify any local perturbations in the *in situ* stress field. These local perturbations are a result of local sources of stress and cannot be accounted for by broad-scale tectonic forces. It is beyond the scope of this project to model the local stress variations, however, a discussion is included on the possible sources of the local stress perturbations in both the Sydney and Perth Basins.

1.4 Thesis Outline

Chapter 2 provides a theoretical description of the *in situ* stress tensor discussing both the far field and near wellbore stress fields. Chapter 3 describes five different methods for determining the *in situ* stress field relevant to this thesis. The five techniques discussed include borehole breakouts, drilling induced tensile fractures, hydraulic fracturing, overcoring and earthquake focal mechanisms. Together, these two chapters review the theory and limitations associated with determining the *in situ* stress field.

Chapters 4 and 5 contain a description of the *in situ* stress field of the Bowen Basin and Sydney Basin, respectively. The *in situ* stress field in these basins was determined using new hydraulic fracturing and overcoring measurements from a Commonwealth Scientific and Industrial Research Organisation (CSIRO) database covering eastern Australia (Hillis *et al.*, 1999). A Mohr-Coulomb analysis of the propensity for failure in these basins was conducted using the shallow engineering measurements and compared to the relative seismicity of the two basins as indicated by deeper earthquakes. The *in situ* stress field of the basins is discussed in the context of both regional and local sources.

Chapter 6 discusses the *in situ* stress field of the Perth Basin and includes new data based on borehole breakout analysis. Stress orientations in the Perth Basin are discussed both in terms of regional plate boundary forces and local fault related effects.

Chapter 7 determines the regional *in situ* stress field within continental Australia by the use of stress province definition and stress trajectory mapping. The stress orientations within 15 of the 16 stress provinces produce mean stress orientations that are statistically significant. The stress trajectories provide a technique for smoothing and interpolating unevenly distributed stress data and thereby clarifying regional trends. Both the stress provinces and stress trajectories reveal the systematic, continental-scale rotation of the stress orientation

throughout continental Australia. The stress orientations defined by 12 of the 16 stress provinces are used to constrain the finite element modelling presented in Chapter 8.

Chapter 8 evaluates the tectonic forces controlling the present day regional intraplate stress field in continental Australia through the use of finite element modelling. Results from Chapter 7 are used to constrain the modelling, which uses a new 'basis-set' method to expedite evaluation of the misfit between the observed and predicted intraplate stresses. The modelling results indicate that the major features of the regional stress field in continental Australia can be explained in terms of a geologically plausible array of tectonic boundary and potential energy forces.

Several parts of this thesis have been published in various forms. Chapter 6 is only slightly modified from a paper published in Geophysical Research Letters. A manuscript version of Chapter 8, describing tectonic force modelling of the IAP has recently been accepted for publication by the Journal of Geophysical Research. In addition I have co-authored several papers related to my thesis work, which have been published in Exploration Geophysics, the Australian Journal of Earth Sciences and the Journal of the Geological Society, London. Reprints of published manuscripts are included in Appendix H.

Chapter 2

The *In Situ* Stress Tensor

2.1 The Stress Tensor

This chapter briefly describes the *in situ* stress tensor and related topics as background to this thesis. Stress (σ) is defined as the force (F) per unit area (A):

$$\sigma = F/A \, . \qquad \text{(Eq. 2.1)}$$

The S.I. unit for measuring stress is the Pascal (Pa). Throughout this thesis mega Pascal (MPa), corresponding to 10^6 Pascals, is used due to the large stresses involved in geological processes. In the fields of rock mechanics and geology the sign convention states that compressive stresses are positive. This is a result of most stresses in the earth's crust being exclusively compressive. Stresses within rocks at depth in the subsurface are referred to as *in situ* stresses.

It is necessary to identify the stresses related to surfaces oriented in three orthogonal directions to give a complete description of the stress state at a point. This description is termed the stress tensor:

$$\begin{pmatrix} \sigma_{xx} & \tau_{xy} & \tau_{xz} \\ \tau_{yx} & \sigma_{yy} & \tau_{yz} \\ \tau_{zx} & \tau_{zy} & \sigma_{zz} \end{pmatrix}.$$

The stress tensor consists of nine component vectors, three components that act in a direction normal to a surface and are referred to as normal stresses (σ_{ii}, $i = x, y, z$) and six components that act in a direction parallel to a surface and are referred to as shear stresses (τ_{ij}, $i \neq j$).

At any point within a homogenous stress field it is always possible to find three mutually orthogonal planes upon which the shear stresses are zero. These three planes are referred to as the principal planes of stress. The normal stresses on the principal planes are the principal stresses, often denoted by σ_1, σ_2 and σ_3 with the convention that $\sigma_1 > \sigma_2 > \sigma_3$. The stress tensor

is fully constrained if the orientations and magnitudes of the three principal stresses are known:

$$\begin{pmatrix} \sigma_1 & 0 & 0 \\ 0 & \sigma_2 & 0 \\ 0 & 0 & \sigma_3 \end{pmatrix}.$$

Since no shear stress can exist in the plane of the earth's surface, one of the principal stresses in the upper crust must be oriented perpendicular to the surface. In general, one principal stress is usually within 20° of vertical except beneath very rough topography (McGarr and Gay, 1978). Thus, the other two principal stresses are oriented approximately horizontal, parallel to the ground surface. Throughout this thesis the assumption that the vertical stress (σ_v) is a principal stress and hence the maximum and minimum horizontal stresses (σ_{Hmax} and σ_{hmin}) are also principal stresses has been used.

Anderson (1951) assumed horizontal and vertical stresses are principal stresses and classified three possible states of stress and associated faulting styles according to the relative magnitudes of the horizontal and vertical stresses (Figure 2.1). The states of stress and associated fault styles are the normal faulting stress regime ($\sigma_v > \sigma_{Hmax} > \sigma_{hmin}$), the strike-slip faulting stress regime ($\sigma_{Hmax} > \sigma_v > \sigma_{hmin}$) and the reverse or thrust faulting stress regime ($\sigma_{Hmax} > \sigma_{hmin} > \sigma_v$). In this thesis the term normal faulting stress regime refers only to the relative magnitudes of the three principal stresses, likewise strike-slip and reverse faulting stress regimes.

In a reverse fault regime the stress tensor is:

$$\begin{pmatrix} \sigma_{Hmax} & 0 & 0 \\ 0 & \sigma_{hmin} & 0 \\ 0 & 0 & \sigma_v \end{pmatrix}.$$

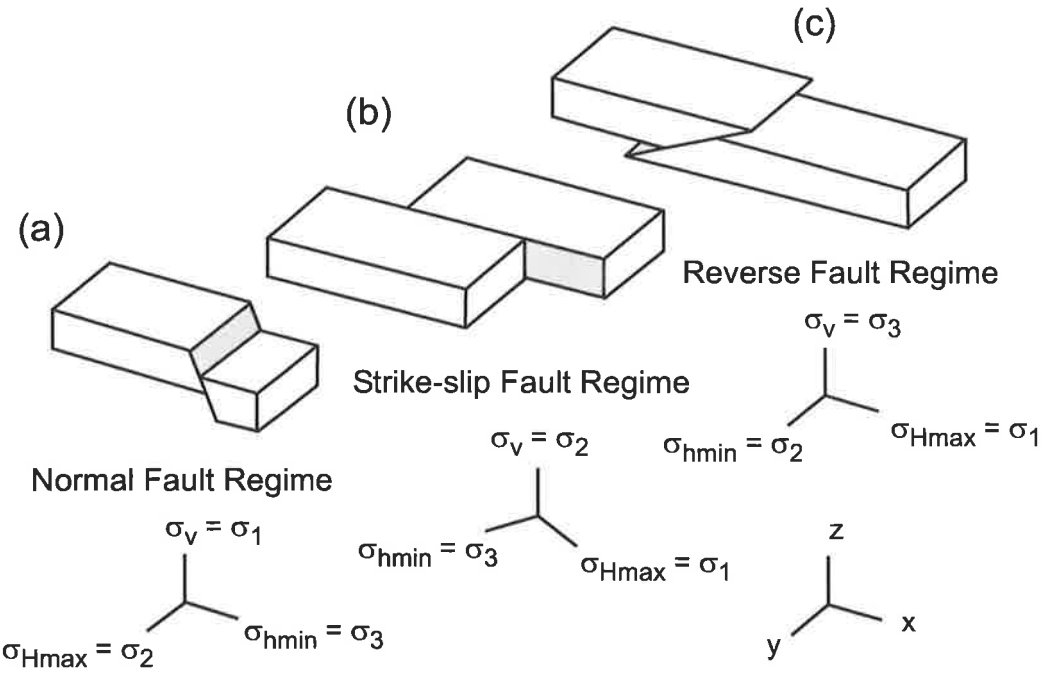

Figure 2.1 The three Andersonian stress states and associated styles of faulting **(a)** normal fault regime, **(b)** strike-slip fault regime and **(c)** reverse fault regime. After Engelder (1993)

2.2 Reference States of Stress

When studying stress it is often convenient to consider the reference state of stress that may occur in the absence of tectonic forces and density heterogeneities (McGarr, 1988). The simplest reference state is that of lithostatic stress found in magma:

$$\sigma_1 = \sigma_2 = \sigma_3 \Rightarrow \sigma_{Hmax} = \sigma_{hmin} = \sigma_v = P_m, \qquad \text{(Eq. 2.2)}$$

where P_m is the pressure within the magma. The lithostatic state of stress implies that the rocks have no long term shear strength and thus behave as a fluid (Engelder, 1993). However, experiments suggest that most rocks support at least a small differential stress for very long periods (Kirby, 1983). The lithostatic state of stress is likely to dominate in the deeper mantle and core, but is likely to be rare in the lithosphere.

The uniaxial strain reference state assumes the rocks in the sub-surface are constrained laterally and deform elastically (Engelder, 1993). Hence, there is no strain in the horizontal direction and horizontal compression is developed due to the inability of the rocks to expand laterally (McGarr, 1988). In the uniaxial strain reference state, horizontal stress increases as a function of the depth of burial, but at a slower rate than the vertical stress:

$$\sigma_{Hmax} = \sigma_{hmin} = \left[\frac{\nu}{1-\nu}\right]\sigma_v = \left[\frac{\nu}{1-\nu}\right]\rho g z, \qquad \text{(Eq. 2.3)}$$

where ν is Poisson's ratio, varying between 0 and 0.5, g is the acceleration due to gravity and z is the depth. When $\nu = 0.5$ (i.e. a fluid) the uniaxial strain reference state is the same as the lithostatic reference state. The uniaxial reference state is thought to approximate that of newly deposited sediments in a sedimentary basin. However, modification in the elastic properties of the sedimentary rocks during diagenesis and creep relaxation may bring the state of stress in sedimentary basins closer to lithostatic (Engelder, 1993).

2.3 Effective Stress and Rock Failure

Rocks under natural conditions generally contain pore fluid at some pressure. Pore fluid pressure has a critical influence on the fracturing of rocks because effective stress, not total stress, controls rock deformation (Terzaghi, 1943; Hubbert and Rubey, 1959). Effective stress (σ') is the difference between the total applied stress (σ) and the pore fluid pressure (P_o):

$$\sigma' = \sigma - P_o . \qquad \text{(Eq. 2.4)}$$

Most porous rocks obey Terzaghi's (1943) effective stress law for rocks, which states that a pressure of P_o in the pore fluid of a rock will cause the same reduction in peak normal stress as caused by a reduction of the confining pressure by an amount equal to P_o (Terzaghi, 1943; Equation 2.4).

A three-dimensional Mohr diagram is commonly constructed to investigate the likelihood of rock failure (Figure 2.2). A detailed description on the construction of the Mohr diagram is outlined in Appendix B. Throughout this thesis the Coulomb criterion is used as the failure envelope (Figure 2.2). For intact rock the Coulomb failure criterion for frictional sliding is defined by (Figure 2.2):

$$\tau = C + \mu (\sigma_n - P_o) , \qquad \text{(Eq. 2.5)}$$

where σ_n and τ are, respectively, the components of normal and shear stress acting on the failure plane, C is the cohesive or shear strength of the rock and μ is the coefficient of internal

friction. For pre-existing planes of weakness with no cohesive strength the Coulomb failure envelope is represented by a straight line passing through zero shear stress (Figure 2.2):

$$\tau = \mu (\sigma_n - P_o) . \qquad \text{(Eq. 2.6)}$$

Laboratory experiments on a wide variety of rock types have suggested that the coeffiecient of internal friction, μ, lies between 0.6 and 1.0 (Byerlee, 1978). This range suggested by laboratory measurements seems to be applicable to crustal faults (Zoback and Healy, 1984). Throughout this thesis Byerlee's (1978) law has been used, which states that at normal stresses less than 200 MPa, the critical shear stress to initiate slip is equal to 0.85 times the effective normal stress. Thus, the coeffiecient of internal friction, μ, equals 0.85.

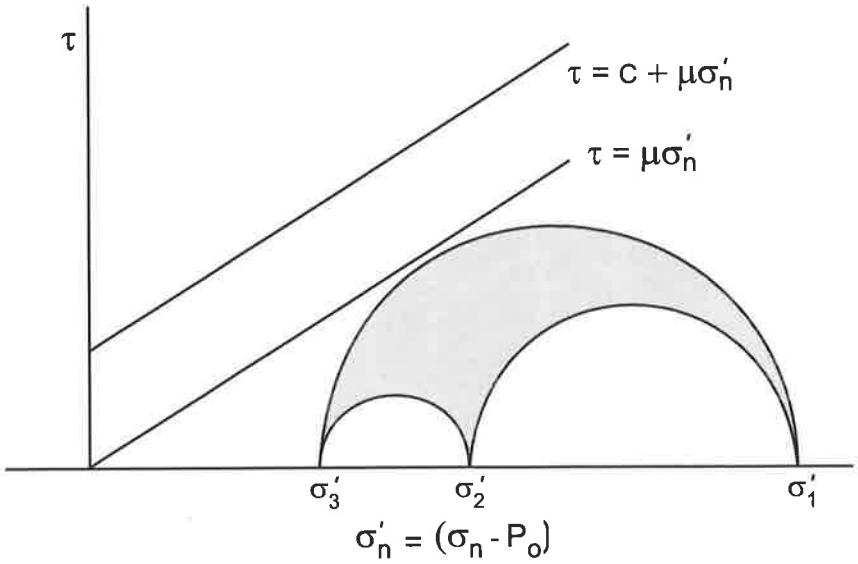

Figure 2.2 Three-dimensional Mohr diagram plotting shear stress versus effective normal stress. Coulomb failure criterions for intact rock (Equation 2.5) and for pre-existing planes of weakness with no cohesive strength (Equation 2.6) have been plotted.

2.4 Frictional Limits to Stress

The stresses at which rocks in the sub-surface fail provide useful limits to *in situ* stresses. Shear failure occurs if the ratio of shear stress to normal stress becomes too large (Byerlee, 1978). Shear failure acts to reduce the ratio of principal stresses to below critical levels (Barton and Zoback, 1994; Figure 2.3). Shear failure in the normal fault regime acts to increase σ_{hmin}, which moves the Mohr circle below the failure envelope and away from failure (Zoback and Healy, 1992; Figure 2.3a). Shear failure in the reverse fault regime acts to decrease σ_{Hmax}, which again moves the Mohr circle below the failure envelope and away from failure (Figure 2.3b).

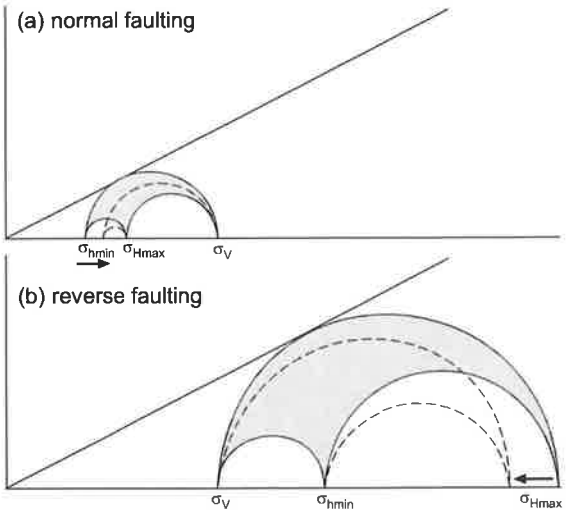

Figure 2.3 Shear failure acts to **(a)** increase σ_{hmin} in a normal fault regime and **(b)** decrease σ_{Hmax} in a reverse fault regime. In both cases the radius of the Mohr circle decreases causing it to move further away from the failure envelope. Note that σ_v (overburden stress) is essentially invariable for a failure event at a given depth. After Barton and Zoback (1994).

The ratio of the maximum to minimum effective stress that causes slip on pre-existing faults that are optimally oriented with respect to the stress field was determined by Jaeger and Cook (1979):

$$\frac{\sigma_1 - P_o}{\sigma_3 - P_o} = \left\{\left(\mu^2 + 1\right)^{1/2} + \mu\right\}^2. \qquad \text{(Eq. 2.7)}$$

This relation provides frictional limits to the ratio of maximum to minimum effective principal stresses provided there exists optimally oriented faults of no cohesion (Zoback and Healy, 1984). For the case of $\mu = 0.6$ the ratio of the effective maximum principal stress to the effective minimum principal stress equals 3.12. For the case of $\mu = 1.0$ the ratio of the effective maximum principal stress to the effective minimum principal stress equals 5.83. If either σ_1 or σ_3 are known, then limits can be placed on the other by using Equation 2.7. This requires the value of μ to either be known or assumed.

In the case of normal faulting Equation 2.7 becomes:

$$\frac{\sigma_v - P_o}{\sigma_{hmin} - P_o} = \left\{\left(\mu^2 + 1\right)^{1/2} + \mu\right\}^2 \qquad \text{(Eq. 2.8)}$$

In the case of strike-slip faulting Equation 2.7 becomes:

$$\frac{\sigma_{Hmax} - P_o}{\sigma_{hmin} - P_o} = \left\{\left(\mu^2 + 1\right)^{1/2} + \mu\right\}^2 \qquad \text{(Eq. 2.9)}$$

In the case of reverse faulting Equation 2.7 becomes:

$$\frac{\sigma_{Hmax} - P_o}{\sigma_v - P_o} = \left\{\left(\mu^2 + 1\right)^{1/2} + \mu\right\}^2 \qquad \text{(Eq. 2.10)}$$

The allowable values for the horizontal principal stresses in the earth's crust are shown in Figure 2.4 following the above equation. The plot has been depth normalized by dividing the horizontal stresses by the vertical stress, which allows data at all depths to be plotted on the one diagram. Normal, reverse and strike-slip faulting environments have been marked out according to Anderson's (1951) theory of faulting (Figure 2.4). The *in situ* stresses are expected to plot within the area bound by the frictional limits (Figure 2.4).

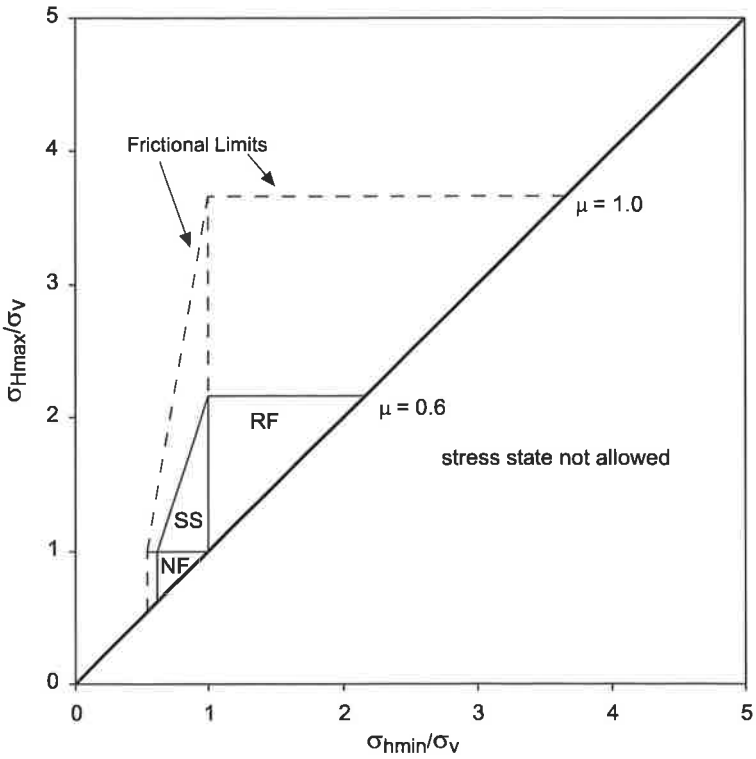

Figure 2.4 Frictional limits to stress based on the frictional strength of favourably oriented fault planes for μ = 0.6 and 1.0. The area within the allowable limits of stress is divided following Anderson's (1951) theory of faulting. RF = reverse fault regime; SS = strike-slip fault regime; NF = normal fault regime. After Moos and Zoback (1990).

2.5 Stresses Around the Wellbore

When a well is drilled, stressed rock is removed and the rock surrounding the wellbore must take up the stress that was previously carried by the removed material. This causes an alteration of the stress state surrounding the wellbore. Kirsch (1898) developed a number of equations describing the stress components around a circular opening subjected to far-field stresses. The stress at the wellbore wall subjected to a uniaxial stress field (σ_{Hmax}) is described by the following equation:

$$\sigma_\theta = \sigma_{Hmax} - 2\sigma_{Hmax}\cos 2\theta \,, \qquad \text{(Eq. 2.11)}$$

where σ_θ is the circumferential stress and θ is the angle around wellbore wall measured from the direction of σ_{Hmax}. Figure 2.5 shows the stress trajectories around a circular hole in a plate of elastic rock subject to uniaxial compression. The maximum circumferential compression around the circular hole occurs at points M and N ($\theta = 90^o$). In this uniaxial case, Equation 2.11 reduces to $3\sigma_{Hmax}$ at those points. The minimum amount of compression occurs at points A and B ($\theta = 0^o$) where Equation 2.11 reduces to $-\sigma_{Hmax}$. Thus, a total circumferential stress difference of $4\sigma_{Hmax}$ occurs around the open hole. In this example the wellbore is subject only to far-field compression, however due to the stress perturbation around the open hole, points A and B are subjected to tension.

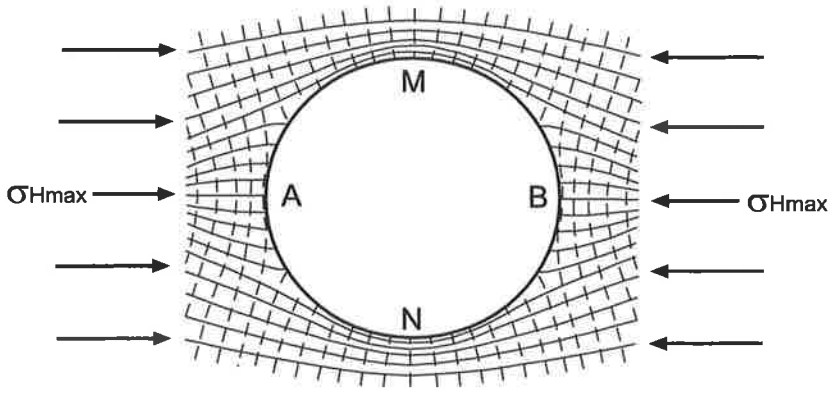

Figure 2.5 Stress perturbations around an open hole. Solid lines indicate σ_1 stress trajectories and dashed lines indicate σ_3 stress trajectories. After Jaeger (1962)

The general equations for the stresses around a vertical circular hole in a homogenous, isotropic and linearly elastic rock mass subjected to effective minimum and maximum principal stresses (σ'_{Hmax} and σ'_{hmin}) are as follows (Kirsch, 1898):

$$\sigma_r = \frac{1}{2}(\sigma'_{Hmax} + \sigma'_{hmin})\left(1 - \frac{a^2}{r^2}\right) + \frac{1}{2}(\sigma'_{Hmax} - \sigma'_{hmin})\left(1 + \frac{3a^4}{r^4} - \frac{4a^2}{r^2}\right)\cos 2\theta - \Delta P\frac{a^2}{r^2} \,, \qquad \text{(Eq. 2.12)}$$

$$\sigma_\theta = \frac{1}{2}(\sigma'_{Hmax} + \sigma'_{hmin})\left(1 + \frac{a^2}{r^2}\right) + \frac{1}{2}(\sigma'_{Hmax} - \sigma'_{hmin})\left(1 + \frac{3a^4}{r^4}\right)\cos 2\theta - \Delta P\frac{a^2}{r^2} \,, \qquad \text{(Eq. 2.13)}$$

$$\tau_{r\theta} = -\frac{1}{2}(\sigma'_{Hmax} + \sigma'_{hmin})\left(1 - \frac{3a^4}{r^4} + \frac{2a^2}{r^2}\right)\sin 2\theta \,, \qquad \text{(Eq. 2.14)}$$

where θ is the angle around wellbore wall measured from the direction of σ_{Hmax} (Figure 2.6), ΔP is the difference between the fluid pressure in the borehole and that in the formation, r is the distance from the centre of a circular hole of radius a (Figure 2.6) and σ_r, σ_θ and $\tau_{r\theta}$ are the radial, circumferential and shear stresses respectively.

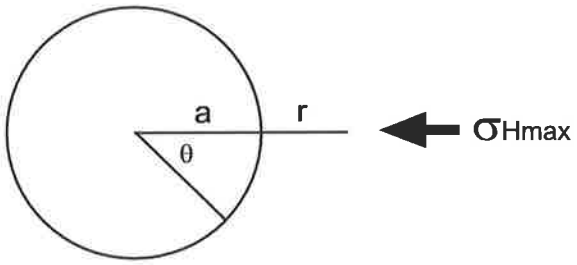

Figure 2.6 Cross section through circular wellbore of radius a. The distance from the centre of the wellbore is r and θ is the angle around wellbore wall measured from the direction of σ_{Hmax}.

At the wellbore wall the three stress components, σ_r, σ_θ and $\tau_{r\theta}$ reduce to (a = r):

$$\sigma_r = \Delta P \,, \qquad \text{(Eq. 2.15)}$$

$$\sigma_\theta = \sigma'_{Hmax} + \sigma'_{hmin} - 2(\sigma'_{Hmax} - \sigma'_{hmin})\cos 2\theta - \Delta P \,, \qquad \text{(Eq. 2.16)}$$

$$\tau_{r\theta} = 0 \,. \qquad \text{(Eq. 2.17)}$$

As with the uniaxial case, the maximum compressive stress is at θ = 90° (direction of σ_{hmin}), while the minimum compressive stress is at θ = 0° (direction of σ_{Hmax}).

Chapter 3

In Situ Stress Indicators

3.1 Introduction

The *in situ* stress field in the earth's crust cannot be measured directly, however, it can be inferred indirectly by disturbing the rock mass using a variety of different methods. These methods include earthquake focal mechanisms, hydraulic fracturing, overcoring, borehole breakouts, drilling induced tensile fractures and geological indicators. Some of the assumptions, difficulties and uncertainties of inferring *in situ* stress information from these indicators are discussed in this chapter. Geological indicators of the stress field, such as recent fault slip and volcanic alignments, are not presented in either the ASM database or this thesis and thus, are not discussed in this chapter.

3.2 Borehole Breakouts

3.2.1 Theory

Borehole breakouts were initially observed by Cox (1970) who was first to identify intervals of elongate cross sections in oil wells. Further studies were conducted by Babcock (1978) who named the elongations 'breakouts' and proposed that breakouts were controlled by pre-existing fractures that the drill bit encountered. However, Bell and Gough (1979) were the first to propose that these features were a stress related phenomenon produced by stress concentrations near the wellbore. Numerous studies (Gough and Bell, 1982; Hickman *et al.*, 1985; Plumb and Hickman, 1985; Zoback *et al.*, 1985; Bell, 1990) have been conducted confirming that elongations of the wellbore cross-section, termed borehole breakouts, are a stress related feature.

Borehole breakouts form when the circumferential stress acting around a wellbore exceeds the compressive strength of the rock (Zoback *et al.*, 1985; Figure 3.1). When this arises in a vertical well conjugate shear fractures form at the wellbore wall centred on the σ_{hmin} direction, causing the rock to spall off (Gough and Bell, 1982). As a consequence, the wellbore becomes enlarged in the σ_{hmin} direction (Figure 3.1). The distribution of circumferential stress around a vertical wellbore is described by:

$$\sigma_0 = \sigma'_{Hmax} + \sigma'_{hmin} - 2(\sigma'_{Hmax} - \sigma'_{hmin})\cos 2\theta - \Delta P \ , \qquad \text{(Eq. 3.1)}$$

for abbreviations see Section 2.5. The distribution of circumferential stress around a vertical wellbore is illustrated in Figure 3.1. Zones of borehole breakouts can be detected on logging tools such as the four-arm dipmeter, the borehole televiewer, the formation microscanner (FMS) and the formation microimager (FMI). Experiments in the laboratory have replicated the development of the shear fractures leading to the elongation of the wellbore and thus confirmed the theory of breakout formation (Figure 3.2).

Four major assumptions are made when using borehole breakouts to infer *in situ* stress directions (Plumb and Cox, 1987).

(1) Failure and elongation of the borehole is due to brittle failure and not plastic deformation.

(2) Elongation is not due to the intersection of natural fractures.

(3) The well is drilled parallel to one of the principal stresses.

(4) The borehole elongation is symmetric.

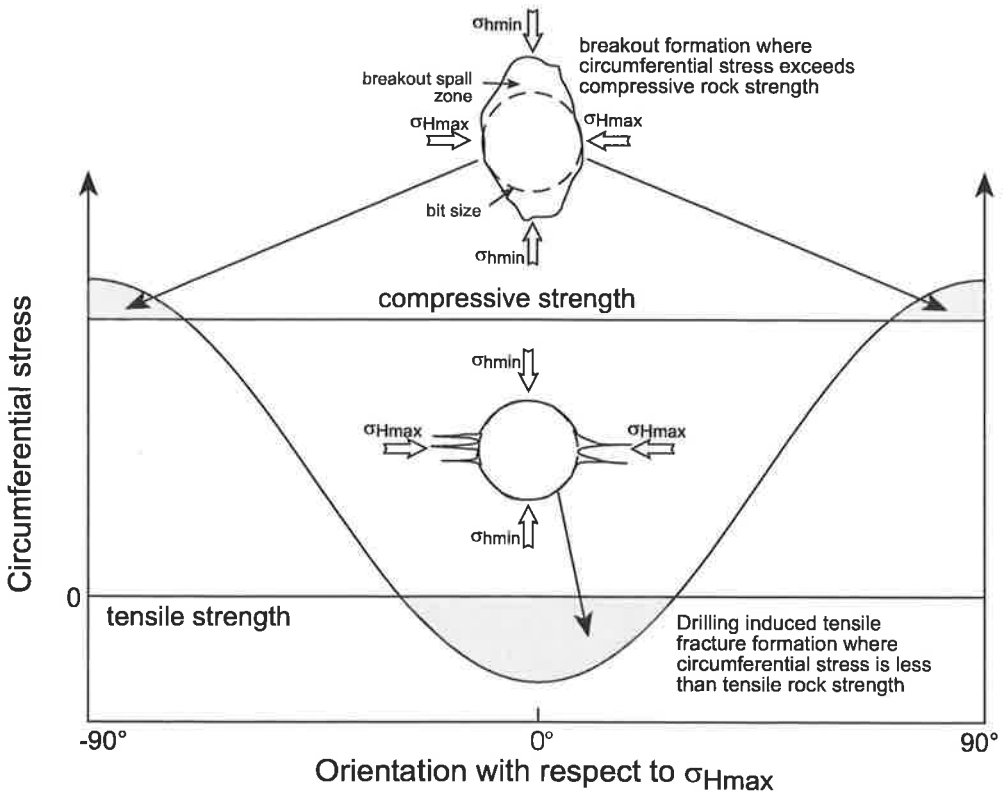

Figure 3.1 Circumferential stress around a vertical wellbore with respect to the σ_{Hmax} orientation. Breakout formation occurs where the circumferential stress exceeds the compressive rock strength. Drilling induced tensile fracture formation occurs at 90° to the breakouts where the circumferential stress is less than the tensile rock strength.

A number of investigators (Zoback *et al.*, 1985; Barton *et al.*, 1988; Vernik and Zoback, 1992) have attempted to derive stress magnitude information from borehole breakouts. Barton *et al.* (1988) proposed a method of magnitude estimation by determining the breakout width from borehole televiewer images. Theoretical and laboratory studies have concluded that breakout geometry is related to the horizontal stress magnitudes (Prensky, 1992). However, significant disagreement exists to the extent at which breakout geometry can be used to determine horizontal stress magnitudes (Detournay and Roegiers, 1986; Bell, 1990; Engelder, 1993). Hence, no stress magnitude information derived from borehole breakouts is present in either the WSM or ASM databases.

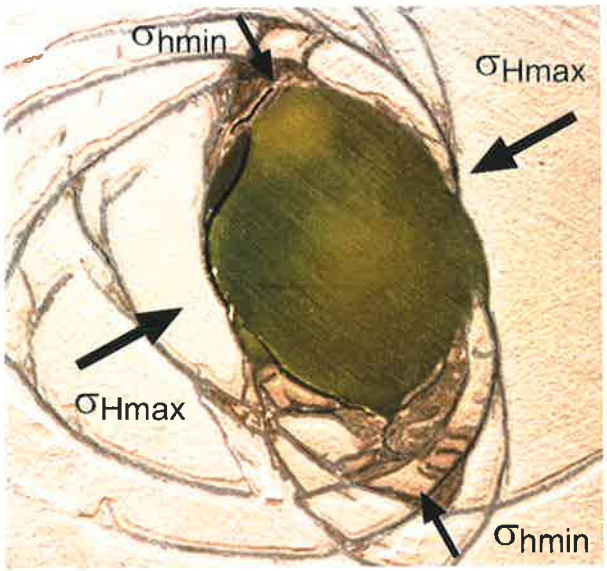

Figure 3.2 Hollow cylinder laboratory test showing shear fracture development due to the stress concentration around a circular hole.

Stress orientations determined from borehole breakouts have been found to be consistent with other, independent *in situ* stress indicators such as overcoring, hydraulic fracturing and earthquake focal mechanisms (Blümling *et al.*, 1983; Fordjor *et al.*, 1983; Hickman *et al.*, 1985; Plumb and Hickman, 1985; Zoback *et al.*, 1985; Plumb and Cox, 1987). Borehole breakouts make up 22% of the reliable data in the WSM (Müller *et al.*, 2000). In comparison, borehole breakouts contribute 43% of the reliable data in the current ASM database (Section 7.2). Borehole breakouts provide important stress data at a depth that is intermediate between earthquake focal mechanisms and engineering type *in situ* stress measurements. Furthermore, they provide multiple measurements over a considerable depth range allowing a statistical determination of the stress orientation and its scatter about the mean (Zoback, 1992).

Borehole breakouts are only reliable indicators of the principal stresses when one principal stress is vertical (Peska and Zoback, 1995). Neither the WSM nor the ASM databases include

observations of wellbore failure in inclined boreholes. This is a result of (1) the four-arm caliper not being able to clearly distinguish between breakouts and key seats in inclined boreholes, which result from mechanical erosion of the wellbore wall (Plumb and Hickman, 1985) and (2) breakout direction in inclined boreholes deviating significantly from what is predicted in vertical boreholes (Mastin, 1988).

3.2.2 Interpretation

Borehole breakouts can be interpreted by either dipmeter or imaging tools. The four-arm dipmeter tool is most commonly used in older wells and has now been largely replaced by the imaging tools. The four-arm dipmeter tool consists of four pad-type electrodes arranged in a coplanar orthogonal pattern (Plumb and Hickman, 1985). The pads are mechanically pressed against the wellbore wall and measure electrical conductivity. Two independent calipers measure the wellbore diameter between pads 1-3 and 2-4. The reference pad (pad 1) is magnetically oriented so all orientations must be corrected for magnetic declination. The four-arm dipmeter tool is pulled up the wellbore and rotates clockwise due to the torque on the logging cable (Bell, 1990). Thus, when a borehole elongation is encountered one pair of pads locks in near the major axis and rotation ceases (Bell, 1990). An example of a four-arm dipmeter log with consistent breakouts in the north-south direction is shown in Figure 3.3.

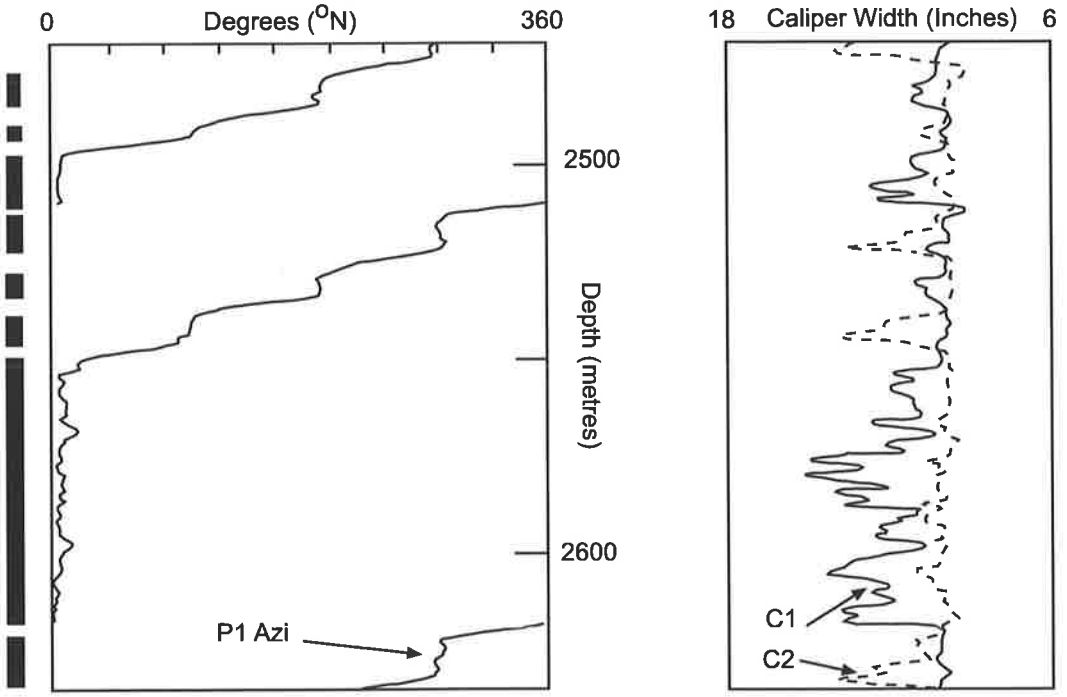

Figure 3.3 Section of four-arm dipmeter log data from Walyering 3 in the Perth Basin showing consistent breakout in a north-south direction (indicated by the black vertical bars at the extreme left), thus the σ_{Hmax} orientation is east-west. C1 and C2 are the two orthogonal borehole diameters. P1Azi is the azimuth of caliper pad 1 with respect to north. These data have been digitised and replotted from the original analogue records for increased clarity.

A number of different wellbore enlargements can occur that are not stress-related features (Figure 3.4). These wellbore enlargements are probably influenced by a variety of factors including lithologic type, formation consolidation, pre-existing fractures and drilling history (Dart and Zoback, 1989). Six types of borehole enlargements have been described by Dart and Zoback (1989). In order to prevent the misidentification of breakouts a set of criteria for their recognition was developed by Plumb and Hickman (1985):

(1) The tool rotation stops in the zone of elongation.

(2) The caliper difference is greater than 0.6 cm.

(3) The smaller caliper readings is close to bit size, or if the smaller caliper reading is greater than bit size, it should exhibit less variation than the larger caliper.

(4) The length of the breakout is greater than 30 cm.

(5) The direction of elongation should not consistently coincide with the azimuth of the high side of the borehole when the hole deviates from vertical.

The above set of criteria has been used as the basis of most breakout-related studies (Hillis, 1991; Gölke and Brudy, 1996; Hillis *et al.*, 1997; Zajac and Stock, 1997; Mildren and Hillis, 2000; Reynolds and Hillis, 2000).

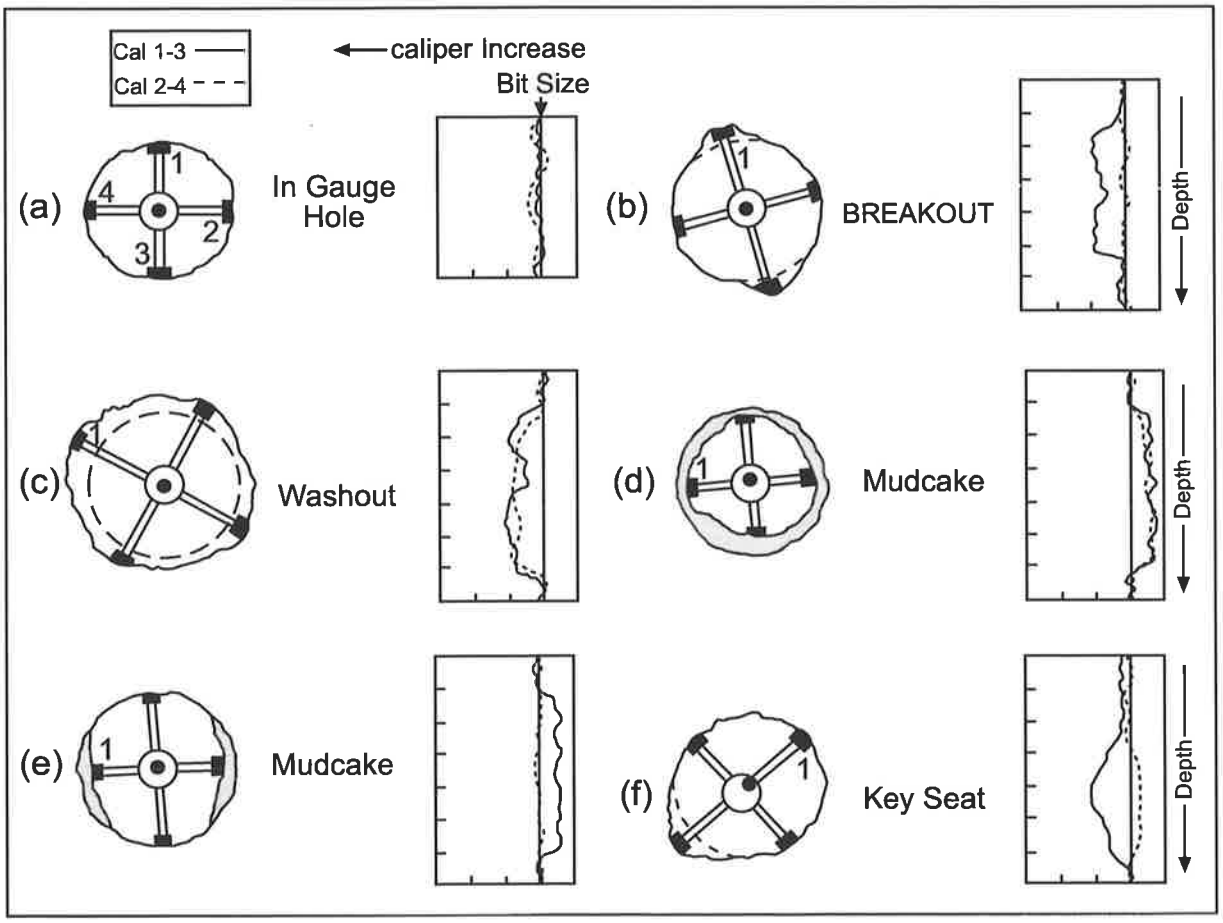

Figure 3.4 Various potential borehole shapes with their corresponding caliper traces. Only example **(b)** is the result of the stress concentration around the wellbore. After Plumb and Hickman (1985)

Image log data allows more confident recognition of breakouts than the older dipmeter data. These tools include acoustic borehole televiewers (Wiley, 1981) and the resistivity-measuring formation microscanners (Ekstrom *et al.*, 1987). Borehole televiewers are rarely used in oil wells as they are time consuming and expensive to run (Bell, 1990). However resistivity imaging logs are now widely run. Borehole breakouts on image logs are generally poorly resolved (poor pad-wall contact), 'blobby' zones of low resistivity where drilling mud has invaded breakout related fractures. Occasionally the fractures that induce spalling are imaged. Image log breakout zones are usually associated with elongation of wellbore diameter, but sometimes incipient breakouts (where spalling of the wellbore wall has not yet occurred) are recognised by image logs. A FMS log showing both breakouts and drilling induced tensile fractures (Section 3.3) in the same wellbore is shown in Figure 3.5.

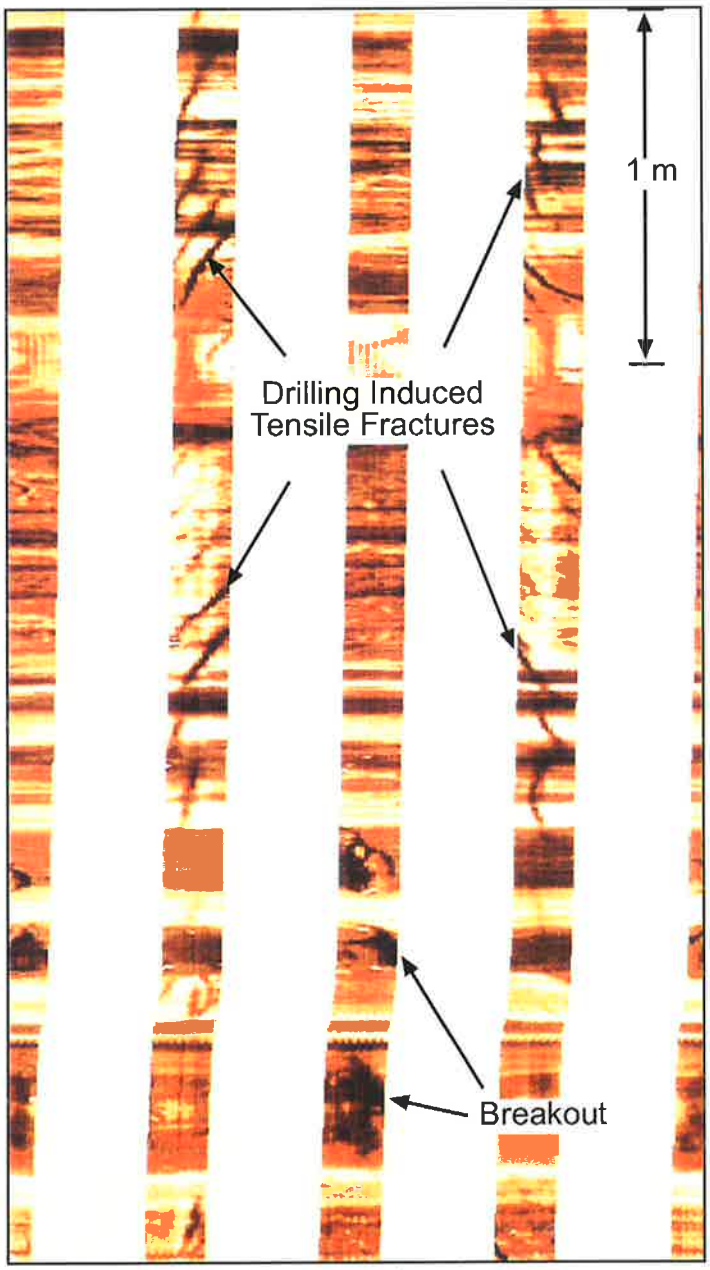

Figure 3.5 FMS log showing breakout and drilling induced tensile fractures occurring in the same well at approximately 90° apart. Breakouts are characterized by dark 'blobby' zones of low resistivity. The vertical drilling induced tensile fractures appear inclined in the image due to the vertical exaggeration.

3.2.3 WSM Quality Ranking Scheme

The WSM quality ranking scheme for borehole breakouts is shown in Table 3.1 (Zoback, 1992). All borehole breakout stress indicators compiled in this thesis and within the ASM database have been quality ranked according to this scheme. The quality ranking ranges from A, which corresponds to a well with many consistently orientated breakouts, to E, which corresponds to a well showing extreme scatter of breakout orientations or no reliable breakouts.

Table 3.1 WSM quality ranking scheme for borehole breakouts (Zoback, 1992).

A	B	C	D	E
Ten or more distinct breakout zones or combined length of >300 m in a single well with s.d. ≤12° Or Average of breakouts in two or more wells in close geographic proximity with combined length >300 m and s.d. ≤12°	At least six distinct breakout zones or combined length >100 m in a single well with s.d. ≤20°	At least four distinct breakout zones or combined length >30 m in a single well with s.d. ≤25°	Less than four consistently oriented breakouts or <30 m combined length in a single well Or Breakouts in a single well with s.d. ≥25°	Wells in which no reliable breakouts detected Or Extreme scatter of orientations, no significant mean determined (s.d. >40°)

3.3 Drilling Induced Tensile Fractures

3.3.1 Theory

Drilling induced tensile fractures (DITF) have only been relatively recently recognised, using image log data, as a stress indicator. Hence, the WSM did not include DITF in the compilation of Zoback (1992). However, the ASM and subsequent versions of the WSM compilations now include DITF as stress indicators.

Drilling induced tensile fractures form when the circumferential stress around the wellbore is less than the tensile strength of the rock (Figure 3.1). Their formation is analogous to the fracture formation during a hydraulic fracture test (Section 3.4), and is the result of the natural stress state being perturbed by drilling. However, DITF do not propagate into the wellbore wall unless the wellbore fluid pressure exceeds the minimum principal stress (Barton *et al.*, 1998). Hence no drilling mud is recorded lost. Drilling induced tensile fractures can form under a wide range of stress conditions and do not necessarily require significant wellbore fluid pressures (Peska and Zoback, 1995). In a vertical wellbore DITF form approximately vertically in the orientation of σ_{Hmax} (Brudy and Zoback, 1993). In deviated wells DITF are inclined to the wellbore wall in an en-echelon pattern (Barton, 2000). However, DITF will not

cut across the entire wellbore wall like a natural fracture and are generally confined to less than 30° around the circumference of the hole (Aadnoy and Bell, 1998). Thus, only the vertical DITF can directly provide the orientation of σ_{Hmax}.

Brudy and Zoback (1999) have identified a number of characteristic features of DITF.

(1) They occur in pairs on opposite sides of the borehole wall.
(2) They trend either approximately parallel to the borehole axis or at an angle to the borehole axis (en-echelon type).
(3) Their lengths commonly range between 0.1 and 2.0 m.
(4) In vertical wells they occur at the azimuth of σ_{Hmax} where the circumferential stresses are least compressive.
(5) Usually the traces of the fractures show small kinks and are not perfectly straight.

Several observations strongly suggest that the tensile fractures are created during the drilling process and are not a pre-existing feature. First, vertical fractures are indicated on image logs but are not present in the removed core (Brudy and Zoback, 1999). Second, the vertical fractures are relatively abundant (Brudy and Zoback, 1999). The chance of intersecting a large number of vertical fractures parallel to the wellbore is relatively small. Thus, interpreting the vertical fractures, as pre-existing natural fractures would imply a vast population of vertical fractures were present, which is most unlikely. Finally, the vertical tensile fractures occur at exactly 90° to the orientation of breakouts (Brudy and Zoback, 1999).

3.3.2 Interpretation

Interpretation of DITF requires the use of image logs such as the borehole televiewer (Wiley, 1981) or formation microscanner/formation microimager (Ekstrom *et al.*, 1987). Drilling induced tensile fractures cannot be recognised on older dipmeter logs. With the use of image logs, the fracture orientation and thus stress orientation can be accurately determined. Figure 3.5 shows a FMS log showing both borehole breakouts and DITF. The DITF are dark in colour as they absorb drilling mud and consequently exhibit high conductivity. In contrast, cemented fractures tend to be resistive.

3.3.3 Quality Ranking Scheme

The quality ranking scheme for DITF is shown in Table 3.2. Unlike the other stress indicators discussed in this thesis, DITF were not recognised as an *in situ* stress indicator at the time of the development of the WSM quality ranking scheme. Thus, no quality ranking scheme had been developed for DITF. The ranking scheme developed below is the same as that used to rank borehole breakouts (Table 3.1), but applied to DITF. All stress indicators based on DITF compiled within the ASM database have been ranked according to this scheme. The quality ranking ranges from A, which corresponds to a well with consistently orientated fractures, to E, which corresponds to a well showing extreme scatter of DITF orientations or no reliable fractures.

Table 3.2 Quality ranking scheme for DITF based on the WSM ranking scheme for borehole breakouts.

A	B	C	D	E
Ten or more distinct tensile fractures or combined length of >300 m in a single well with s.d. ≤12°	At least six distinct tensile fractures or combined length >100 m in a single well with s.d. ≤20°	At least four distinct tensile fractures or combined length >30 m in a single well with s.d. ≤25°	Less than four consistently oriented tensile fractures or <30 m combined length in a single well Or Tensile fractures in a single well with s.d. ≥25°	Wells in which no reliable tensile fractures detected Or Extreme scatter of orientations, no significant mean determined (s.d. >40°)

3.4 Hydraulic Fracturing Measurements

3.4.1 Theory

Hydraulic fracturing was initially used in the petroleum industry to enhance recovery from oil wells. Hubbert and Willis (1957) first used the theory of elasticity to conclude that the direction of the induced hydraulic fracture and the pressures recorded were directly related to the principal *in situ* stresses. Hydraulic fracturing has subsequently become a common method for estimating the state of *in situ* stress at great depths. The technique involves fracturing the rock surrounding a borehole by increasing the pressure within a sealed off test interval. The magnitude and direction of the *in situ* stresses can then be calculated from the pressure-time record and wellbore logging tools.

The main aim in hydraulic fracture testing is to produce a vertical fracture within a test interval that propagates perpendicular to σ_{hmin}. This enables the direction and magnitudes of the two horizontal stresses to be determined. As previously discussed, a borehole causes perturbations in the local stress field (Figure 2.5). When fluid is pumped into the sealed off

test interval, the pressure on the wall of the borehole is reduced and at some point around the wellbore becomes tensile (Amadei and Stephansson, 1997). As shown by Equation 3.1 and Figure 3.1, in a vertical well, the stresses become tensile and a hydraulic fracture is formed at the orientation of σ_{Hmax}.

When applying the hydraulic fracturing technique in vertical boreholes, one principal stress is assumed to be coaxial with the borehole and equal to the overburden pressure. It is then expected that a vertical fracture will initiate at the borehole wall along an orientation perpendicular to σ_{hmin}. These assumptions may not hold true in areas of high topographic relief, complex structural geology or shallow measurements (Haimson, 1978b; Haimson, 1980). When σ_v is the minimum principal stress then hydraulic fracture initiation is typically unaffected, but the fracture may rotate into the horizontal plane some distance away from the borehole (Haimson, 1993).

Elastic Model

The elastic model described in this section applies to vertical wellbores and vertical induced fractures. Determination of the magnitude of the σ_{Hmax} requires the assumption that the concentration around a circular borehole is perfectly elastic. A number of other assumptions apply to the elastic model (Haimson, 1993).

(1) Plane strain is maintained in the test interval.
(2) The tested rock is brittle (i.e. will not undergo excessive deformation), isotropic and homogeneous.
(3) The pore fluid obeys Terzaghi's (1943) effective stress law.
(4) Pressurization fluid injected into the test interval does not permeate into the surrounding rock.
(5) Failure leading to hydraulic fracturing is controlled by the maximum effective tensile stress criterion.

Haimson and Fairhurst (1967) derived the following equation from the results of Hubbert and Willis (1957), which forms the basis of stress determination from hydraulic fracturing measurements:

$$P_b = 3\sigma_{hmin} - \sigma_{Hmax} - P_o + T\,, \qquad \text{(Eq. 3.2)}$$

where P_b is the breakdown pressure (at which time there is a dramatic drop in pressure in the test interval as discussed in Section 3.4.3), P_o the formation pore pressure and T the tensile strength of the formation. The magnitude of σ_{hmin} is determined directly from the test pressure record while the tensile strength is determined from laboratory tests (Section 3.4.3). The magnitude of σ_{Hmax} is calculated using Equation 3.2 assuming all the parameters stated above are known. If the tensile strength of the rock has not been laboratory determined then the equation developed by Bredehoeft *et al.* (1976) can be used:

$$T = P_b - P_r , \qquad \text{(Eq. 3.3)}$$

where P_r is the reopening pressure of the fracture in a subsequent cycle of pressurization (Section 3.4.3). For Equation 3.3 to hold the fracture must completely close between each cycle of pressurization and the reopening pressure must be the pressure at which the pre-existing hydraulic fracture just begins to open (Amadei and Stephansson, 1997). Equation 3.2 can thus be modified to eliminate the need to calculate the tensile strength of the rock:

$$P_r = 3\sigma_{hmin} - \sigma_{Hmax} - P_o \qquad \text{(Eq. 3.4)}$$

Poroelastic Model

Equations 3.2 and 3.4 used in the elastic model are only valid if the pore pressure remains constant throughout the hydraulic fracturing test. Thus the fracturing fluid cannot infiltrate the surrounding rock (Haimson, 1993). Experimental evidence indicates that fracturing fluid does penetrate into the surrounding rock causing a subsequent increase in the pore pressure of the formation (Haimson, 1968). This creates an additional stress field, which has not been incorporated in Equations 3.1 and 3.3. For the equations describing the poroelastic model the reader is referred to Haimson and Fairhurst (1967).

3.4.2 Operational Procedure

The equipment set-up required to conduct a hydraulic fracture test is shown in Figure 3.6. A brief description of the operational procedure is discussed here, however a detailed description for rock stress determination using the hydraulic fracturing technique can be found in Kim and Franklin (1987). Packers are used to isolate the test interval, by maintaining the pressure in the packers just above that in the test interval. Pressure transducers are either

located adjacent to the packers or at the surface recording the pressure in both the test interval and the packers.

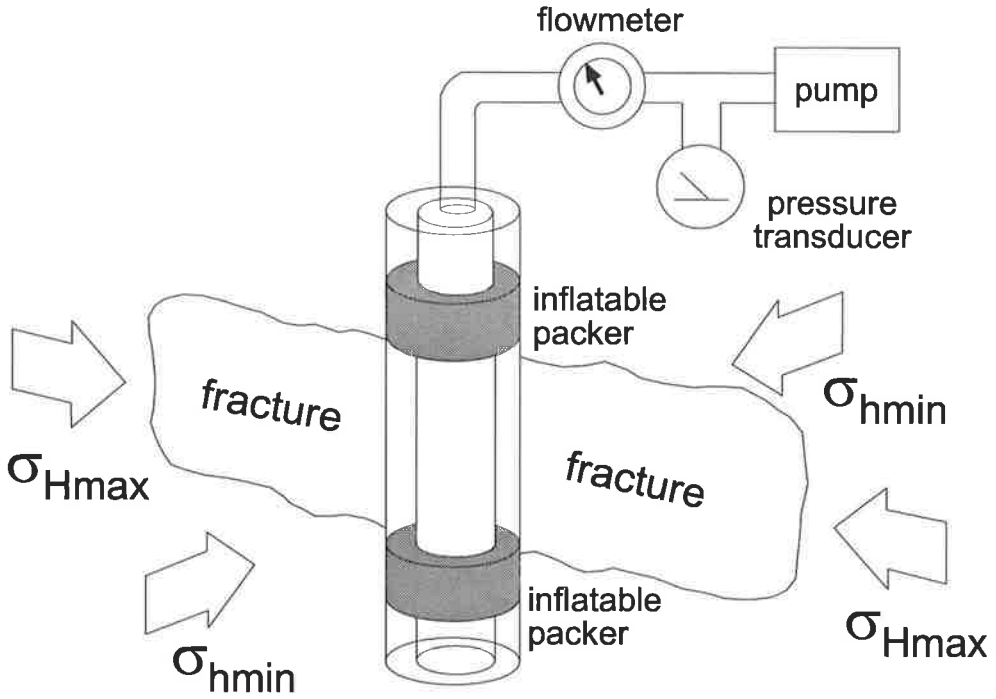

Figure 3.6 Simplified schematic diagram showing the equipment set-up and the direction of propagation of the induced fracture during a hydraulic fracturing test when σ_{hmin} is the smallest principal stress. Modified from Bell (1996).

The first step in performing a hydraulic fracture test is to locate a test interval without the presence of natural fractures. A natural fracture within the test interval will preferentially open when the pressure is increased and prevent the formation of an induced fracture. Opening a natural fracture will prevent the calculation of the *in situ* stresses and hence invalidate the test. The test interval, once selected, is sealed off and pressurisation begins at a constant flow rate.

Slow rates of pressurization are used when testing in relatively impermeable rocks to reduce the chance of the initiated crack changing orientation from that revealed at the borehole wall before pressurization can be stopped and an initial shut-in established (Enever and Walton, 1995). In the case of more permeable rocks, the injection interval is pressurized very rapidly to achieve breakdown as quickly as possible (Engelder, 1993). This approach minimises the time for wellbore fluids to penetrate the rock formation. A large amount of infiltration of wellbore fluids increases the pore pressure close to the wellbore and lowers the effective stress causing a premature breakdown (Engelder, 1993). The initial packer pressure should be below the anticipated breakdown pressure and increased at the same rate as the injection

interval. This reduces the chance of a packer induced fracture and also minimizes the level of uncertainty with regards to the initiation pressure (Enever, 1993).

A sharp peak, followed by a dramatic pressure drop in the pressure-time record signifies breakdown of the formation in the test interval (Figure 3.7). As soon as breakdown is achieved the flow is terminated and the well shut-in. Initially the pressure drops very rapidly eventually slowing down and coming to an equilibrium pressure above hydrostatic. After a few minutes the pressure is released allowing the test interval to drain back to hydrostatic. This represents the completion of one cycle. A number of cycles are normally run over the same test interval to obtain all required parameters and to allow a comparison of the test results. An orientated impression packer or image log maybe used to obtain the orientation of the induced fracture following the pressurization cycles.

3.4.3 Interpretation of Results

Fracture Breakdown Pressure

A sharp peak and rapid decline on the pressure-time record during the initial pressurization cycle marks the breakdown pressure (P_b) of the fracture (Figure 3.7). It is generally possible to pick the breakdown pressure within a small range.

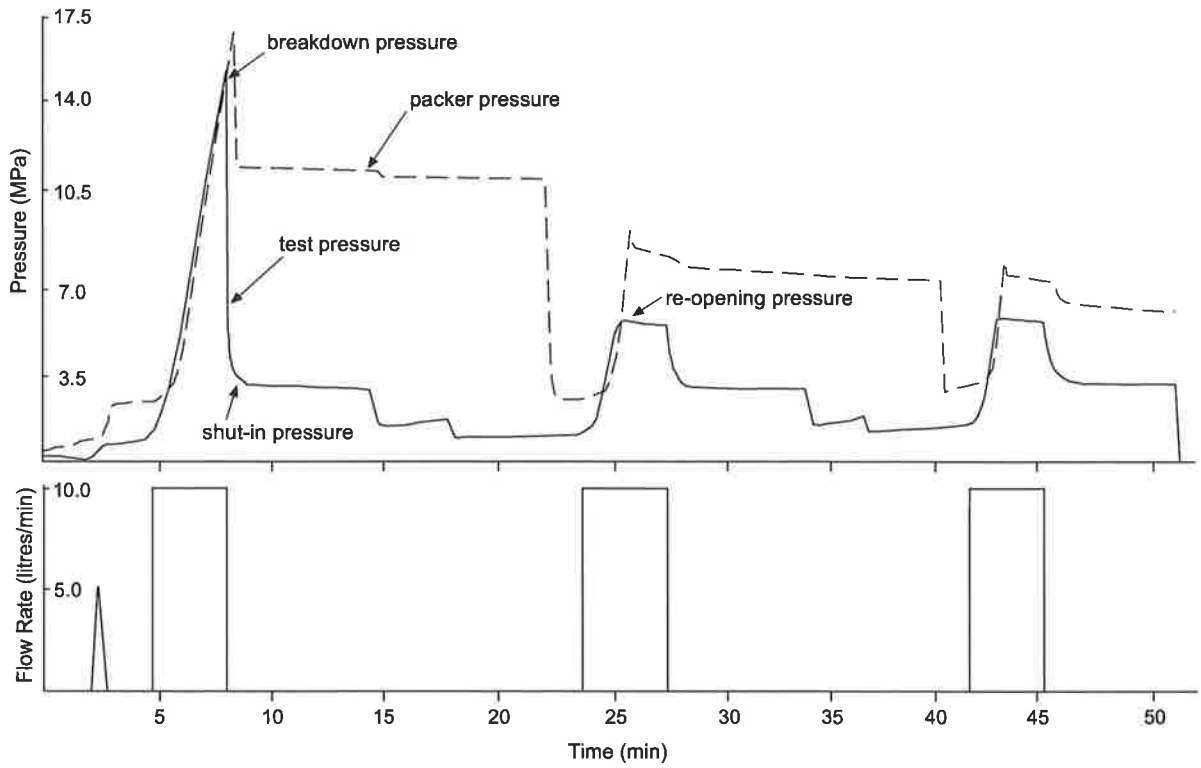

Figure 3.7 Pressure versus time record for a hydraulic fracture test. Dashed line indicates packer pressure and solid line indicates pressure within the test interval. Also plotted is pump flow rate versus time.

Shut-In Pressure

The pressure decline after shut-in is the most important and ambiguous aspect of interpretation of the hydraulic fracturing record. A single pressure exists on the shut-in curve that represents the point at which the fracture initially closes. At this instant the pressure from the fluid no longer supports the crack walls and for a vertical fracture is equal to σ_{hmin} acting to close the fracture. However, a number of definitions and techniques have been developed and used due to the subjective nature of defining the shut-in pressure (de Bree and Walters, 1989; Lee and Haimson, 1989; Woodland and Bell, 1989; Enever, 1993; Jones and Sargeant, 1993; Wright *et al.*, 1996; Desroches and Kurkjian, 1998). Terms used to describe this section of the pressure-time record include the shut-in pressure, instantaneous shut-in pressure (ISIP) and closure pressure. The following definitions have been used to distinguish the above terms (Enever, 1993):

1. The ISIP is the pressure immediately after pumping into the test interval has ceased. It does not mark the pressure when the walls of the hydraulic fracture have come in contact and hence does not equal σ_{hmin}.
2. Shut-in pressure represents the pressure at which the walls of the fracture have come into contact in an impermeable formation. This pressure represents the magnitude of σ_{hmin} in an impermeable formation and is defined using a number of graphical techniques.
3. Closure pressure represents the pressure at which the walls of the fracture have come into contact in a permeable formation. This pressure represents the magnitude of σ_{hmin} in a permeable formation.

The ISIP represents an upper bound to σ_{hmin}, as the fracture may still be open at this point (de Bree and Walters, 1989). A more reliable estimation of σ_{hmin} can be obtained through the use of shut-in pressure or closure pressure depending on the permeability of the formation. Rocks with low to very low permeability exhibit minimal fluid leak-off resulting in a well defined shut-in curve (Enever, 1993). Rocks with higher permeability (e.g. sandstones), produce shut-in curves with a larger radius of curvature making determination of a shut-in pressure ambiguous. To some degree, using a higher viscosity test fluid and increasing the pressurization rate can enhance the pressure-time record (Enever, 1993). Closure pressure must be used in defining σ_{hmin} in highly permeable formations. Fracture closure represents the change from the combination of linear and radial flow to predominantly radial flow (Fjær *et al.*, 1992).

A number of data enhancement techniques have been established to determine both shut-in and closure pressures with varying degrees of accuracy. These include:

- Inflection point method (Gronseth and Kry, 1983);
- Tangent intersection method (Enever and Chopra, 1986);
- Maximum curvature method (Hardy, 1973);
- Exponential Pressure-Decay Method (Aamodt and Kuriyagawa, 1983);
- Pressure-Flowrate Method (Lee and Haimson, 1989), and;
- Bilinear Pressure-Decay-Rate Method (Turnbridge, 1989).

Reopening Pressure

By definition the fracture reopening pressure (P_r) is the pressure in subsequent pressurization cycles where the pressure-time curve departs from that of the first pressurization cycles (Amadei and Stephansson, 1997). The reopening pressure is conventionally determined graphically by superimposing a latter pressurization cycle over the first pressurization cycle. This can often be subjective due to the indistinct change in slope. Lee and Haimson (1989) developed the 'reference threshold' method to over come the subjective nature of this analysis. This method defines the point where the difference in pressure between the two cycles is larger than a statistical 'reference threshold', provided the difference continues to increase from that point on (Lee and Haimson, 1989).

Tensile Strength

The tensile strength of the rock must be known to apply Equation 3.2. Tensile strength may be determined by laboratory tests (Haimson, 1978a; Bjarnason *et al.*, 1989). These tests are usually carried out on rock specimens obtained from normal-size core form the hydraulic fracture tests interval. If the tensile strength is not available then Equation 3.4 must be used.

Stress Orientation

The orientation of an induced vertical fracture indicates the orientation of σ_{Hmax}. The fracture orientation is determined from either an orientated impression packer or an image log. A vertical fracture appears as two vertical traces separated by 180° around the wellbore. In contrast, an inclined fracture produces a complete cycle of a sinusoidal curve. The dip direction of the inclined fracture can be determined from the azimuth of the lower peak while the dip angle is calculated from the arc tangent of the sinusoidal amplitude divided by the borehole radius (Lee and Haimson, 1989). The orientation of the σ_{Hmax} cannot be determined directly from an inclined fracture.

3.4.4 Hydraulic Fracturing Data in this Thesis

The majority of the hydraulic fracturing data for the Bowen and Sydney Basins used in this thesis were from a CSIRO database compiled over many years by Jim Enever (e.g. Enever *et al.*, 1989; Enever, 1993; Enever and Clark, 1997; Enever *et al.*, 1998; Enever, 1999). The work in this thesis includes compiling these data into the ASM and interpreting them within the context of the other ASM data (Hillis *et al.*, 1999). In the course of this thesis the author participated in a hydraulic fracturing experiment with Jim Enever at the Hunter Valley in the Sydney Basin. An interpreted record from this test is shown in Figure 3.8.

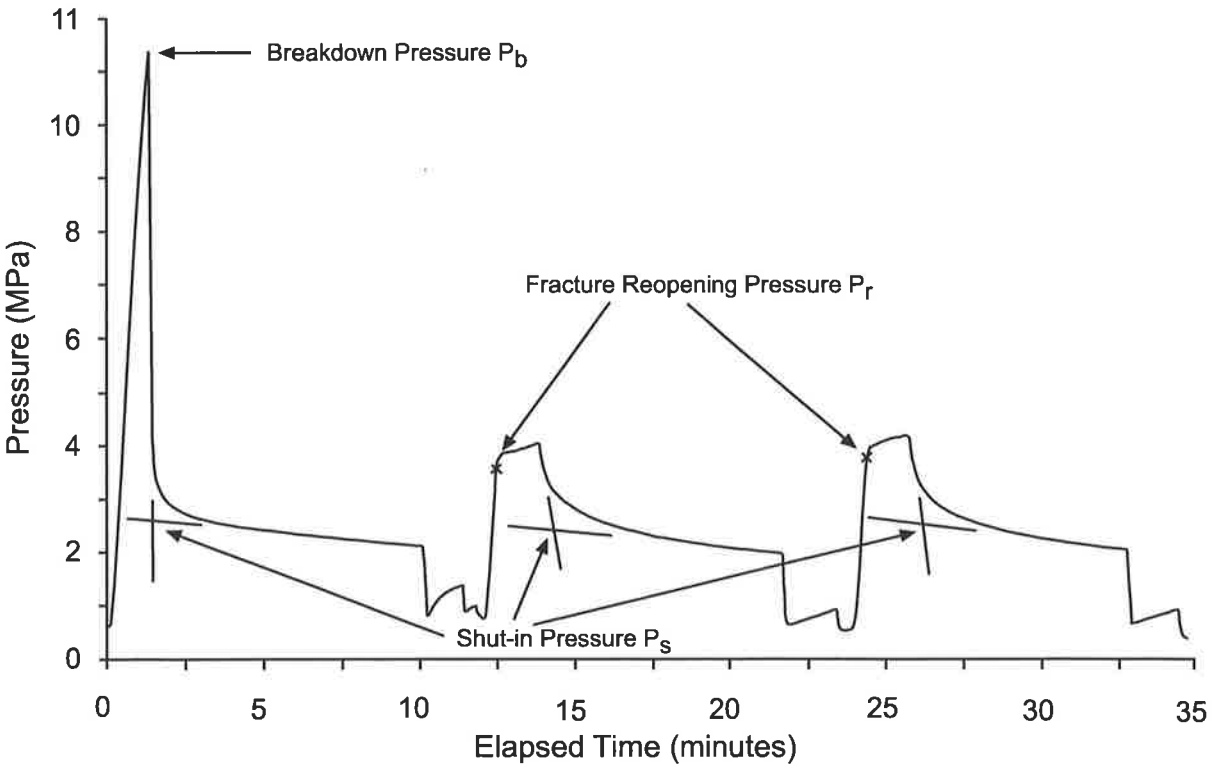

Figure 3.8 Hydraulic fracturing experiment from the Hunter Valley showing fracture breakdown pressure (P_b), shut-in pressure (P_s) and fracture reopening pressure (P_r).

3.4.5 WSM Quality Ranking Scheme

The WSM quality ranking scheme for hydraulic fracturing measurements is shown in Table 3.3 (Zoback, 1992). All hydraulic fracturing stress indicators compiled in this thesis and within the ASM database have been ranked according to this scheme. The quality ranking ranges from A, which corresponds to a site with consistently orientated hydraulic fractures, to E, which corresponds to a site where only stress magnitudes, and not stress orientations have been determined.

Table 3.3 WSM quality ranking scheme for hydraulic fracturing measurements (Zoback, 1992).

A	B	C	D	E
Four or more hydrofrac orientations in single well with s.d. ≤12°, depth >300 m Or Average of hydrofrac orientations for two or more wells in close geographic proximity, s.d. ≤12°	Three or more hydrafrac orientations in a single well with s.d. <20°	Hydrofrac orientations in a single well with 20° < s.d. <25°; distinct hydrofrac orientation change with depth, deepest measurement assumed valid	Single hydrofrac measurement at <100 m depth	Wells in which only stress magnitudes measures, no information on orientations

3.5 Overcoring Measurements

3.5.1 Theory

Overcoring is a term used to describe a variety of strain relief measurement techniques involving the cutting of core with stress-measuring gauges attached. A large variety of overcoring techniques exist (e.g. USBM gauge, Doorstopper, CSIR-type triaxial strain cell, CSIRO HI cell). Only a generalised discussion of the technique is presented here. New overcoring data for the Bowen and Sydney Basins were compiled in the ASM from the CSIRO database. However, the author did not under take any new overcoring experiments or analysis. The overcoring techniques are principally used in engineering and geo-technical work for relatively inexpensive and rapid stress measurements. Overcoring is often grouped together with hydraulic fracturing and classed as an engineering type stress measurement. The technique is able to determine the three-dimensional stress tensor by measuring the strain relief in a body of rock when isolated from the surrounding rock volume. When strain relaxation occurs the amount of expansion is directly proportional to the stress within the rock (Engelder, 1993). The *in situ* stress can subsequently be calculated provided the elastic modulus of the rock is known.

The overcoring technique requires that measurements be made close to a free surface with the strain relief determined over very small areas (McGarr and Gay, 1978). These two issues restrict the usefulness of the overcoring technique as a tectonic stress indicator (Zoback, 1992). The majority of overcoring measurements are made near surface and are affected by things such as local topography, rock anisotropy and nature fracturing (Engelder and Sbar, 1984). Furthermore, a large number of measurements have been performed for specific engineering applications, places where topography, fracturing or nearby excavations could

strongly perturb the regional stress field (Zoback, 1992). Moreover, the stress field needs to be homogeneous throughout the volume of interest before conducting any overcoring measurements.

The successful interpretation of stress relief measurements depends to a great extent on the following factors (Amadei and Stephansson, 1997):

(1) To establish a stress-strain (or displacement) relationship.

(2) To be able to determine rock mass properties from tests on samples.

(3) To have instrumentation sensitive enough to capture small strains or displacements.

Comparison tests (Enever, 1993) have been conducted between overcoring and hydraulic fracturing measurement techniques. These tests have been conducted at sites representing a wide range of geological settings and stress states. A range of hole orientations were also employed. In general both measurement techniques produce similar results and hence validate both techniques (Enever, 1993).

3.5.2 Operational Procedure

Three main steps are commonly followed with all the main overcoring techniques.

1. A large-diameter hole is initially drilled ranging from 60 to 220 mm in diameter in the rock volume being investigated (Figure 3.9a). The hole is drilled to a sufficient distance that any excavation or ground surface effects on the stress measurements can be neglected. For underground excavations, a distance of a least 1.5 to 2.5 opening diameters or spans is generally used (Amadei and Stephansson, 1997).
2. A small pilot hole is then drilled at the end of the larger hole (Figure 3.9b). The pilot hole must be long enough to neglect the effects of its own end as well as the effect of the larger hole. Pilot hole lengths can vary between 300 and 500 mm (Amadei and Stephansson, 1997). The pilot and larger holes must be as concentric as possible. An instrumented device designed to measure small displacements or strains is inserted into the pilot hole (Figure 3.9c).
3. Drilling of the large-diameter hole is resumed with the stresses and strains within the hollow cylinder of rock being partially or totally relieved (Figure 3.9d). The instrumented device records the changes in strains or displacements as the overcoring front proceeds beyond the plane of measurement.

The recovered overcore containing the instrumented device is tested to determine the elastic properties of the rock following overcoring. This is often done in a biaxial (radial) chamber or by axial loading of the overcore. However, the elastic properties of the rocks change on relaxation (Engelder, 1981), hence the laboratory elastic property values permit a close but not exact estimate of the *in situ* stresses.

The instrumented device inserted into the pilot hole for measuring the *in situ* stress can be either a strain cell or a stressmeter. The strain cell allows the pilot hole to deform as if the instrument were not present during strain relaxation (Engelder, 1993). In contrast, the stressmeter acts to resist deformation of the pilot hole as the device has an elastic moduli significantly greater than those of rock (McGarr and Gay, 1978). During overcoring the stress from the host rock is transferred to the active component of the stressmeter. After calibration the stressmeter allows the direct interpolation of absolute stress or stress changes within the rock without requiring information on the elastic properties of the rock (McGarr and Gay, 1978).

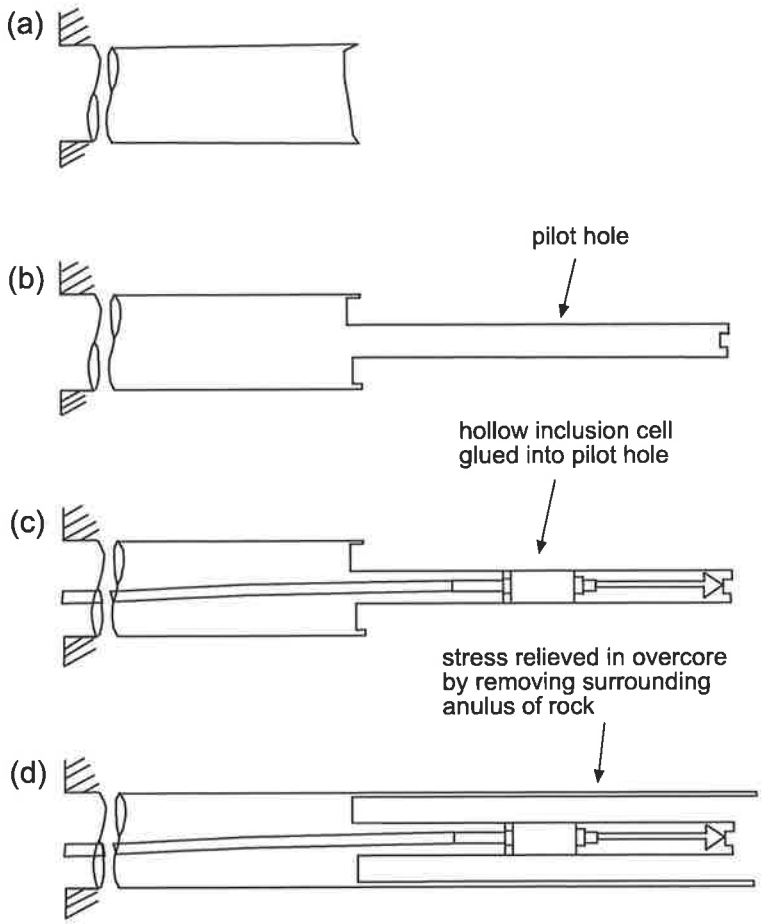

Figure 3.9 Procedure used in the overcoring *in situ* stress measurement technique. **(a)** Initially a large-diameter hole is drilled which is then **(b)** extended with a smaller diameter pilot hole. **(c)** The instrumented device is then placed within the pilot hole and **(d)** the drilling of the larger diameter hole is resumed. Changes in strains or displacements are then recorded on the instrument. Modified from Enever and Walton (1995).

3.5.3 Interpretation of Results

Interpretation of the overcoring test results depends on the technique used. An informative summary of the interpretation procedures can be found in Amadei and Stephansson (1997). Nevertheless, a number of general assumptions are made for the analysis of overcoring measurements in a borehole (Amadei and Stephansson, 1997).

1. The stresses that are relieved during overcoring are equal to the stresses when the rock was in its pre-cored environment.
2. The size of the overcoring diameter does not influence the stress measurement.
3. The response of the rock is linearly elastic during the unloading process associated with overcoring.
4. The rock is assumed to be isotropic. Thus, any anisotropy may reduce the accuracy of the stress measurements.
5. The borehole is circular with smooth surfaces.
6. The rock deforms in plane strain or plane stress.
7. The *in situ* stress field is three-dimensional.

3.5.4 WSM Quality Ranking Scheme

The WSM quality ranking scheme for overcoring measurements is shown in Table 3.4 (Zoback, 1992). All overcoring stress indicators compiled in this thesis and within the ASM database have been ranked according to this scheme. The quality ranking ranges from A, which corresponds with two or more consistently orientated measurements, to E, which corresponds to a site showing extreme scatter with no significant mean. All new overcoring measurements in Chapters 4 and 5 have been given a D quality ranking because details of the individual tests at each site were not available and therefore statistical analysis of the data was not possible. Hence, the new overcoring data represent averaged values at each site with no statistical details. The D quality ranking given to the new overcoring data represents a conservative estimate of the quality of the data.

Table 3.4 WSM quality ranking scheme for overcoring measurements (Zoback, 1992).

A	B	C	D	E
Average of consistent (s.d. ≤12°) measurements in two or more boreholes extending more than two excavation radii from the excavation wall and far from any known local disturbances, depth >300 m	Multiple consistent (s.d. <20°) measurements in one or more boreholes extending more than two excavation radii from excavation well, depth >100 m	Average of multiple measurements made near surface (depth >5-10 m) at two or more localities in close proximity with s.d. ≤25° Or Multiple measurements at depth >100 m with 20° < s.d. <25°	All near-surface measurements with s.d. >15°, depth <5 m Or All single measurements at depth Or Multiple measurements at depth with s.d. >25°	Multiple measurements at a single site or locality with no significant mean (s.d. >40°)

3.6 Earthquake Focal Mechanisms

3.6.1 Theory

Earthquake focal mechanisms provide valuable information on the orientation and the relative magnitudes of the principal stresses. They record the stress-induced deformation involving a large volume of rock at a considerable depth within the earth's crust (Zoback and Zoback, 1991). No other *in situ* stress indicator can provide information at such substantial depths. Earthquake focal mechanisms contribute 66% of the reliable *in situ* stress data in the WSM (Müller *et al.*, 2000). In comparison, earthquake focal mechanisms contribute to less than 30% of the reliable *in situ* stress data in the ASM (Section 7.2). The percentage of earthquake focal mechanisms contributing to the ASM is significantly lower than the WSM because of the relatively few earthquakes with large enough magnitude for focal mechanism determination given the regional seismograph network in Australia.

Fault plane solutions and the centroid-moment tensor (Dziewonski *et al.*, 1981) are just two of the techniques that are used to determine earthquake focal mechanisms. The fault plane solution is based on the first motions of the earthquake, while the centroid-moment tensor is derived from filtering of the whole wave train (Anderson, 1988). The discussion below only describes the application of the more prominently used fault plane solutions. As with overcoring measurements, although new earthquake focal mechanisms data were compiled in the ASM during the course of this thesis, new earthquake focal mechanisms analysis were not undertaken by the author.

Fault plane solutions were developed by seismologists to map the radiation pattern of a particular wave type (i.e. P or S wave) on a sphere about the hypocenter of an earthquake. The fault plane solution is based on the principle that motion on a fault controls the pattern of seismic wave radiation, particularly the first motion of the compressional P-wave recorded at distant seismographs (Engelder, 1993). If the first arrival of a P wave is a compressive pulse, the stress release and fault motion must be towards the seismograph. However, if the first wave is a dilational pulse, then the fault motion must be away from the seismograph.

Most fault plane solutions are constructed on a stereographic projection displaying where the ray paths to distant stations cut the focal sphere. The earthquake hypocenter is at the centre of the stereographic projection. Two nodal planes are represented on the stereographic projection, which splits the compressional and dilational first arrivals (Figure 3.10). One

nodal plane represents the fault plane on which the earthquake occurred, while the other represents the auxiliary plane. A procedure for drawing the two nodal planes is given in Kasahara (1981). The auxiliary plane gives exactly the same P-wave radiation pattern as the actual fault but has no geological significance. Additional information is generally required to discriminate between the two nodal planes and clearly identify the fault plane (Figure 3.10). Aftershocks and geological evidence, such as surface rupture are used in the identification process (Amadei and Stephansson, 1997).

Composite fault plane solutions are often constructed when the main shock is so small that detection only occurs inside a limited region. These solutions are constructed by superimposing data from aftershocks (Sbar *et al.*, 1972). However, this method assumes that all aftershocks have the same earthquake focal mechanism (Rivera and Cisternas, 1990). This assumption is only reasonable if the aftershocks occur along the same fault as the primary earthquake (Engelder, 1993).

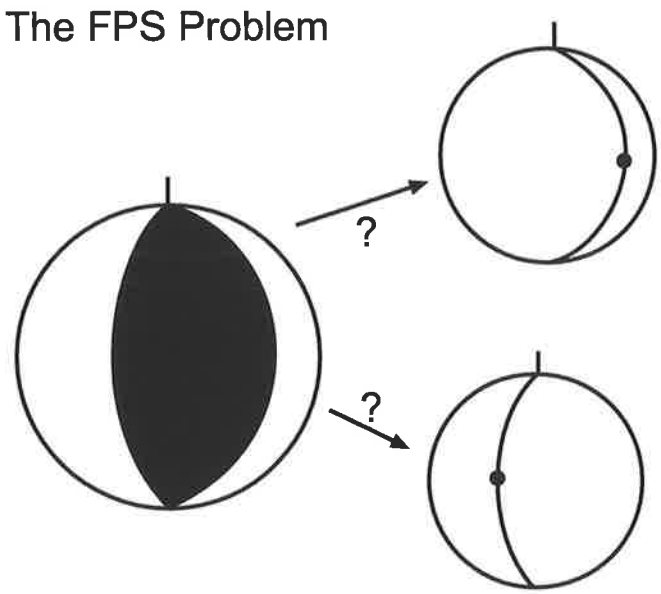

Figure 3.10 Fault plane solution illustrating the ambiguity associated with the two nodal planes. One plane corresponds to the fault plane where slip occurred, while the other plane corresponds to the auxiliary plane that has no geological significance.

Fault plane solutions are a representation of slip on a fault with the pressure (P) and tension (T) axes representing the axes of maximum shortening and maximum extension respectively (Engelder, 1993). The pressure or *P* axis is located in the middle of the compressional quadrant with the tension or *T* axis located in the middle of the tensional quadrant (Engelder, 1993). The *B* axis is located at the intersection of the fault and the auxiliary planes (Engelder,

1993). Fault plane solutions corresponding to the three main fault regimes are shown in Figure 3.11. The *P*, *T* and *B* axes are at 90° to each other as shown by the fault plane solutions in Figure 3.11.

In general the stress orientation is inferred by assuming that σ_1, σ_2 and σ_3 fall near the *P*, *B* and *T* axes respectively. However, the early assumption that earthquakes reflected the rupture of virgin rock was discovered not to hold (McKenzie, 1969a). Hence, the *P* axis does not necessarily correspond to σ_1 and may be strongly influenced by pre-existing rock heterogeneities (McKenzie, 1969a). Evidence from both the field and the laboratory suggested that earthquakes occurred along pre-existing faults (McKenzie, 1969a; Engelder, 1993). Earthquakes that ruptured the surface were observed to follow pre-existing faults. Furthermore, experimental results suggest stress drops accompanying fracture of virgin rock are 100 MPa or larger, while seismic source theory predicts that earthquake stress drops are generally less than 10 MPa (Chinnery, 1964; Wyss and Brune, 1968). Consequently, fault plane solutions do not provide precise stress orientations in the crust (Engelder, 1993). Nevertheless, compilation of focal mechanism solutions and comparisons with other techniques have shown the average orientation for *P* axes determined from a number of earthquakes gives a good indication of the maximum compressive stress orientation throughout a region (Sbar and Sykes, 1973; Zoback and Zoback, 1980; Sbar, 1982).

A number of algorithms have been developed for inverting the focal mechanisms for the stress field (Isacks and Molnar, 1971; Angelier, 1984; Gephart and Forsyth, 1984; Carey and Mercier, 1987; Michael, 1987). A quantitative approach to the determination of stress orientation from fault plane solutions has been devised by Gephart and Forsyth (1984). Their analyses of fault planes is based on the constraint that fault slip occurs in the direction of maximum resolved shear stress (Bott, 1959). This constraint narrows the possible stresses on a particular fault. Slip occurring on a family of faults of different orientations will correspond to a relatively small set of stress tensors that has activated slip on all of the faults involved. The technique developed by Gephart and Forsyth (1984) determines a best-fitting regional stress tensor from the observed earthquake focal mechanisms.

Relative stress magnitudes, which indicate the stress regime, can be inferred for earthquake focal mechanism from the plunges of the *P*, *T* and *B* axes (Zoback, 1992; Table 3.5). Five main stress regimes categories have been defined, including normal faulting (NF), predominantly normal with strike-slip component (NS), strike-slip faulting (SS), reverse

faulting (TF) and predominantly reverse with strike-slip component (TS). All earthquake focal mechanisms in the WSM and ASM databases have been categorised using the scheme defined in Table 3.5.

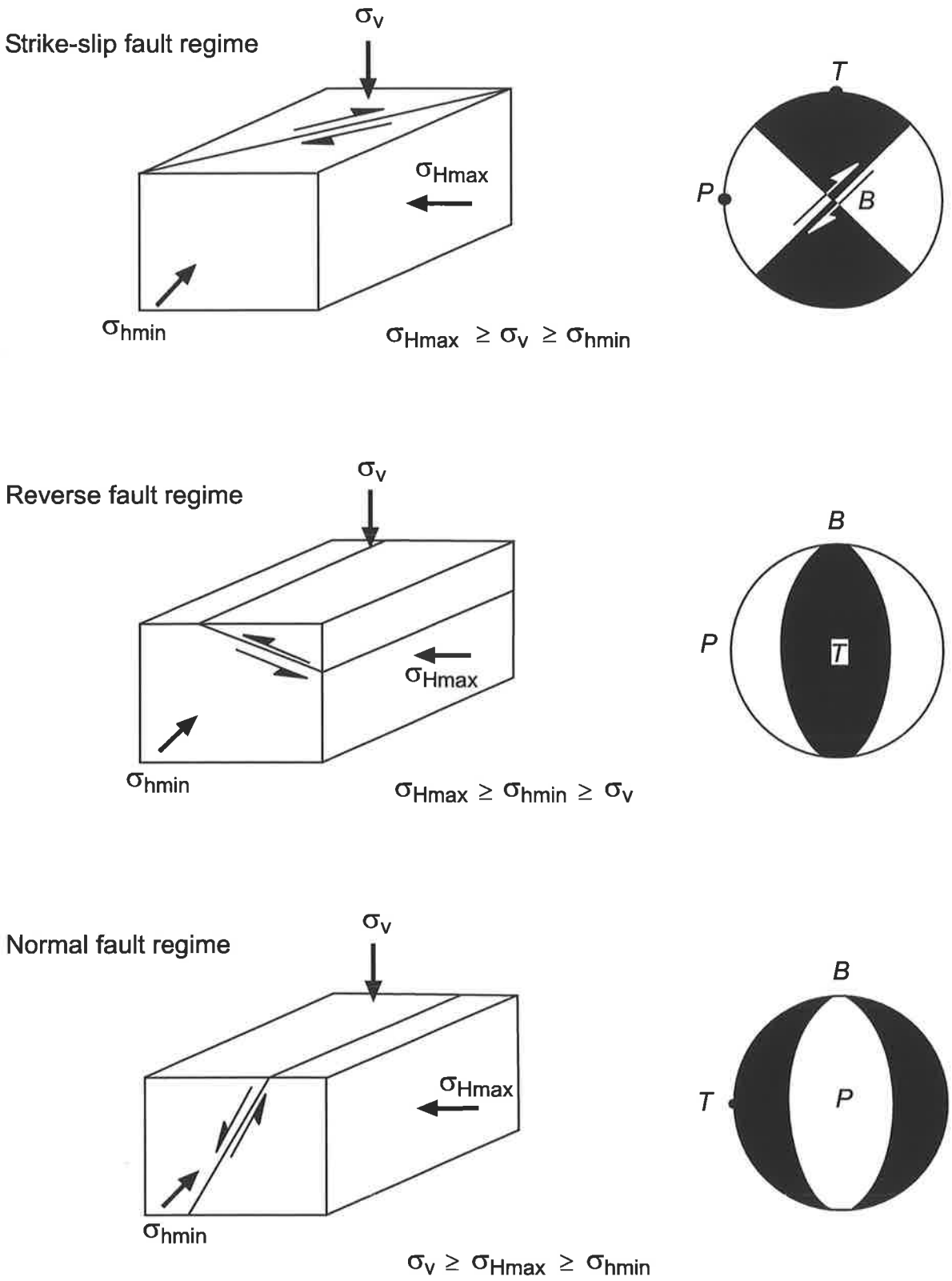

Figure 3.11 The three main fault regimes defined by Anderson (1951) and their corresponding fault plane solutions. After Amadei and Stephansson (1997).

Table 3.5 Stress regime characterization based on plunge of *P*, *B* and *T* axes for earthquake focal mechanisms. The five regimes include normal faulting (NF), normal with strike-slip component (NS), strike-slip faulting (SS), reverse with strike-slip component (TS) and reverse faulting (TF). After Zoback (1992).

Plunge of Axes				
P	*B*	*T*	Regime	σ_{Hmax} Azimuth
pl ≥ 52°		pl ≤ 35°	NF	Azimuth of *B* axis
40° ≤ pl < 52°		pl ≤ 20°	NS	Azimuth of *T* axis + 90°
pl < 40°	pl ≥ 45°	pl ≤ 20°	SS	Azimuth of *T* axis + 90°
pl ≤ 20°	pl ≥ 45°	pl < 40°	SS	Azimuth of *P* axis
pl ≤ 20°		40° ≤ pl < 52°	TS	Azimuth of *P* axis
pl ≤ 35°		pl ≥ 52°	TF	Azimuth of *P* axis

3.6.2 WSM Quality Ranking Scheme

The WSM quality ranking scheme for earthquake focal mechanisms is shown in Table 3.6 (Zoback, 1992). All earthquake focal mechanism stress indicators compiled within the ASM database have been ranked according to this scheme. The quality ranking ranges from A, which corresponds to four or more inversions of a single-event in close geographic proximity, to E, which corresponds to historical events or events with *P*, *T* and/or *B* axes that are significantly plunging. No single focal mechanism receives an A quality ranking as the actual stress orientation producing slip along a fault may differ from the orientation of the *P* and *T* axes. Very small magnitude events (M < 2.5) are assigned a D quality as they may represent deformation due to the complex interaction of active faults rather than deformation in response to the regional stress field (Zoback, 1992).

Table 3.6 WSM quality ranking scheme for earthquake focal mechanisms (Zoback, 1992).

A	B	C	D	E
Average *P* axis or formal inversion of four or more single-event solutions in close geographic proximity (at least one event M ≥ 4.0, other events M ≥ 3.0)	Well-constrained single-event solution (M ≥ 4.5) or average of two well-constrained single-event solutions (M ≥ 3.5) determined from first motions and other methods (e.g. moment tensor waveform modelling or inversion)	Single-event solution (constrained by first motions only, often based on author's quality assignment) (M ≥ 2.5) Or Average of several well-constrained composites (M > 2)	Single composite solution Or Poorly constrained single-event solution Or Single-event solution for M < 2.5 event	Large historical event with no reliable focal mechanism Or Event with *P*, *T*, *B* axes all plunging 25°-40° Or Event with *P* and *T* axes both plunging 40°-50°

Chapter 4

The *In Situ* Stress Field of the Bowen Basin

4.1 Introduction

The Bowen Basin is a large sedimentary basin located in eastern Queensland (Figure 4.1). Only six stress measurements were included in the 1998 version of the ASM for the Bowen Basin (Hillis *et al.*, 1998; Figure 4.2). In addition, only sparse amounts of data were available for contiguous regions of northeastern Australia. The lack of data throughout this region meant the stress field was poorly known. The only data available for the Bowen Basin comprised five hydraulic fracture measurements and one focal mechanism solution (Figure 4.2). The existing data were of average quality, consisting of three B, two C and one D quality measurements. The average σ_{Hmax} orientation of the six existing data points was 023°N with a standard deviation of 18°.

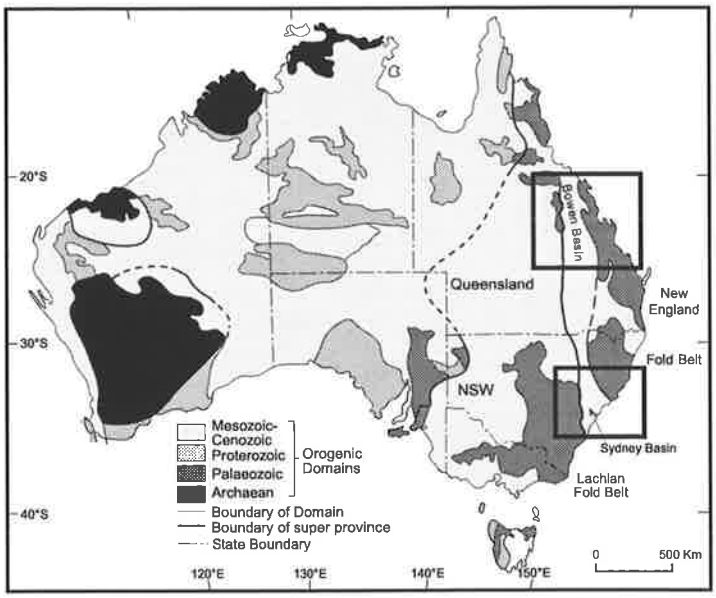

Figure 4.1 Regional geology of Australia showing the main orogenic domains. The Bowen Basin is located in eastern Queensland indicated by the top box (Chapter 4). The Sydney Basin is located on the eastern coastline of New South Wales (NSW) indicated by the bottom box (Chapter 5).

The new data presented in this chapter consists of hydraulic fracturing and overcoring measurements undertaken by the CSIRO in the course of civil engineering, coal mining and coal-bed methane projects in eastern Australia. The measurements are a subset from a larger CSIRO database covering eastern Australia (Hillis *et al.*, 1999). Only measurements considered unperturbed by local site effects were incorporated into the ASM and discussed here. The data are unusually deep for engineering type measurements going to a depth of 800 m with over half the measurements below a depth of 300 m. Hence, unlike many

engineering measurements, these measurements reflect the tectonic stress field and not near-surface effects such as local topography, rock anisotropy and natural fracturing (Haimson, 1978a ; Engelder and Sbar, 1984).

The aim of this chapter is to constrain the stress field of the Bowen Basin using the new *in situ* stress data. Existing measurements from the ASM have not been included in the analysis because individual measurements from which site averages are determined were not available. This chapter begins with a brief description of the geological setting of the Bowen Basin, emphasising the tectonic history and structural style. Following this, both the orientation and magnitude of the *in situ* stress field are discussed. The *in situ* stress data are subsequently used to determine whether relatively shallow *in situ* stress measurements are representative of the state of stress at greater, seismogenic depths. This chapter concludes with a discussion of the possible origin of the stress field of the Bowen Basin and by comparing the Bowen Basin stress field with nearby areas of the Australian continent.

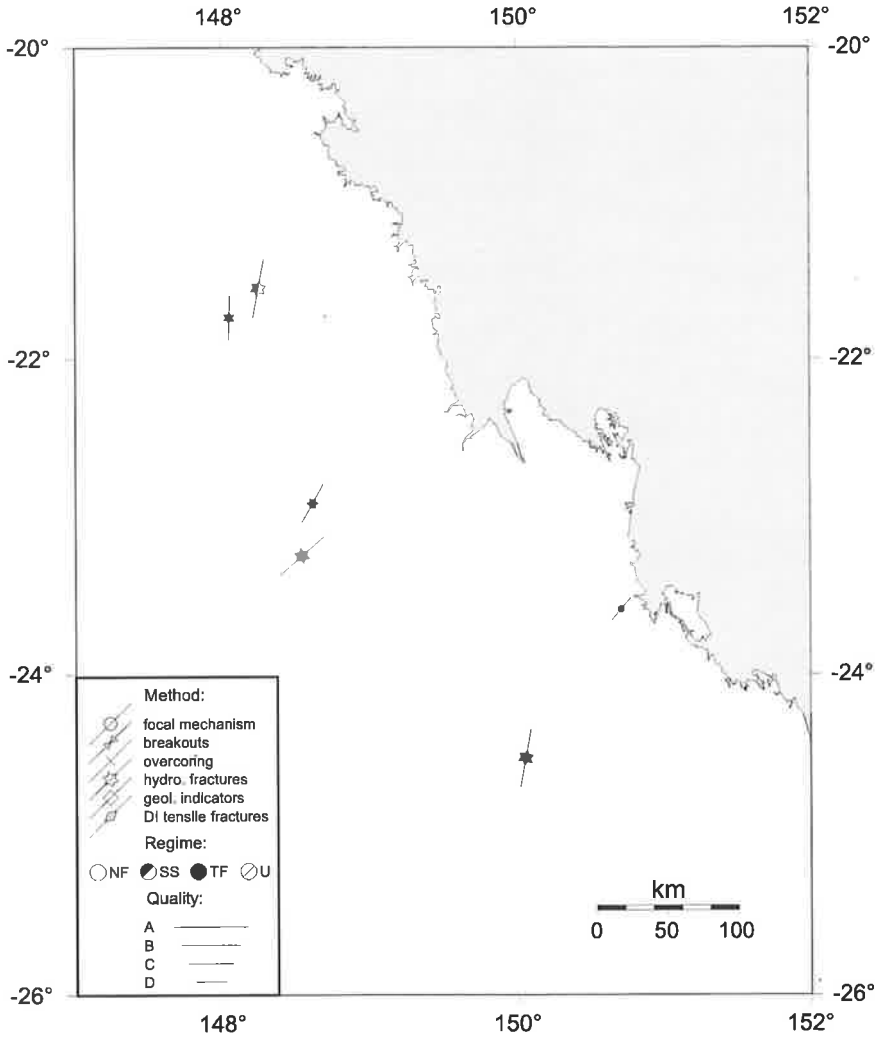

Figure 4.2 Stress map of the Bowen Basin showing the data available in the 1998 version of the ASM (Hillis *et al.*, 1998).

4.2 Geological Setting of the Bowen Basin

4.2.1 Overview

The Bowen Basin makes up the northern most portion of the 1800 km long Bowen-Gunnedah-Sydney Basin system (Figure 4.1). The basin is elongate in a north-south direction and gradually broadens southwards (Figure 4.3). The exposed section of the basin extends some 550 km to the south from its apex in the north and is 250 km across at its widest point in the south.

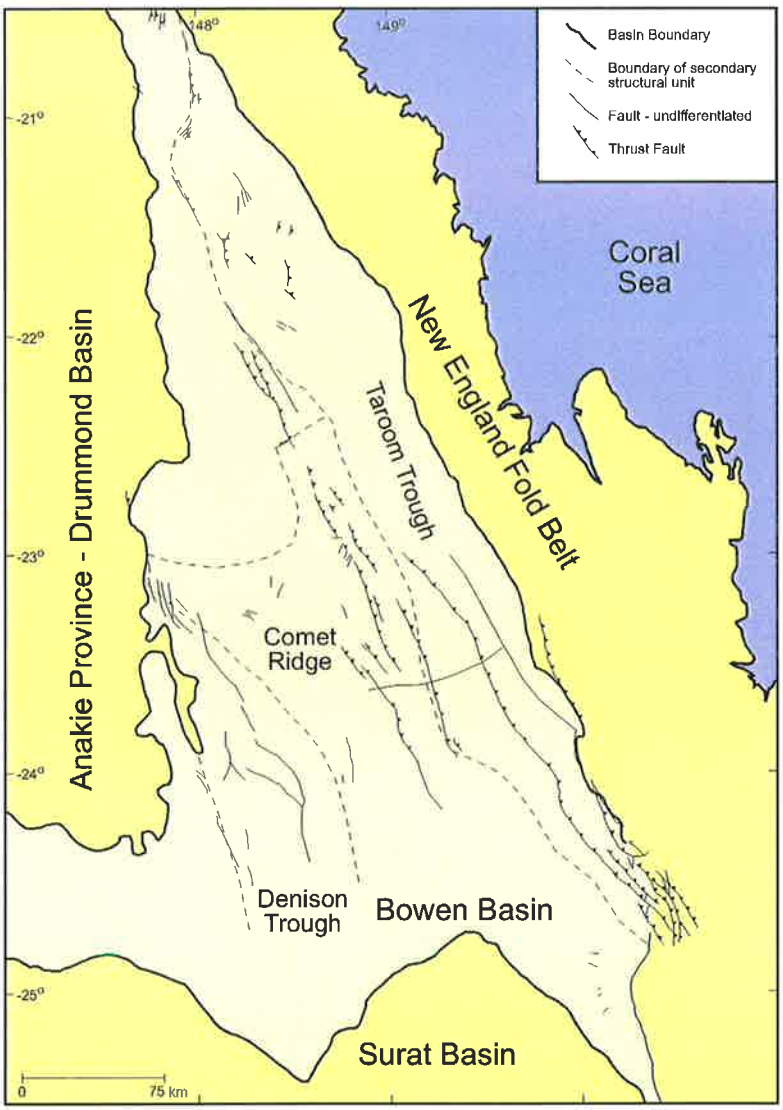

Figure 4.3 Regional structural map of the Bowen Basin showing the prominent north-northwest fault orientation. Base geological map from Queensland Department of Mines and Energy.

To the east the basin is bounded by the Gogango Thrust where Palaeozoic metamorphic and volcanic rocks have been thrust over Permian sediments (Leach *et al.*, 1986). To the west sediments of the basin onlap Devonian rocks which form local basement (Leach *et al.*, 1986). The northern section of the basin terminates in an apex where the Gogango Thrust intersects

the outcrop of Devonian sediments. To the south, the basin is overlain by the relatively flat-lying Jurassic and Cretaceous sedimentary rocks of the Surat Basin (Baker *et al.*, 1993). Internally the basin consists of two troughs divided by the Comet Ridge (Figure 4.3). The Comet Ridge has remained a structural and topographic high throughout most of the depositional history of the basin (Ziolkowski and Taylor, 1985). The Denison Trough forms the western section of the basin with the Taroom Trough the eastern section (Figure 4.3).

The Bowen Basin is almost entirely composed of clastic rocks with minor limestone and volcanics (Elliott, 1989). It contains voluminous economic reserves of Permian black coal. Sediments are of Permian and Triassic age with a maximum thickness of 10 km in the Taroom Trough and 6.5 km in the Denison Trough (Baker *et al.*, 1993). A large part of the basin is characterized by low topographic relief with flat or gently undulating plains.

4.2.2 Tectonic History

Recent work by a number of authors (Fielding *et al.*, 1990; Murray, 1990) has proposed that the Bowen Basin represents a complex, retroarc foreland basin. This concept has been further supported by more recent work (Gallagher, 1990; Caritat and Braun, 1992; Allen and Chappell, 1993; Gust *et al.*, 1993). Fielding *et al.* (1996) summarised these ideas and the discussion herein is based on that summary, unless otherwise stated.

The tectonic history of the Bowen Basin is characterised by three separate phases. Phase 1 began in the Early Permian with the formation of a series of north-trending grabens and half-grabens in response to limited back-arc extension. The back-arc setting was associated with the convergent plate margin and west dipping subduction zone to the east. The tectonic setting is thought to have been similar to the present day Andes Mountains of South America (Elliott, 1989). The formation of grabens and half-grabens was particularly prevalent along the western margin of the basin (Denison Trough). In contrast, the eastern margin experienced a period of volcanic activity with intrusives, extrusives and volcaniclastics.

Following the initial extension, the basin experienced a phase of passive thermal sag with minor episodic compression during late Early Permian to early Late Permian times (Phase 2). This phase produced slower subsidence rates driven by thermal relaxation of the lithosphere (Korsch and Totterdell, 1995). The volcanic activity on the eastern margin temporarily ceased, while modest amounts of quartz-rich sediments entered the western part of the basin. Fine-grained detrital sediments accumulated in offshore marine environments over much of

the basin. Major coal sequences were deposited throughout the Permian on the western and northern margins of the basin (Elliott, 1989).

During the late Late Permian to Middle Triassic a phase of flexural loading and increased compression developed (Phase 3). The basin became a true retroarc foreland basin during this final stage. The Taroom Trough experienced rapid subsidence that has been interpreted as resulting from foreland loading due to thrusting and crustal thickening in the New England Orogen to the east (Korsch and Totterdell, 1995). A resurgence of volcanic activity on the eastern margin resulted in the deposition of voluminous fresh volcanic lithic detritus. Sedimentation was effectively terminated in the Middle Triassic as the thrusts from the New England Orogen propagated westwards into the basin (Korsch and Totterdell, 1995). Some parts of the basin were uplifted by as much as 3000 m (Elliott, 1989). Erosion during the Late Triassic produced a peneplain surface on which the Surat Basin was deposited (Korsch and Totterdell, 1995). This unconformity represents a hiatus of approximately 35 million years duration (Korsch and Totterdell, 1995).

4.2.3 Structural Style

The Bowen Basin consists of a major north-south trending synclinal structure. Numerous smaller folds that also trend approximately north-south are superimposed on the major fold structure (Fielding *et al.*, 1996). The Taroom Trough is the major axis of the basin, trending northward in the southern Bowen Basin and rotating to north-northwest in the northern and central parts of the Basin. The Taroom Trough is asymmetrical in shape with the steeper, shorter limb lying on the eastern side. The dominant structural style throughout the region can be associated with deformation under a compressive stress regime (Elliott, 1993).

Faults of various orientations occur throughout the Bowen Basin. However, north-south and north-northwest to south-southeast are by far the most dominant fault trends (Mallet *et al.*, 1988; Lohe and McLennan, 1991; Fielding *et al.*, 1996). The majority of the north-south faults are normal faults that penetrate to the basement, or normal faults that were subsequently inverted (Fielding *et al.*, 1996). These faults are particularly common along the western basin margin and were interpreted to have been active during the early stages of the basin's history (Fielding *et al.*, 1996). The north-northwest to south-southeast faults are more variable in origin with many being high-angle reverse faults and a number being strike-slip faults (Fielding *et al.*, 1996). The high-angle reverse faults are particularly common in the eastern section of the basin (Fielding *et al.*, 1996).

4.3 The *In Situ* Stress Field

4.3.1 Stress Orientations

Analysis of the *in situ* stress field of the Bowen Basin was performed on four subregions, the northern, central, south-central and southern regions, as a consequence of the geographic clustering of the new data (Figure 4.4). Each subregion has a lateral extent of approximately 100 km. The new CSIRO data covers 40 sites, containing a total of 179 individual measurements. Two sites covered by new data, which were in the previous ASM database, have been updated with the new detailed data and included in the statistical analysis performed here. Table 4.1 summarises the new and existing data for each site. The individual measurements from which site averages have been determined and upon which the statistical analysis is based are listed in Appendix D.

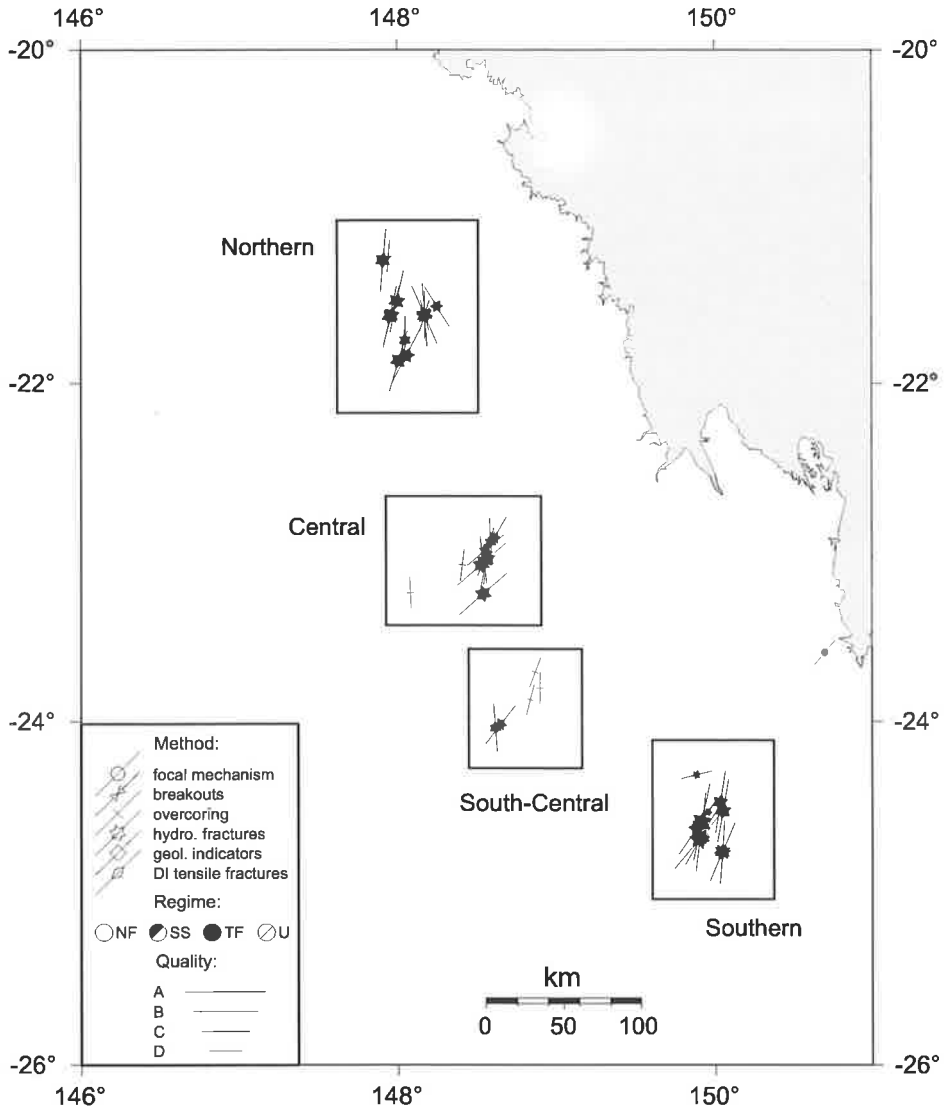

Figure 4.4 Stress map for the Bowen Basin showing both the new CSIRO data and the existing ASM data. The data were subdivided into four subregions (northern, central, south-central and southern) for the statistical analysis.

Table 4.1 Stress data for the Bowen Basin incorporating the new CSIRO data. Mean orientation in °N and all depths are in metres. Lat.: latitude, Long.: longitude, No.: number, Std Dev: circular standard deviation in degrees , HF: hydraulic fracture measurement, OC: overcoring measurement, FMS: single focal mechanism.

Site	Region	Lat.	Long.	Type	No. of Measurements			Mean	Std Dev	Quality	Depth Range	
					σ_{hmin}	σ_{Hmax}	Orientation	Orientation			Top	Bottom
AU121 *	Bowen Basin	-24.520	150.050	HF	N/A	N/A	6	010	9	B	166	228
AU122 #	Central	-23.094	148.502	HF	6	6	6	049	13	B	62	171
AU123 *	Bowen Basin	-22.920	148.610	HF	N/A	N/A	9	029	22	C	51	201
AU124 *	Bowen Basin	-21.740	148.050	HF	N/A	N/A	2	001	8	C	115	131
AU125 #	Northern	-21.592	148.173	HF	9	9	9	017	29	D	88	250
AU149 *	Bowen Basin	-23.590	150.700	FMS	N/A	N/A	N/A	040	0	D	N/A	N/A
AU196	Northern	-21.602	147.957	HF	16	16	8	012	16	B	489	684
AU197	Northern	-21.592	147.966	HF	7	7	5	015	12	B	275	469
AU198	Northern	-21.833	148.058	HF	9	9	6	027	14	B	310	485
AU199	Northern	-21.510	148.000	HF	5	5	5	012	8	B	85	175
AU200	Northern	-21.866	148.009	HF	6	5	6	016	6	B	196	327
AU201	Northern	-21.264	147.914	HF	6	6	6	005	7	B	107	165
AU202	Northern	-21.540	148.250	HF	5	5	5	149	22	C	50	89
AU203	Northern	-21.592	148.173	HF	4	4	4	157	11	B	277	315
AU204	Central	-23.043	148.564	HF	4	4	4	012	2	B	151	175
AU205	Central	-23.051	148.542	HF	5	5	5	172	22	C	67	123
AU206	Central	-23.058	148.563	HF	3	2	2	008	0	C	192	196
AU207	Northern	-21.592	148.173	HF	4	4	4	165	32	D	163	218
AU208	Central	-23.078	148.528	HF	6	6	6	048	13	B	88	115
AU209	Central	-23.012	148.560	HF	4	4	4	021	18	C	110	175
AU210	Central	-22.946	148.586	HF	4	4	4	178	21	C	54	102
AU211	Central	-22.995	148.554	HF	3	3	3	049	16	C	138	200
AU212	South Central	-24.033	148.614	HF	10	9	11	176	23	C	81	218
AU213	South Central	-24.014	148.646	HF	7	6	7	037	26	C	87	125
AU214	Southern	-24.673	149.911	HF	5	5	5	030	14	B	328	499
AU215	Southern	-24.621	149.882	HF	9	9	3	034	17	B	561	633
AU216	Southern	-24.585	149.914	HF	9	9	6	012	9	A	320	456
AU217	Southern	-24.684	149.900	HF	11	11	10	040	11	A	407	620
AU218	Southern	-24.644	149.908	HF	8	8	4	007	12	A	348	477
AU219	Southern	-24.310	149.882	HF	9	9	7	076	29	D	533	661
AU220	Southern	-24.470	150.031	HF	10	10	7	009	14	B	531	615
AU221	Southern	-24.528	149.954	HF	7	7	6	036	27	D	583	792
AU252	Southern	-21.592	148.173	HF	4	4	4	176	8	B	186	206
AU253	Southern	-21.592	148.173	HF	4	4	4	000	21	C	227	281
AU274	Southern	-24.760	150.045	HF	7	7	3	004	11	B	382	463
AU275	Southern	-24.760	150.045	HF	6	4	0	-	-	E	392	436
AU276	Southern	-24.760	150.045	HF	4	4	3	023	6	B	398	437
AU277	South Central	-23.800	148.894	OC	1	1	1	000	0	D	230	230
AU278	South Central	-23.867	148.833	OC	1	1	1	015	0	D	120	120
AU279	Northern	-21.240	147.947	OC	1	1	1	004	0	D	110	110
AU280	Central	-23.080	148.410	OC	1	1	1	007	0	D	90	90
AU281	Northern	-21.764	148.038	OC	1	1	1	005	0	D	170	170
AU282	Central	-23.240	148.082	OC	1	1	1	178	0	D	230	230
AU283	South Central	-23.707	148.864	OC	1	1	1	020	0	D	400	400

* Data in Hillis *et al.* (1998) compilation (not updated here and not included in the statistical compilation of Table 4.2, nor in Figures 4.5 - 4.14).

Data in the Hillis *et al.* (1998) compilation for which new, detailed CSIRO data are included in the statistical analysis performed here.

The new data, consisting of hydraulic fracturing and overcoring measurements, were quality ranked according to the WSM ranking scheme as outlined in Chapter 3. The new overcoring measurements from the CSIRO database were all quality ranked D for reasons previously outlined in Section 3.5.4.

The averaged site σ_{Hmax} orientations for the new and existing stress data are shown in Figure 4.4. The Bowen Basin stress field displays an approximately north-northeast to south-southwest σ_{Hmax} orientation. The direction appears to be consistent over the four subregions. Rose diagram plots of the individual measurements for the entire basin and the four subregions confirm the north-northeast trend (Figure 4.5). A slight easterly rotation of the σ_{Hmax} orientation is evident between the northern region and the southern region, however, this is not thought to be significant. Therefore the σ_{Hmax} orientation appears to be consistent over most of the Bowen Basin. Trends in the Bowen Basin data are relatively straightforward. Nonetheless, the same detailed statistical analysis has been performed on the Bowen Basin data as on the more variable Sydney Basin data discussed in the next chapter.

A statistical analysis was conducted on the four subregions as well as the basin as a whole using the individual measurements. The analysis was performed using the Rayleigh test, which assumes that random orientations sample a von Mises distribution, the circular equivalent to the normal distribution (Mardia, 1972). The Rayleigh test was used to determine if the null hypothesis, that the σ_{Hmax} orientations are random, could be rejected. A detailed description of the procedure is outline in Appendix C. All four subregions and the entire Bowen Basin indicate a unimodal distribution of σ_{Hmax} orientations at a 99.9% confidence level (Figure 4.6). The Rayleigh test confirms that the observed unimodal stress trend is statistically significant. The mean σ_{Hmax} orientation ranges from 007°N in the northern region, 024°N in the central region, 010°N in the south-central region and 026°N in the southern region (Table 4.2). The mean σ_{Hmax} orientation of the entire Bowen Basin is 016°N (Table 4.2).

Histograms of σ_{Hmax} orientations for the Bowen Basin highlight the unimodal nature of the data (Figure 4.7). To further confirm the unimodal nature, a semi-circular normal distribution was used to approximate σ_{Hmax} orientations for each region using the procedure outline in Appendix C (Figure 4.7). The mean value derived for each region using this technique was the same as that calculated using standard circular statistical techniques (Table 4.2). The

concentration parameter determined from the semi-circular normal distribution approach is equivalent to, but opposite in magnitude to the standard deviation calculated using circular statistics. A high value for the concentration parameter is associated with a narrow semi-circular normal distribution curve. The semi-circular normal distribution curves of the four subregions and the entire Bowen Basin show excellent correlation with the histograms (Figure 4.7).

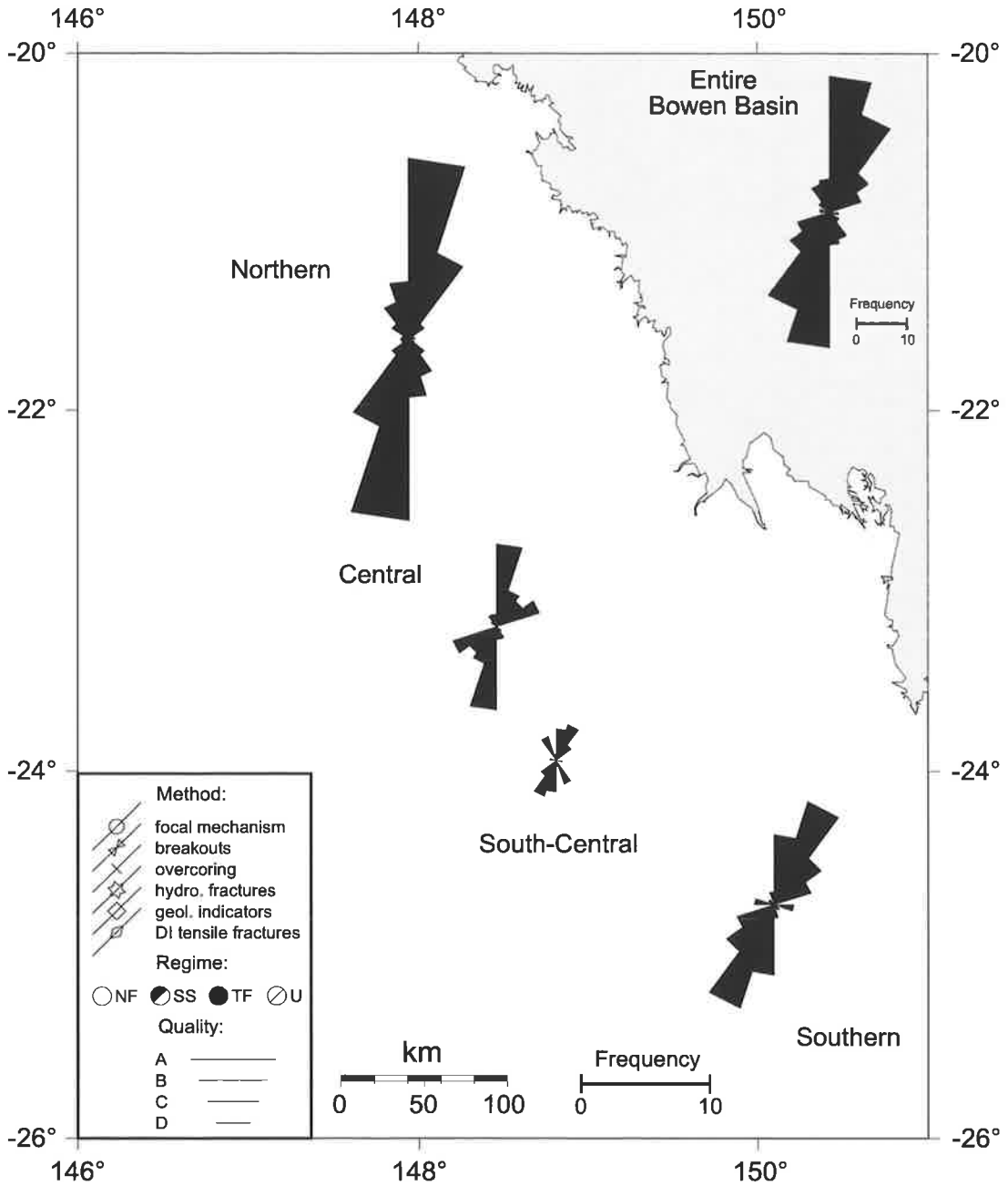

Figure 4.5 Rose diagrams of σ_{Hmax} orientations for the four subregions of the Bowen Basin. Rose diagram for the entire Bowen Basin shown in the top right. Note the rose diagrams of the four subregions are at the same scale (bottom). The rose diagram of the entire Bowen Basin is at a different scale to the four subregions (top). All rose diagrams use a bin size of 18°.

Table 4.2 Summary of results from unimodal analysis of the Bowen Basin data. Std Dev: standard deviation. Conf. Level: Confidence level passed when the Rayleigh test was applied (see Appendix C).

Region	Unimodal Analysis			
	Mean (°N)	Std Dev	Number	Conf. Level
Northern	007	23	68	99.9
Central	024	28	36	99.9
South-Central	010	29	21	99.9
Southern	026	26	54	99.9
Entire Basin	016	27	179	99.9

Although the σ_{Hmax} orientations for the Bowen Basin are consistent laterally over a distance of approximately 500 km, these results do not preclude the possibility of a systematic variation of stress orientation with depth. The σ_{Hmax} orientations were plotted against depth to determine whether there is a trend with depth (Figure 4.8). It is apparent from Figure 4.8 that no depth trend is present in the data, either for the entire Bowen Basin or for the four subregions. Thus the σ_{Hmax} orientation for the Bowen Basin is consistent with depth to around 900 m and over a lateral extent in excess of 500 km.

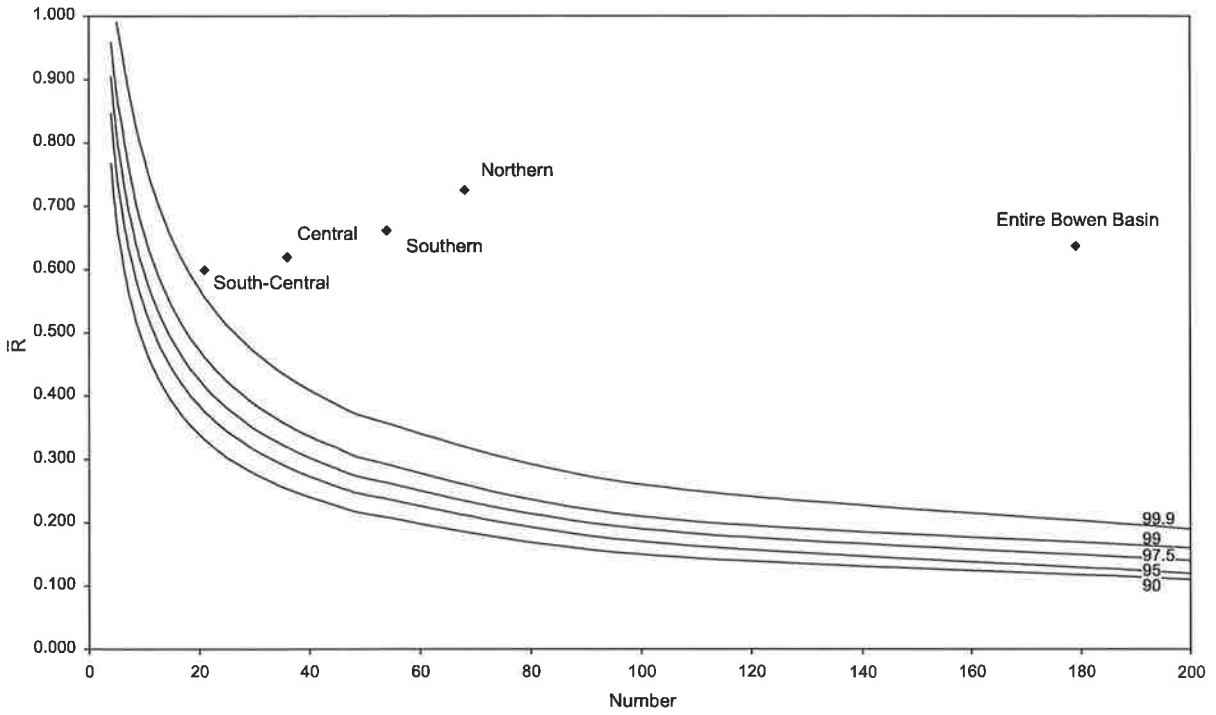

Figure 4.6 $\bar{R}$ value versus number of data points for the four subregions and the entire Bowen Basin. Curved lines correspond to the $\bar{R}$ value needed to pass the Rayleigh test for confidence levels ranging from 90% to 99.9% when using a specific number of data points. The $\bar{R}$ value is the length of the mean resultant vector of σ_{Hmax} orientations within a region (see Appendix C).

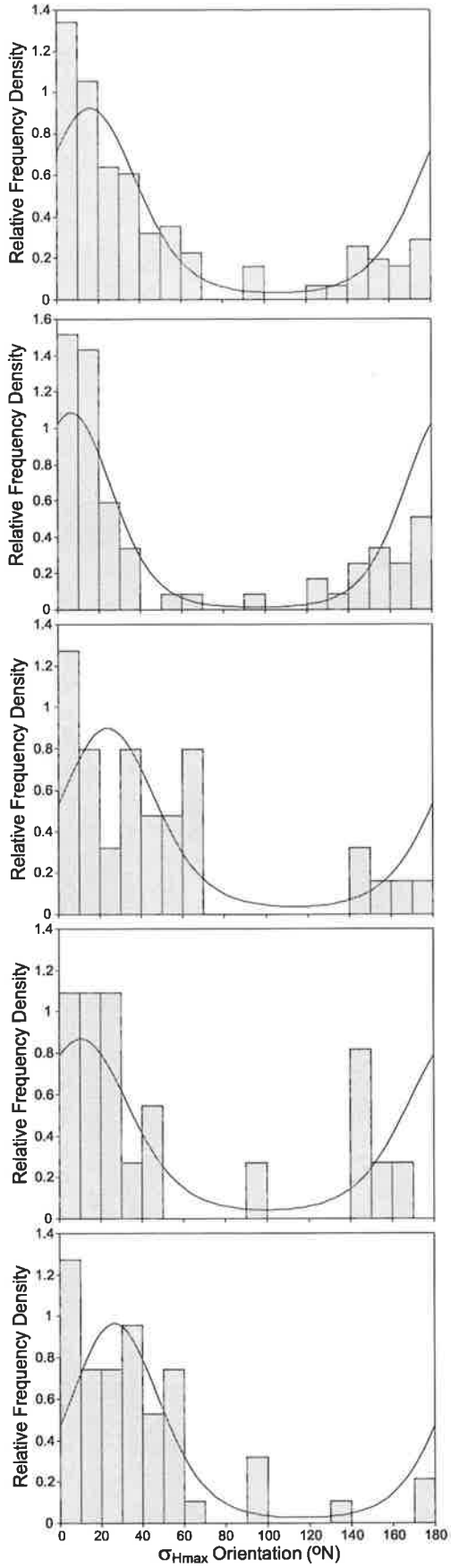

(a) Entire Bowen Basin

Mean = 016°N
Concentration Parameter = 1.67

(b) Northern Bowen Basin

Mean = 007°N
Concentration Parameter = 2.18

(c) Central Bowen Basin

Mean = 024°N
Concentration Parameter = 1.60

(d) South-Central Bowen Basin

Mean = 010°N
Concentration Parameter = 1.51

(e) Southern Bowen Basin

Mean = 026°N
Concentration Parameter = 1.79

Figure 4.7 (a) Maximum horizontal stress orientation histogram for the entire Bowen Basin and **(b)-(e)** histograms for Bowen Basin subregions. Bin sizes are in 10° increments plotted against relative frequency density. Histograms are overlain by a circular normal distribution curve calculated from the data. See Appendix C for the methodology for the calculation of the circular normal distribution curves. The concentration parameter indicates the spread of data and is equivalent to, but opposite in magnitude to standard deviation from circular statistics.

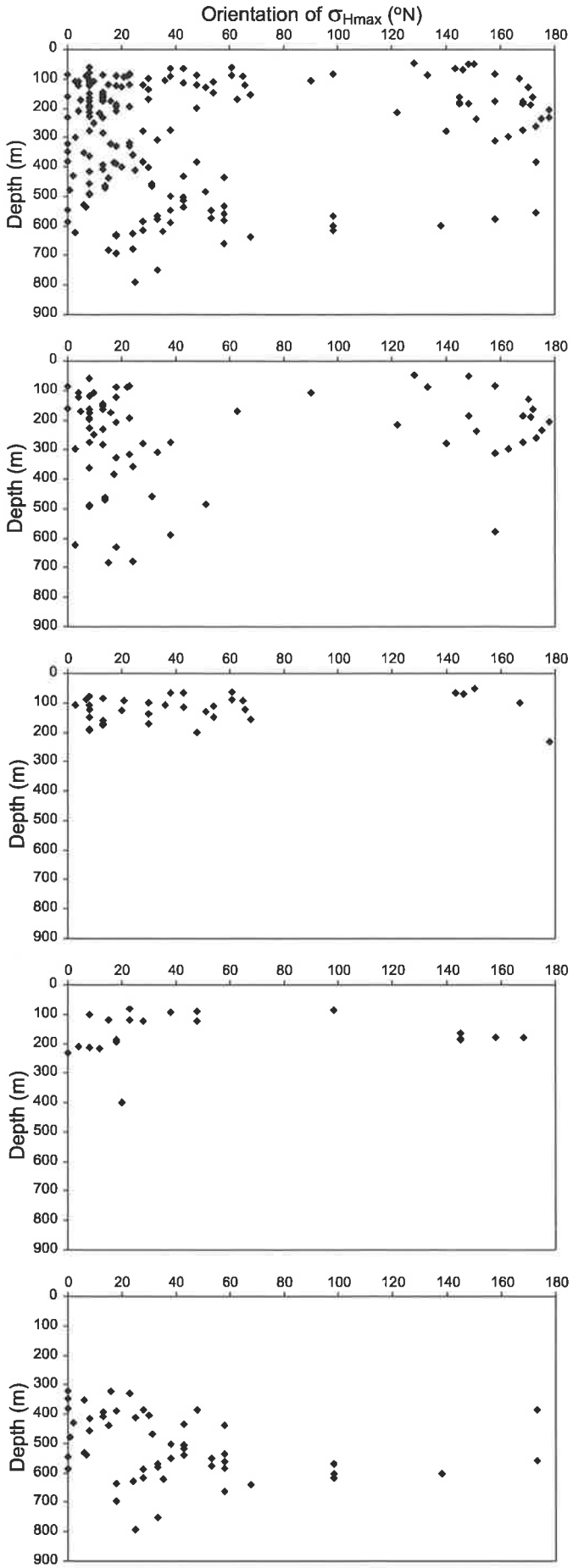

Figure 4.8 Maximum horizontal stress orientation versus depth for **(a)** entire Bowen Basin and **(b)-(e)** Bowen Basin subregions. No apparent systematic variation in σ_{Hmax} orientation occurs with depth.

4.3.2 Stress Magnitudes

Hydraulic fracturing and overcoring tests allow the magnitudes of σ_{Hmax} and σ_{hmin} to be estimated as discussed in Sections 3.4 and 3.5. Throughout this analysis σ_v has been estimated using an overburden density of 2308 kgm^{-3} (equivalent to an overburden stress gradient of 22.6 MPa/km or 1 psi/ft) on the basis of density log data. The fault conditions reverse ($\sigma_{Hmax}>\sigma_{hmin}>\sigma_v$), strike-slip ($\sigma_{Hmax}>\sigma_v>\sigma_{hmin}$) and normal ($\sigma_v>\sigma_{Hmax}>\sigma_{hmin}$) are used to describe relative stress magnitudes in the following discussion. It should be noted, however, that this does not necessarily imply the *in situ* stress data are consistent with failure (see Section 4.4 for further discussion).

The majority of the *in situ* stress data for the Bowen Basin, over 80%, indicate a reverse faulting stress regime (Figure 4.9). Small amounts of data indicate a strike-slip faulting stress regime (17%), with few data indicating a normal faulting stress regime (3%). These results are consistent with the only focal mechanism solution for the area, which indicates a reverse faulting stress regime. Thus the relatively shallow (less than 1 km) hydraulic fracture and overcoring tests are at least consistent with the deeper (6 km) focal mechanism solution in the Bowen Basin. A large amount of scatter is evident in both the σ_{Hmax} and σ_{hmin} magnitudes, with the degree of scatter increasing with depth (Figure 4.9).

Depth-normalized plots of σ_{Hmax} versus σ_{hmin} for the Bowen Basin data are shown in Figure 4.10. These plots display the three stress regimes bounded by frictional failure lines for three different values of the coefficient of friction, μ (0.6, 0.85 and 1.0). The frictional limits to stress and the polygon describing the allowable state of stress (Figure 4.10) were discussed in Section 2.4. Approximately 40% of the data lie below the failure line for $\mu = 0.6$ and within the reverse faulting stress regime. Furthermore, 85% of the data are in either the strike-slip or reverse faulting stress regimes, within the failure line for $\mu = 0.85$. Only 8% of the data lie outside the failure line for $\mu = 1.0$, indicating possible failure. This topic will be discussed further in Section 4.4, where the *in situ* stress field and seismicity for the Bowen Basin are compared.

Removal of the depth trend in the magnitude data requires some reference state of stress to be assumed and subtracted from the data. The two main reference states are the lithostatic and the uniaxial (Section 2.2). Removing the appropriate reference state of stress should provide some approximation of the magnitude of the tectonic stress provided the tectonic stress does

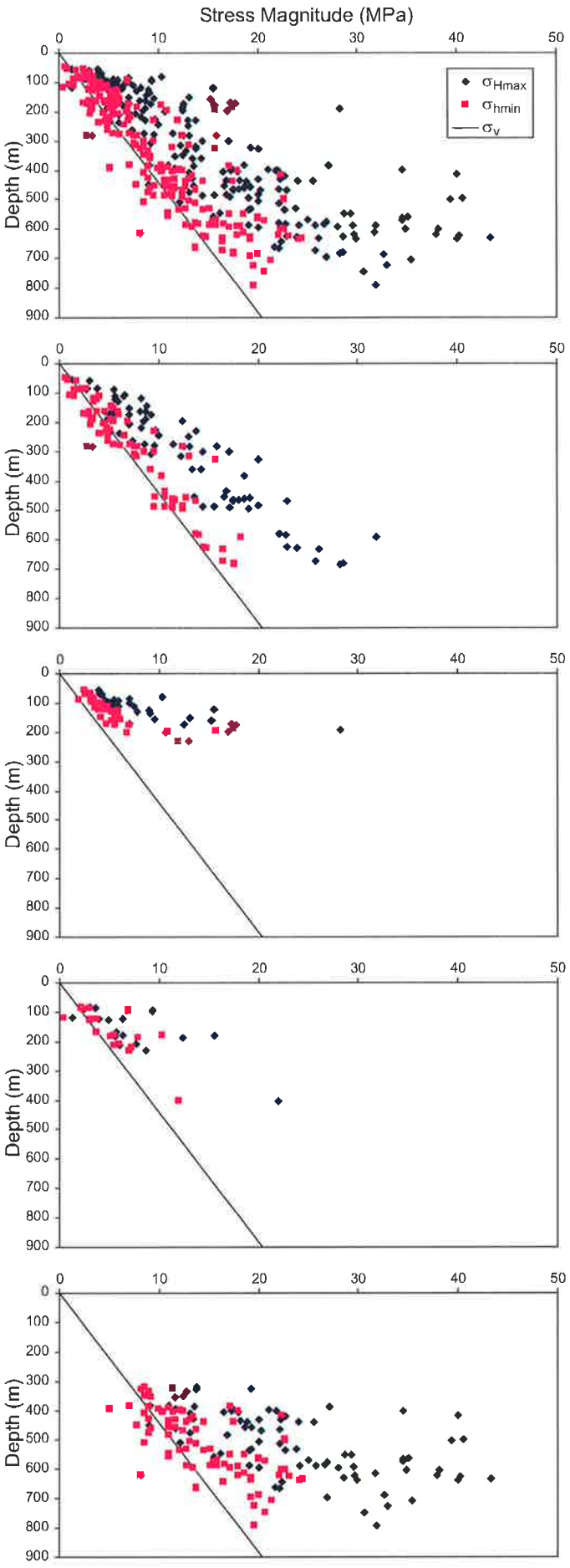

(a) Entire Bowen Basin

(b) Northern Bowen Basin

(c) Central Bowen Basin

(d) South-Central Bowen Basin

(e) Southern Bowen Basin

Figure 4.9 Stress magnitude versus depth for **(a)** entire Bowen Basin and **(b)-(e)** Bowen Basin subregion. The reference line is the vertical stress with an overburden density of 2308 kgm^{-3}.

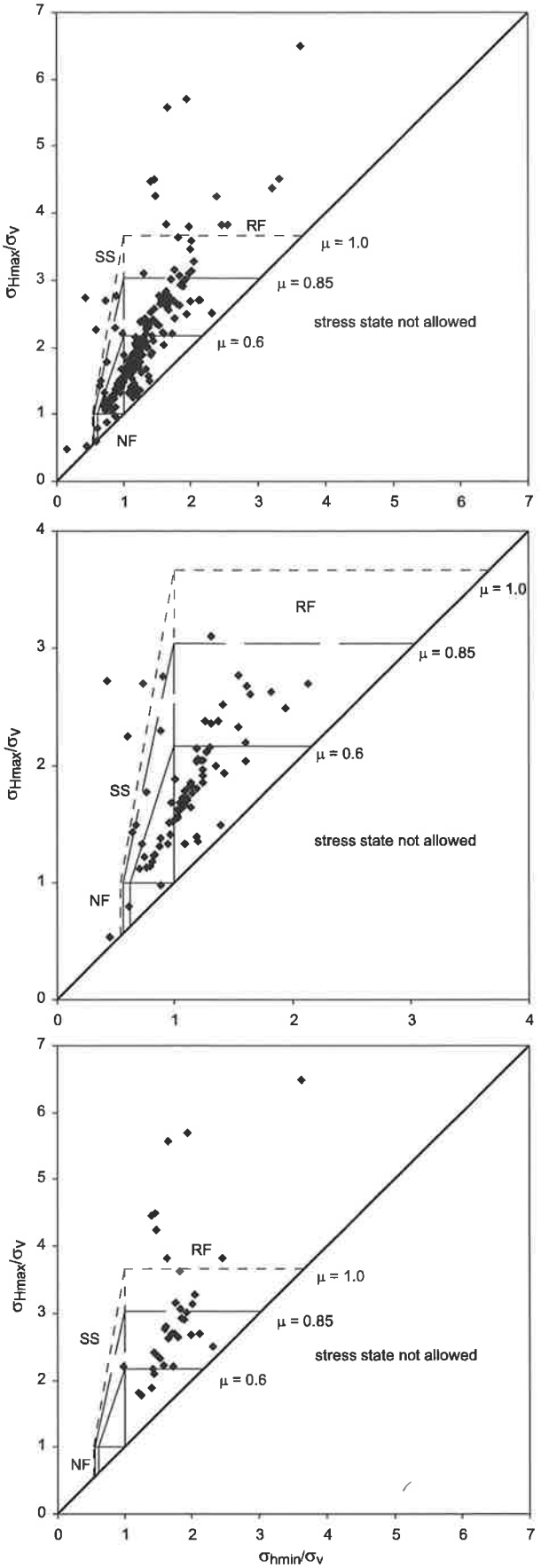

Figure 4.10 Depth-normalized σ_{Hmax} versus σ_{hmin} plots for **(a)** entire Bowen Basin, **(b)** the northern Bowen Basin and **(c)** the central Bowen Basin. RF = reverse faulting stress regime, SS = strike-slip faulting stress regime, NF = normal faulting stress regime. ...continued over page.

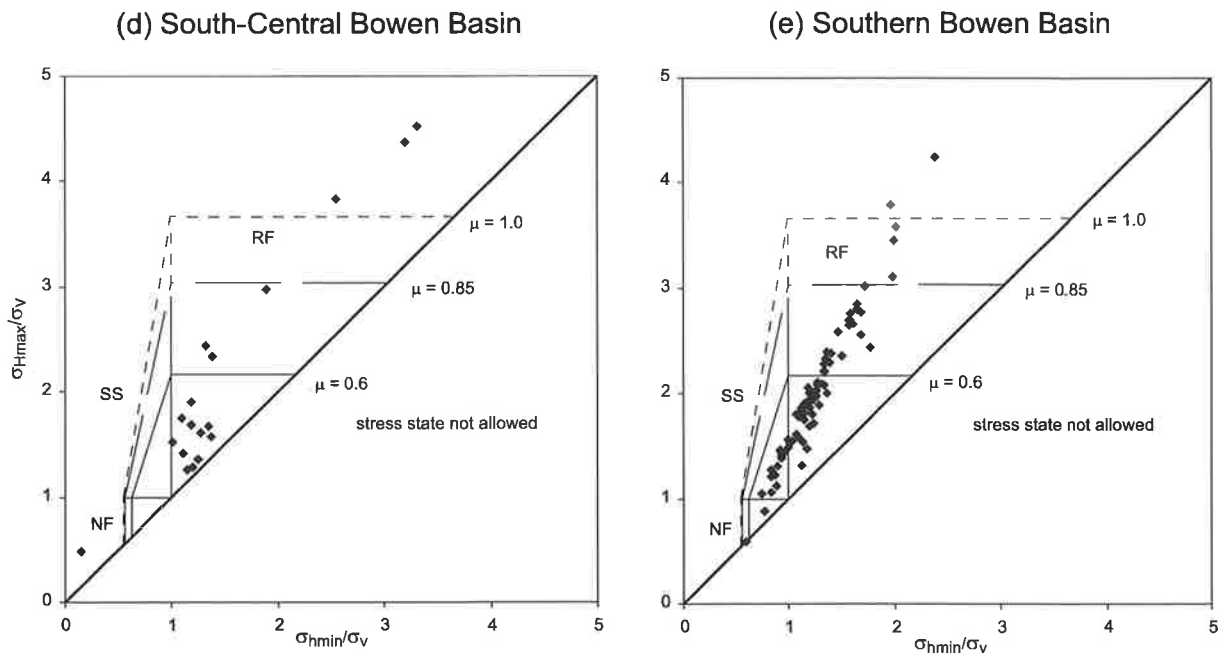

Figure 4.10 continued... Depth-normalized σ_{Hmax} versus σ_{hmin} plots for **(d)** the south-central Bowen Basin and **(e)** the southern Bowen Basin. RF = reverse faulting stress regime, SS = strike-slip faulting stress regime, NF = normal faulting stress regime.

not vary with depth. Indeed in order to compare modelled tectonic stresses such as those presented in Chapter 8 with measured stress magnitudes, the purely depth-related component of stress must be removed from the measured data. For example, Cloetingh and Wortel (1986) and Coblentz *et al.* (1998) described the modelled stresses as the non-lithostatic stresses assuming a lithostatic references state. Coblentz *et al.* (1995) described the modelled stresses as deviatoric, assuming that the mean stress is the reference state. The lithostatic and uniaxial reference states were removed from the data for the Bowen Basin (Figure 4.11).

In the case of the uniaxial reference state a Poisson's ratio (ν) of 0.25 was used. The lithostatic reference state is a special case of the uniaxial reference state whereby the Poisson's ratio is 0.5 (i.e. fluid). It is apparent from Figure 4.11 that the lithostatic reference state removes the depth trend in the data more effectively than the uniaxial reference state. However a slight depth trend is still present when the lithostatic reference state has been removed, especially in the case of the σ_{Hmax} magnitude data. Nevertheless the lithostatic reference state is preferred over the uniaxial reference state. Using the lithostatic reference state the average tectonic stress based on engineering measurements across the Bowen Basin is 5.2 MPa for σ_{Hmax} and 2.0 MPa for σ_{hmin}.

Figure 4.11 Stress magnitude versus depth for the entire and subregions of the Bowen Basin with the lithostatic and uniaxial reference states removed. Removing the lithostatic reference state from the data better removes depth trends than does the uniaxial reference. A Poisson's ratio of 0.25 was used to calculate the uniaxial reference state.

4.4 *In Situ* Stress and Seismicity

The Bowen Basin is a relatively aseismic area compared to other areas of eastern Australia such as the Sydney Basin (Figure 4.12). The lack of seismicity in the Bowen Basin suggests that stresses in the area are not close to failure. To investigate this further a Mohr-Coulomb analysis of the propensity for failure was undertaken. Here the stress data discussed in Section 4.3 are combined with the structural data for the Bowen Basin to help determine the likelihood of failure (Figure 4.13). The average σ_{Hmax} orientation from the four subregions was used in the analysis below (Table 4.2). It should be noted that the *in situ* stress data used in this study are from a shallow (0-1 km) depth range compared to deeper earthquake focal depths for eastern Australia (2-20 km). The intention of this analysis is to observe whether the shallow *in situ* stress data from the upper kilometre of the crust are consistent with the observed lack of seismicity at seismogenic depths.

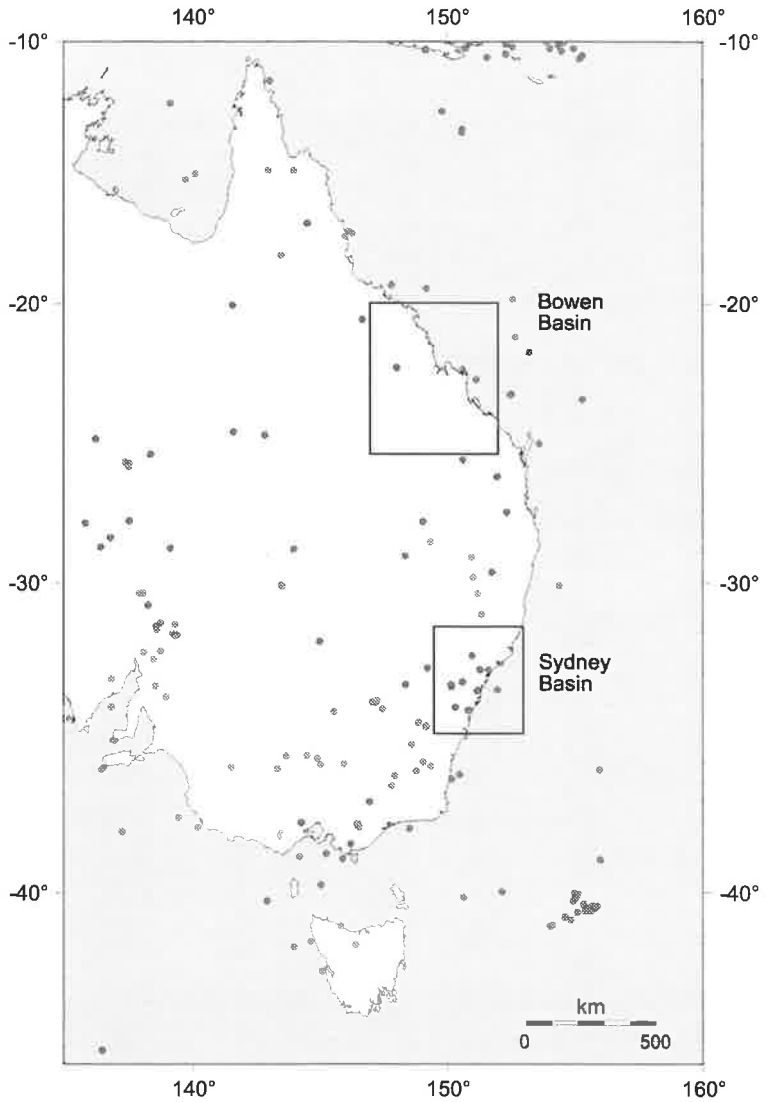

Figure 4.12 Seismicity map of eastern Australia showing epicentre locations for M≥4 events since 1970. The post-1970 and M≥4 conditions have been applied in order to remove bias in the pre-1970 and M<4 dataset associated with the distribution of recording stations. Data from K. McCue (personal communication, 1999).

Mohr-Coulomb analysis was undertaken assuming Byerlee's (1978) Law, which states that at normal stresses up to 200 MPa the shear stress required to cause sliding on a pre-existing fault is approximately 0.85 times the normal stress. The data were normalised for depth by dividing by σ_v, in order to plot all the stress data from different depths on the same diagram. Each full stress measurement produces a 3D Mohr's circle, but only the point (i.e. plane) on the circle closest to failure for $\mu = 0.85$ is shown on Figure 4.14 (See Appendix B for full discussion). If the 3D Mohr's circle for each stress measurement were shown, the diagram would be too cluttered. For a given stress measurement, the plane most prone to failure is stable if it plots below the failure line. In the case of the Bowen Basin only 13% of the stress data indicates failure when Byerlee's (1978) Law is used (Figure 4.14a). This analysis assumes that there are pre-existing zones of weakness of no cohesion that are optimally oriented for each measured stress orientation. For $\mu = 0.85$ the optimally oriented plane has a normal oriented at 65.2° to the maximum principal stress.

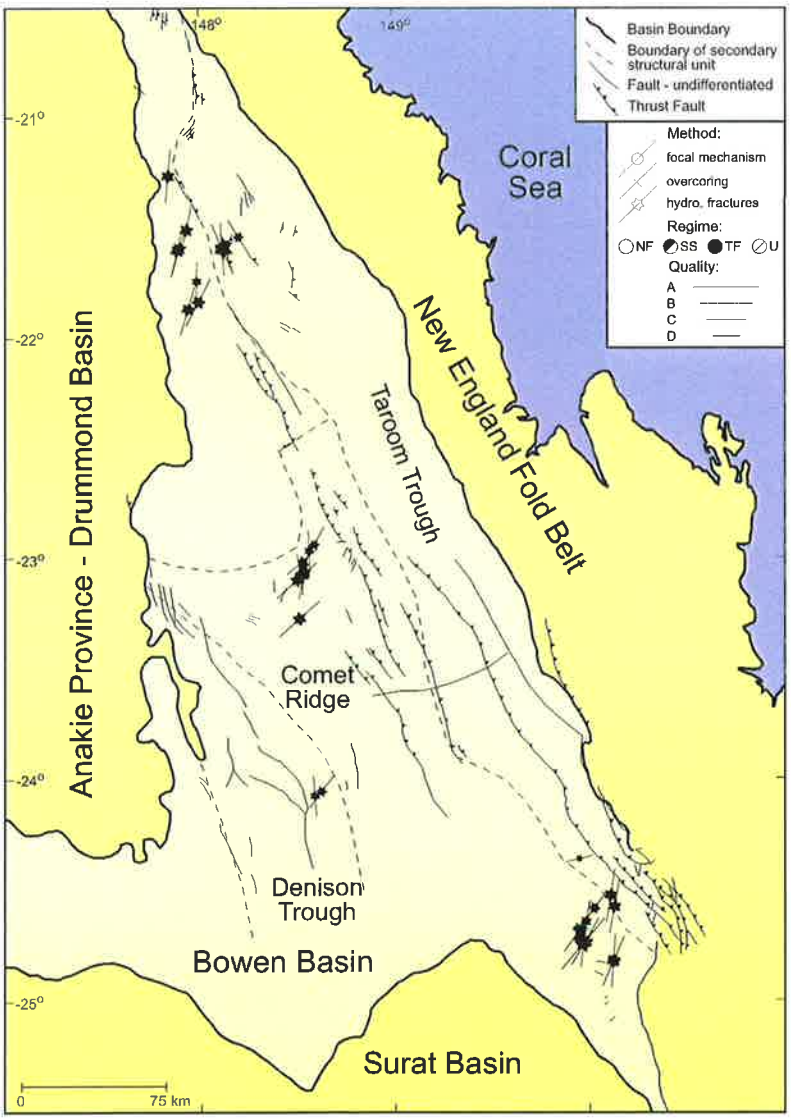

Figure 4.13 Overlay of structural map (Figure 4.3) with stress orientations for the Bowen Basin.

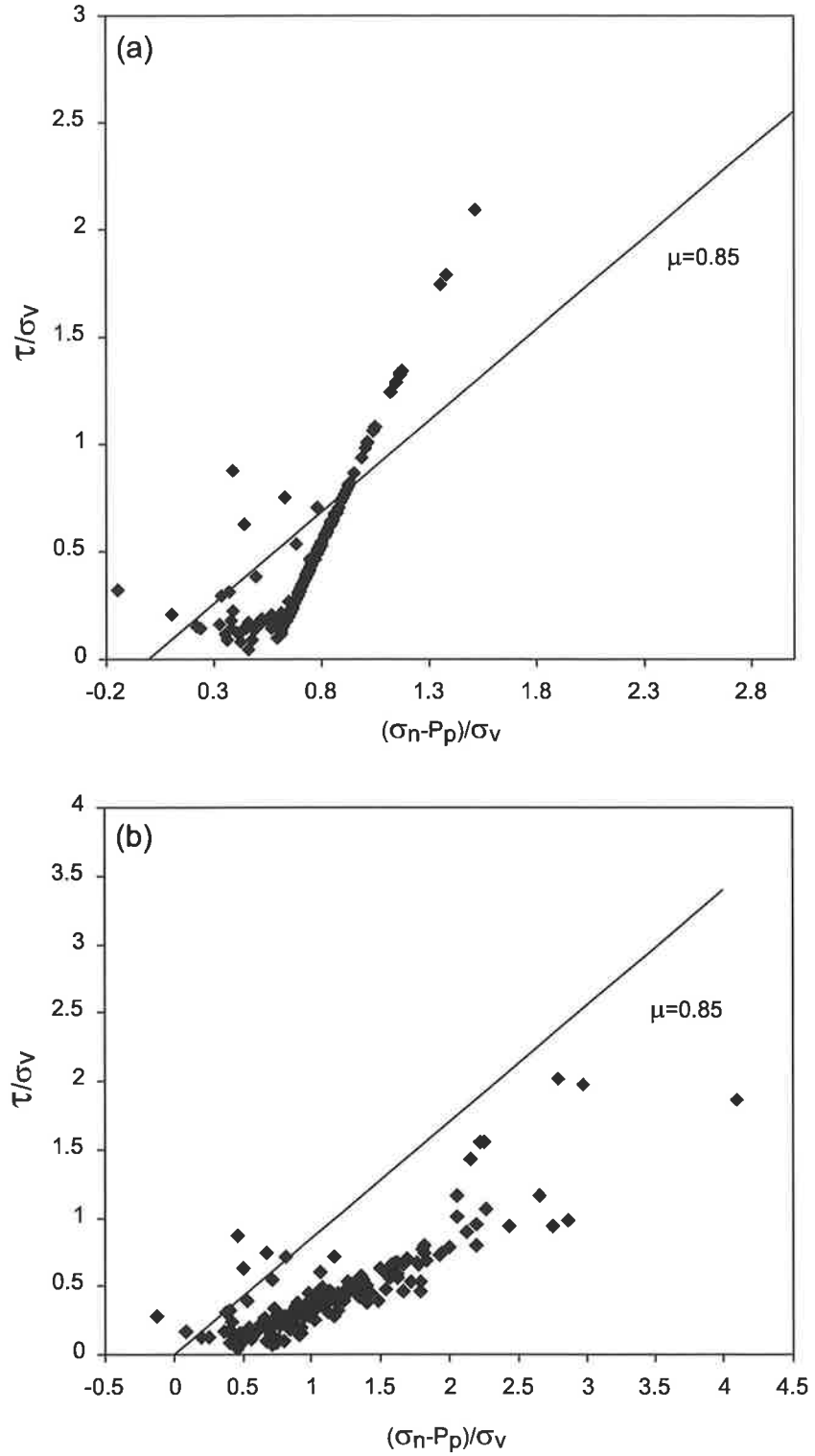

Figure 4.14 Effective normal stress versus shear stress normalised for depth. **(a)** Most critically stressed points on the 3D Mohr's circles based on *in situ* stress data from the Bowen Basin and assuming $\mu = 0.85$. **(b)** Stresses acting on planes striking 340° and dipping at 70°. Byerlee's (1978) failure line ($\mu = 0.85$) is shown.

The Mohr-Coulomb analysis outlined above was repeated in order that the structural history of the Bowen Basin could be taken into account. The structural history of the Bowen Basin has resulted in pre-existing planes of weakness with a preferential orientation that may not be optimal for faulting with respect to the *in situ* stress field. The predominant structural grain in

the Bowen Basin was taken to be steeply dipping (70°) faults striking north-northwest (340°). The normalized effective normal and shear stresses acting on the predominant structural grain were determined (Figure 4.14b). When the structural grain for the Bowen Basin is taken into consideration, only 3% of the *in situ* stress data indicate failure. This is an extremely low percentage, which is in good agreement with the low levels of seismicity that characterize the basin.

4.5 Discussion

The *in situ* stress field of the Bowen Basin has a regional σ_{Hmax} orientation of approximately north-northeast to south-southwest. The regional stress field could be controlled by a number of sources of stress ranging from large-scale tectonic forces to the more local structural effects. The direction of the stress field is oblique to the continental margin so is presumably not controlled by stresses originating from the continental margin as described by Bott and Dean (1972) and Stein *et al.* (1989). Similarly, the stress field is unlikely to be affected by the structural grain of the area to which it is also oriented obliquely. The fact that the stress field is consistent for a distance of approximately 500 km indicates the controlling force exerts a long wavelength control, such as plate boundary forces. Furthermore, the stress field is broadly consistent with a variety of plate boundary force models that indicate a roughly north-south stress field (Coblentz *et al.*, 1995; Coblentz *et al.*, 1998). Thus, the stress field in the Bowen Basin appears to be controlled by plate boundary forces. Chapter 8 presents a detailed model of the plate boundary forces acting on the IAP based on the most recent *in situ* stress data.

The north-northeast to south-southwest oriented stress field in the Bowen Basin is consistent with other parts of northern Australia, such as the Amadeus Basin, which have a broadly north-south σ_{Hmax} orientation (Figure 4.15). In contrast, the southern half of Australia appears to have a dominantly east-west σ_{Hmax} orientation, such as the Perth region, the Cooper Basin and the Flinders Ranges (Figure 4.15). Areas of southeastern Australia, such as the Otway and Gippsland Basins, exhibit a strong southeast-northwest σ_{Hmax} orientation (Figure 4.15).

Prior to the new data presented herein, only six stress measurements were available for the Bowen Basin. Thus the new *in situ* stress data in the Bowen Basin has added greatly to our understanding of the stress field in northeastern Australia. However, outside of the Bowen Basin, northeastern Australia is still only very sparsely populated by stress data. These data

include four borehole breakouts and one focal mechanism. More data are still required in areas outside the Bowen Basin to further strengthen our understanding of the stress field in northeastern Australia.

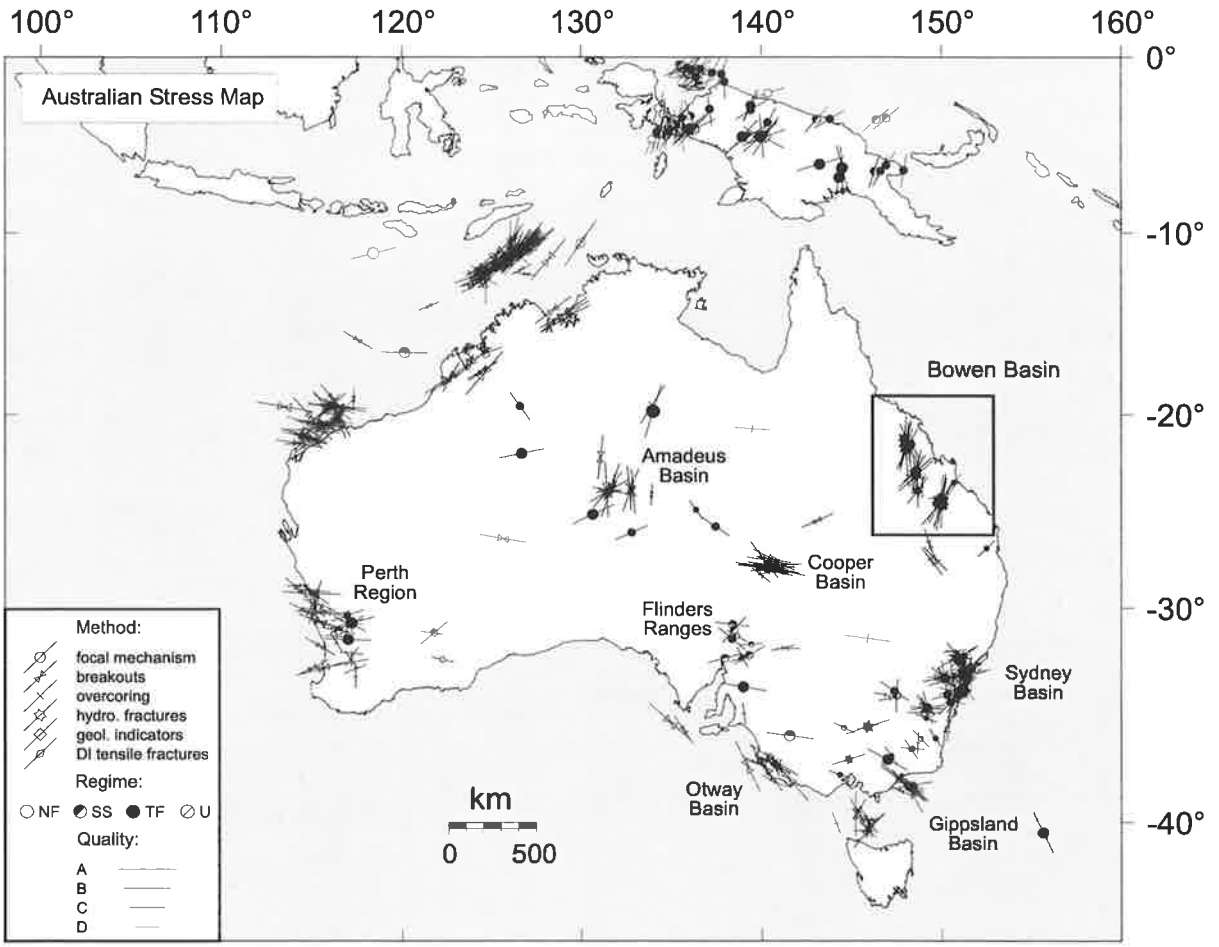

Figure 4.15 The Australian stress map using A-D quality data with the new stress data for the Bowen Basin.

4.6 Summary

1. A significant new database of engineering stress measurements has elucidated the *in situ* stress field of the Bowen Basin.
2. The mean σ_{Hmax} orientation ranges from 007°N in the northern region, 024°N in the central region, 010°N in the south-central region and 026°N in the southern region. All regions pass the Rayleigh test at a 99.9% confidence level.
3. The mean σ_{Hmax} orientation of the entire Bowen Basin is 016°N and passes the Rayleigh test at a 99.9% confidence level.
4. The majority of the stress magnitude data indicate a reverse faulting stress regime.
5. The lithostatic reference state is the preferred reference state of stress.

6. The relatively shallow engineering stress data are consistent with the lack of seismicity for the area with only a small number of measurements indicating possible failure.
7. The stress field in the Bowen Basin appears to be controlled by forces exerting a long wavelength control, such as plate boundary forces.

Chapter 5

The *In Situ* Stress Field of the Sydney Basin

5.1 Introduction

The Sydney Basin is a Permo-Triassic sedimentary basin located on the eastern coastline of Australia (Figure 4.1). Only 14 *in situ* stress indicators were included in the 1998 version of the ASM for the Sydney Basin (Hillis *et al.*, 1998; Figure 5.1). These data consisted of six focal mechanism solutions and eight hydraulic fracturing measurements. The quality of the data was relatively poor with one B, eleven C and two D quality measurements. In addition, the existing stress measurements appear highly scattered showing no preferred σ_{Hmax} orientation. Nonetheless, the average σ_{Hmax} orientation of the 14 data points was 056° with a very high standard deviation of 42°.

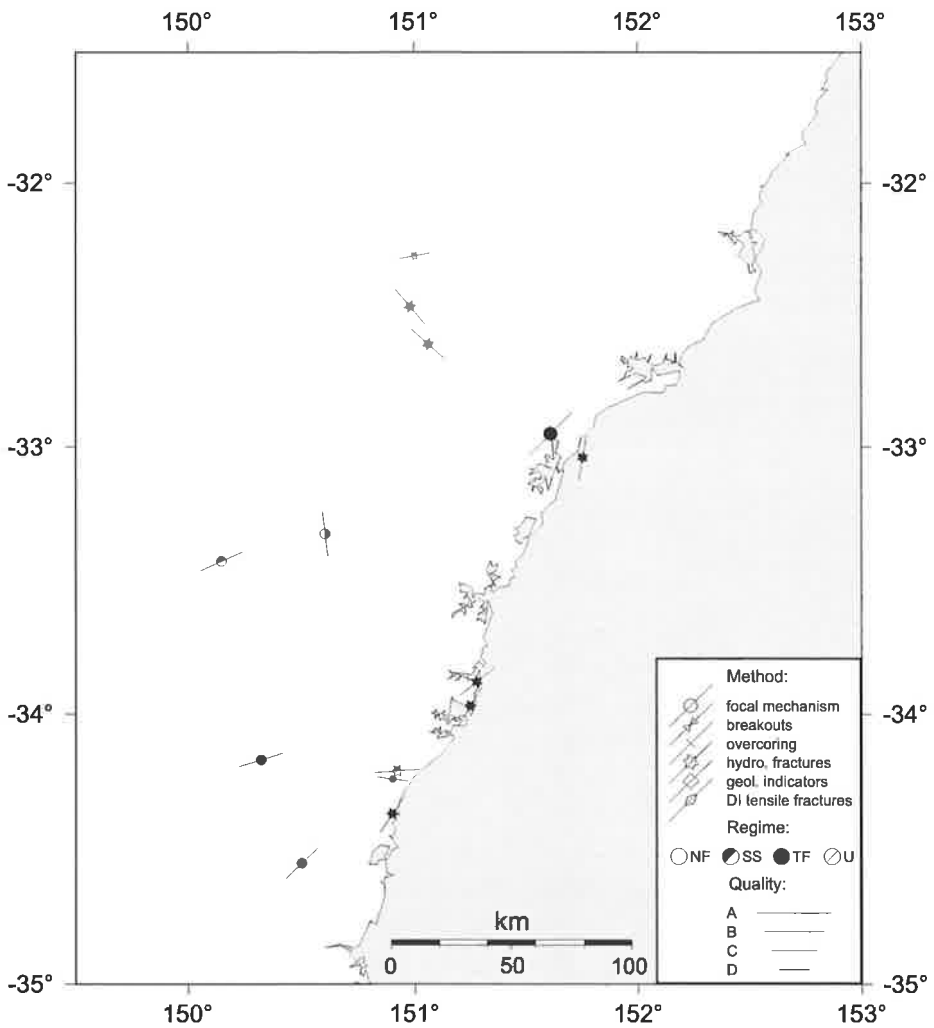

Figure 5.1 Stress map of the Sydney Basin showing the data available in the 1998 version of the ASM (Hillis *et al.*, 1998).

The majority of the new data presented in this chapter consist of hydraulic fracturing and overcoring measurements undertaken by the CSIRO in the course of civil engineering, coal mining and coal-bed methane projects in eastern Australia. The measurements are a subset from a larger CSIRO database covering eastern Australia (Hillis *et al.*, 1999). Only measurements considered unperturbed by local site effects were incorporated into the ASM and discussed here. The data are unusually deep for engineering type measurements, extending to a maximum depth of 1 km, with approximately half the measurements from below 300 m. In addition to the engineering type measurements, one well (Appin-1) has also been analysed by the author and found to contain borehole breakouts.

The aim of this chapter is to constrain the stress field of the Sydney Basin using the new *in situ* stress data. Existing measurements from the ASM have not been included in the analysis because individual measurements from which site averages are determined were not available. This chapter begins with a brief description of the geological setting of the Sydney Basin, emphasizing the tectonic history and structural style. Following this, both the orientation and magnitude of the *in situ* stress field are discussed. The *in situ* stress data are subsequently used to determine whether relatively shallow *in situ* stress measurements are representative of the state of stress at greater, seismogenic depths. This chapter concludes with a discussion of the possible origin of the stress field of the Sydney Basin and by comparing the Sydney Basin stress field with nearby areas of the Australian continent.

5.2 Geological Setting of the Sydney Basin

5.2.1 Overview

The Sydney Basin is a Permo-Triassic basin representing the southern section of the Sydney-Gunnedah-Bowen Basin system. The length of the basin is approximately 350 km north to south and on average 100 km wide (Figure 5.2). The basin covers an area of 52,000 km^2 comprising 37,000 km^2 onshore and 15,000 km^2 offshore. Gravity and magnetic data suggest that sediments within the basin are approximately 9000 m thick (Alder *et al.*, 1998). Sediments in the south and west of the Sydney Basin unconformably overlie Lower to Middle Palaeozoic magmatics and metasediments of the Lachlan Fold Belt, while sediments to the north, and in offshore portions of the basin unconformably overlie Upper Carboniferous volcanics and volcaniclastics (Alder *et al.*, 1998). The onshore Lower Permian sediments are

dominantly marine, the Upper Permian sediments are marginal marine to non-marine, and the Triassic sediments are dominantly fluvial (Alder *et al.*, 1998).

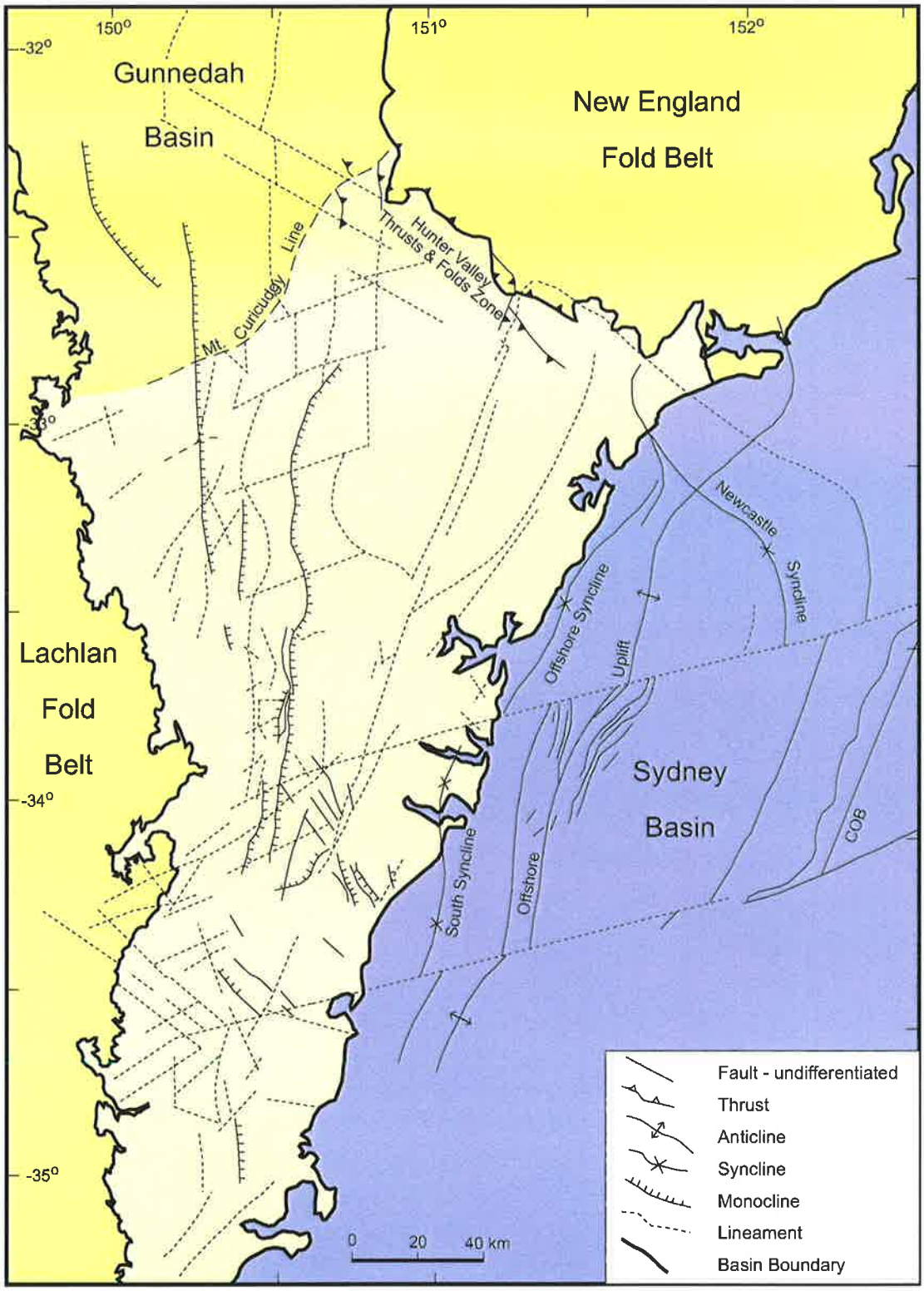

Figure 5.2 Structural map of the Sydney Basin. After Scheibner (1993).

The Hunter-Mooki thrust marks the northeastern boundary of the basin and separates the basin from the New England Fold Belt to the east (Bemebrick *et al.*, 1980; Figure 5.2). To the

north, the boundary of the basin is marked by the Mount Curicudgy Anticline, which divides the Sydney Basin from the Gunnedah Basin (Figure 5.2). This anticline probably developed as the result of a basement ridge, which was active during sedimentation (Bemebrick *et al.*, 1980). The western and southern boundaries of the Sydney Basin are marked by the thinning and onlapping of the Permo-Triassic units onto the lower Palaeozoic rocks of the Lachlan Fold Belt (Bemebrick *et al.*, 1980). The Permo-Triassic units represent relatively stable platform facies (Bemebrick *et al.*, 1980). To the southeast the boundary has been shown on marine seismic to extend to the continental shelf (Mayne *et al.*, 1974).

5.2.2 Tectonic History

The tectonic history of the Sydney Basin described here has been summarised from Herbert (1980) unless otherwise stated. The Sydney Basin developed as a tensional volcanic rift between the Lachlan and New England Fold Belts as part of the Sydney-Gunnedah-Bowen Basin system (Murray, 1990; Scheibner, 1993; Veevers and Powell, 1994). During the Late Carboniferous and Early Permian sediments were being deposited over a considerable portion of northeastern New South Wales and southeastern Queensland. The Sydney Basin attained its current structural outline after the Hunter Orogeny during the Middle Permian. The Hunter Orogeny was probably initiated following the cessation of Early Permian subduction to the east. However, a continuously moving plate pushed against the New England Fold Belt. This resulted in the development of the Hunter-Mooki Thrust System where the New England Fold Belt is thrust over the stable Lachlan Fold Belt.

The Hunter-Mooki Thrust system cushioned, to some extent, the early sediments of the Sydney Basin from the New England Fold Belt tectonism. Moderate folding occurred in the northern Sydney Basin adjacent to the thrust system. Deformation decreased in intensity towards the southwest where sediments onlapped stable parts of the Lachlan Fold Belt. While the Early Permian was dominated by marine deposition, the Late Permian was characterised by regressive clastic sediments (Alder *et al.*, 1998). The Late Permian sediments were largely derived from the New England Fold Belt, which was undergoing episodic uplift adjacent to the Hunter-Mooki Thrust system. These sediments filled the rapidly subsiding foredeep, which developed with the cessation of the subducting slab to the east. The major coal bearing facies of the Tomago, Newcastle and Illawarra coal measures were deposited during another foredeep loading episode (Alder *et al.*, 1998).

Quartz-rich sands from the Lachlan Fold Belt to the west were deposited in the basin during the intervening periods of structural quiescence and foreland bulging (Alder *et al.*, 1998). Extensive uplift at the end of the Permian culminated in the subsequent Triassic being dominated by fluvial sedimentation and an overall marine retreat to the east (Alder *et al.*, 1998). Evidence from maturity trends and burial history analyses suggest that a substantial thickness (1.5 – 3 km) of younger rocks was deposited during the Jurassic and Cretaceous, following a late Triassic hiatus (Mayne *et al.*, 1974; Sullivan *et al.*, 1995).

5.2.3 Structural Style

The Sydney Basin can be divided into a total of 8 structural subunits with characteristic structural features (Bemebrick *et al.*, 1980). However, this discussion will mainly focus on the broad scale structural features of the basin. Overall the fracture pattern present in the Sydney Basin is remarkably complex for relatively flat lying sedimentary rocks (Shepherd and Huntington, 1981). The Hunter Thrust system consists of low-angle thrusts along which Carboniferous rocks have been thrust south over Permian Sydney Basin rocks marking the northeastern boundary of the basin (Figure 5.2). A series of lesser thrusts run broadly parallel to the main thrust system in a northwest-southeast direction (Mayne *et al.*, 1974). The Hunter Valley region displays a complex structural lineament pattern (Lohe and McLennan, 1989), which is characterised by a series of north-trending anticlines and synclines with associated normal faults (Mayne *et al.*, 1974).

The prominent fault directions in the eastern section of the basin include northwest to north-northwest and north to north-northeast trending normal faults, north to north-northeast trending thrust faults and numerous other fault trends that are not as prevalent (Lohe and McLennan, 1991). The Sydney region has thrust faults in a number of orientations, ranging from northwest, north to north-northeast and northeast (Lohe and McLennan, 1991). Most of these faults are low angle or bedding parallel structures (Branagan *et al.*, 1988). The available information suggests that the north to north-northeast structures are probably the most dominant (Lohe and McLennan, 1991). The western section of the basin has normal faults ranging in strike from north-south, north-northwest and north-northeast and thrust faults typically striking north-northeast (Lohe and McLennan, 1991). Again, the majority of the thrust faults are at low angles (Lohe and McLennan, 1991).

5.3 The *In Situ* Stress Field

5.3.1 Stress Orientations

The *in situ* stress data for the Sydney Basin were divided into four subregions, Hunter Valley, Central Coast, western and Sydney-Wollongong (Figure 5.3). This was a consequence of the geographic spread of the data and the geology of the Sydney Basin. The new CSIRO data covers 58 sites, containing a total of 229 individual measurements. Four sites covered by the new data, which were in the previous ASM database, have been updated with the new detailed data and included in the statistical analysis performed here. It was also found that another four sites had been incorrectly entered into the ASM database as hydraulic fracturing measurements when they were in fact overcoring measurements. Table 5.1 summarises the new and existing data for each site. The individual measurements from which site averages have been determined and upon which the statistical analysis is based are listed in Appendix D. A new borehole breakout stress measurement (AU301) has also been added to the database but was not included in the statistical analysis, as it provides no magnitude information.

Table 5.1 Stress data for the Sydney Basin incorporating the new CSIRO data. Mean orientation in °N and all depths are in metres. Lat.: latitude, long.: Longitude, No.: number, Std Dev: circular standard deviation in degrees, Orient.: orientation, HF: hydraulic fracture measurement, OC: overcoring measurement, FMS: single focal mechanism. … continued over page.

Site	Region	Lat.	Long.	Type	No. of Measurements			Mean	Std Dev	Quality	Depth Range	
					σ_{hmin}	σ_{Hmax}	Orient.	Orient.			Top	Bottom
AU12 *	Sydney Basin	-34.170	150.320	FMS	-	-	0	073	0	C	-	-
AU75 *	Sydney Basin	-34.240	150.900	FMS	-	-	2	098	0	D	-	-
AU94 *	Sydney Basin	-34.550	150.500	FMS	-	-	-	046	-	C	-	-
AU113 @	Sydney-Wollongong	-34.318	150.880	OC	1	1	1	033	0	D	430	430
AU114 @	Hunter Valley	-32.373	150.978	OC	1	1	1	088	0	D	180	180
AU115 #	Hunter Valley	-32.591	151.044	HF	3	3	3	146	15	B	96	112
AU116 #	Hunter Valley	-32.661	151.147	HF	5	5	5	145	23	C	47	86
AU117 @	Central Coast	-33.173	151.500	OC	1	1	1	005	0	D	90	90
AU118 @	Sydney-Wollongong	-34.200	150.772	OC	1	1	1	086	0	D	480	480
AU119 #	Sydney-Wollongong	-33.959	151.250	HF	8	8	2	023	10	C	103	123
AU120 #	Sydney-Wollongong	-33.892	151.261	HF	2	2	2	048	0	C	81	105
AU140 *	Sydney Basin	-33.330	150.604	FMS	-	-	-	173	0	C	-	-
AU143 *	Sydney Basin	-33.432	150.149	FMS	-	-	-	066	0	C	-	-
AU147 *	Sydney Basin	-32.950	151.610	FMS	-	-	-	044	0	B	-	-
AU240	Western Sydney	-33.366	150.140	HF	3	3	7	171	26	C	220	358
AU241	Western Sydney	-33.385	150.140	HF	6	6	6	092	24	C	271	345
AU242	Western Sydney	-33.384	150.145	HF	6	5	4	081	21	C	291	353
AU243	Western Sydney	-33.392	150.145	HF	8	7	8	086	33	D	307	364
AU244	Western Sydney	-33.394	150.149	HF	8	8	8	113	35	D	326	384
AU245	Western Sydney	-33.382	150.145	HF	6	4	5	100	36	D	240	276
AU246	Western Sydney	-33.386	150.150	HF	7	7	7	080	16	B	309	375

Table 5.1 continued...

Site	Region	Lat.	Long.	Type	No. of Measurements			Mean	Std Dev	Quality	Depth Range	
					σ_{hmin}	σ_{Hmax}	Orient.	Orient.			Top	Bottom
AU247	Western Sydney	-33.392	150.160	HF	4	4	6	129	21	C	330	395
AU248	Western Sydney	-33.396	150.158	HF	7	7	8	150	34	D	315	383
AU249	Western Sydney	-33.391	150.162	HF	2	2	1	133	0	D	273	273
AU250	Western Sydney	-33.363	150.163	HF	3	3	7	080	16	B	309	375
AU251	Western Sydney	-33.361	150.161	HF	3	2	4	142	30	D	311	340
AU254	Hunter Valley	-32.188	150.849	HF	11	9	10	103	29	D	60	334
AU255	Hunter Valley	-32.441	150.802	HF	7	7	5	060	5	B	171	318
AU256	Hunter Valley	-32.438	150.835	HF	7	7	5	061	11	B	270	372
AU257	Sydney-Wollongong	-33.825	151.264	HF	4	4	3	036	28	D	102	125
AU258	Sydney-Wollongong	-33.972	151.247	HF	6	6	6	025	17	B	92	139
AU259	Central Coast	-33.377	151.383	HF	2	2	3	070	1	B	612	653
AU260	Central Coast	-33.082	151.400	HF	5	3	5	017	30	D	208	234
AU261	Central Coast	-33.082	151.400	HF	2	0	2	164	9	C	45	247
AU262	Central Coast	-33.082	151.400	HF	4	3	3	043	2	B	184	228
AU263	Central Coast	-33.241	151.196	HF	9	9	7	079	8	A	694	936
AU264	Central Coast	-32.900	151.244	HF	5	5	5	078	22	C	187	328
AU265	Hunter Valley	-32.355	151.256	HF	2	2	2	052	3	C	491	492
AU266	Sydney-Wollongong	-33.897	151.193	HF	4	4	8	041	21	B	143	1046
AU267	Sydney-Wollongong	-33.972	151.229	HF	6	6	6	037	12	A	407	583
AU268	Sydney-Wollongong	-33.892	151.249	HF	6	6	6	037	32	D	20	50
AU269	Sydney-Wollongong	-33.872	151.200	HF	11	11	11	008	16	D	2	17
AU270	Sydney-Wollongong	-33.882	151.197	HF	2	2	3	011	2	D	5	7
AU271	Sydney-Wollongong	-33.880	151.196	HF	5	3	6	179	56	D	3	14
AU272	Sydney-Wollongong	-33.830	151.226	HF	1	1	2	140	7	C	89	98
AU273	Sydney-Wollongong	-33.819	151.251	HF	6	6	5	178	29	D	67	97
AU284	Hunter Valley	-32.109	150.745	OC	1	1	1	084	0	D	190	190
AU285	Hunter Valley	-32.500	150.952	OC	1	1	1	086	0	D	80	80
AU286	Central Coast	-32.900	151.211	OC	1	1	1	059	0	D	550	550
AU287	Central Coast	-32.909	151.500	OC	1	1	1	016	0	D	190	190
AU288	Central Coast	-32.900	151.600	OC	1	1	1	000	0	D	100	100
AU289	Central Coast	-33.182	151.228	OC	1	1	1	066	0	D	250	250
AU290	Sydney-Wollongong	-33.959	151.250	OC	1	1	1	029	0	D	125	125
AU291	Sydney-Wollongong	-33.982	150.473	OC	1	1	1	104	0	D	173	173
AU292	Sydney-Wollongong	-34.018	150.457	OC	1	1	1	074	0	D	472	472
AU293	Sydney-Wollongong	-34.182	150.755	OC	1	1	1	075	0	D	450	450
AU294	Sydney-Wollongong	-34.200	150.554	OC	1	1	1	038	0	D	430	430
AU295	Sydney-Wollongong	-34.236	150.707	OC	1	1	1	072	0	D	500	500
AU296	Sydney-Wollongong	-34.200	150.880	OC	1	1	1	060	0	D	500	500
AU297	Sydney-Wollongong	-34.168	150.951	OC	1	1	1	048	0	D	500	500
AU298	Sydney-Wollongong	-34.255	150.913	OC	1	1	1	000	0	D	350	350
AU299	Sydney-Wollongong	-34.473	150.701	OC	1	1	1	107	0	D	400	400
AU300	Western Sydney	-33.436	150.239	OC	1	1	1	063	0	D	200	200
AU301	Sydney-Wollongong	-34.191	150.77	BO	-	-	3	018	9	A	150	638

* Data in Hillis *et al.* (1998) compilation (not updated herein and not included in the statistical compilation of Table 4.2, nor in Figures 5.3 - 5.13).

Data in the Hillis *et al.* (1998) compilation for which new, detailed CSIRO data are included in the statistical analysis herein.

@ Four of the data points in the ASM compilation of Hillis *et al.* (1998) had been incorrectly entered as based on hydraulic fracture testing when they were in fact based on overcoring.

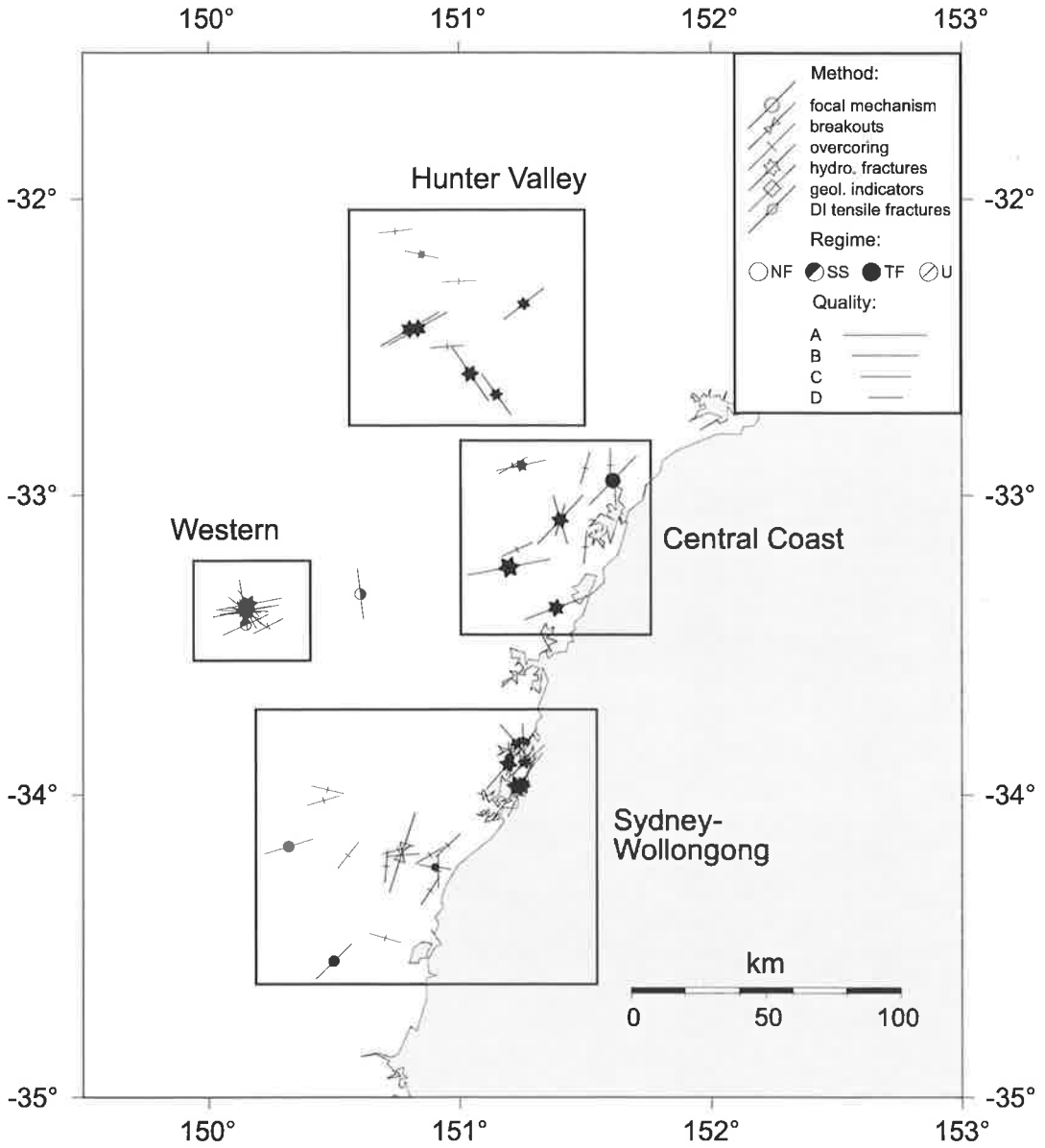

Figure 5.3 Stress map for the Sydney Basin with both the new CSIRO data and the existing ASM data plotted. The data were divided into four subregions (Hunter Valley, Central Coast, western and Sydney-Wollongong) for the statistical analysis.

The stress data for each site were averaged using circular statistics and quality ranked according to the WSM scheme as outlined in Chapter 3. The overcoring measurements were conservatively ranked as D quality for the same reason the Bowen Basin overcoring data were ranked D quality (Section 4.3.1). The new data have significantly increased the number of higher quality *in situ* stress data available for the Sydney Basin with two A and nine B quality measurements added. This compares to only one B quality measurement in the existing ASM database (Hillis *et al.*, 1998).

In contrast to the Bowen Basin (Chapter 4), there is no clear σ_{Hmax} trend across the Sydney Basin data (Figure 5.3). However, rose diagrams of the individual σ_{Hmax} orientation data do highlight some more localised trends (Figure 5.4). The most obvious trend is in the Sydney-

Wollongong subregion where the σ_{Hmax} orientation is dominantly north-northeast to south-southwest. This trend is approximately parallel to the coast. The western subregion has a very scattered σ_{Hmax} orientation with an east-west average. The Central Coast subregion has a dominantly northwest-southeast σ_{Hmax} orientation. Finally, the Hunter Valley subregion has two distinct σ_{Hmax} orientations. A more dominant northeast-southwest trend and a less dominant northwest-southeast trend. To test whether these trends are significant a statistical analysis of the σ_{Hmax} orientations was conducted.

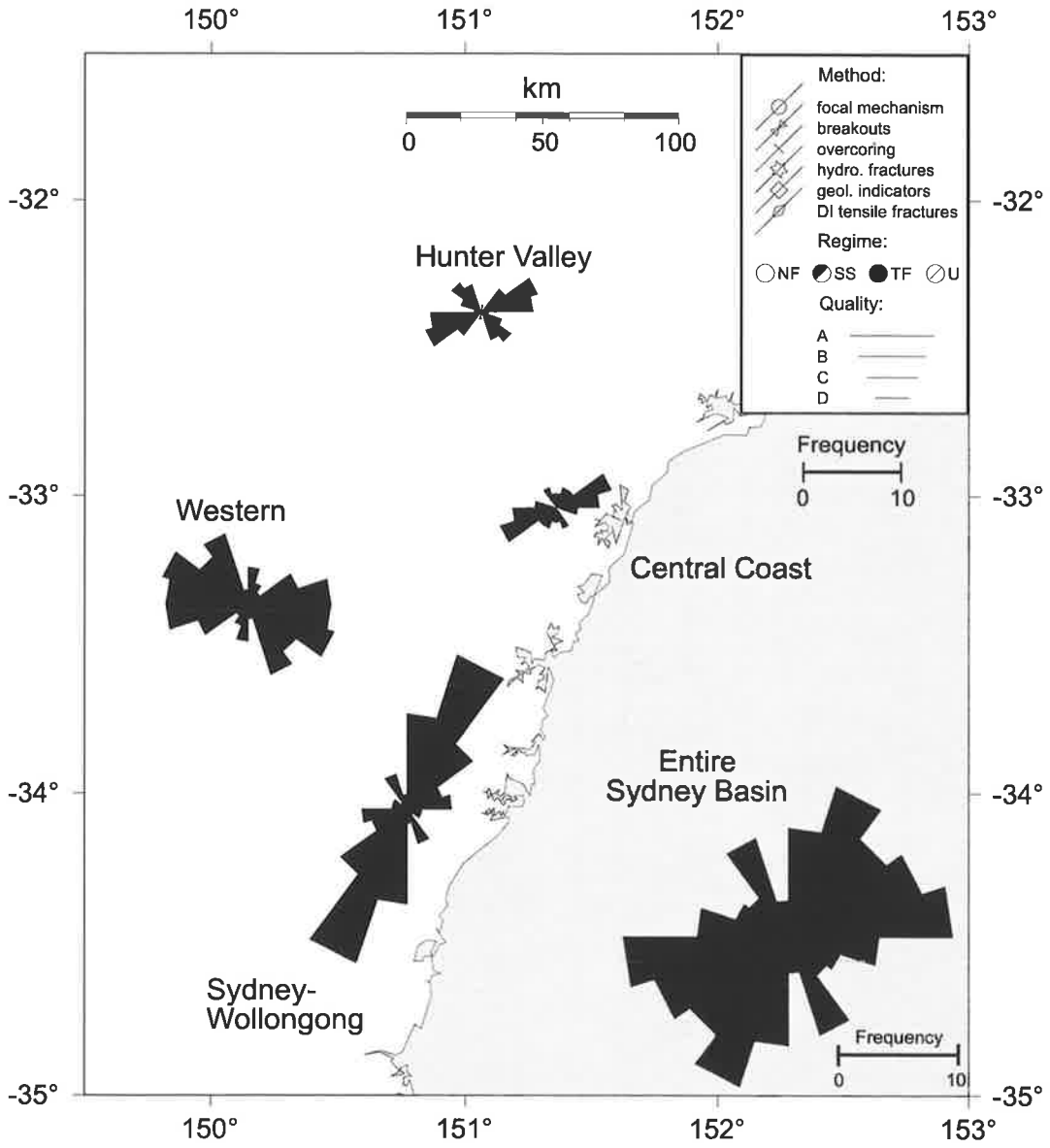

Figure 5.4 Rose diagrams of σ_{Hmax} orientations for the four subregions of the Sydney Basin. Rose diagram for the entire Sydney Basin shown in bottom right. Note the rose diagrams of the four subregions are at the same scale (top). The rose diagram of the entire Sydney Basin is at a different scale to the four subregions (bottom). All rose diagrams use a bin size of 18°.

A statistical analysis was conducted on the four subregions as well as the basin as a whole using all individual measurements. The analysis was performed following the procedure

outlined in Appendix C and as undertaken on the Bowen Basin data. The Rayleigh test was used to determine if the null hypothesis that the σ_{Hmax} orientations are random could be rejected. This test assumes that random orientations sample a von Mises distribution, the circular equivalent to the normal distribution (Mardia, 1972). The western and Sydney-Wollongong regions both exhibit a unimodal distribution of σ_{Hmax} orientations at a 99.9% confidence level (Figure 5.5). The Central Coast region and the entire Sydney Basin exhibit a unimodal distribution of σ_{Hmax} orientations at a 99% confidence level (Figure 5.5). The distribution of σ_{Hmax} orientations for the Hunter Valley region indicated a unimodal distribution at a 97.5% confidence level and thus, is not considered unimodal as the confidence level was below the 99% level. The mean σ_{Hmax} orientation for the unimodal analysis ranges from 058°N in the Central Coast region, 108°N in the western region and 028°N in the Sydney-Wollongong region (Table 5.2). The mean σ_{Hmax} orientation of the entire Sydney Basin is 058°N (Table 5.2). The statistics for the Hunter Valley region have been listed in Table 5.2, but as previously mentioned, the distribution of orientations is not considered unimodal. The borehole breakout stress indicator (018°N) has not been included in this statistical analysis, but is consistent with the mean σ_{Hmax} orientation for the Sydney-Wollongong region (028°N) where it is situated. Unlike the Bowen Basin, the Sydney Basin does not have a consistent σ_{Hmax} orientation trend laterally over the basin.

Histograms of the σ_{Hmax} orientations in the four subregions and the entire Sydney Basin further highlight the features of each distribution (Figure 5.6). A semi-circular normal distribution curve was used to approximate σ_{Hmax} orientations for each region using the procedure outline in Appendix C (Figure 5.6). Both the Sydney-Wollongong, Central Coast and western subregions have a reasonable match between their respective histograms and theoretical curves. The fit for the entire Sydney Basin is considered adequate given the broad scatter of data points. The optimal unimodal curve has been placed over the Hunter Valley histogram to illustrate the poor fit to the observed orientation data. Moreover, the mean of the theoretical distribution falls mid-way between the two peaks in the histogram illustrating the inappropriateness of applying unimodal analysis.

A bimodal analysis was conducted on the stress orientation data from the Hunter Valley region. The bimodal analysis attempts to minimize the fit of a bimodal circular normal distribution to the observed σ_{Hmax} orientation data. A bimodal circular normal distribution is essentially two unimodal circular normal distributions superimposed on one another.

Appendix C contains a more detailed description of this procedure. In the case of the Hunter Valley region, a bimodal distribution with the following parameters best fits the orientation data; mean and concentration parameter of distribution one are 066°N and 5.30 respectively; mean and concentration parameter of distribution two are 134°N and 1.99 respectively. The proportion of measurements in the first distribution is 0.56 (Figure 5.7). Both distributions individually indicate a significant trend at a 99.9% confidence level. Hence, the σ_{Hmax} orientations in the Hunter Valley data are considered bimodal. The fit of the bimodal circular normal distribution curve to the histogram of Hunter Valley σ_{Hmax} orientations is shown in Figure 5.7. The bimodal theoretical distribution produces a significantly better fit to the data than the unimodal distribution. The mean σ_{Hmax} orientation from the first distribution of the Hunter Valley data is consistent with the mean σ_{Hmax} orientation obtained from the nearby Central Coast. Thus the northeast-southwest orientation appears to be the regional trend for the northeastern part of the Sydney Basin.

Table 5.2 Summary of results from the unimodal analysis of the Sydney Basin data. Std Dev: standard deviation. Conf. Level: Confidence level passed when the Rayleigh test was applied (see Appendix C).

Region	Unimodal Analysis			
	Mean (°N)	Std Dev	Number	Conf. Level
Hunter Valley	085	41	33	97.5
Central Coast	058	39	31	99
Western	108	43	71	99.9
Sydney-Wollongong	028	33	72	99.9
Entire Basin	058	55	207	99

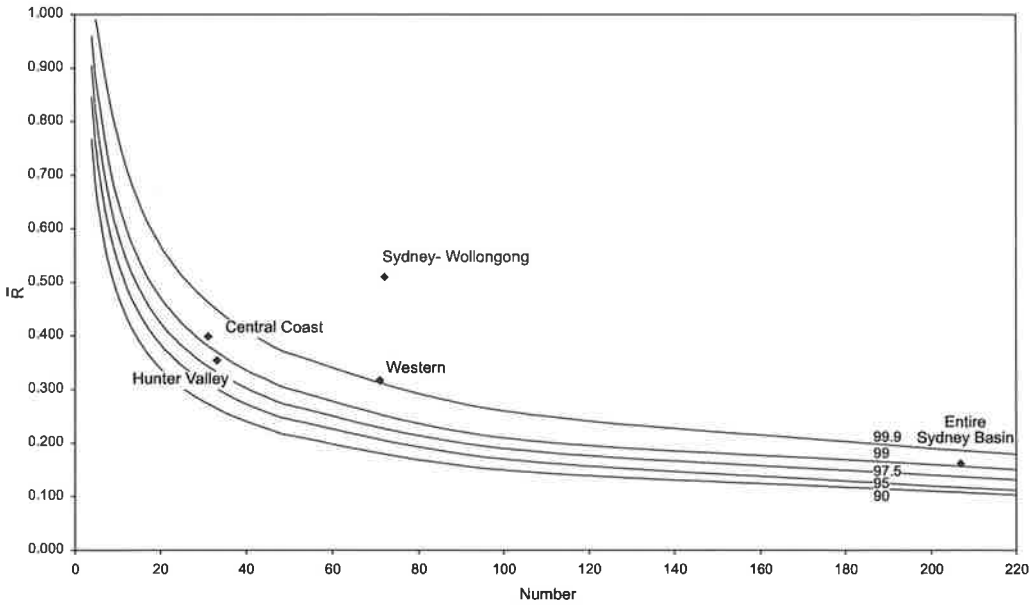

Figure 5.5 $\bar{R}$ value versus number of data points for the four subregions and the entire Sydney Basin. Curved lines correspond to the $\bar{R}$ value needed to pass the Rayleigh test for significance levels ranging from 90% to 99.9% when using a specific number of data points. The $\bar{R}$ value is the length of the mean resultant vector of σ_{Hmax} orientations within a region (see Appendix C).

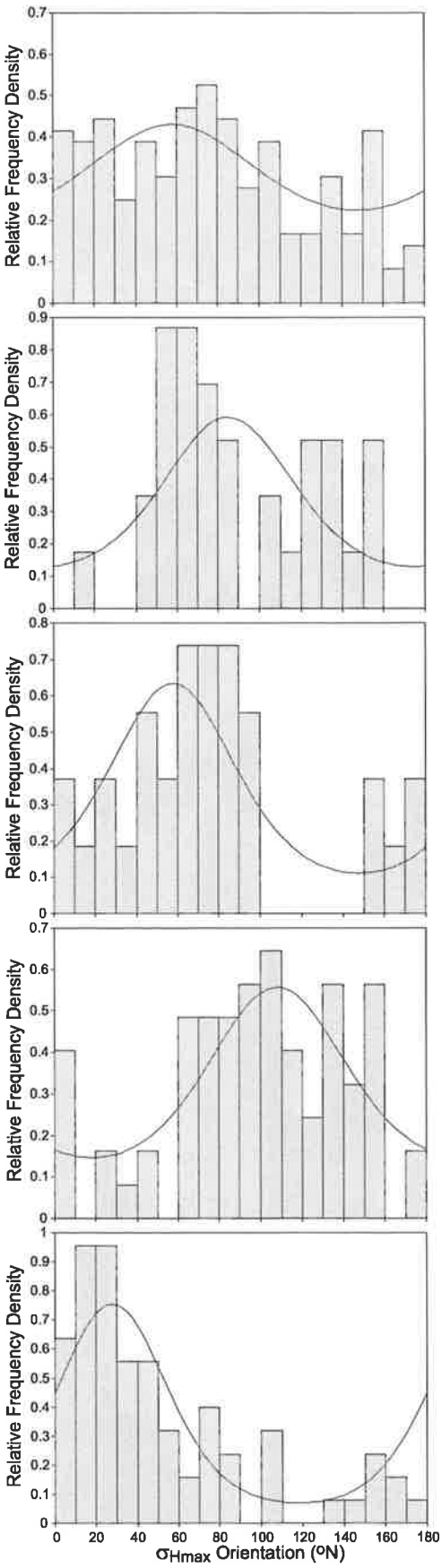

(a) Entire Sydney Basin

Mean = 058°N
Concentration Parameter = 0.33

(b) Hunter Valley

Mean = 085°N
Concentration Parameter = 0.76

(c) Central Coast

Mean = 058°N
Concentration Parameter = 0.87

(d) Western Sydney Basin

Mean = 108°N
Concentration Parameter = 0.67

(e) Sydney-Wollongong

Mean = 028°N
Concentration Parameter = 1.19

Figure 5.6 (a) Maximum horizontal stress orientation histogram for the entire Sydney Basin and **(b)-(e)** histograms for Sydney Basin subregions. Bin sizes are in 10° increments plotted against relative frequency density. Histograms are overlain by a circular normal distribution curve calculated from the data. See Appendix C for the methodology for the calculation of the circular normal distribution curves. The concentration parameter indicates the spread of data and is equivalent to, but opposite in magnitude to standard deviation from circular statistics.

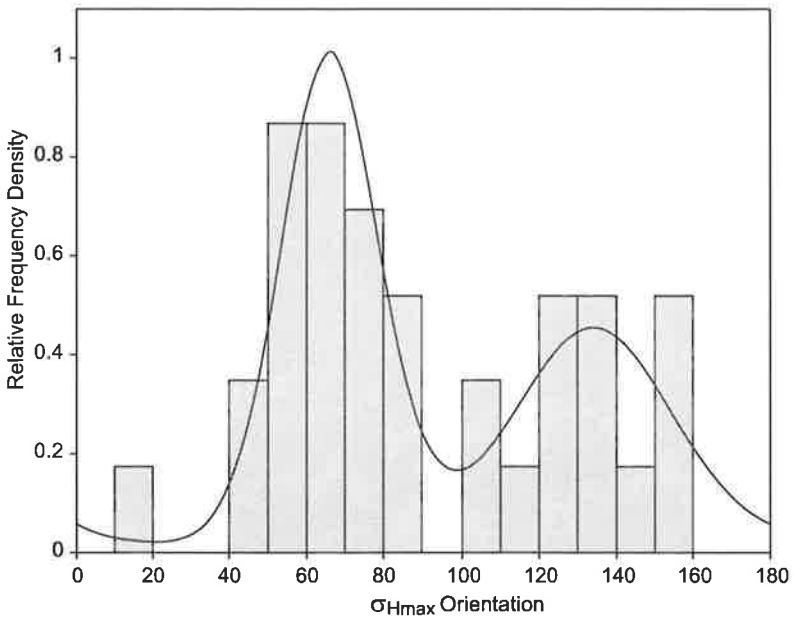

Figure 5.7 Maximum horizontal stress orientation histogram for the Hunter Valley subregion using a bimodal circular normal distribution. Parameters to generate the curve are as follows: mean one = 066°N, mean two = 134°N, concentration one = 5.30, concentration two = 1.99 and the proportion of data in the first distribution is 0.56. Both trends are significant at a 99.9% confidence level. Thus the distribution of data is considered bimodal.

The σ_{Hmax} orientations have been plotted against depth to determine if the σ_{Hmax} orientations schematically vary with depth (Figure 5.8). The σ_{Hmax} orientation data in the Hunter Valley, Sydney-Wollongong and Central Coast subregions appear to become more consistent with depth. The Central Coast region shows a large amount of scatter in stress orientations above 300 m in depth, but becomes more consistent, between 060°N and 100°N, below 300 m. Similarly the stress orientations in the Sydney-Wollongong region are fairly scattered above 300 m depth and more consistent below 300 m. However, the stress orientations below 300 m in the Sydney-Wollongong region are not as consistent as in the Central Coast region, ranging between 000°N and 110°N.

The σ_{Hmax} orientation data in the Hunter Valley can be subdivided into two groups, one above approximately 200 m and the other below 200 m (Figure 5.8). These two groups correspond to each of the modes of the bimodal distribution previously identified for the Hunter Valley data. The measurements below 200 m correspond to the distribution with a mean of 066°N. This data appears to correspond to the regional σ_{Hmax} trend for the northeast area of the Sydney Basin with the data above 200 m depth being reoriented by local features. Such local features could possibly include structure, topography or density heterogeneities. Stress orientation patterns in the western region are not clarified in the orientation versus depth plot (Figure 5.8).

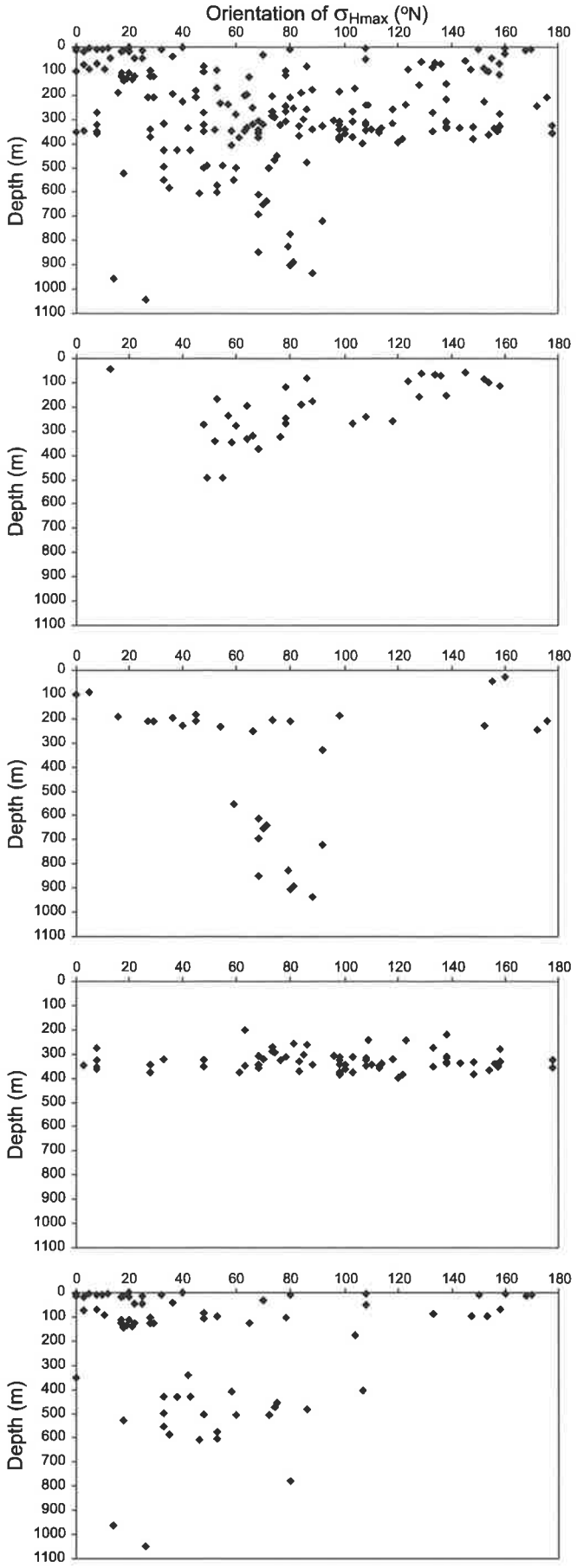

Figure 5.8 Maximum horizontal stress orientation versus depth for **(a)** entire Sydney Basin and **(b)-(e)** Sydney Basin subregions. No orientation trend is apparent with depth. Note however that the data appears slightly more consistent with depth for the Central Coast, Sydney-Wollongong and Hunter Valley subregions. Note also the group of locally reoriented data centred on 140° in the Hunter Valley subregion.

5.3.2 Stress Magnitudes

Hydraulic fracturing and overcoring tests allow the magnitudes of σ_{Hmax} and σ_{hmin} to be estimated as discussed in Sections 3.4 and 3.5. Throughout this analysis σ_v has been estimated using an overburden density of 2308 kgm^{-3} (equivalent to an overburden stress gradient of 22.6 MPa/km or 1 psi/ft) on the basis of density log data. The fault conditions reverse ($\sigma_{Hmax}>\sigma_{hmin}>\sigma_v$), strike-slip ($\sigma_{Hmax}>\sigma_v>\sigma_{hmin}$) and normal ($\sigma_v>\sigma_{Hmax}>\sigma_{hmin}$) are used to describe relative stress magnitudes in the following discussion. It should be noted, however, that this does not necessarily imply the *in situ* stress data are consistent with failure (see Section 4.4 for further discussion).

The majority (90%) of the *in situ* stress data for the Sydney Basin indicate a reverse faulting stress regime (Figure 5.9). Around 9% of the data indicate a strike-slip faulting stress regime, while only 1% of the data indicate a normal faulting stress regime. These results are broadly consistent with the six focal mechanism solutions for the Sydney Basin, with four indicating a reverse faulting stress regime and two indicating a strike-slip faulting stress regime. The four focal mechanisms indicating a reverse faulting stress regime are the four deepest earthquakes ranging from 9 km to 21 km in depth. The two strike-slip earthquakes are relatively shallow at 2 km and 5 km in depth. The available data overwhelmingly indicate a reverse faulting stress regime for the Sydney Basin. In general, the scatter of the σ_{Hmax} and σ_{hmin} magnitudes increases with depth (Figure 5.9).

Depth-normalized plots of σ_{Hmax} versus σ_{hmin} for the Sydney Basin data are shown in Figure 5.10. These plots display the three stress regimes bounded by frictional failure lines for three different values of the coefficient of friction, μ (0.6, 0.85 and 1.0). Approximately 61% of all values lie in the reverse faulting stress regime as indicated by Figure 5.10. However, 42% of the total data lies between the failure line for $\mu = 0.6$ and $\mu = 1.0$ in the reverse faulting stress regime. Furthermore, approximately 29% of all data points lie above the failure line for $\mu = 1.0$. Some of the values in the Sydney-Wollongong region are so high they could not be represented on the one plot (see insert to Figure 5.10e). Hence much of the engineering stress data for the Sydney Basin suggests stress regimes at, or very close to failure. This topic will be discussed further in Section 5.4, where the *in situ* stress field and seismicity for the Sydney Basin are compared.

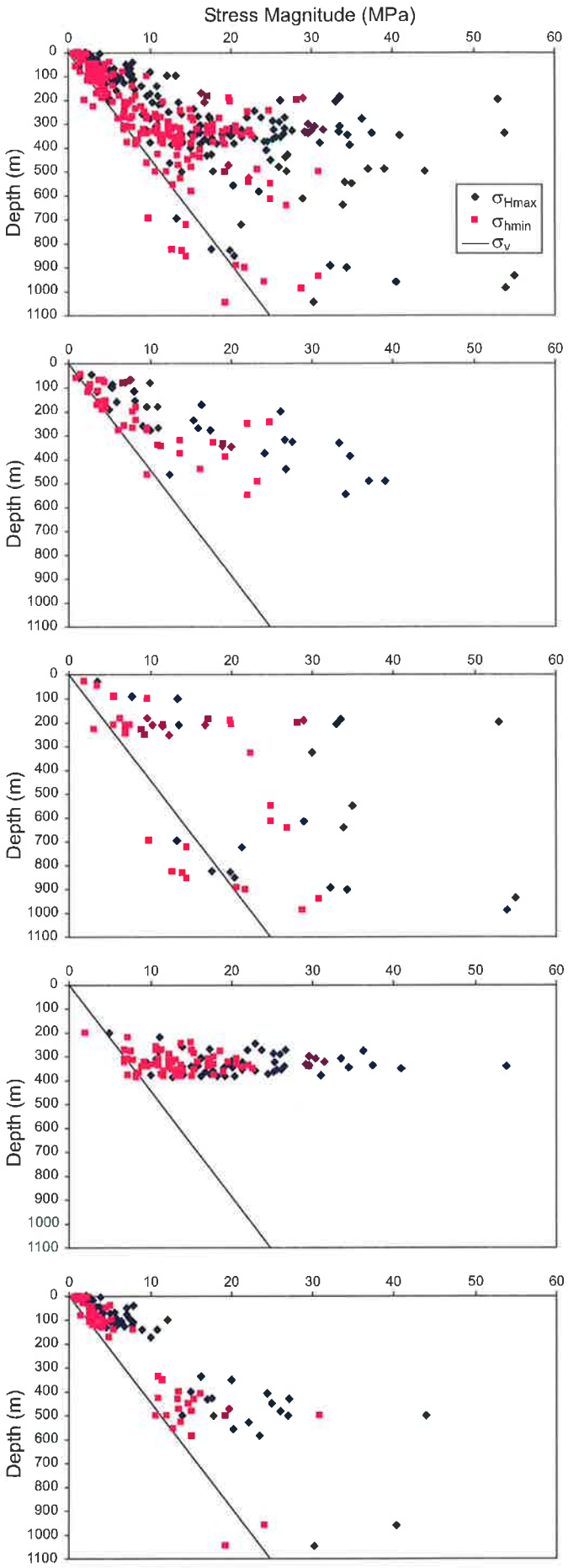

Figure 5.9 Stress magnitude versus depth for **(a)** entire Sydney Basin and **(b)-(e)** Sydney Basin subregion. The reference line is the vertical stress with an overburden density of 2308 kgm^{-3}.

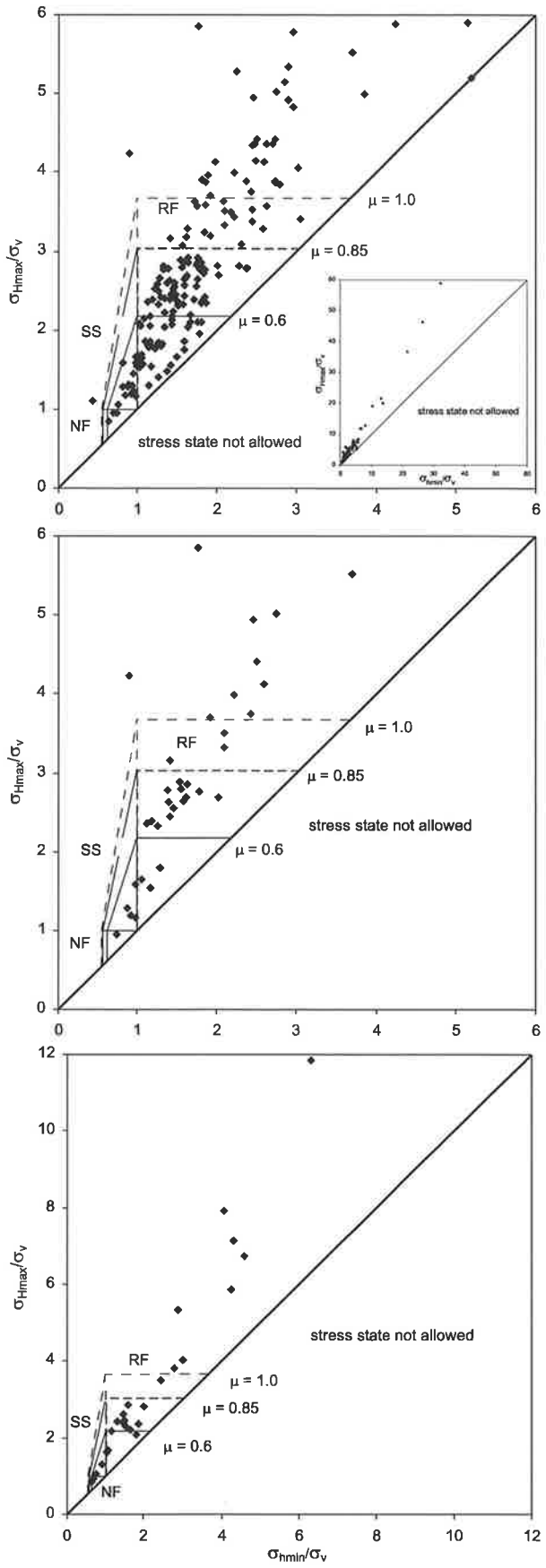

Figure 5.10 Depth-normalized σ_{Hmax} versus σ_{hmin} plots for **(a)** entire Sydney Basin, **(b)** the Hunter Valley and **(c)** the Central Coast. RF = reverse faulting stress regime, SS = strike-slip faulting stress regime, NF = normal faulting stress regime. ...continued over page.

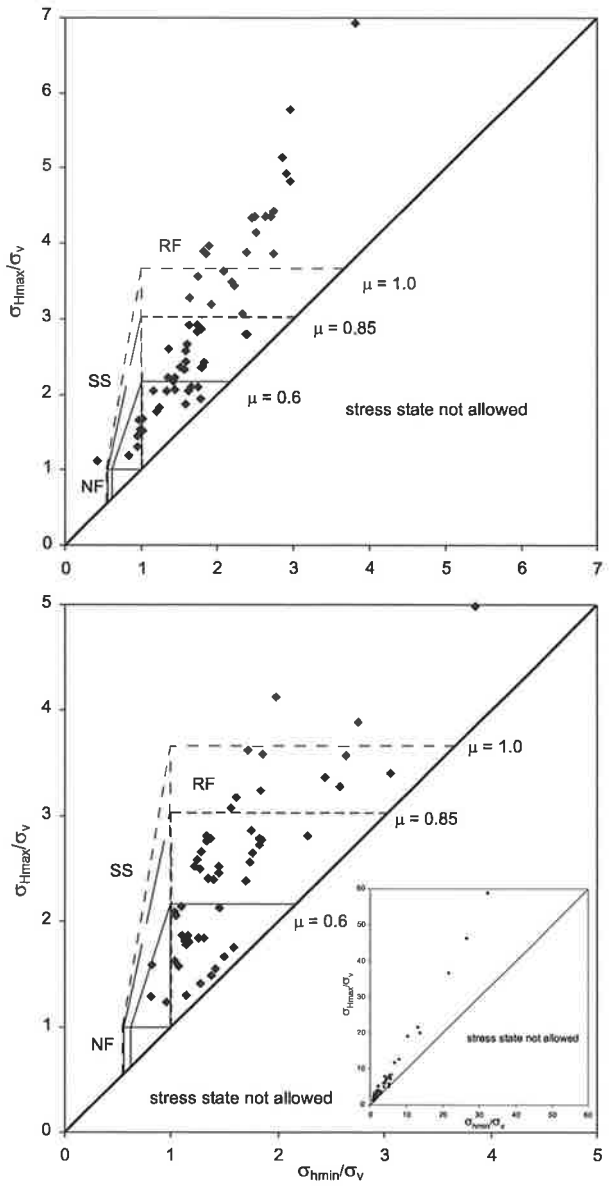

Figure 5.10 continued... Depth-normalized σ_{Hmax} versus σ_{hmin} plots for **(d)** the western Sydney Basin and **(e)** the Sydney-Wollongong. RF = reverse faulting stress regime, SS = strike-slip faulting stress regime, NF = normal faulting stress regime.

The lithostatic and uniaxial references states were removed from the Sydney Basin data for the same reasons and using the same techniques as in the Bowen Basin (Section 4.3.2). Neither reference state successfully removes the depth trends in the data (Figure 5.11). Nonetheless, the lithostatic reference state is significantly better than the uniaxial reference state and is thus the preferred reference state of stress. Hence, both in the Sydney and Bowen Basins the modelled tectonic stress appears best considered as non-lithostatic. Using the lithostatic reference state the average tectonic stress across the Sydney Basin was 10.15 MPa for σ_{Hmax} and 4.04 MPa for σ_{hmin}. This compares to a value of 5.21 MPa for σ_{Hmax} and 1.95 MPa for σ_{hmin} in the Bowen Basin. Thus, the tectonic stress magnitudes are approximately twice as high in the Sydney Basin than the Bowen Basin. However, the Sydney Basin has a higher standard deviation due to the large scatter in stress magnitude.

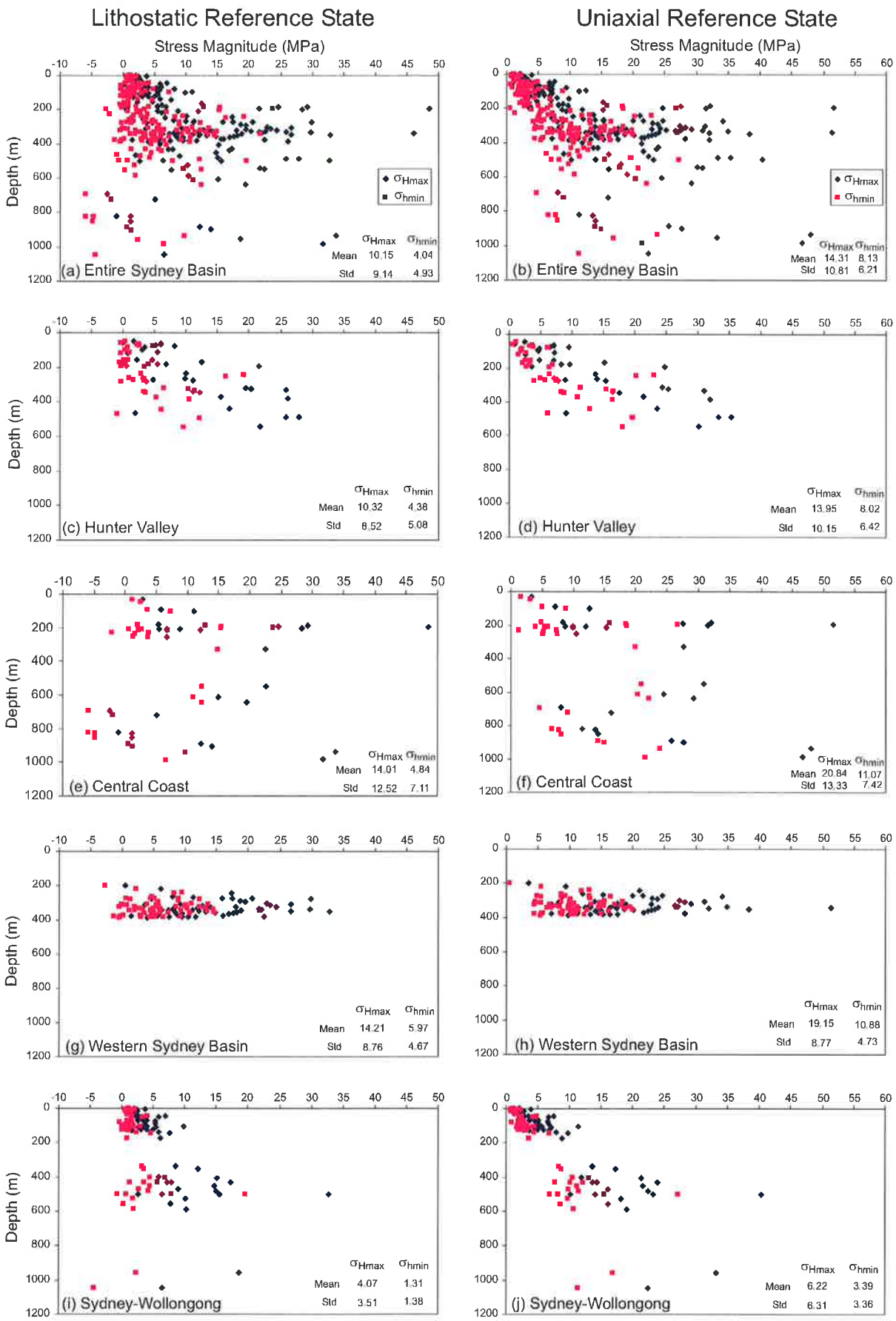

Figure 5.11 Stress magnitude versus depth for the entire and subregions of the Sydney Basin with the lithostatic and uniaxial reference states removed. Removing the lithostatic reference state from the data better removes depth trends than does the uniaxial reference. A Poisson's ratio of 0.25 was used to calculate the uniaxial reference state.

5.4 *In Situ* Stress and Seismicity

The Sydney Basin is one of Australia's most seismically active areas (Figure 4.12). A number of large earthquakes have occurred in the region (Denham, 1980; McCue *et al.*, 1989; Spassov and Kennett, 2000) including the damaging Newcastle earthquake of 1989, which resulted in 12 deaths, hundreds of injuries, and serious damage to thousands of homes and buildings (McCue *et al.*, 1990b). The seismicity in the area, as with most intraplate seismicity, occurs at relatively shallow focal depths. The ASM database contains a total of seven focal mechanism solutions from earthquakes in eastern Australia with estimated focal depths ranging from 2 to 21 km. The intention of this section is to investigate whether the relatively shallow (0-1 km) engineering measurements are consistent with the high levels of seismicity for the area. In order to evaluate this a Mohr-Coulomb analysis of the propensity for failure was conducted. This involved combining the stress data defined in Section 5.3 with the structural data outlined in Section 5.2 (Figure 5.12). The rationale and procedure was as for that in the Bowen Basin (Section 4.4) and as further outlined in Appendix B.

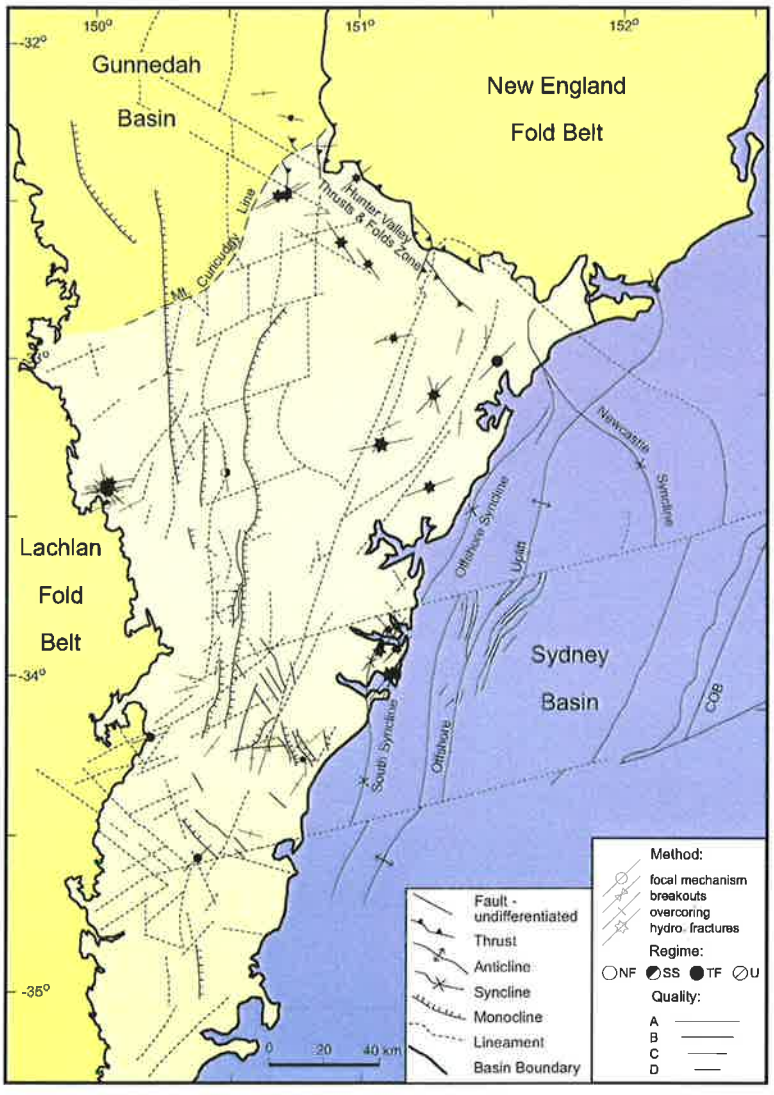

Figure 5.12 Overlay of structural map (Figure 5.2) with stress orientations of the Sydney Basin.

The Mohr-Coulomb analysis indicates approximately 41% of the depth-normalised shear and normal stresses for the Sydney Basin lie above Byerlee's (1978) failure line and thus indicate failure (Figure 5.13a). A number of points plot well above the failure line due to the very large shear stresses and are shown on the insert in Figure 5.13. These points are the result of a number of shallow stress measurements producing large values for the magnitude of σ_{Hmax} and σ_{hmin} and may be due to near-surface effects. Nonetheless, only 13% of the stress measurements in the Bowen Basin were indicative of failure. Hence there appears to be some correlation between the shallow *in situ* stress measurements and the levels of seismicity in the two regions.

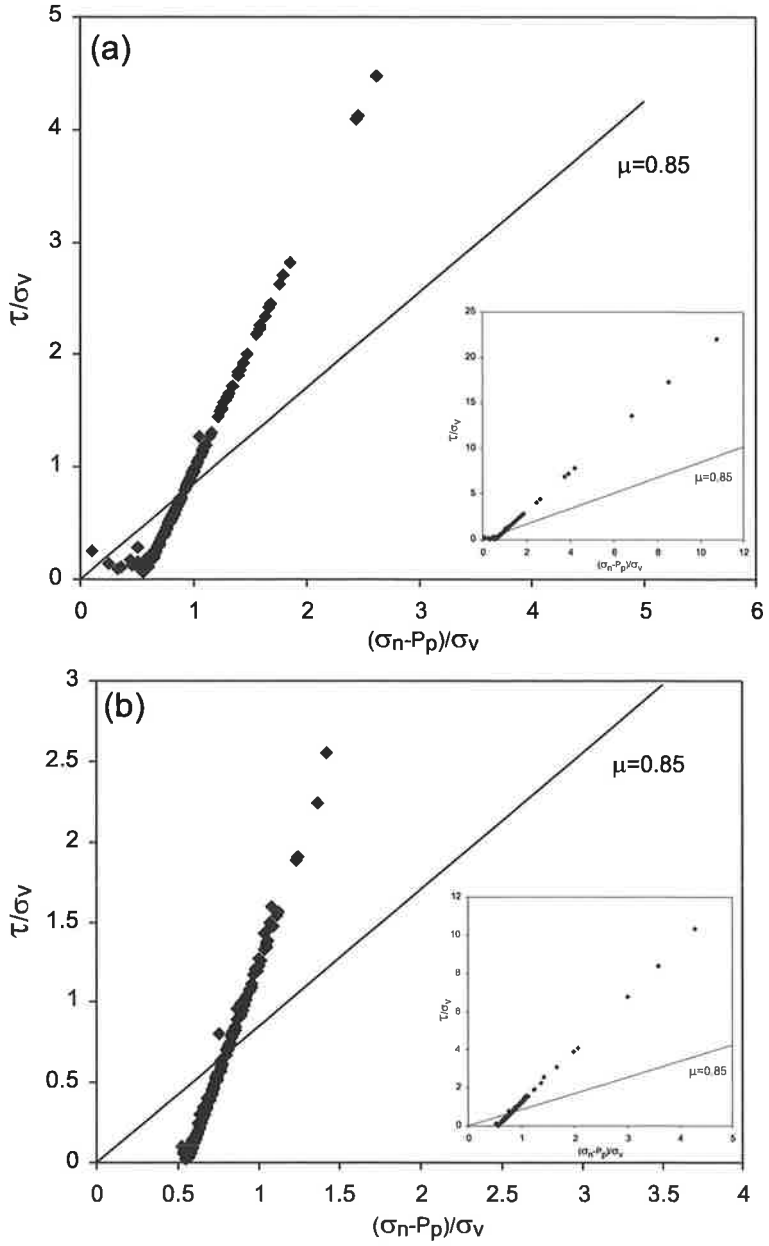

Figure 5.13 Effective normal stress versus shear stress normalised for depth. **(a)** Most critically stressed points on the 3D Mohr's circles based on *in situ* stress data from the Sydney Basin and assuming $\mu = 0.85$. **(b)** Stresses acting on planes striking 020° and dipping at 20°. Byerlee's (1978) failure line ($\mu = 0.85$) is shown. Insert to both plots are at different scale showing a number of points with high shear stress not apparent on the main plots.

As in the Bowen Basin, the Mohr-Coulomb analysis above was repeated allowing for the structural history of the Sydney Basin. Unlike the Bowen Basin, the Sydney Basin does not have a dominant structural grain over the entire basin (Lohe and McLennan, 1991). Thus, the choice of structural grain for the Sydney Basin is somewhat arbitrary. The predominant structural grain for the Sydney Basin was taken to be a shallow-dipping (20°) plane striking north-northeast (020°N). Figure 5.13b displays the depth normalized effective normal and shear stresses acting on this assumed predominant structural grain. When the structural grain is considered the number of stress measurements indicative of failure is reduced to 31%. In contrast, the number of stress measurements indicative of failure in the Bowen Basin was reduced to 3% when the structural grain was considered. Thus, the relative amount of seismicity in the Bowen and Sydney Basins appears to be reflected in the shallow (0-1 km) engineering *in situ* stress measurements when considering the structural grain of the regions.

5.5 Discussion

Analysis of σ_{Hmax} orientations in the Sydney Basin suggests there is no consistent regional trend. However, three main trends have been identified within the basin. These include east-west in the western section of the basin, north-northeast to south-southwest in the southeastern section of the basin and northeast-southwest in the northeastern section of the basin. The apparent variation in the σ_{Hmax} orientation within the basin cannot be attributed to plate boundary forces, which would produce long wavelength variations in the stress field. Hence a local source or sources of stress must strongly influence the present-day stress field in the Sydney Basin.

The observed *in situ* stress data in the Sydney Basin shows little evidence of the margin-normal σ_{Hmax} orientation predicted by the modelling of Zhang *et al.* (1996) based on the density structure of the passive margin for the region. The majority of the stress orientations in the Sydney Basin are approximately margin-parallel with only the western region of the basin indicating a margin-normal σ_{Hmax} orientation. A margin-parallel σ_{Hmax} orientation has been predicted by Bott and Dean (1972) and Stein *et al.* (1989) to occur on the continental side of the continental margin. This is a result of the lateral variation in crustal thickness and density along continental margins. Another effect that can produce margin parallel σ_{Hmax} orientation is flexural stresses as a result of sediment loading on the continental margin (Stein *et al.*, 1989). However, very little sediment has accumulated on the continental margin in the

region (Conolly, 1969; Ringis, 1972). Thus, sediment loading is unlikely to be the cause of the stress field in the Sydney Basin.

Plate boundary and potential energy force modelling has indicated an approximately east-west σ_{Hmax} orientation for the Sydney Basin (Chapter 8). More importantly the modelling has predicted a relatively isotropic stress field ($\sigma_{Hmax} \approx \sigma_{hmin}$) for much of eastern Australia. This result is consistent with the predictions of Coblentz *et al.* (1995) and Coblentz *et al.* (1998). An isotropic regional stress field would allow local sources of stress, such as structure, topography and density heterogeneities to strongly influence the observed stress field (Zoback, 1992). Topography and density heterogeneities in the lithosphere can generate substantial horizontal stress magnitudes of the same order as the regional tectonic stress (Artyushkov, 1973; Fleitout and Froidevaux, 1982; Mareschal and Kuang, 1986; Sonder, 1990; Assameur and Mareschal, 1995). The topography within the Sydney Basin ranges from sea level on the eastern coastline to over 1000 m in the western part of the basin. The elevated section of the Sydney Basin contributes to the eastern highlands of continental Australia. These highlands stretch approximately north to south across a large part of eastern Australia and have the potential to significantly influence the near-surface stress field in the region. Nonetheless, it is beyond the scope of this project to calculate the stresses generated by this topography. Numerous stress studies have identified structure as an important controlling factor in the orientation of the stress field (Aleksandroski *et al.*, 1992; Dart *et al.*, 1995; Ask, 1997). As previously mentioned in Section 5.2, the Sydney Basin has numerous structural trends and hence structure cannot be discounted as a major influence to the stress field in the basin. Rigid crustal block modelling has been conducted by Enever and Clark (1997) demonstrating that local stress rotations in the Sydney Basin could be accounted for in terms of block faulting within east-west and north-south stresses. However, the relatively local scale at which these processes appear to operate is beyond the resolution of the available stress/structural data.

The stress field of the Sydney Basin is interpreted to be the result of an approximately east-west regional σ_{Hmax} orientation upon which continental margin effects due to variations in crustal thickness and density are superimposed near the coastline. The bimodal σ_{Hmax} orientation seen in the Hunter Valley region is likely to be the result of local sources of stress such as structure or density contrasts, but the resolution of this is beyond the available stress/structural data. A change of the σ_{Hmax} orientation occurs above approximately 200 m in

depth indicating a near surface source. The general scatter seen in the western subregion is probably the result of the higher topography in the region.

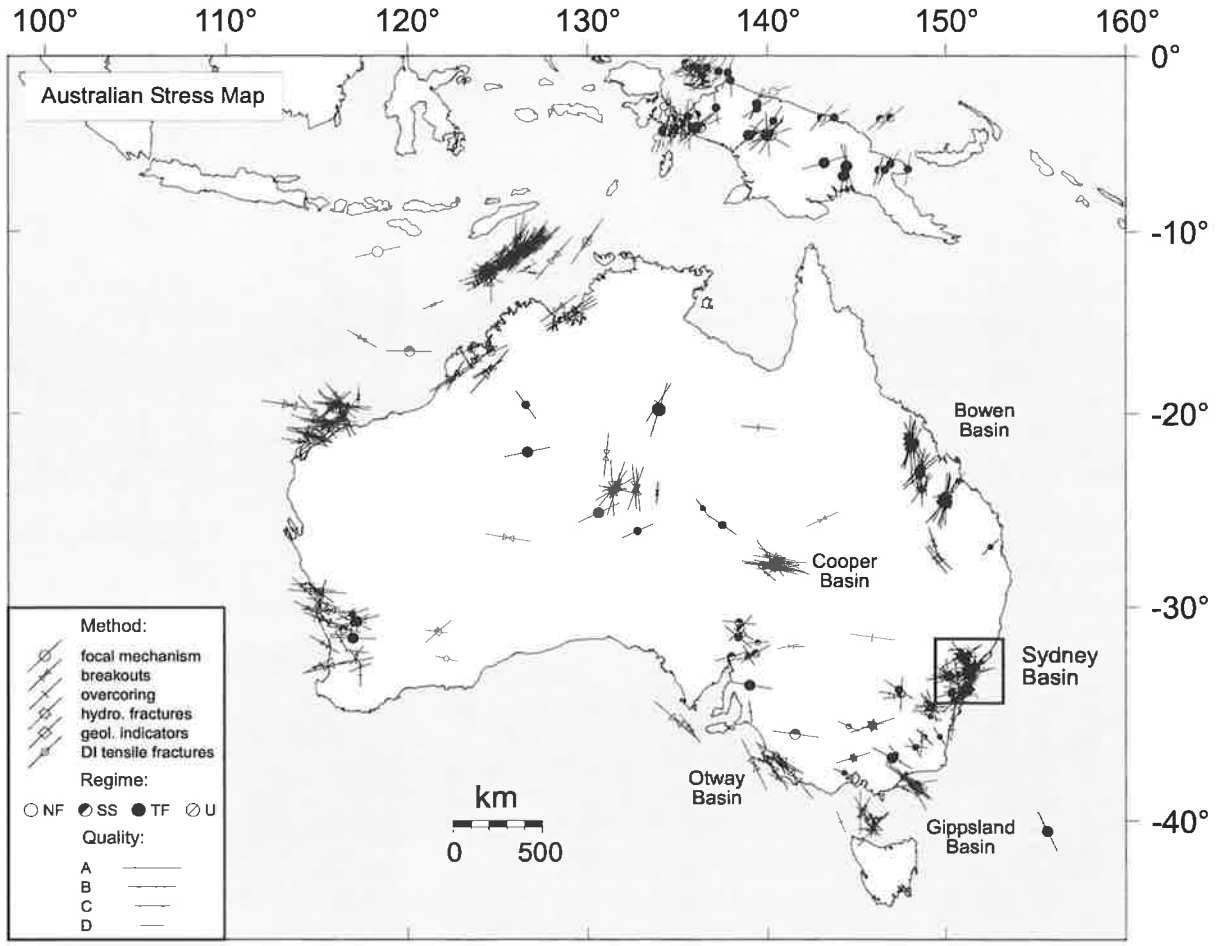

Figure 5.14 The Australian stress map using A-D quality data with the new stress data for the Sydney Basin.

The approximate east-west σ_{Hmax} orientation present in the western region of the Sydney Basin is consistent with other *in situ* stress indicators throughout New South Wales (Figure 5.14). As with the western region of the Sydney Basin, these indicators show a significant degree of scatter. Further to the west a more consistent east-west σ_{Hmax} orientation is seen in the Cooper Basin (Figure 5.14). To the north the σ_{Hmax} orientation has rotated to a consistent approximately north-south direction in the Bowen Basin (Chapter 4). Both the Otway and Gippsland Basins to the southwest of the Sydney Basin show a consistent southeast-northwest σ_{Hmax} orientation (Figure 5.14). Thus, regions with consistent σ_{Hmax} orientation surround a large area of New South Wales characterised by variable σ_{Hmax} orientations. The variable σ_{Hmax} orientations are considered to reflect relatively isotropic horizontal stresses in the area related to plate boundary forces.

5.6 Summary

1. A significant new database of engineering stress measurements has elucidated the *in situ* stress field of the Sydney Basin.
2. The mean σ_{Hmax} orientation of the entire Sydney Basin is 058°N and passes the Rayleigh test at a 99% confidence level.
3. The mean σ_{Hmax} orientation ranges from 058°N in the Central Coast region, 108°N in the western region and 028°N in the Sydney-Wollongong region.
4. The Hunter Valley data indicate a bimodal trend, which is depth dependent.
5. The majority of the stress magnitude data indicate a reverse faulting stress regime.
6. The lithostatic reference state is the preferred reference state of stress.
7. The relatively shallow engineering stress data are consistent with the high levels of seismicity for the area with a large number of measurements indicating possible failure.
8. The stress field in the Sydney Basin appears to be dominated by local sources of stress due to the isotropic stress field produced by plate boundary forces.

Chapter 6

The *In Situ* Stress Field of the Perth Basin

6.1 Introduction

This chapter is based very closely on a paper published in Geophysical Research Letters and attached in Appendix H (Reynolds and Hillis, 2000). Limited previous data suggested a regional east-west σ_{Hmax} orientation in the Perth area (e.g. ASM release of Hillis *et al.*, 1998). This east-west orientation is almost orthogonal to the north-northeast direction of absolute plate velocity. Hence the Perth area is an important location with which to test whether σ_{Hmax} orientations parallel absolute plate velocity in the IAP. Previous *in situ* stress data in the Perth area were restricted to the Yilgarn Block, a major Precambrian basement province separated from the Perth Basin by the Darling Fault (Figure 6.1). Furthermore, 14 of the 18 previously existing stress indicators in the Yilgarn Block were poor quality (C and D), shallow overcoring and hydraulic fracturing measurements. In addition, four earthquake focal mechanisms were available in the Yilgarn Block. These data indicated a broadly east-west σ_{Hmax} orientation. In this chapter borehole breakout data are presented from the Perth Basin. These new data add significantly to our knowledge of the stress field in southwestern Australia (Figure 6.1).

6.2 Geological Setting

The Perth Basin is a deep linear trough located in the southwest of Western Australia (Figure 6.1b). The basin extends in a north-south direction for approximately 1000 km both onshore and offshore. Sedimentation commenced in the northern Perth Basin in the Ordovician and had spread throughout most of the basin by the Carboniferous to early Permian (Harris, 1994). Up to 15 km of Phanerozoic sedimentary rocks may have been deposited in parts of the basin (Playford *et al.*, 1976). The basin has a half graben configuration and is situated along a passive continental margin bounded on the east side by the Darling Fault (Harris, 1994). The Darling Fault is the major structural feature of the basin separating the Phanerozoic sedimentary rocks from Archaean rocks of the Yilgarn Block to the east. The Darling Fault extends in a north-south direction for about 1000 km with a maximum throw possibly exceeding 15 km (Playford *et al.*, 1976). The prominent fault trend

throughout the basin is north to north-northwest (Dentith *et al.*, 1994) with most faults moderately to steeply dipping (Playford *et al.*, 1976).

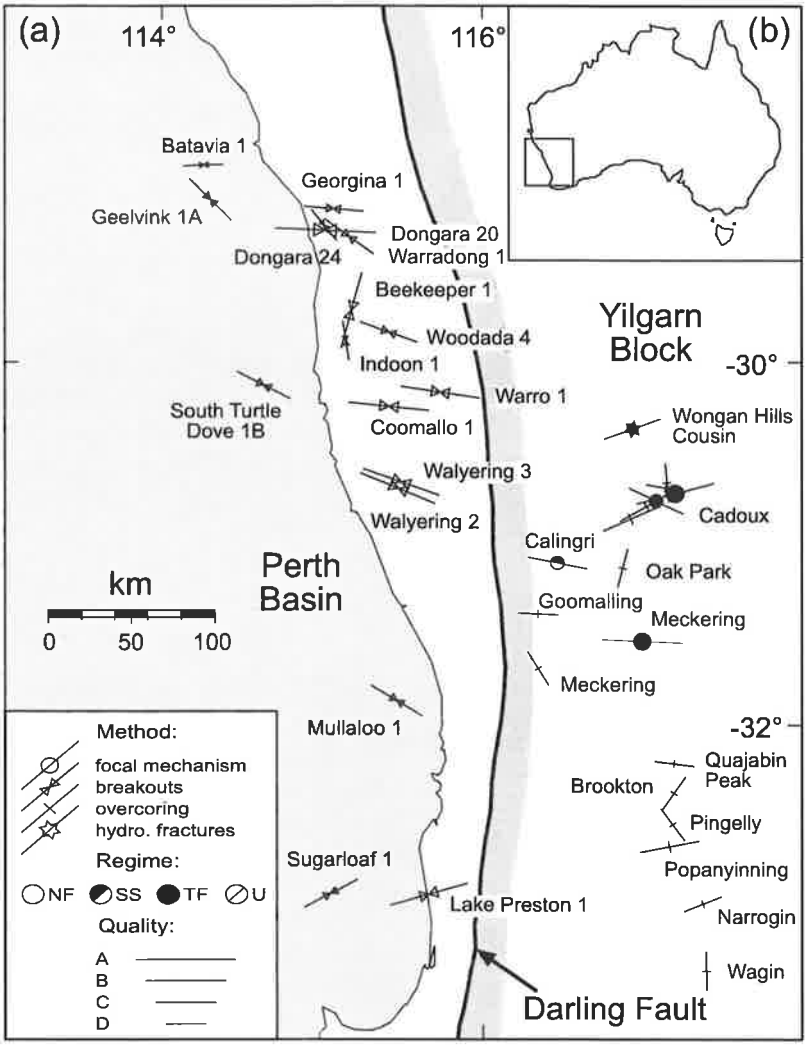

Figure 6.1 (a) Stress map of the Perth Basin and the Yilgarn Block showing A-D quality stress indicators. **(b)** Location map of the Perth Basin in relation to the Australian continent.

6.3 Methodology

This section summarises the theory and methodology of borehole breakout analysis with special reference to the Perth Basin. See Section 3.2 for a more complete discussion of borehole breakouts. Borehole breakout occurs when the concentrated stress around a wellbore exceeds the compressive strength of the rock (Zoback *et al.*, 1985). When this arises conjugate shear fractures form in the side of the wellbore causing the rock to break off (Gough and Bell, 1982). This results in a vertical wellbore being elongated in the direction perpendicular to the orientation of σ_{Hmax}. The four-arm dipmeter tool can be used to identify and orient these elongate zones. All breakout interpretation in the Perth Basin was done using

the caliper data on paper logs from Schlumberger's high-resolution dipmeter tool (HDT). It is assumed that one of the principal stresses is parallel with the axis of the borehole.

Identification of the breakouts was based on the criteria of Plumb and Hickman (1985). Only wells with deviations of less than 10° were used in the study. Wells with deviations greater than 5° were checked for key seating. Breakout orientations were corrected for magnetic declination of either 2° or 3° west depending on the location. Many wells in the Perth Basin exhibited well-developed, consistently north-south oriented breakouts (Figure 6.2). The mean σ_{Hmax} orientation from breakouts in each well was quality ranked using the WSM scheme (Section 3.2.3).

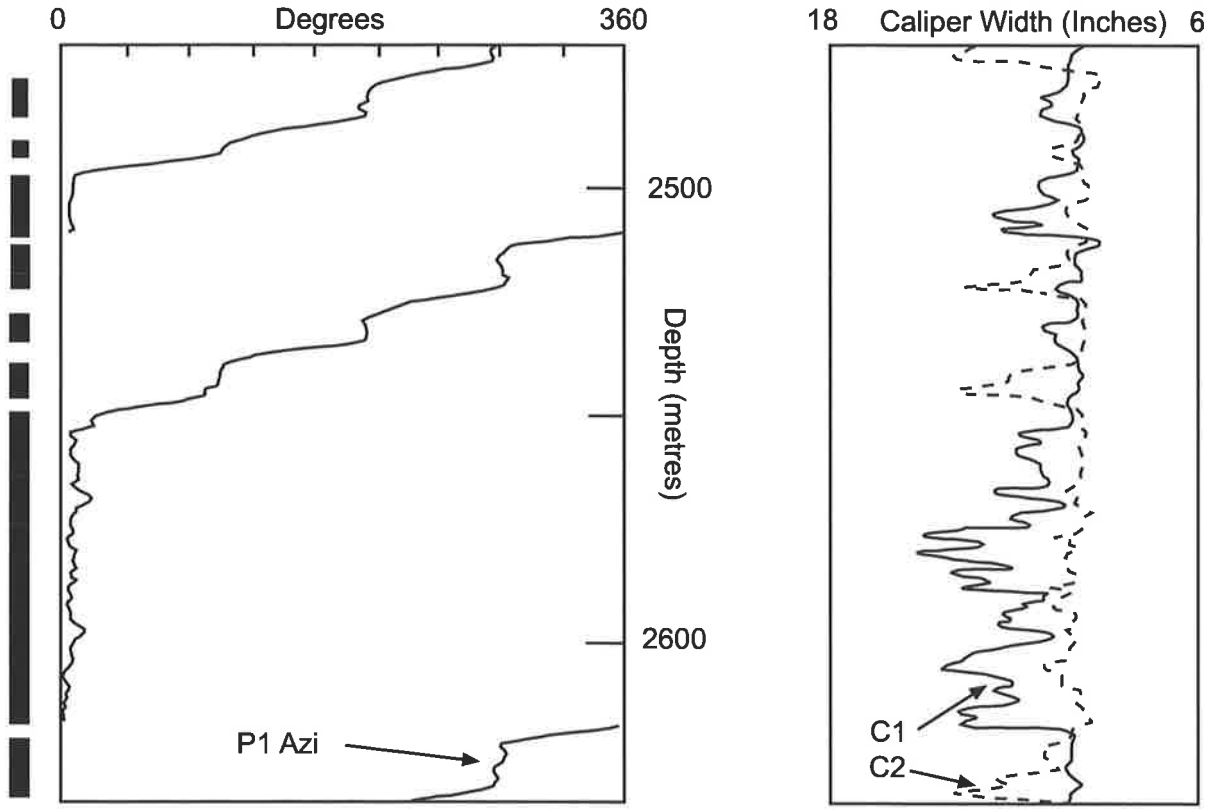

Figure 6.2 Section of 4 arm dipmeter data from Walyering 3 showing consistent breakout in a north-south direction (indicated by the black vertical bars at the extreme left), thus the σ_{Hmax} orientation is east-west. C1 and C2 are the two orthogonal borehole diameters. P1Azi is the azimuth of caliper pad 1 with respect to north. These data have been digitised and replotted from the original analogue records for increased clarity.

6.4 Results

A total of 114 breakouts with a combined length of 3.2 km were interpreted in 17 wells throughout the Perth Basin. The breakouts covered a depth range from 720 m to 4150 m. The mean σ_{Hmax} orientation inferred from the individual breakouts is 101°N (Table 6.1). This compares to a σ_{Hmax} oriantation of 108°N when the mean orientation from all 17 wells are

themselves averaged (Table 6.2). Figure 6.1 shows the stress map (A-D quality indicators) for the Perth Basin and the Yilgarn Block. Much of the scatter present in the stress orientations across the Perth region is a result of the less reliable D quality indicators. Unweighted and length-weighted statistics were calculated for each well (Table 6.1). The length-weighted statistics were calculated by weighting each individual breakout by the breakout length and then dividing by the total length of breakout in each well. The quality allocated to each well was based on the highest WSM quality determined from either the unweighted or length-weighted statistics (Table 6.1). The unweighted rose diagram for σ_{Hmax} orientations inferred from individual breakouts in the Perth Basin clearly displays the east-west trend (Figure 6.3a), while the length-weighted plot has slightly more scatter but still exhibits the east-west σ_{Hmax} trend (Figure 6.3b). A few individual wells show a north-south trend, such as Beekeeper-1 and Indoon-1 (Figure 6.1; Table 6.1). However, at the basin scale, the north-south trend is not significant (Figure 6.3). A substantial decrease in the standard deviation of mean σ_{Hmax} orientations in the region is observed if the poorer, D-quality data are omitted (Table 6.2).

Table 6.1 Summary of breakouts in the Perth Basin. Depth and lengths are all in metres. Azi: mean orientation of σ_{Hmax} in °N, S.D.: circular standard deviation in degrees, Lat.: latitude, Long.: longitude, Q: quality ranking.

Well	Location		No.	Depth		Unweighted			Length Weighted			
	Lat.	Long.		Top	Bot	Azi	S.D.	Q	∑length	Azi	S.D.	Q
Batavia 1	-28.900	114.260	1	2320	2349	088	-	D	29	088	-	D
Beekeeper 1	-29.715	115.185	4	2590	3000	016	9	B	264	015	8	B
Coomallo 1	-30.249	115.416	3	2941	3185	096	2	B	105	098	1	B
Dongara 20	-29.268	115.022	13	738	1781	093	9	A	150	093	9	A
Dongara 24	-29.237	115.017	2	1142	1198	142	7	D	29	138	5	D
Geelvink 1A	-29.096	114.298	3	2919	3095	134	5	C	37	135	5	C
Georgina 1	-29.145	115.074	4	1109	1549	100	12	C	45	095	11	C
Indoon 1	-29.884	115.151	2	1377	2136	171	13	D	29	161	8	D
Lake Preston	-32.920	115.661	17	2941	4150	074	20	B	864	080	17	B
Mullaloo 1	-31.867	115.462	7	940	1995	108	33	D	413	122	23	C
Sth. Turtle Dove 1B	-30.130	114.636	3	1151	1242	112	24	C	94	118	21	C
Sugarloaf	-32.915	115.052	5	3371	3524	062	8	C	27	061	8	C
Walyering 2	-30.702	115.473	8	3108	3710	113	3	B	152	113	2	B
Walyering 3	-30.667	115.493	28	1880	2980	110	17	B	641	106	16	B
Warradong 1	-29.301	115.171	4	3213	3587	127	14	C	54	131	6	C
Warro 1	-30.168	115.736	7	1156	1214	099	11	B	52	105	15	B
Woodada 4	-29.835	115.141	3	1740	1935	115	18	C	90	110	17	C
Perth Basin			114	738	4150	101	28		3193	101	30	

Table 6.2 Summary of breakout data for the Perth Basin and Yilgarn Block

Region	Quality	Mean (°N)	Std (°)
Perth Basin Wells	A-D	108	30
Yilgarn Block Data (FMS/OC/HF)	A-D	085	43
Perth Basin + Yilgarn Block	A-D	100	38
Perth Basin Wells	A-C	105	26
Yilgarn Block Data (FMS/OC/HF)	A-C	082	18
Perth Basin + Yilgarn Block	A-C	096	26

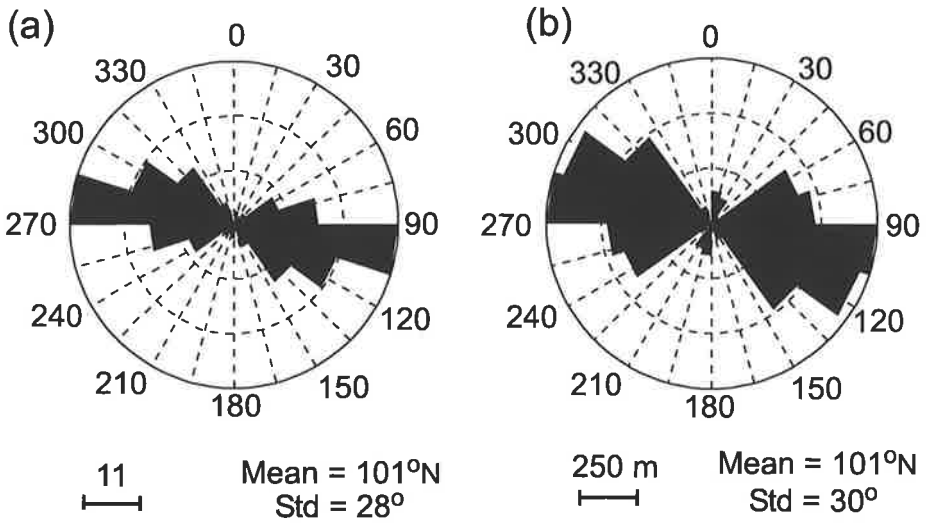

Figure 6.3 Rose diagram showing individual breakouts from the Perth Basin, **(a)** unweighted and **(b)** length-weighted.

6.5 Discussion

6.5.1 Plate Boundary Effects

Stress orientations in the Perth Basin and Yilgarn Block cover two distinct geological provinces and are inferred from a variety of different stress determination techniques. Shallow (0-100 m) overcoring and hydraulic fracturing experiments along with deeper (1-5 km) earthquake focal mechanism are available in the Yilgarn Block, whereas in the Perth Basin stress indicators have been inferred from borehole breakouts at depths of 700 m to 4 km (Figure 6.4). Thus the new breakout data provides a large number of observations over a considerable depth range. There is a broadly consistent east-west σ_{Hmax} orientation in both the Yilgarn Block and Perth Basin. This east-west σ_{Hmax} orientation, which is consistent over an area of approximately 300 km by 500 km and across different stress indicators, depths and geological provinces, is likely to be a first order stress trend *sensu* Zoback (1992).

The Perth region, which includes both the Perth Basin and the Yilgarn Block, is an important area that highlights the misfit between the direction of absolute plate velocity of the IAP and σ_{Hmax} orientations in Australia. The mean σ_{Hmax} orientation for the Perth region, when only considering the more reliable A-C data, is 096°N. This orientation is approximately orthogonal to the direction of absolute plate velocity.

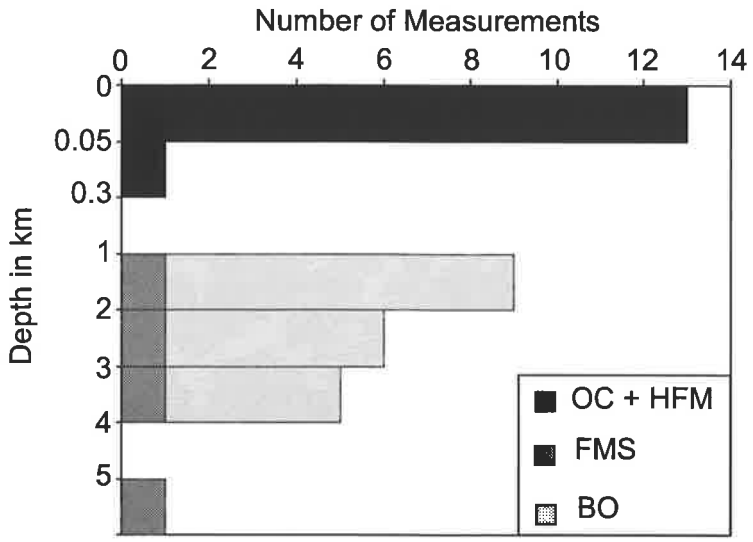

Figure 6.4 Distribution of all stress data from the Perth region divided by type and depth. Breakout depths represent an averaged value for each well. OC: overcoring, HFM: hydraulic fracture measurement, FMS: single earthquake focal mechanism, BO: breakout.

Cloetingh and Wortel (1986) and Coblentz *et al.* (1995) showed that the variable orientations of the Australian stress field can be modelled as originating from plate boundary forces if the heterogenous nature of the northeastern convergent plate boundary is recognised. In continental areas such as Western Europe and South America where σ_{Hmax} parallels the direction of absolute plate motion, plate boundary configurations, and the associated forces, are relatively simple (Gölke and Coblentz, 1996). The IAP has an extremely complex convergent northeastern boundary comprising segments of continent-continent collision, continent-island arc collision, oceanic-island arc subduction and oceanic-oceanic subduction. Stresses are focussed by the collisional segments of the boundary (i.e. Himalaya, New Guinea and New Zealand), being normal to those segments and rotating between them. The broad rotation between σ_{Hmax} normal to both the Himalayan and New Guinea boundaries results in the east-west σ_{Hmax} orientation seen in the western part of Australia in general and the Perth Basin/Yilgarn Block in particular (Coblentz *et al.*, 1998; Chapter 8).

6.5.2 Local Structural Effects

Numerous regional stress studies have identified local variations in stress orientations that differ substantially from the regional trend. A number of authors have attributed this variation from the regional as being due to local structures (e.g. Aleksandroski *et al.*, 1992; Ask, 1997).

Local deflections from the regional stress trend are often hard to assign to specific structures due to the lack of detail in the stress and/or structural data. Nonetheless, perturbations of the stress field due to local structures should not be unexpected as most petroleum exploration wells are drilled on anomalous structures (Aleksandroski *et al.*, 1992).

Bell *et al.* (1992) described how non-sealing faults and open fractures may act as free surfaces within the rock body. These free surfaces deflect stress trajectories such that the minimum principal stress is rotated perpendicular to the free surface. Sealed fractures without strong rheological contrast with the surrounding rock do not deflect stress trajectories.

The regional east-west σ_{Hmax} orientation has clearly been established throughout the Perth region. However, a number of wells exhibit a more north-south σ_{Hmax} orientation (Figure 6.5). The dominant structural grain throughout the Perth Basin is north-south to northwest-southeast (Dentith *et al.*, 1994). Thus, it is suggested that the observed north-south σ_{Hmax} orientations result from the reorientation of the regional east-west σ_{Hmax} orientation by north-south oriented structures via a mechanism analogous to that described by Bell *et al.* (1992). The two wells in which stresses are most clearly locally reoriented are Indoon 1 and Beekeeper 1. These wells are located in close proximity to the Beagle Ridge, a north-south trending horst (Figure 6.5). The breakouts in Beekeeper 1 are extensive throughout the well and consistently oriented approximately east-west (well is ranked B quality in WSM scheme). This consistent stress orientation, at right angles to the regional trend, suggests that the structure perturbing the stress field is likely to be a regional feature adjacent to the well rather than a local feature cutting the well. A number of wells, namely Dongara 20 and Georgina 1, display the regional east-west stress trend but are at a similar proximity to the Beagle Ridge as Indoon 1 and Beekeeper 1. This highlights the problematic nature in determining sources of local stress deflection due to the lack of detail in the regional stress/structural datasets.

The stress orientation for two wells in the Dongara oil field, together with a detailed structural map of the field at approximately 2000 m depth, are shown in Figure 6.5b. One well shows the regional east-west trend while the other has a northwest-southeast trend, parallel to an adjacent fault. This has also been interpreted as a local stress re-orientation associated with the nearby fault.

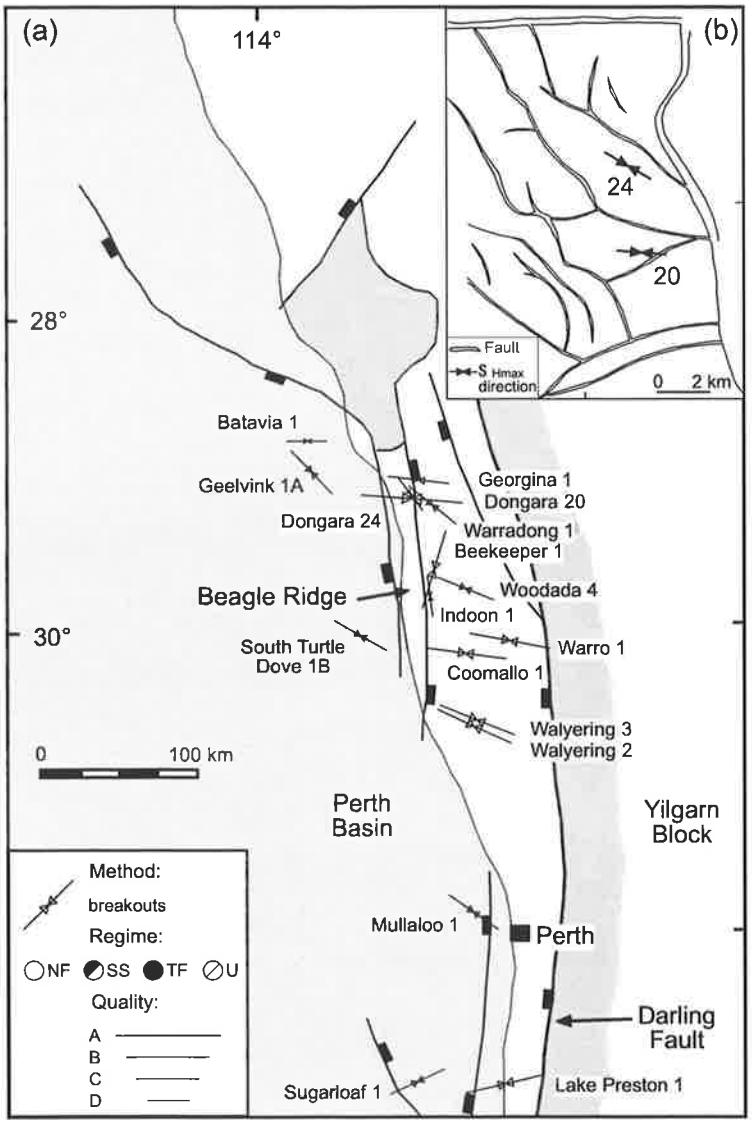

Figure 6.5 (a) Regional structural map of the Perth Basin adapted from Ellis and Bruce (1998) overlain by the new stress data for the Perth Basin. **(b)** Local structural map of the Dongara oil field (Ellis and Bruce, 1998) showing the maximum horizontal stress orientation for wells 20 and 24.

6.6 Conclusions

Breakouts from 17 wells in the Perth Basin yield an average σ_{Hmax} orientation of 108°N. The east-west σ_{Hmax} orientation inferred here for the Perth Basin is consistent with that from the adjacent Yilgarn Block based on hydraulic fracturing, overcoring and earthquake focal mechanism data. Thus, the east-west σ_{Hmax} orientation is consistent between different stress indicators, different depths and different geological provinces and is interpreted as a first-order stress trend. The broadly east-west σ_{Hmax} orientation in the Perth region is orthogonal to the direction of absolute plate velocity. Nonetheless, this orientation can be modelled as resulting from plate boundary forces if the heterogenous nature of the northeastern convergent boundary of the IAP is recognised (Coblentz *et al.*, 1995). Some local stress rotations are observed in the Perth Basin breakout data. These are interpreted as being due to stress re-orientation around north-south trending structures.

Chapter 7

The Regional *In Situ* Stress Field of Continental Australia

7.1 Introduction

The *in situ* stress field of the Australian continent was poorly constrained at the time of compilation of the WSM (Zoback, 1992). Nonetheless, the available data indicated that the Australian continent had a highly variable and complex stress field (Richardson, 1992). In more recent times, and in particular due to the data presented in the previous three chapters, there has been a significant increase in the stress data available for the Australian continent. This has allowed the complex Australian stress field to be better defined. This chapter describes the regional σ_{Hmax} orientations and stress regimes within continental Australia, as defined by the use of stress provinces and by mapping stress trajectories. Defining the regional stress field highlights the broad scale, long wavelength features which can be attributed to first-order sources such as plate boundary forces, lateral density contrasts and buoyancy forces (Zoback, 1992). Thus, the regional stress field can provide information on the direction and magnitude of these forces. Also, identification of the regional trend across Australia enables any local variations to be recognized. The regional σ_{Hmax} orientations defined in this chapter are subsequently used in Chapter 8 to constrain the finite element modelling of the origin of the Australian stress field. A significant amount of the results in this chapter have been published in Hillis and Reynolds (2000); (Appendix H).

7.2 Australian Stress Map Database

The ASM database is a sub-set of the WSM database containing *in situ* stress measurements for continental Australia. New Guinea, the continental crust of which is contiguous with that of Australia, is also included in the ASM database. New stress measurements are continually added to the ASM database, however, for the purpose of this study the ASM database contained a total of 538 stress measurements (A-E quality ranked). A sub-section of the database has been listed in Appendix E with the full database included on the accompanying CDROM. Since the compilation of the WSM the number of reliable (A-C quality ranked) data in continental Australia has increased from 95 in Zoback (1992) to 322 in this study.

The ASM database contains the following stress measurement types; focal mechanisms, borehole breakouts, drilling induced tensile fractures, hydraulic fracturing, overcoring and geological indicators. A description of the first five indicator types can be found in Chapter 3. In the case of geological indicators, a description can be found in Zoback (1992). Each stress measurement in the database has been quality ranked from A (highest) to E (lowest) according to the WSM ranking scheme (Zoback, 1992). Details of the ranking scheme can be found for each indicator type in Chapter 3.

Table 7.1 is a summary of the type and quality of the stress measurements in the ASM database. A breakdown of the A-C quality data by indicator type is shown in Figure 7.1a. Approximately half of the reliable data have been sourced from borehole breakouts and drilling induced tensile fractures in petroleum wells. Focal mechanism solutions represent fewer than 30% of the reliable data. In contrast, focal mechanisms make up 66% of the reliable data in the WSM database (Müller *et al.*, 2000). This reflects the relatively aseismic nature of continental Australia and the rather sparse seismic network across Australia. A breakdown of the A-C quality data by depth and indicator type shows the distinct depth range each indicator type is recorded over (Figure 7.1b).

Table 7.1 Summary of ASM database by quality and type.

Type	Quality					Total
	A	B	C	D	E	
Focal Mechanisms (FM)	1	29	66	22	10	128
Breakouts (BO)	40	59	40	78	32	249
DITF	11	10	3	3	0	27
Hydraulic Fracturing (HF)	5	27	25	18	1	76
Overcoring (OC)	0	2	4	49	1	56
Geological Indicators (G)	0	0	0	0	2	2
Total	57	127	138	171	46	538

DITF: drilling induced tensile fracture.

The ASM database also includes information relating to the relative magnitude of the three principal stresses. As outlined in Chapter 3, only hydraulic fracturing measurements, overcoring measurements and focal mechanisms can provide magnitude information. Thus, the stress regime can only be determined for approximately half of the reliable stress indicators (Figure 7.1c). Of the stress regime information available, approximately 30% indicate a reverse regime, 13% strike-slip, 3% normal and 3% a mixed regime (Figure 7.1c). Thus, Australia is dominated by a reverse faulting stress regime ($\sigma_{Hmax}>\sigma_{hmin}>\sigma_v$) with areas

of strike-slip faulting stress regime ($\sigma_{Hmax}>\sigma_v>\sigma_{hmin}$). This designation refers only to the relative stress magnitudes and does not imply the *in situ* stress data are consistent with failure per se.

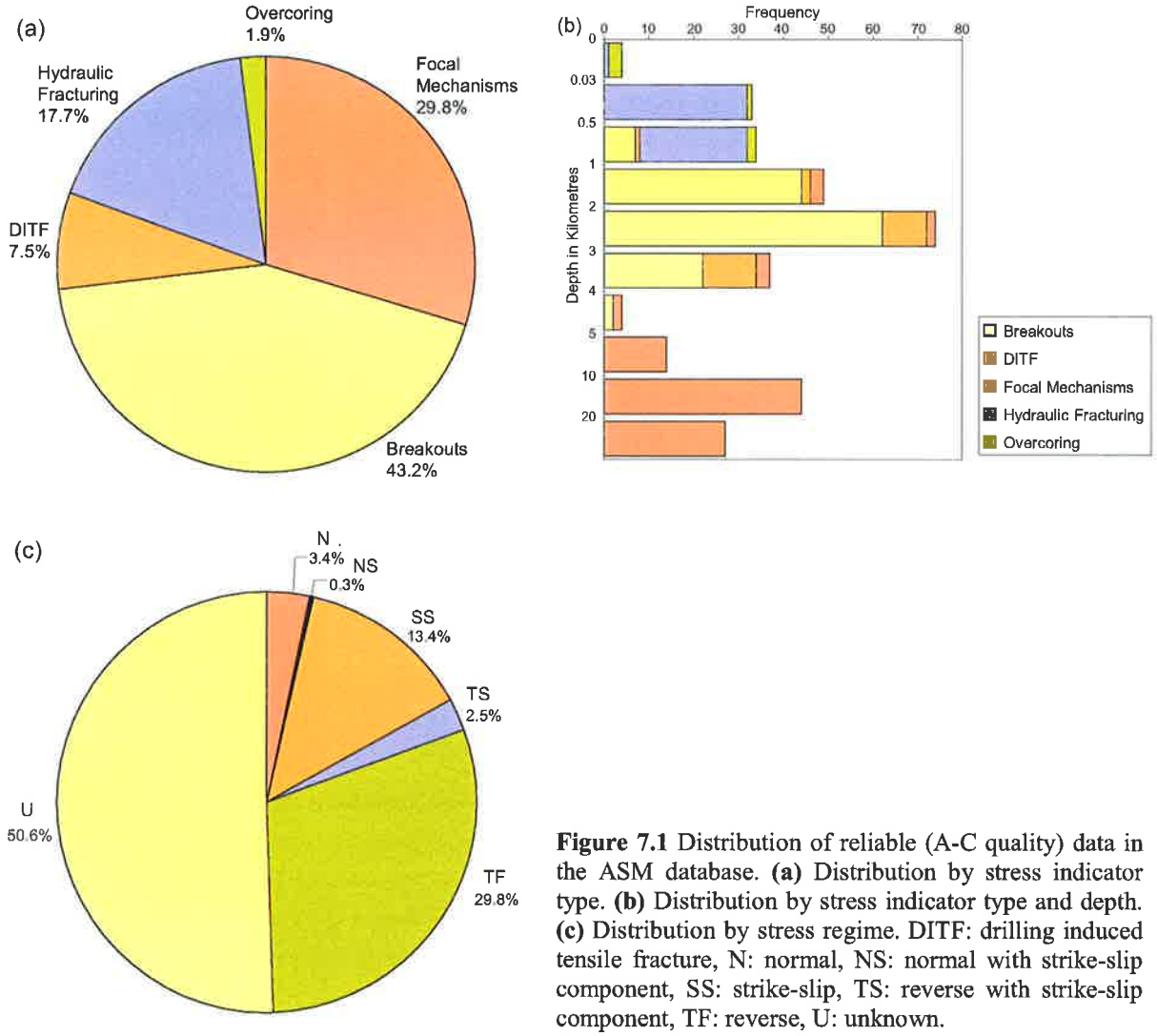

Figure 7.1 Distribution of reliable (A-C quality) data in the ASM database. **(a)** Distribution by stress indicator type. **(b)** Distribution by stress indicator type and depth. **(c)** Distribution by stress regime. DITF: drilling induced tensile fracture, N: normal, NS: normal with strike-slip component, SS: strike-slip, TS: reverse with strike-slip component, TF: reverse, U: unknown.

Figure 7.2 shows the 322 reliable (A-C) stress measurements in the ASM database. A large degree of variation of the σ_{Hmax} orientation occurs across Australia. The origin and significance of this trend are discussed further in this chapter and Chapter 8. Figure 7.3 shows the ASM including A-D quality data. Due to the large number of D quality indicators, and possibly their lower reliability, there is significantly more scatter in the observed σ_{Hmax} orientations.

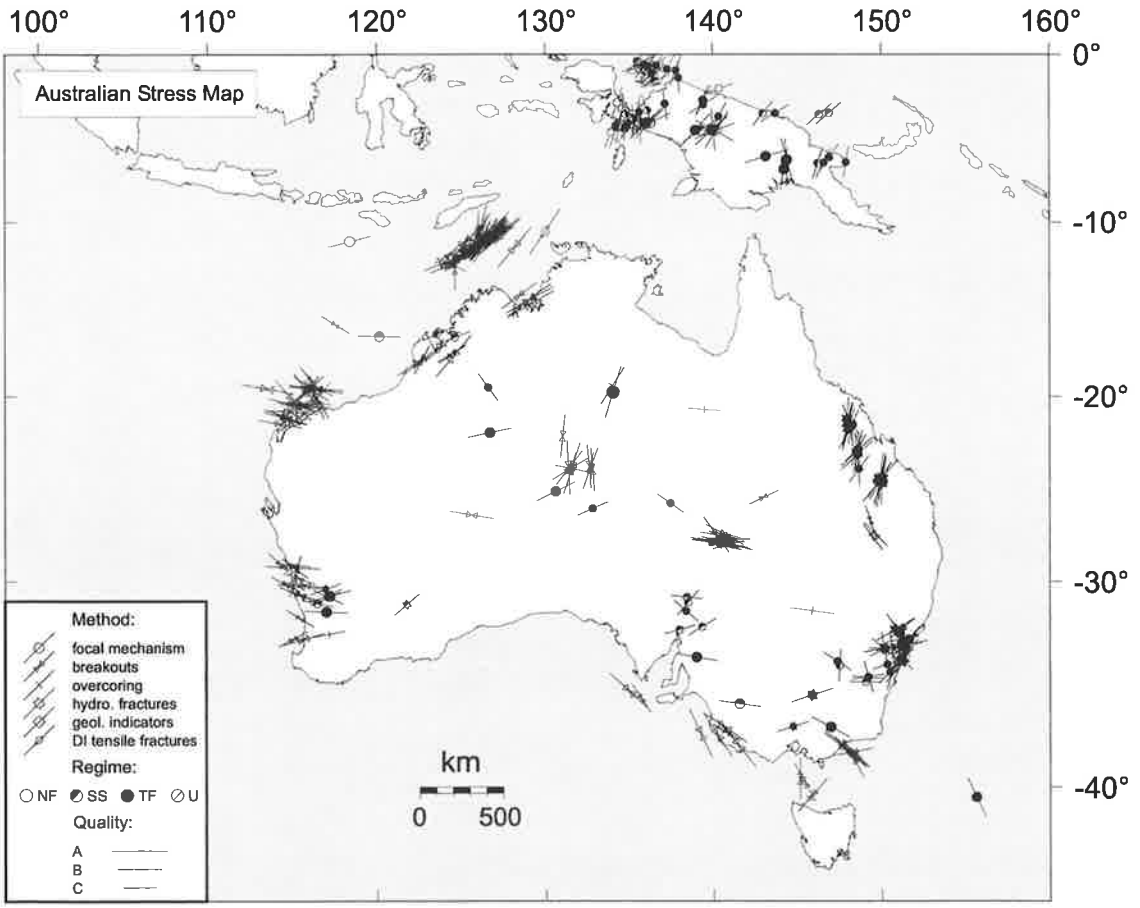

Figure 7.2 Australian Stress Map: A-C quality data.

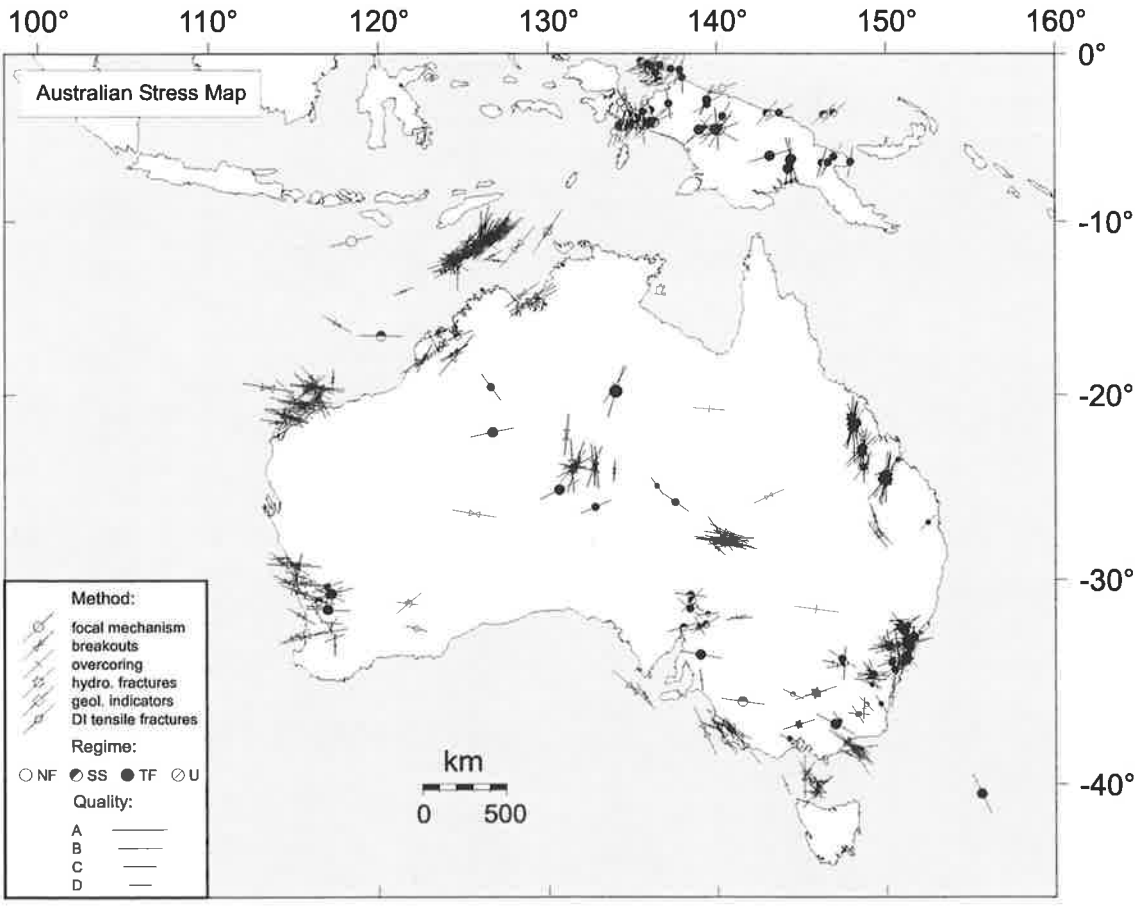

Figure 7.3 Australian Stress Map: A-D quality data.

7.3 Australian Stress Provinces

7.3.1 Definition

Stress orientations across the Australian continent are highly variable (Figures 7.2 and 7.3). Previous attempts to define the regional stress field within Australia have relied on the use of a grid-based approach (e.g. average stress orientations in $5^{\circ}\times5^{\circ}$ blocks Coblentz and Richardson (1995) and $3^{\circ}\times3^{\circ}$ blocks Coblentz *et al.* (1995)). This approach can prove inadequate due to the irregular spacing and clustering of the stress indicators. Depending on the grid used, there is a potential for the averaged σ_{Hmax} orientation to be located some distance from the data source or to even be an incorrect representation of the regional stress field for the area. Stress provinces were defined to avoid the potential problems associated with a grid-based approach.

The stress indicators within the Australian continent are largely clustered in distinct geographic regions. These regions vary from one hundred to a few hundred square kilometres in area. Within these regions, σ_{Hmax} orientations are generally broadly consistent. The Australian stress provinces were based on the clustering of the data, with the Australian continent divided into 16 distinct regions (Figure 7.4). Each stress province is required to have a minimum of 4 A-C quality indicators within a distinct geographic region. Approximately 90% of the A-C quality stress data are located within the 16 Australian stress provinces defined. Of the data lying outside the stress provinces, only the A and B quality indicators are represented on the final regional stress map (Figure 7.7).

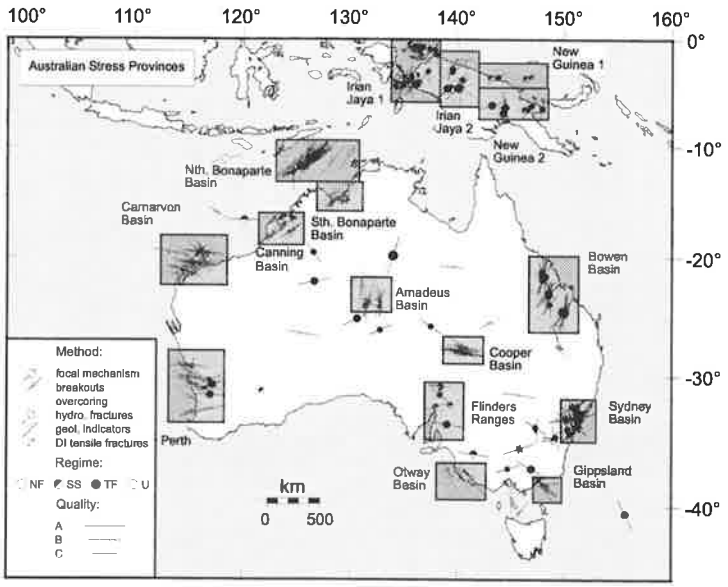

Figure 7.4 A-C quality stress indicators for the Australian continent and the 16 stress provinces defined. Approximately 90% of the A-C quality stress data are located within the 16 stress provinces.

The stress data within each province were examined for consistency by averaging the different quality data (Figure 7.5). Both number and quality weighted averages were determined. The mean σ_{Hmax} orientation does not vary significantly within a province when based upon different quality stress measurements (Figure 7.5). Hence, the mean σ_{Hmax} orientation is reasonably consistent over the different quality indicators within the 16 stress provinces. Nonetheless, this does not indicate whether the mean σ_{Hmax} orientation is statistically significant. When examining the *in situ* stress data for regional trends the choice of data quality is somewhat arbitrary. However, the A-C quality data are a good compromise between having a statistically significant number of measurements and also reducing the scatter associated with the D quality measurements. A detailed map and breakdown of the statistics for each stress province is included in Appendix F.

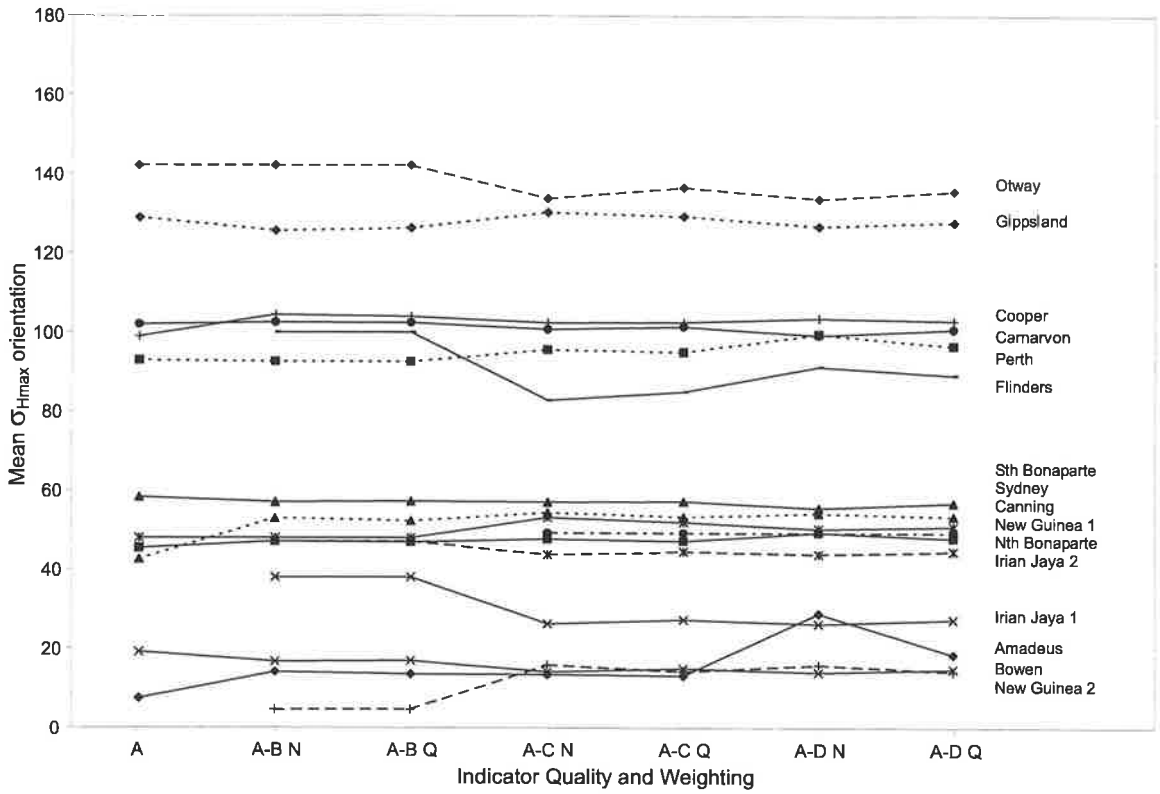

Figure 7.5 Graph of the mean σ_{Hmax} orientations for each stress province using a range of indicator qualities and weighting systems. N indicates number weighted mean while Q indicates quality weighted mean.

7.3.2 Statistical Significance

The Rayleigh test was applied to investigate whether the mean σ_{Hmax} orientation within each stress province was statistically significant (Mardia, 1972; Coblentz and Richardson, 1995). A detailed description of the Rayleigh test can be found in Appendix C. The results from the Rayleigh test are listed in Table 7.2 and are shown in Figure 7.6. The stress provinces were

divided into six types based on the results of the Rayleigh test. A type 1 stress province indicates that the null hypothesis that σ_{Hmax} orientations in the province are random can be rejected at a 99.9% confidence level, type 2 at the 99% confidence level, type 3 at the 97.5% confidence level, type 4 at the 95% confidence level and type 5 at the 90% confidence level. A type 6 stress province indicates that the null hypothesis that the σ_{Hmax} orientations in the province are random can not be rejected at a 90% confidence level. This six-fold province division, contrasts with the province definition of Hillis and Reynolds (2000) largely because additional data have meant that the overall quality of a number of provinces has increased. As a result additional categories are required to adequately subdivide the data. The mean σ_{Hmax} orientation and quality ranking given to each stress province is shown in Figure 7.7.

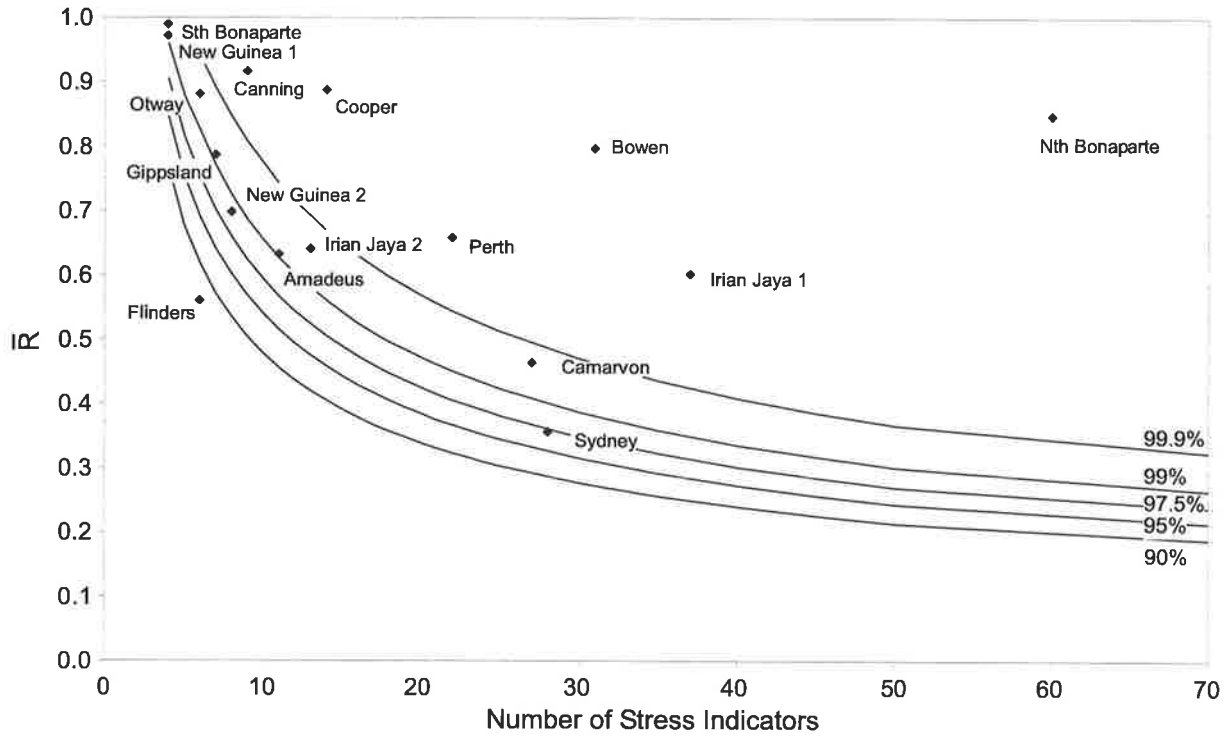

Figure 7.6 Rayleigh test graph for the 16 stress provinces. Points on the right hand side of a line indicate they have passed the Rayleigh test at the particular percentage corresponding to that line. The $\bar{R}$ value is the length of the mean resultant vector of σ_{Hmax} orientations within a province.

The quality rating (1 to 6) given to the stress provinces should not be confused with the WSM ranking scheme (A to E) given to each stress indicator. The stress province rating reflects how scattered the individual σ_{Hmax} orientations are within a province, not the quality of the stress indicators. The σ_{Hmax} orientations in a type 6 stress province may be no less reliable than a type 1 stress province, however they display a more scattered σ_{Hmax} orientation. The stress

province ranking scheme is believed to reflect the degree to which local sources of stress influence the regional horizontal stress field within a province. Thus, type 1 stress provinces are likely to have pronounced horizontal stress anisotropy.

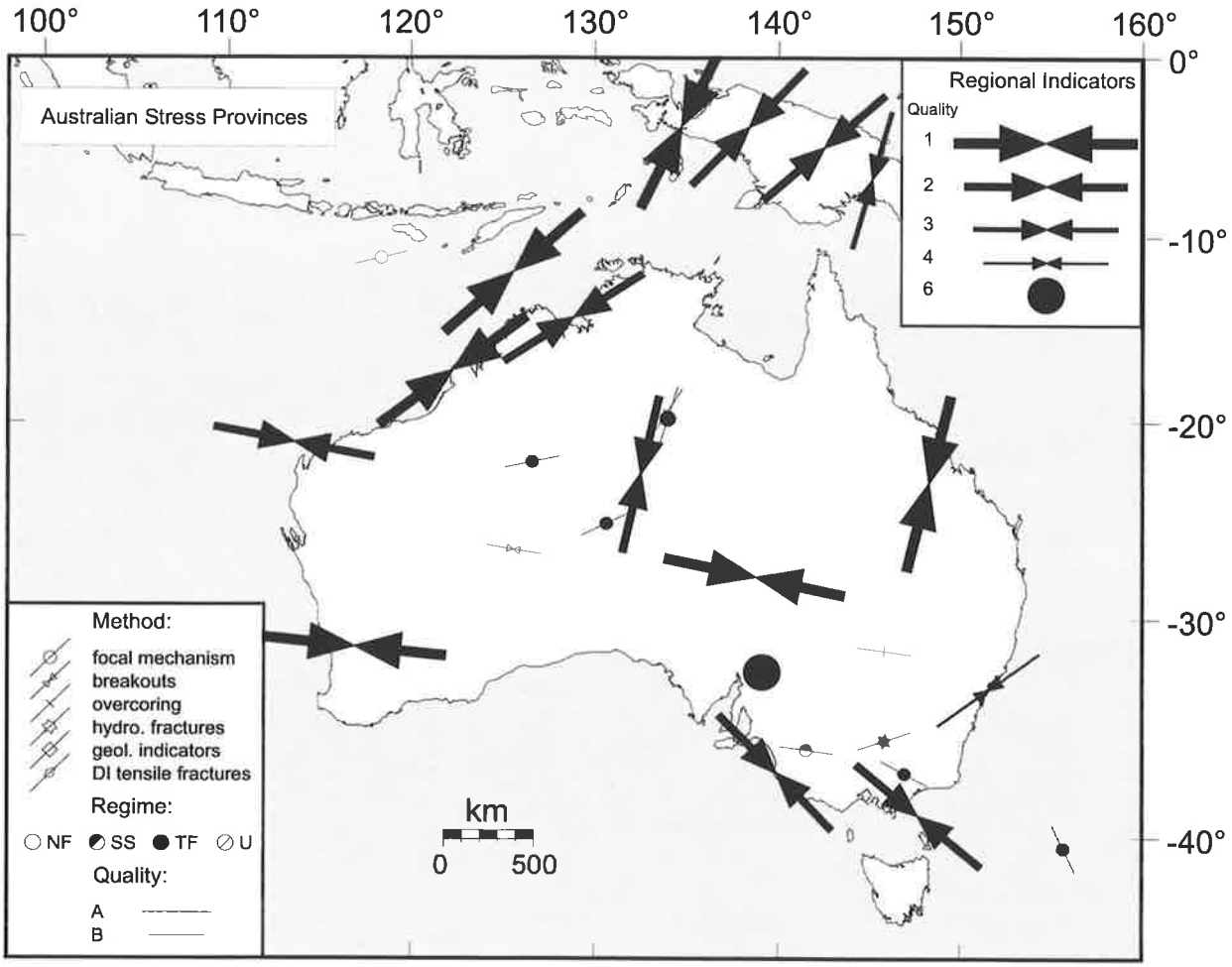

Figure 7.7 Australian stress province map. Arrows indicate mean σ_{Hmax} orientation within a stress province. The size of the arrow indicates how consistent the averaged σ_{Hmax} orientations are within each stress province.

Information on the stress regimes in the Australian continent is limited, with less than 50% of the A-C quality indicators providing magnitude data (Figure 7.1c). The stress regime for each stress province was calculated using the Coblentz and Richardson (1995) parameter, α (Table 7.2). Each stress indicator, which contained stress regime information, was allocated an α of 1 for a normal faulting stress regime, 0.5 for strike-slip faulting stress regime and 0 for a reverse faulting stress regime. Mixed mode faulting was allocated an α value of 0.75 for normal with strike-slip component and 0.25 for reverse with strike-slip component. The average value for each stress province was calculated and is listed in Table 7.2. Seven of the stress provinces did not provide stress regime information.

Table 7.2 Summary of stress indicator statistics for the 16 stress provinces in the Australian continent.

Province	No	Type					Quality			Statistics				Regime
	A-C	FM	BO	HF	OC	DITF	A	B	C	Mean	SD	$\overline{R}$	Conf.	α
Amadeus Basin	11	0	11	0	0	0	2	6	3	013	27	0.632	99	-
N. Bonaparte Basin	60	0	40	0	0	20	24	28	8	048	16	0.85	99.9	-
S. Bonaparte Basin	4	0	4	0	0	0	3	1	0	057	4	0.990	99	-
Bowen Basin	31	0	0	31	0	0	3	17	11	014	19	0.798	99.9	0.05
Canning Basin	9	2	7	0	0	0	2	1	6	053	12	0.917	99.9	0.5
Carnarvon Basin	27	0	27	0	0	0	7	13	7	101	35	0.465	99	-
Cooper Basin	14	0	10	0	0	4	4	8	2	102	14	0.888	99.9	-
Flinders Ranges	6	6	0	0	0	0	0	1	5	083	31	0.561	< 90	0.33
Gippsland Basin	7	0	7	0	0	0	2	2	3	130	20	0.787	99	-
Irian Jaya 1	37	37	0	0	0	0	0	6	31	026	29	0.602	99.9	0.48
Irian Jaya 2	13	13	0	0	0	0	0	8	5	044	27	0.641	99	0.31
New Guinea 1	4	4	0	0	0	0	0	0	4	049	7	0.973	99	0.38
New Guinea 2	8	8	0	0	0	0	0	4	4	016	24	0.698	97.5	0.06
Otway Basin	6	0	6	0	0	0	3	0	3	134	14	0.882	99	-
Perth	22	4	14	1	3	0	1	8	13	096	26	0.658	99.9	0.16
Sydney Basin	28	5	1	22	0	0	3	10	15	054	41	0.356	95	0.04

No: number. SD: circular standard deviation. $\overline{R}$: length of the mean resultant vector of σ_{Hmax} orientations within a province (Mardia, 1972). If $\overline{R}$ exceeds a certain critical value dependent on the number of data, then the null hypothesis that stress orientations in the province are random can be rejected at the stated confidence level (Conf). <90% indicates that the null hypothesis cannot be rejected at the 90% confidence level. Regime is the average stress regime determined using Coblentz and Richardson (1995) parameter, α. For a normal faulting stress regime α=1, for a strike-slip faulting stress regime α=0.5, and for a reverse faulting stress regime α=0. See text for further discussion of the determination of average stress regime. See Table 7.1 for abbreviations of the stress data types.

7.4 Stress Trajectories

7.4.1 Introduction

The significant increase in available stress data over the past 20 years has led to the development of statistical methods for estimating stress fields and stress trajectories based on the observed directional data (Hansen and Mount, 1990; Rebai *et al.*, 1992; Lee and Angelier, 1994). The stress trajectory mapping technique used in this thesis was developed by Hansen and Mount (1990). The reader is referred to this reference for a full description of the technique. A stress trajectory is a curve whose tangent is in the direction of one of the principal stresses at that point (Jaeger and Cook, 1979). Stress trajectory mapping provides a technique for smoothing and interpolating unevenly distributed stress data, thereby clarifying the regional trend.

Stress trajectories map out the σ_{Hmax} orientation at a given point. However, they do not provide any information on the magnitude of the stress field. Thus, the spacing between the stress trajectories provides no information on the magnitude of the stress field and should not be compared to conventional contouring techniques.

The stress trajectory method applies a statistical smoothing algorithm to create an estimated stress field at each observed data location. In the technique, fidelity to the raw data must be balanced against the degree of smoothing. If there is too much fidelity to the raw data, the calculated stress trajectories simply reflect the input stress data, and if there is too much smoothing, variations are obscured. A complete listing of the stress trajectory code used herein can be found in Appendix G.

The two parameters that control the degree of smoothness and fidelity are F and λ. The parameter λ is a scalar value used to control the degree of smoothing calculated in the objective function. A small λ value ($\lambda = 0.1$) places the emphasis on fidelity, while a large λ value ($\lambda = 10$) places the emphasis on smoothness. The F parameter defines the number of data points used in any one evaluation of the smoothing function, thus:

$$R = F \times n, \qquad \text{(Eq. 7.1)}$$

where n is the total number of data points. R is rounded off to the nearest integer and is the number of closest data points used in any one evaluation. Thus, F must be greater than zero and less than or equal to one. A small value for F ($F = 0.1$) means only the nearby stress data are considered, while a large value ($F = 0.6$) increases the number of stress data used to create the trajectory. A full description of the smoothing algorithm can be found in Hansen and Mount (1990).

7.4.2 Weighting System

Three weighting systems were applied to the raw data to determine the stress trajectories. Firstly, data were weighted according to their proximity to the observed stress indicator being smoothed. Secondly, relative weightings of 4 were given to A-quality data, 3 to B-quality data, 2 to C-quality data and 1 to D-quality data. Thirdly, a robustness weight was applied to eliminate the presence of anomalous observed data that may differ substantially from other observed data in the region. Thus, any locally reoriented stress orientation will be down weighted or possibly eliminated from the analysis. The smoothed stress field is calculated at each of the observed data points, which is then used to calculate the stress trajectories.

The stress trajectory technique differs to the stress province definition as it uses all the available *in situ* stress data (A-D) instead of just the more reliable A-C quality data. All data

were used in order to obtain the maximum data coverage across continental Australia from which the stress trajectories were calculated. This disparity in data quality used in the techniques is not considered a significant difference, as the data quality was appropriately weighted during the stress trajectory calculations.

7.4.3 Results

A detailed description of the results of the technique and a comparison to the stress provinces is presented in Section 7.5. However, a number of generalized results are discussed here. A number of stress trajectory maps were produced using different combinations of the F and λ parameters. The combination that best emphasized the regional trend resulted when $F = 0.5$ and $\lambda = 10$ (Figure 7.8). This was assessed only in terms of a qualitative analysis of the different stress trajectory maps. The emphasis was placed on producing a map with smooth trajectories, as the intension was to highlight the regional long wavelength trends.

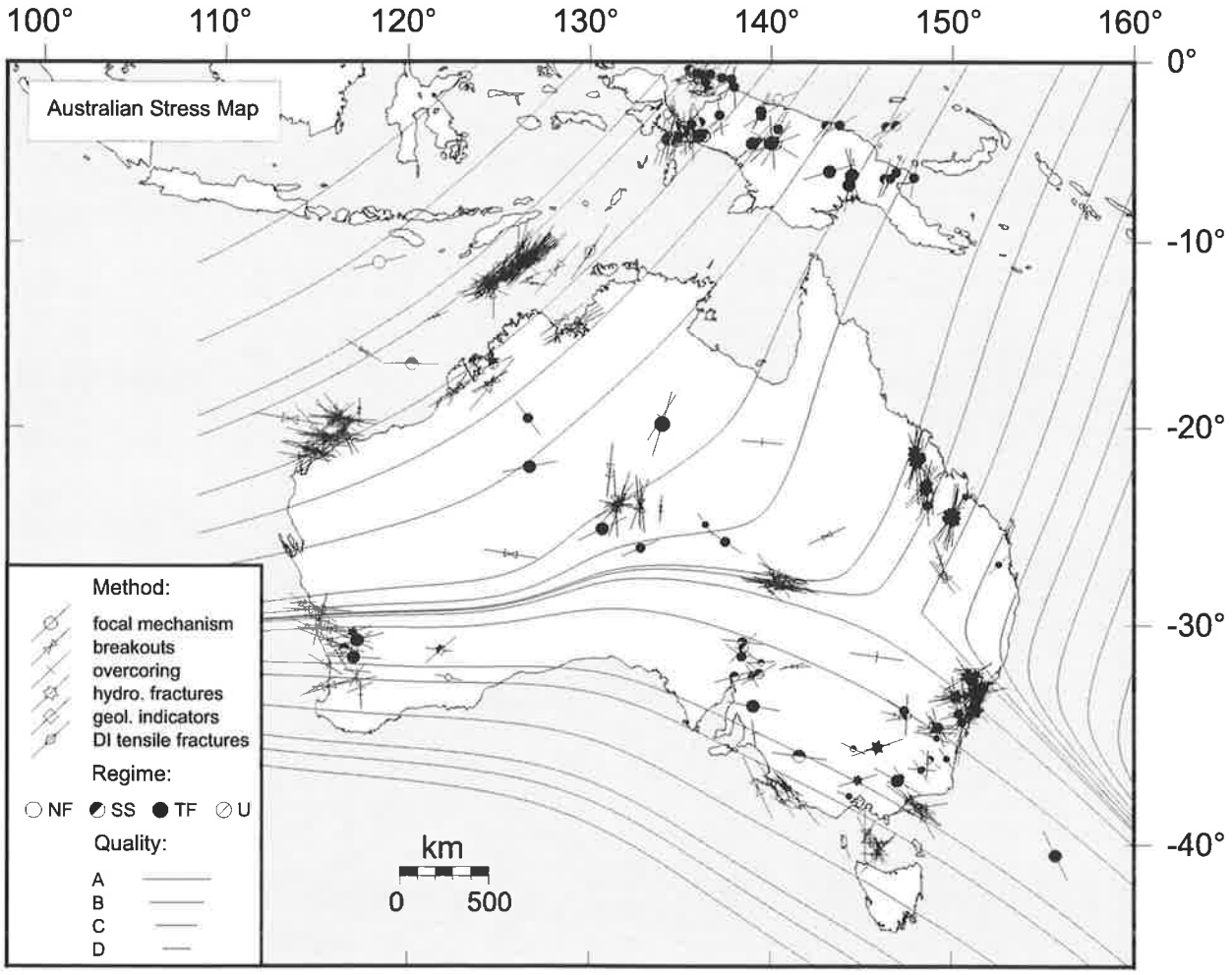

Figure 7.8 Stress trajectories using the A-D quality data from the ASM database. The parameters used to produce this map were $F = 0.5$, $\lambda = 10$ and M = 100 (number of iterations in calculation). See text for definition of F and λ. The code used to produce these trajectories is listed in Appendix G.

The stress trajectories over Australia are generally fairly smooth, as intended, except for one area of eastern Australia, between the Sydney and Bowen Basins. In this area the trajectories display a sharp change in direction. Increasing the amount of smoothing could not remove the sharp change in direction without degrading the rest of the map. This is an unusual feature, which is discussed further in Section 7.5. Caution must be used when interpreting the results close to the edge of the map. In some areas the stress trajectories have been calculated using observed stress data that are some distance away. The observed stress data used in the interpretation should be displayed with the stress trajectories to avoid any misinterpretation. Overall the stress trajectories appear to give a similar result to that defined by stress province analysis.

7.5 Regional Stress Orientations in the Australian Continent

The regional stress field of the Australian continent has been constrained by the use of stress provinces and stress trajectories. Both techniques reveal a consistent stress pattern across the Australian continent (Figures 7.7 and 7.8). Indeed stress provinces can be grouped together into even larger areas of consistent σ_{Hmax} orientation such as the Canning Basin/Bonaparte Basin/New Guinea/Irian Jaya, Carnarvon/Cooper/Perth Basins, Otway/Gippsland Basins and Amadeus/Bowen Basins (Figure 7.9).

The western side of the Australian continent is dominated by an east-west σ_{Hmax} orientation, seen in both the Carnarvon Basin and Perth stress provinces. Both the stress province and stress trajectory maps indicate approximately the same σ_{Hmax} orientation in these areas (Figure 7.10). There is a small discrepancy between the two techniques in the Carnarvon Basin, with the stress trajectories predicting a more northeasterly σ_{Hmax} orientation. This small discrepancy results from the influence of northeast-southwest orientated stress data to the north of the Carnarvon Basin (i.e. Canning and Bonaparte Basins) in the calculation of the stress trajectories.

Moving east in the northern half of Australia the σ_{Hmax} orientation rotates from east-west to northeast-southwest in the Canning Basin, South and North Bonaparte Basins, New Guinea and Irian Jaya stress provinces. Orientations from both stress trajectories and stress provinces coincide well in these regions (Figure 7.10). Moving west to east in central Australia, the east-west trend in the western portion of the continent rotates to a north-northeast to south-southwest orientation in the Amadeus and Bowen Basins. Stress trajectories in the Amadeus

Basin suggest a more northeast-southwest trend than that of the stress province (Figure 7.10). This is due to the strongly developed east-west σ_{Hmax} orientation in the Cooper Basin, which influences the relatively small amount of data in the Amadeus Basin and thus influencing the stress trajectories. Maximum horizontal stress orientations from both the province data and stress trajectories coincide well in the Bowen Basin.

In the southern half of Australia the east-west σ_{Hmax} orientation present in the Perth region continues through to the Cooper Basin province. The Flinders Ranges stress province to the south has a very scattered east-west σ_{Hmax} orientation that can be seen in the stress trajectories but not the stress province data. In southeastern Australia the σ_{Hmax} orientation has rotated to a southeast-northwest orientation in the Otway and Gippsland Basins. The stress trajectories and stress province data are again consistent in this region (Figure 7.10).

The Sydney Basin stress province on the eastern coastline of Australia has a weakly defined northeast-southwest σ_{Hmax} orientation. However, this trend appears rather ambiguous when compared to the surrounding stress data. The stress trajectories for this region indicate a southeast-northwest σ_{Hmax} orientation, approximately perpendicular to the stress province data (Figure 7.10). The σ_{Hmax} orientation determined from the stress trajectories appears more consistent with the surrounding stress data than the trend determined from the stress province data. In discussion of the stress field of the Sydney Basin (Chapter 5) it was suggested that the northeast-southwest σ_{Hmax} orientation might be influenced by margin-normal extension produced on the continent side of continental margins (Bott and Dean, 1972; Stein *et al.*, 1989).

The stress trajectory map has highlighted an apparent nodal point situated over eastern Australia (Figures 7.8 and 7.10). This feature is the result of the east-west σ_{Hmax} orientation in western Australia diverging over eastern Australia. To the north the σ_{Hmax} orientation rotates in an anticlockwise direction while in the south the σ_{Hmax} orientation rotates in a clockwise direction. The apparent nodal point may indicate an area of low horizontal stress anisotropy. The stress provinces also indicate an area of low horizontal stress anisotropy in central eastern Australia, with both the Flinders Ranges and Sydney Basin provinces having poorly defined stress trends.

The regional stress field throughout continental Australia, as shown by the stress provinces and stress trajectories, is variable and does not parallel the north-northeast direction of

absolute plate velocity. In contrast, North and South America and Western Europe are all characterised by broad regions where the σ_{Hmax} orientation is consistent and parallel to the direction of plate velocity (Zoback *et al.*, 1989; Richardson, 1992; Zoback, 1992). Nevertheless, the new stress data for the Australian continent reveals consistent trends, which are modelled using an array of plate boundary and tectonic forces in Chapter 8 of this thesis.

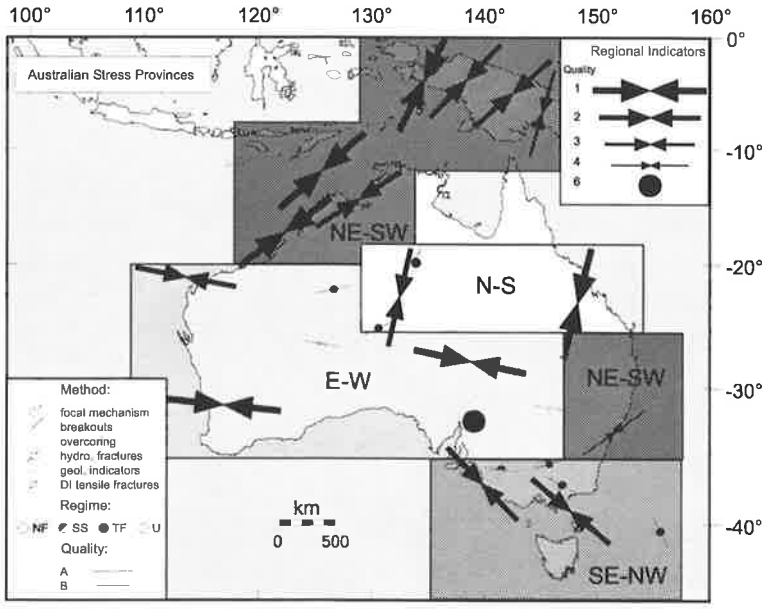

Figure 7.9 Australian stress provinces with the four main stress trends across the Australian continent. The sharp change from east-west in southern Australia to north-south in northern Australia can clearly be recognized. The northeast-southwest trend on the eastern side of Australia is a result of the Sydney Basin stress province and is not considered to represent a regional trend.

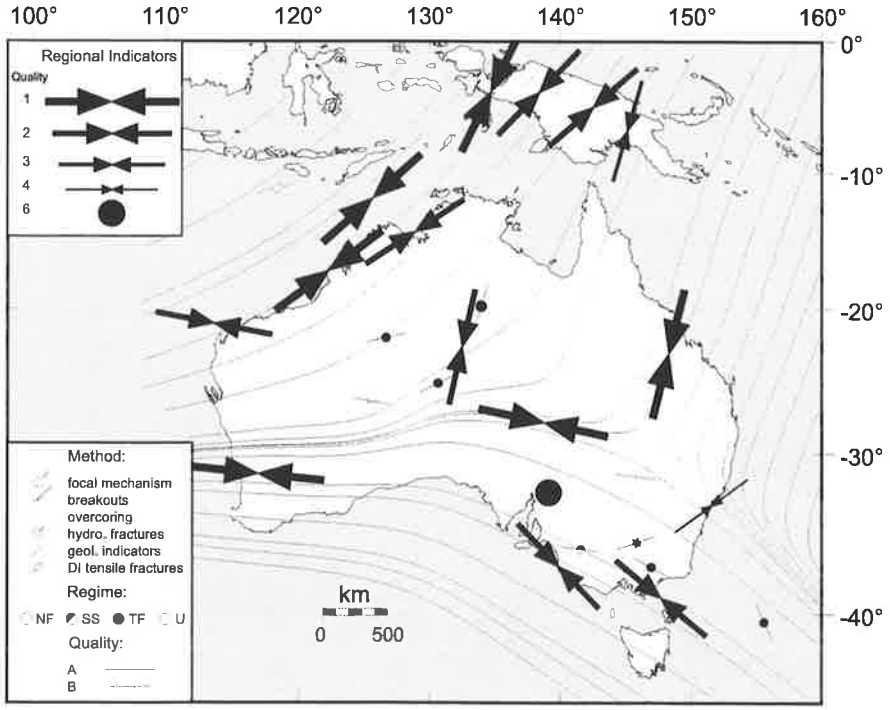

Figure 7.10 Comparison of the 16 stress provinces (Figure 7.7) with the stress trajectory map (Figure 7.8) for continental Australia. Results from the two techniques correspond very closely. The areas of largest discrepancies between the two methods are in the Sydney, Amadeus and Carnarvon Basins.

7.6 Regional Stress Regimes for the Australian Continent

Stress regime information for the Australian continent is limited. Seven of the sixteen stress provinces yield no information on the stress regime (Table 7.3). These are generally basins where stress orientations have come exclusively from borehole breakout and DITF orientations. Of the nine stress provinces that yield information on the stress regime, five exhibit a strike-slip faulting stress regime ($\sigma_{Hmax}>\sigma_v>\sigma_{hmin}$) and four a reverse faulting stress regime ($\sigma_{Hmax}>\sigma_{hmin}>\sigma_v$); (Table 7.3). No province displays a normal faulting stress regime ($\sigma_v>\sigma_{Hmax}>\sigma_{hmin}$). The provinces were considered either normal, strike-slip or reverse stress regime depending on their average α value (Table 7.2). The slight dominance of strike-slip faulting stress regimes over reverse faulting stress regimes, contrasts with the dominantly reverse faulting stress regimes indicated by the raw data (Figure 7.1c). This apparent paradox can be explained by the clustering of the indicators displaying a reverse faulting stress regime in the Sydney and Bowen Basins (Figure 7.11). Moreover, a significant amount of stress regime data are not included in the calculation of stress regimes for the stress provinces because these indicators lie outside the defined stress provinces. These stress indicators are primarily from earthquake focal mechanisms.

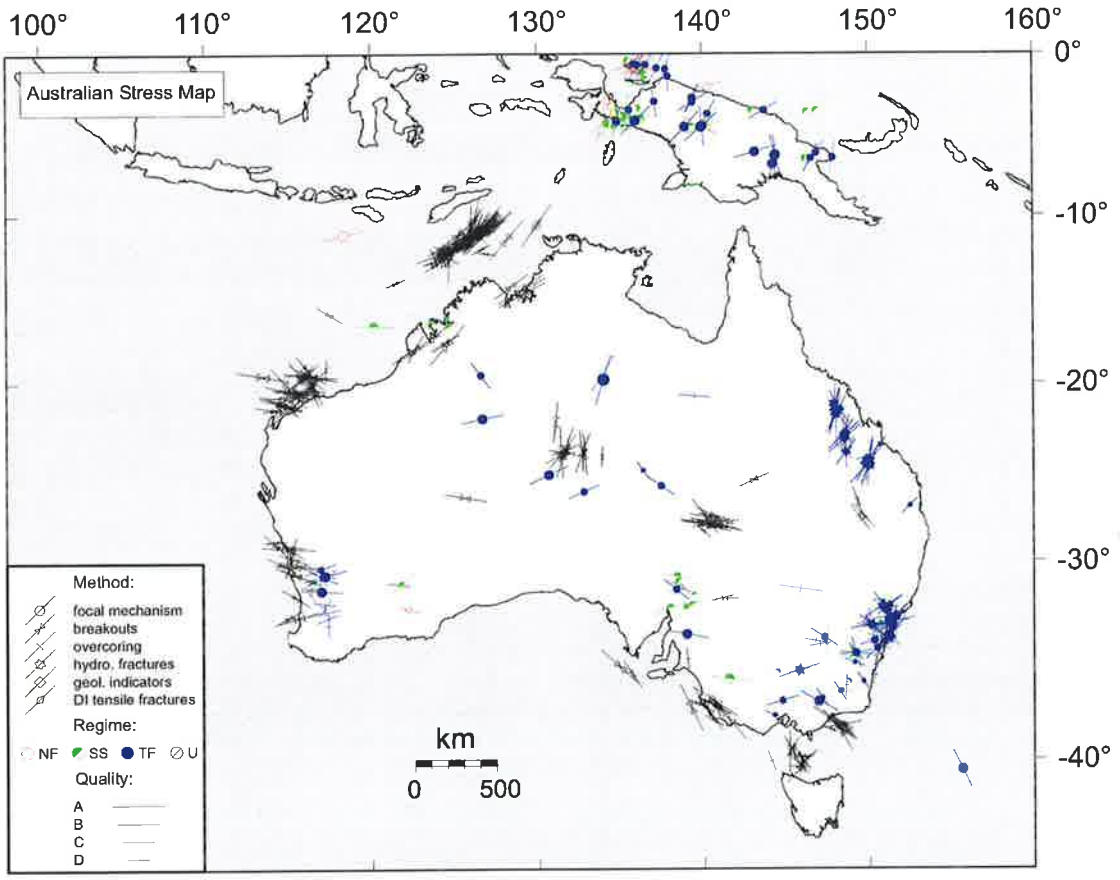

Figure 7.11 The Australian stress map using A-D quality data colour coded depending on stress regime. Red indicates a normal faulting stress regime, green a strike-slip faulting stress regime and blue a reverse faulting stress regime.

Table 7.3 Breakdown of the stress regime information within each stress province.

Province	No. A-C	Overall Regime	No. NF	No. NS	No. SS	No. TS	No. TF	No.U
Amadeus Basin	11	U	0	0	0	0	0	11
N. Bonaparte Basin	60	U	0	0	0	0	0	60
S. Bonaparte Basin	4	U	0	0	0	0	0	4
Bowen Basin	31	TF	0	0	3	0	28	0
Canning Basin	9	SS	0	0	2	0	0	7
Carnarvon Basin	27	U	0	0	0	0	0	27
Cooper Basin	14	U	0	0	0	0	0	14
Flinders Ranges	6	SS	0	0	4	0	2	0
Gippsland Basin	7	U	0	0	0	0	0	7
Irian Jaya 1	37	SS	8	1	18	0	10	0
Irian Jaya 2	13	SS	2	0	4	0	7	0
New Guinea 1	4	SS	0	0	3	0	1	0
New Guinea 2	8	TF	0	0	1	0	7	0
Otway Basin	6	U	0	0	0	0	0	6
Perth	22	TF	0	0	1	3	4	14
Sydney Basin	28	TF	0	0	2	0	25	1

NF: normal faulting stress regime. NS: normal with strike-slip component. SS: strike-slip faulting stress regime. TS: reverse with strike-slip component. TF: reverse faulting stress regime. U: Unknown

The eastern portion of the Australian continent is dominated by reverse faulting stress regime as indicated by engineering type measurements in the near surface (Chapters 4 and 5) and earthquake focal mechanisms at seismogenic depths (Everingham and Smith, 1979; Denham, 1980; McCue *et al.*, 1990a). The information on stress regimes throughout the rest of continental Australia is based mainly on earthquake focal mechanisms, which indicate a mixture of strike-slip and reverse faulting stress regimes. Petroleum wells can provide information on the minimum horizontal stress magnitude through the use of leak-off and extended leak-off tests (Hillis *et al.*, 1998). However, leak-off tests are not compiled in the ASM database, as they provide no information of the orientation of the stress field. Nevertheless, given that leak-off test data indicate that σ_{hmin} is less than σ_v in the Bonaparte and Cooper Basins, these areas must have a stress regime that is either normal or strike-slip (Hillis *et al.*, 1998). Stress regimes seem to vary depending on the stress indicator type/depth. Hence information on stress regimes should not be extrapolated to different depths.

Chapter 8
Finite Element Modelling of the Indo-Australian Plate

8.1 Introduction

In most continental areas such as Western Europe, South America and stable North America, σ_{Hmax} orientations broadly parallel the direction of absolute plate velocity (Zoback *et al.*, 1989; Richardson, 1992; Gölke and Coblentz, 1996). This observation has led many investigators to conclude that plate boundary forces are the principal control on the character of the first-order intraplate stress field (Zoback *et al.*, 1989; Zoback and Magee, 1991; Richardson, 1992; Stefanick and Jurdy, 1992; Coblentz and Richardson, 1996; Gölke and Coblentz, 1996). In contrast to these other plates, σ_{Hmax} orientations in the Australian continent do not parallel the north-northeast direction of absolute plate velocity. Hence, a cursory evaluation of the Australian intraplate stress field may result in the conclusion that the plate boundary forces do not exert a first order control on the intraplate stress field, as is observed in other continental regions. However, the results of finite element modelling of the IAP have shown that the plate boundary forces do indeed play a major role in determining the first order stress field in continental Australia (Cloetingh and Wortel, 1985; Cloetingh and Wortel, 1986; Coblentz *et al.*, 1995; Coblentz *et al.*, 1998). These studies focussed on evaluating the relative contribution of topographic and plate boundary forces on the intraplate stress field, and demonstrated that the complex convergent northeastern plate boundary could account for the broad rotation of the stress field in the IAP and its lack of parallelism to the direction of absolute plate velocity.

The present study builds on these previous modelling results in three respects. Firstly, whereas previous studies relied on a *qualitative* assessment of the fit between predicted and observed stresses, here a *quantitative* assessment was employed. Previous qualitative studies failed to develop a satisfactory model for the intraplate stress field of the entire Australian continent, particularly in areas of eastern Australia. The quantitative assessment between the observed and predicted stress field has allowed the determination of the optimal boundary force combination for the current observed stress field. Secondly, the observed stress field used in the present study was significantly more refined than those used in previous

investigations. Since the compilation of the WSM the number of reliable A-C stress indicators for the Australian continent has increased from 95 in the WSM Zoback (1992) release to 322 in this study. As previously mentioned, the majority of the new data have come from the analysis of borehole breakouts and drilling induced tensile fractures. A significant amount of new data have been compiled for areas in eastern and central Australia, including that presented in Chapters 4 and 5 of this thesis, where the stress field was previously poorly constrained or totally unknown. The increase in stress data across continental Australia has allowed the definition of 16 stress provinces (Chapter 7). Finally, the present study employed a 'basis-set' approach to computing the predicted intraplate stress field. This method allows rapid evaluation of a very large number of models (millions of boundary force combinations) and quantitative assessment of the fit between the observed and predicted stress fields.

It is worth emphasizing that the primary aim of this study was to fit the regional intraplate stress field of continental Australia using the primary tectonic forces (e.g. boundary and topographic) acting on the plate. The conclusions drawn from this modelling are, as in previous studies, limited by the inherent non-uniqueness of the problem. A large number of different boundary force combinations can predict very similar stress fields. Despite this caveat, the refined approach to modelling the intraplate stress field of continental Australia has allowed an important advance in understanding of the dynamics of the IAP.

8.2 The Regional Australian Intraplate Stress Field

Previous modelling by Coblentz *et al.* (1995) and Coblentz *et al.* (1998) averaged *in situ* stress data in 3° latitude by 3° longitude bins to characterise the observed stress field. Although this approach allows the regional trend to be identified in most areas, it can produce anomalous orientations that may not represent the regional trend. The current modelling study used stress provinces to define the observed stress field. The stress provinces define significant regions of the earth's surface where the stress orientations are broadly consistent (Chapter 7). Twelve of the sixteen stress provinces defined in Chapter 7 are used to compare the modelled stress field (Figure 8.1). The four provinces that are not used are located adjacent to the collisional plate boundary at Papua New Guinea, and are characterized by σ_{Hmax} orientations that are perpendicular to the plate boundary. Hence, σ_{Hmax} orientations from these provinces are parallel to the force applied at the Papua New Guinea boundary and thus provide no additional constraints on the modelled stress field.

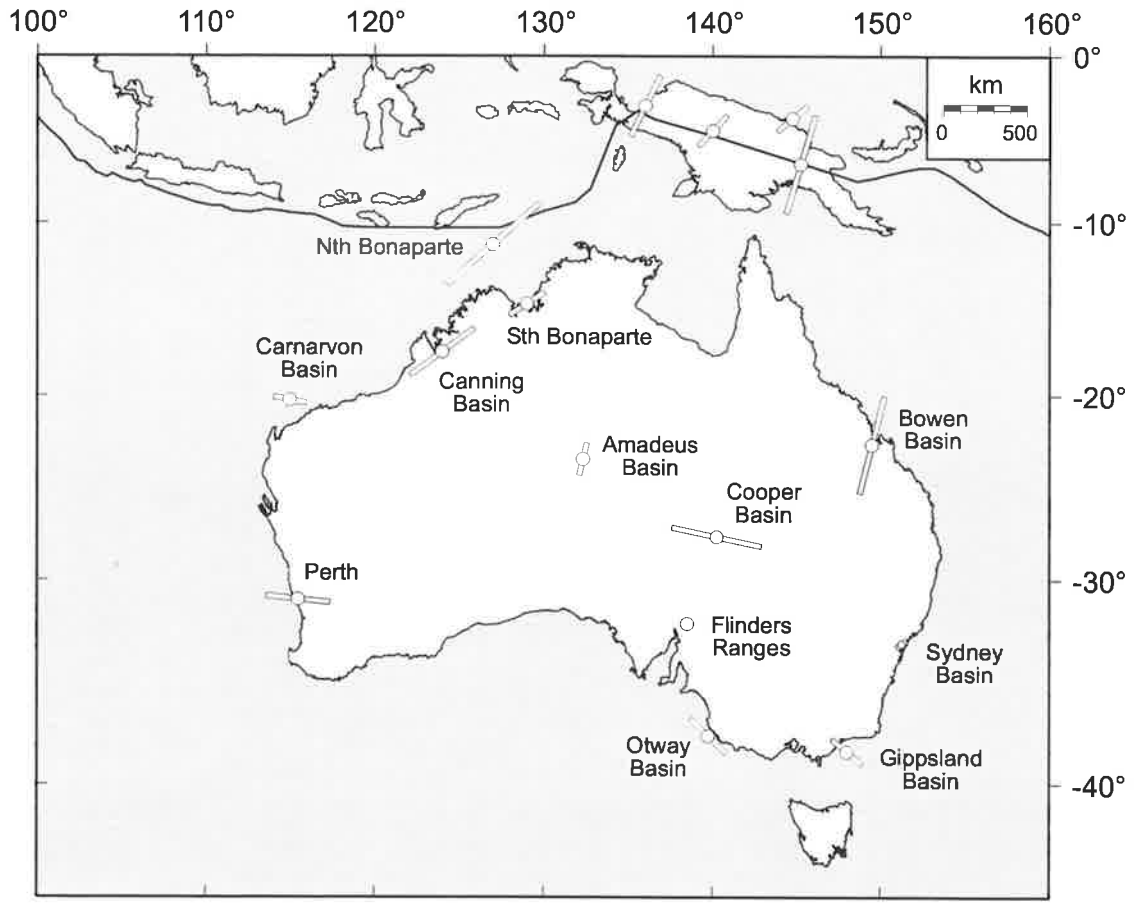

Figure 8.1 The 12 stress provinces used to constrain the predicted stress field. The orientation of the bar indicates the orientation of σ_{Hmax} and the length is proportional to the weight used in the calculation of the misfit value. The four stress provinces in Papua New Guinea are represented for comparison but are not used in the calculations.

The systematic variation in the orientation of the regional stress field is summarized in Figure 8.1. The western part of the Australian continent is characterized by an east-west σ_{Hmax} orientation (Perth and Carnarvon Basin provinces). Across the northern margin of Australia the σ_{Hmax} orientation becomes northeast-southwest (Bonaparte Basin and Canning Basin provinces). The Amadeus Basin in central Australia and the Bowen Basin in eastern Australia both exhibit a north-northeast to south-southwest σ_{Hmax} orientation. In addition, central Australia is also characterized by a strong east-west σ_{Hmax} orientation in the Cooper Basin stress province. Southeastern Australia is characterized by a southeast-northwest σ_{Hmax} orientation in both the Otway Basin and Gippsland Basin provinces, with a weak northeast-southwest trend in the Sydney Basin province. A more detailed description of the Australian stress field is given in Chapter 7.

As outlined earlier in Chapter 7 there is significantly less information on stress magnitudes than on stress orientations within the ASM database, with approximately half of the 322 A-C

quality σ_{Hmax} orientations having information on the stress regime. Of the data available, 60% indicate a reverse stress faulting, 27% indicate a strike-slip faulting stress regime, 7% indicate a normal faulting stress regime and 6% indicate a mixed stress regime. Since, magnitude data are available for only around half of the stress provinces, and given the paucity of this data, the available magnitudes are used only as a guide during the modelling. Furthermore, as discussed in Chapter 7 stress magnitudes (unlike stress orientations) appear to be sensitive to stress indicator type/depth and thus exhibit a depth-control that cannot be removed in the plate scale modelling when the derived stresses are lithospheric averages.

The reliability of the mean σ_{Hmax} orientation from the 12 stress provinces varies depending on the number of measurements and their standard deviation. As a consequence each of the 12 observed stress orientations were given a weighting between one (maximum) and zero (minimum). This weighting was used to calculate the fit of each model and is a direct measure of how consistent the stress orientations are within each stress province (Table 8.1). Each weight was determined by computing the $\overline{R}$ value for the province and then subtracting the $\overline{R}$ value from the 90% confidence level used in the Rayleigh test (Davis, 1986; Coblentz and Richardson, 1995). The weights were then scaled so the maximum weight applied was one. Any province with an $\overline{R}$ value less than the 90% confidence level was automatically given a weight of zero, as the data within that stress province were considered random. Thus the weights range between one and zero. Figure 8.1 displays the orientation of each stress province with the length of the bar indicating the amount of weighting applied. The Flinders Ranges stress province was allocated a weight of zero, as it fails the Rayleigh test at the 90% confidence level and is represented by a circle on Figure 8.1.

Table 8.1 The stress province data used to constrain the predicted stress field. A weight between one (highest) and zero (lowest) was given to each province based on how well it passed the 90% confidence level of the Rayleigh test.

Province	Lat.	Long.	σ_{Hmax} Orientation	$\overline{R}$	90% confidence level	Scaled Weight
Amadeus Basin	132.25	-23.50	013	0.632	0.456	0.278
Nth. Bonaparte Basin	127.00	-11.25	048	0.849	0.214	1.000
Sth. Bonaparte Basin	129.00	-14.75	057	0.990	0.768	0.350
Bowen Basin	149.50	-22.75	014	0.798	0.273	0.827
Canning Basin	124.00	-17.50	053	0.917	0.504	0.650
Carnarvon Basin	115.00	-20.25	101	0.465	0.293	0.271
Cooper Basin	140.25	-27.75	102	0.888	0.405	0.759
Flinders Ranges	138.50	-32.25	083	0.561	0.618	0.000
Gippsland Basin	148.00	-38.50	130	0.787	0.572	0.339
Otway Basin	139.75	-37.75	134	0.882	0.618	0.416
Perth	115.50	-31.00	096	0.658	0.323	0.527
Sydney Basin	151.25	-33.25	054	0.356	0.287	0.108

8.3 Modelling Method

The magnitude and orientation of the tectonic stresses in the IAP were predicted using a two-dimensional elastic finite-element analysis. The finite element grid consisted of 2527 constant-strain triangular elements composed of a network of 1374 nodes, which provided a spatial resolution of about 2° in both latitude and longitude. It should be noted, that the sensitivity of the modelled stresses was therefore limited to large-scale tectonic features with wavelengths of a few hundred kilometers. The assumption of a purely elastic rheology was an oversimplification, however it is justifiable as the first-order stresses can be considered to be in steady state (Coblentz *et al.*, 1995). The stress magnitudes were calculated for a lithosphere of constant thickness, assumed to be 100 km, and stress concentrations may occur where variations in the lithospheric thickness are present. In addition, any bending moment stresses associated with the subducting plates were ignored, and the predicted stresses cannot be regarded as significant for locations within the flexural wavelength of such boundaries. The predicted stresses in this study were those stresses that deviated from the reference state of stress with the vertical stress and any associated horizontal component having been removed. The lithostatic reference state appears to be the most appropriate for at least the Sydney and Bowen Basins (Chapters 4 and 5). All elements were assigned a nominal Young's modulus of 7×10^{10} Nm^{-2} and a Poisson's ratio of 0.25. Based on the fact that the plate is not accelerating, static equilibrium was assumed.

This study has used three principal tectonic processes to model the forces acting on the IAP: (1) ridge push, (2) boundary tractions (representing both compressive collisional and slab pull forces) and (3) buoyancy forces resulting from lithospheric density variations associated with continental margins and elevated continental crust (Cloetingh and Wortel, 1986; Richardson and Reding, 1991; Coblentz *et al.*, 1994; Coblentz *et al.*, 1995). Figure 8.2 illustrates the various tectonic forces acting on the IAP. In order to ensure mechanical equilibrium, basal drag was applied only as needed to balance the net torque acting on the plate (Richardson *et al.*, 1979).

In addition to the basic tectonic forces discussed above, the buoyancy force resulting from the lithospheric density variation associated with the Lord Howe Rise and the force associated with the plate boundary south of New Zealand were also included (Figure 8.2). Lord Howe Rise is a large section of continental crust that separated from the eastern side of continental Australia approximately 95-83 Ma as a result of the opening of the Tasman Sea (Gaina *et al.*, 1998). These two additional forces were included primarily to achieve a better fit to the

observed stress field in eastern Australia. Throughout this study a positive force was defined as one that acts towards the centre of the plate, termed 'pushing', and a negative force was defined as one that applies a force away from the centre of the plate, termed 'pulling'.

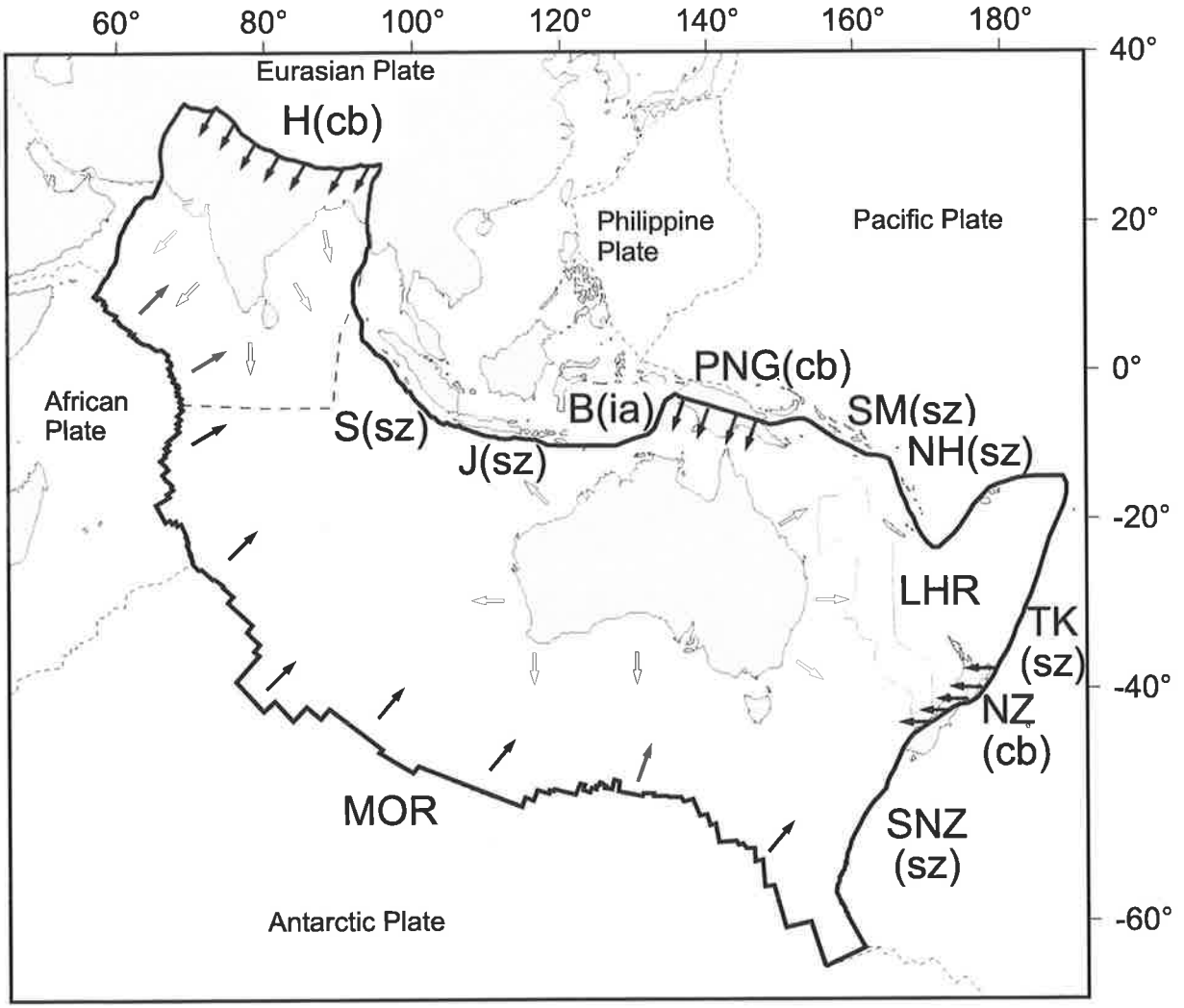

Figure 8.2 Indo-Australian plate with the boundaries and forces used in the modelling. Solid-filled arrows represent the boundary forces acting on the plate and open arrows represent the force associated with continental margins. Note that some boundary forces (S, J, B, SM, NH, TK and SNZ) are not represented, as their force direction was unrestricted during the modelling. Also note that force arrows are not drawn to scale. H = Himalaya; S = Sumatra Trench; J = Java Trench; B = Banda Arc; PNG = Papua New Guinea; SM = Solomon Trench; NH = New Hebrides; TK = Tonga-Kermadec Trench; NZ = New Zealand; SNZ = south of New Zealand; MOR = Mid Ocean Ridge; LHR = Lord Howe Rise; cb = collisional boundary; sz = subduction zone; ia = island arc.

The finite-element modelling approach herein has been extended from that used in previous intraplate stress modelling studies (e.g. Richardson *et al.*, 1979; Cloetingh and Wortel, 1986; Richardson and Reding, 1991; Coblentz *et al.*, 1995; Coblentz *et al.*, 1998) through the use of a 'basis-set' approach. The basis-set approach works by exploiting the linearity of the purely elastic model used for the analysis. In this way, the modelling compensates for some of the shortcomings of assuming an elastic model. In the basis-set approach, the predicted stresses

and resistive basal drag required to balance the torque exerted on the plate for each of the tectonic forces were calculated individually. The predicted stress field for various combinations of the tectonic forces was a weighted linear sum of the basis-set. Thus, various combinations of the boundary forces acting on the plate were evaluated in a matter of seconds rather than minutes as required by a new run of the finite-element model. This approach greatly increased the speed of the analysis and allows a detailed search for the best solution. For example, consideration of only three values for each of 20 tectonic forces would require approximately 10^9 finite-element runs, which in turn would require a prohibitive amount of computing time, despite the availability of fast computing platforms. An algorithm that computed the predicted stress through the addition of weighted linear combinations reduced the computation time required by several orders of magnitude. Evaluation of each model combination involved the determination of a misfit value for the predicted stress fields by averaging the difference between the 12 observed stress orientations (i.e. the regional stress provinces) and the closest modelled stress orientations. The difference between the observed and modelled stress orientations was multiplied by the weight given to the observed data, as described above. Consequently each model was ranked according to its misfit value.

Throughout the model runs topographic forces such as ridge push, elevated topography, continent margins and other lithospheric density anomalies remain unchanged, since they can be determined with relative confidence. The topographic forces range in magnitude from 2-3×10^{12} Nm^{-1} for ridge push, 1-2×10^{12} Nm^{-1} for continental margins and 6×10^{12} Nm^{-1} for continental lithosphere with an elevation of 5000 m (Lister, 1975; Parsons and Richter, 1980; Coblentz *et al.*, 1994). Only plate boundary forces at convergent plate margins and drag at the base of the plate have varied over the model runs. The magnitude of collisional forces at convergent plate boundaries and basal drag forces are poorly constrained with estimates varying by orders of magnitude (Solomon and Sleep, 1974; Forsyth and Uyeda, 1975; Solomon *et al.*, 1975). For example, slab pull theoretically generates a large tensional force on the subducted surface plate for a fully developed slab (McKenzie, 1969b; Turcotte and Schubert, 1971). However, the large amount of seismicity associated with subduction zones indicates resistance to subduction dissipates much of the energy. Thus, the surface plates may not experience a large slab pull force (Richardson, 1992). As previously mentioned, basal drag was only used to balance the total torque exert on the plate by the other forces.

An initial coarse run of five million models was undertaken to constrain a more detailed second run (Table 8.2). In the initial coarse run, forces on the 10 plate boundaries were

allowed to vary between –6 and $+6\times10^{12}$ Nm^{-1}, except for the three collisional boundaries Himalaya, Papua New Guinea and New Zealand, which were allowed to vary between 0 and $+6\times10^{12}$ Nm^{-1} (Table 8.2). This enabled the boundaries to range over values thought to be geologically plausible and also included values used in previous modelling studies (Cloetingh and Wortel, 1986; Coblentz *et al.*, 1995; Coblentz *et al.*, 1998). The second more detailed run of approximately 23 million models was based on the average obtained from the best 10% of models in the initial coarse run. The constraints placed on each boundary for the more detailed run are shown in Table 8.2. The torque magnitudes and torque pole locations used for the basis-set of tectonic boundary forces (1×10^{12} Nm^{-1}, directed towards the plate interior) are listed in Table 8.3.

Table 8.2 The parameters used in the initial coarse and second detailed runs. Each boundary was allowed to vary between the maximum and minimum force magnitude by the increment stated. All forces are $\times 10^{12}$ Nm^{-1}.

Boundary	Initial Coarse Run			Second Detailed Run		
	Minimum	Maximum	Increment	Minimum	Maximum	Increment
Himalaya	0	6	2	1	5	1
Papua New Guinea	0	6	2	1	5	1
Sumatra	-6	6	3	-3	3	1
Java	-6	6	3	-4	0	1
Banda	-6	6	3	1	3	1
Solomon	-6	6	3	-3	3	1
New Hebrides	-6	6	3	-3	3	1
Tonga-Kermadec	-6	6	3	-4	4	1
New Zealand	0	6	2	1	4	1
South of New Zealand	-6	6	3	0	4	1

Table 8.3 Tectonic force magnitudes and relative torque contributions. Note that for the purposes of creating the basis-set all boundary forces are directed towards the interior of the plate.

Force	Magnitude, $\times 10^{12}$ Nm^{-1}	Total Torque, $\times 10^{25}$ Nm	Latitude, °N	Longitude, °E
Himalaya	1	1.59	-10.4	167.1
Papua New Guinea	1	0.94	-84.3	-37.3
Sumatra	1	0.93	-19.0	-170.4
Java	1	1.04	-18.7	-156.3
Banda	1	1.02	-15.7	-141.8
Solomon	1	0.77	79.9	159.5
New Hebrides	1	0.49	73.0	166.5
Tonga-Kermadec	1	1.46	-64.1	9.8
New Zealand	1	0.79	-48.0	-6.8
South of New Zealand	1	1.12	-42.8	-13.8
Ridge Push	-	8.30	40.7	31.7
Continental margins	-	2.19	-22.5	-179.2
Elevated continent	-	3.66	-7.6	176.5
Lord Howe Rise	-	0.12	-24.1	14.2

8.4 Modelling Results

Examination of the results from the second model run indicated that averaging the force combination from a number of the top models lowers the misfit value. The misfit value is minimized when the forces from the top five models of the second model run are averaged. Also, this boundary force ensemble is considered to be more tectonically plausible than the forces associated with the absolute lowest misfit value from the second model run, since it reduces the forces acting along a number of boundaries. The average of the top five models is considered the 'best fitting' model for this study (Table 8.4; Figure 8.3). The best fitting model, while non-unique, can be considered to be a plausible representation of the tectonic force acting on the IAP, which produces the intraplate stress field most consistent with the observed stress field shown in Figure 8.1. The torques resulting from the force on each boundary used in the best fitting model are listed in Table 8.4. The boundaries at Himalaya and south of New Zealand produce significantly more torque on the IAP than the other boundaries. However, the combined torque of both these boundaries is less than that produced by ridge push alone. Thus, the results from this modelling study are consistent with previous studies in that ridge push is the principal contributor to the intraplate stress field in the IAP (Coblentz *et al.*, 1995; Coblentz *et al.*, 1998).

A third run over the boundary forces was undertaken to investigate the character of the solution space in the vicinity of the best fitting model. This third, more detailed run revealed that further refinement of the boundary force magnitudes exceeds the resolution of the problem as it results in only minor observable changes in the predicted stress field.

Table 8.4 Force magnitudes applied to the different boundaries for the average of the top five (best fitting model) and the average of the top 100 models from the second run. Total torque calculated from the forces applied in the best fitting model. For comparison the force magnitudes used in Coblentz *et al.* (1998) have been listed. Also listed are the standard deviations (stdev) and the maximum and minimum values from the top 100 models. Statistics were calculated on the top 100 models to show the variability in force acting at each boundary that produced a close fit between the predicted and observed stress fields. All forces are $\times 10^{12}$ Nm^{-1}.

Boundary	Average of top five	Total Torque, $\times 10^{25}$ Nm	Coblentz et al. (1998)	Average of top 100	Stdev of top 100	Max of top 100	Min of top 100
Himalaya	2.2	3.49	4.0	2.04	0.942	1	5
Papua New Guinea	1.6	0.73	2.0	1.46	0.558	1	3
Sumatra	1.6	1.50	4.0	1.18	1.598	-3	3
Java	-0.6	0.93	-4.0	-1.29	1.200	-4	0
Banda	1.6	0.62	1.0	1.37	0.485	1	2
Solomon	3.0	1.63	-1.0	2.96	0.197	2	3
New Hebrides	2.8	2.32	-1.0	2.54	0.642	1	3
Tonga-Kermadec	1.0	1.39	2.0	0.98	0.141	0	1
New Zealand	1.4	1.46	1.0	1.64	0.718	1	4
South of New Zealand	3.0	3.36	-	3.39	0.764	1	4

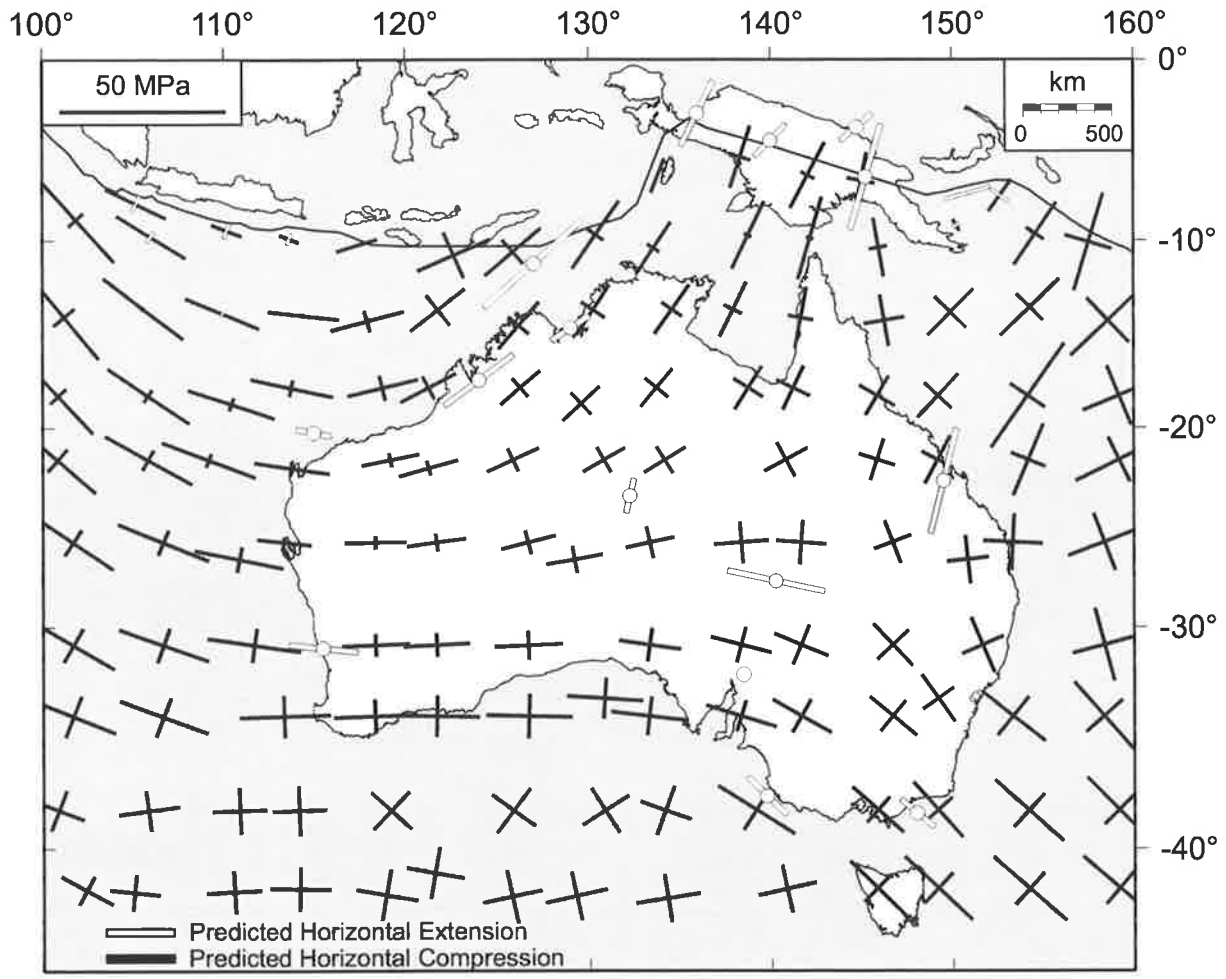

Figure 8.3 Predicted stresses for continental Australia using the average of the top five models, considered to be the best fitting model. Forces used on each boundary are listed in Table 8.4.

Despite using a greatly improved observed stress data set, the results of the modelling demonstrate that a significant amount of ambiguity continues to exist when modelling the *in situ* stress field of continental Australia. For example, the top 100 models from the detailed run predict stress orientations across the continent that are visually similar, but result from substantially different forces on certain boundaries (Table 8.4). Four distinctly different boundary force combinations are shown in Figure 8.4. These four different models occur within the top 100 models and predict very similar stress orientations across continental Australia. However, the four models do predict different stress magnitudes across some areas of continental Australia. The forces on each boundary used to generate the four models are listed in Table 8.5. These four models are also visually similar to the best fitting model (Figure 8.3).

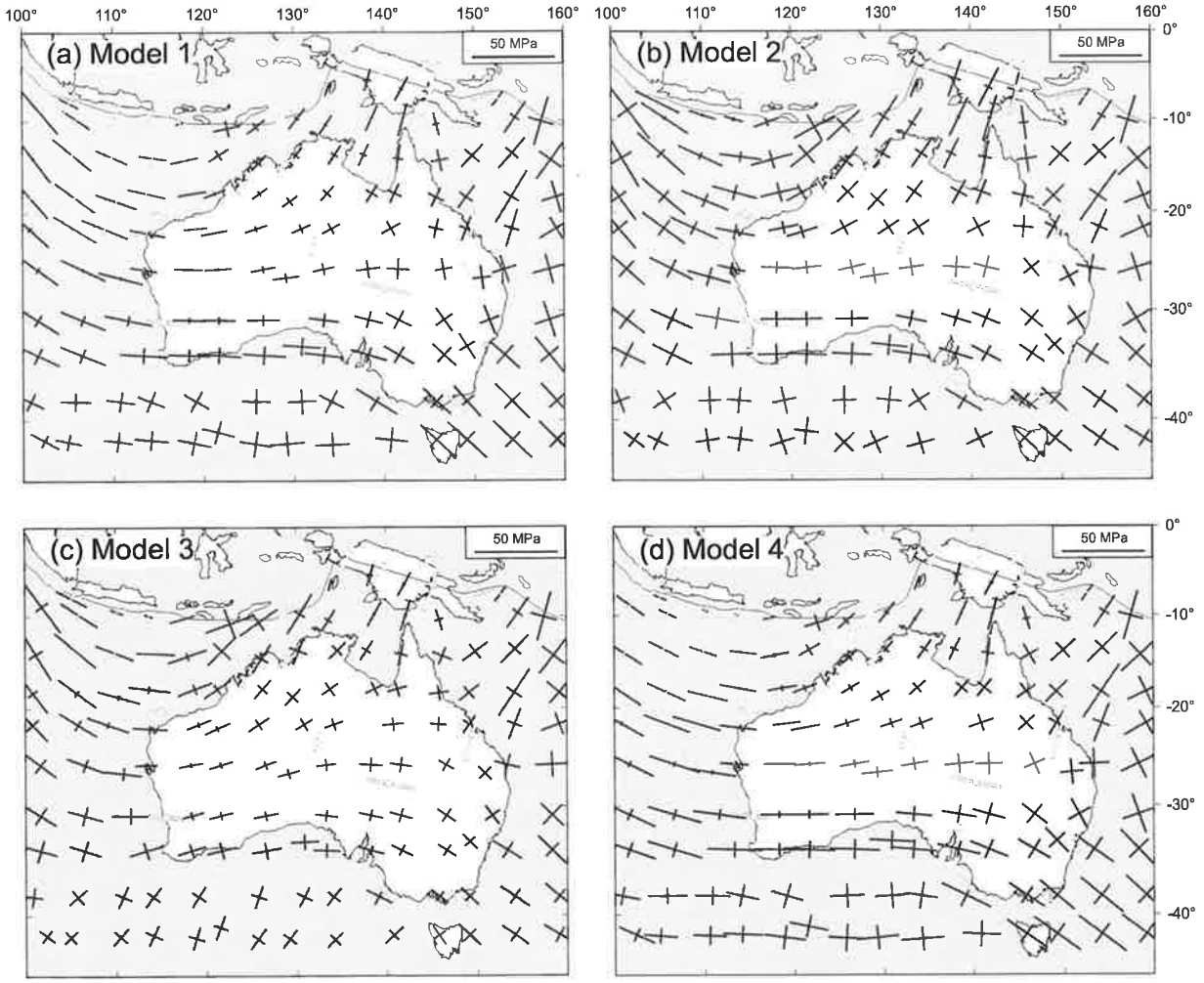

Figure 8.4 Predicted stresses for continental Australia using four combinations of boundary forces from the top 100 models. Boundary force combinations for the four models are listed in Table 8.5. All four models display a similar stress field with regards to the orientation, but have a distinctly different combination of boundary forces (Table 8.5). Solid bars indicate horizontal compression; open bars indicate horizontal tension.

Table 8.5 Force magnitudes applied to each boundary for four models from the top 100 models. The variable combination of forces on the boundaries can produce a very similar stress field as illustrated in Figure 8.4.

Boundary	Model 1	Model 2	Model 3	Model 4
Himalaya	1	3	1	2
Papua New Guinea	1	2	1	1
Sumatra	2	3	3	-1
Java	-2	0	-1	-1
Banda	1	2	2	1
Solomon	3	3	3	3
New Hebrides	2	3	2	3
Tonga-Kermadec	1	1	1	1
New Zealand	1	2	2	2
South of New Zealand	4	2	1	4

Despite the non-uniqueness, a number of broad conclusions can be made from the results of both the coarse and detailed runs. First, the subduction zone at Sumatra has very little

influence on the Australian stress field due to its position on the plate relative to the Australian continent. Second, a compressive force is required along the Solomon, New Hebrides, Tonga-Kermadec subduction zones as well as the boundary south of New Zealand. Importantly, results indicate that a comprehensive fit to the observed stress field of continental Australia is not possible with all the subduction boundaries exerting a pull on the IAP.

Information on the stress regime (stress magnitudes) was not included in the calculation of the misfit in this analysis. This was due to the lack of stress regime data available for all the stress provinces as outlined in Chapter 7. Nevertheless, in the best fitting model, and most of the top models, all stress provinces are characterized by reverse faulting conditions ($\sigma_{Hmax}>\sigma_{hmin}>\sigma_v$), which is broadly consistent with the limited stress regime information available. Consequently, including information on the stress regime would only have a very minor effect on the modelling results. The stress field produced from the top 100 models predicts relatively low tectonic stress magnitudes for the Australian continent of between 20 MPa and 45 MPa averaged over the thickness of the lithosphere (100 km). In contrast, modelling by Cloetingh and Wortel (1986) calculated tectonic stress magnitudes of over 100 MPa for the Australian continent. The lower tectonic stress magnitudes are principally due to the inclusion of topographic forces throughout all of the models, which has reduced the tectonic stress magnitudes on the Australian continent.

The lithospheric density variation associated with Lord Howe Rise was included in the modelling in an attempt to account for the scattered and variable stress field observed throughout eastern Australia, which had not been satisfactorily explained by previous modelling results (Cloetingh and Wortel, 1986; Coblentz *et al.*, 1995; Coblentz *et al.*, 1998). The torque on the IAP generated from the Lord Howe Rise reduced the calculated misfit value to a minor extent but produced no observable change in the modelled stress field. The region was included in all model calculations, however Lord Howe Rise is not considered a major source of stress throughout eastern Australia.

The sensitivity of the modelled stress field was investigated by calculating the circular standard deviation of σ_{Hmax} orientation at each element centre for the top 100 models. The resultant values were grided using one degree cell spacing (Figure 8.5). A significant proportion of the predicted Australian stress field shows very minor variation in the orientation of σ_{Hmax} over the top 100 models. This confirms the observation that predictions

of the Australian stress field are robust and can be adequately matched using a number of plate boundary force combinations. Two areas that exhibit high standard deviation are northeastern Australia (A) and an area to the south of Australia (B). The stress field in these two areas is significantly affected by the plate boundary force combination. This result can be explained by considering the differential horizontal stress field, the difference between the maximum and minimum horizontal stress. Figure 8.6 represents the averaged differential horizontal stress field from the top 100 models. The areas of high standard deviation correspond with areas of low differential horizontal stress, indicating that the variability in the stress field is a result of the stress field being isotropic. The stress field in these areas is highly sensitive to changes in the forces applied to the plate boundaries. As a consequence the areas of low differential stress have the potential to be dominated by local stress sources and thus produce a highly variable observed stress field.

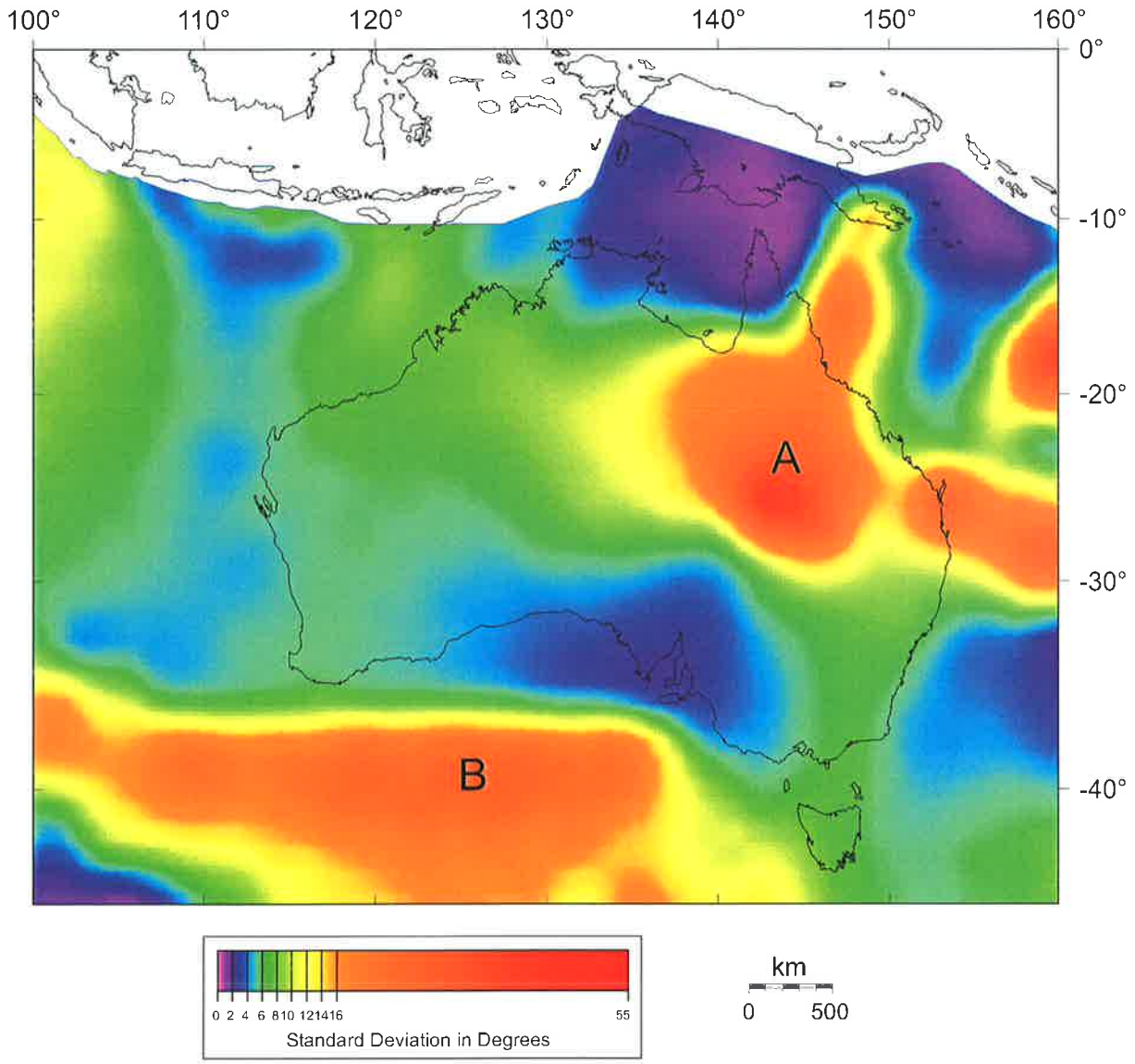

Figure 8.5 Circular standard deviation in predicted σ_{Hmax} orientations of the top 100 models.

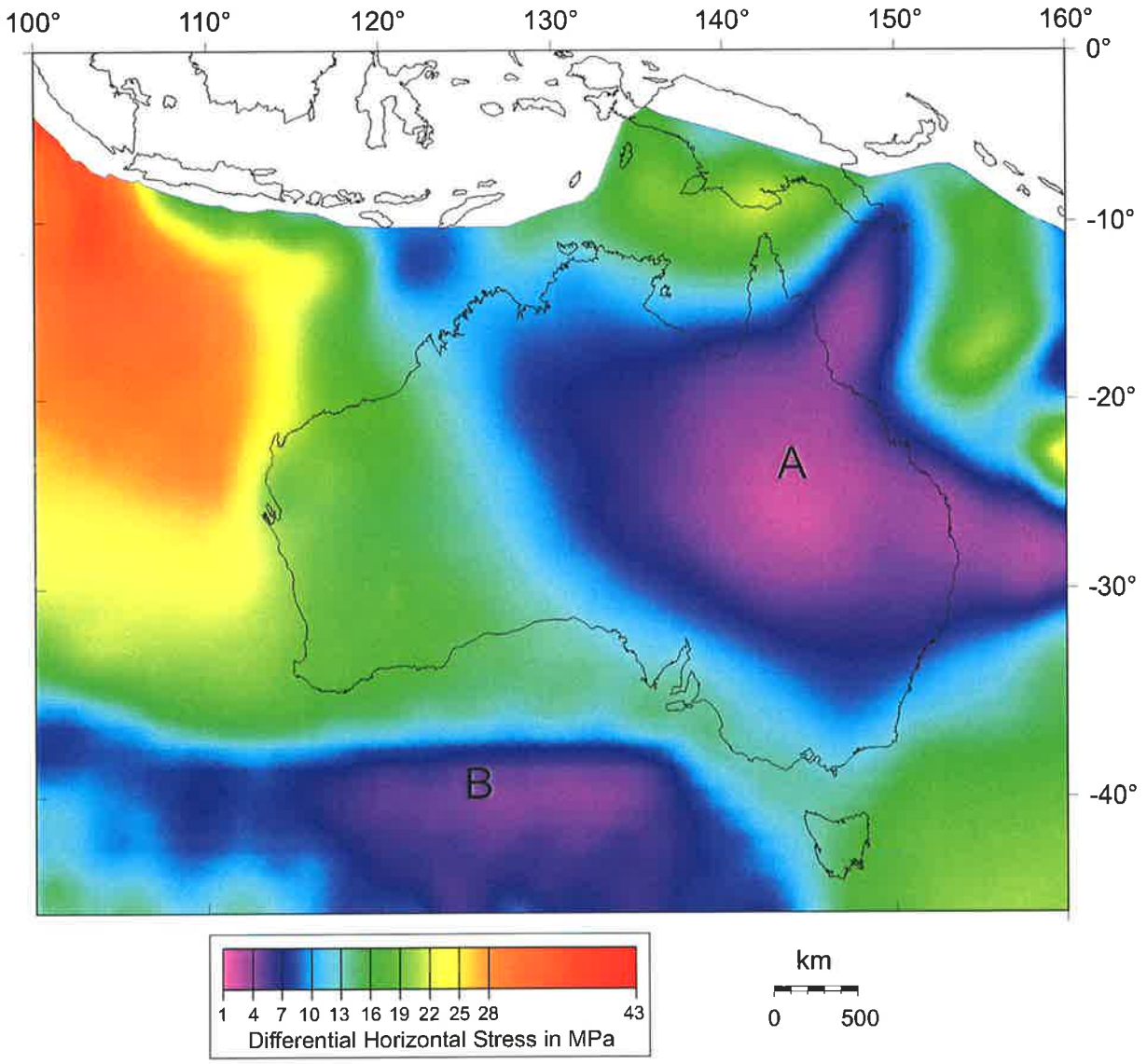

Figure 8.6 Average differential horizontal stress field (σ_{Hmax} magnitude minus σ_{hmin} magnitude) of the top 100 models.

Stress provinces and stress trajectory mapping were used in Chapter 7 to characterise the regional first-order trends in the observed stress field. It is not possible to use the stress trajectory map to constrain the modelling, however a comparison can be made with the modelling results. The stress trajectory map produced from the individual observed stress data is found to be consistent with the best fitting model (Figure 8.7). It should be noted that the stress trajectory map in a number of areas, such as the Amadeus and Sydney Basins, corresponds with the modelled stress field better than the stress province data used to constrain the model. For example, the stress province data in the Sydney Basin indicates a weak northeast-southwest σ_{Hmax} orientation. In contrast, both the modelled stress field and the stress trajectory map indicate a southeast-northwest σ_{Hmax} orientation. As outlined in Chapter 7, the Sydney Basin stress province trend is poorly defined and different from that in

the stress trajectory map, suggesting that the regional trend cannot be clearly identified in the Sydney Basin.

Some areas near the edges of the stress trajectory map correspond poorly with the modelled stress field. This possibly relates to the lack of observed stress data near the edges of the stress trajectory map and suggests the technique used to create stress trajectories is good at interpolating between data points but poor for extrapolation. A further point of interest in the stress trajectory map is the apparent nodal point over eastern Australia. This coincides with the region of isotropic stress field in areas of eastern Australia produced by the stress models (Figure 8.6).

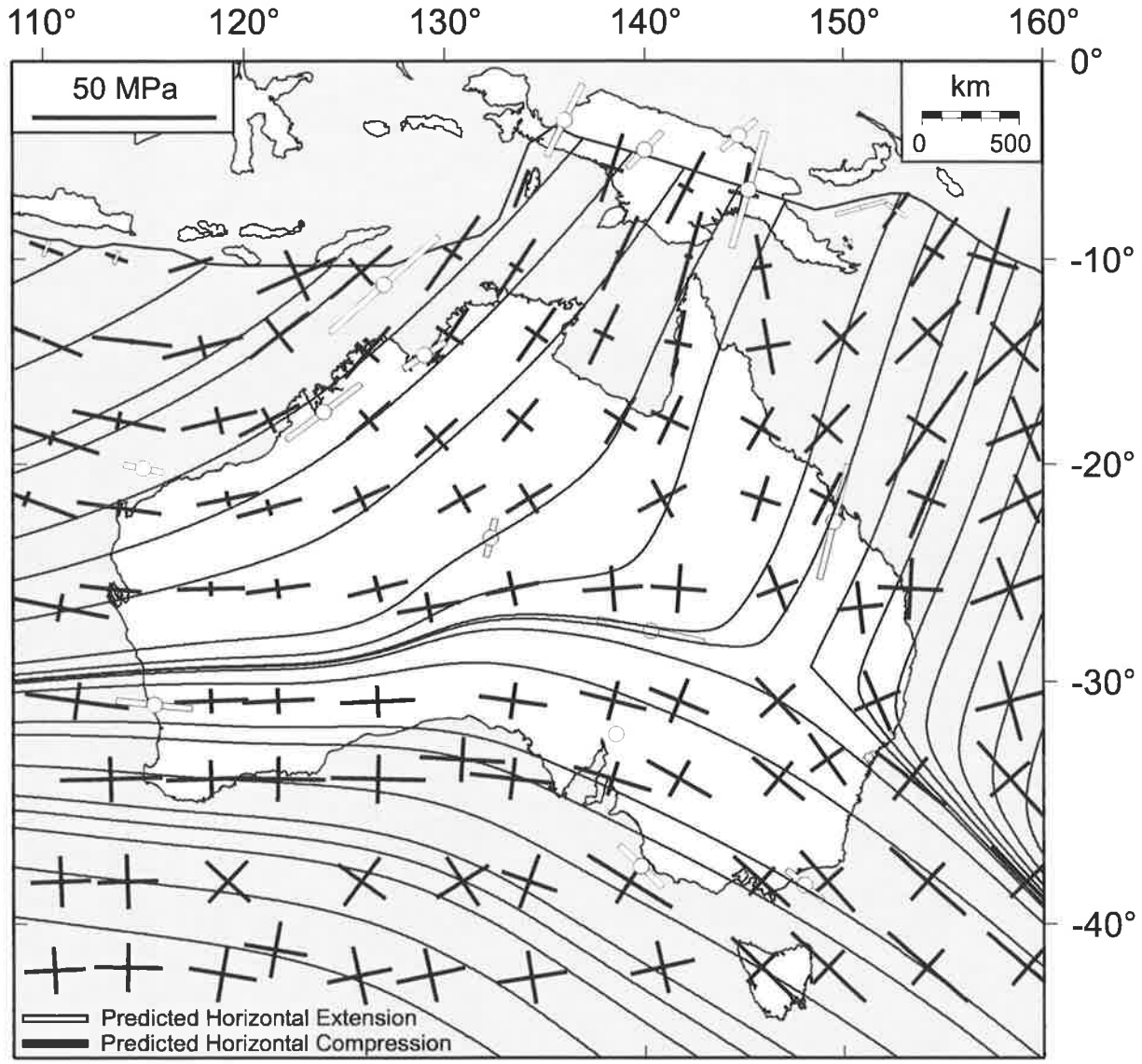

Figure 8.7 The best fitting stress model overlain by the stress trajectory map produced in Chapter 7.

8.5 Discussion

8.5.1 Comparison to Previous Models

The results presented here are broadly similar to previous studies (Cloetingh and Wortel, 1986; Coblentz *et al.*, 1995; Coblentz *et al.*, 1998), however a number of significant differences do exist, which are discussed in this section. Model 4 of Coblentz *et al.* (1998) adequately fits the observed stress data in the western half of Australia, but does not fit the observed stress data in the eastern half of the continent (Figure 8.8). In contrast, the results presented here provide a good fit to the observed stress indicators throughout the entire continent. The best fitting model presented here and the results of previous studies principally differ in the nature of the boundary forces acting along the Solomon and New Hebrides subduction zones. Whereas the forces along these boundaries predicted by the model herein are compressional, the previous studies predicted extensional forces (Cloetingh and Wortel, 1986; Coblentz *et al.*, 1995; Coblentz *et al.*, 1998). Furthermore, the plate boundary south of New Zealand has been included in the present modelling and application of a compressional force at this boundary improves the fit to the observed stress field in southeastern Australia.

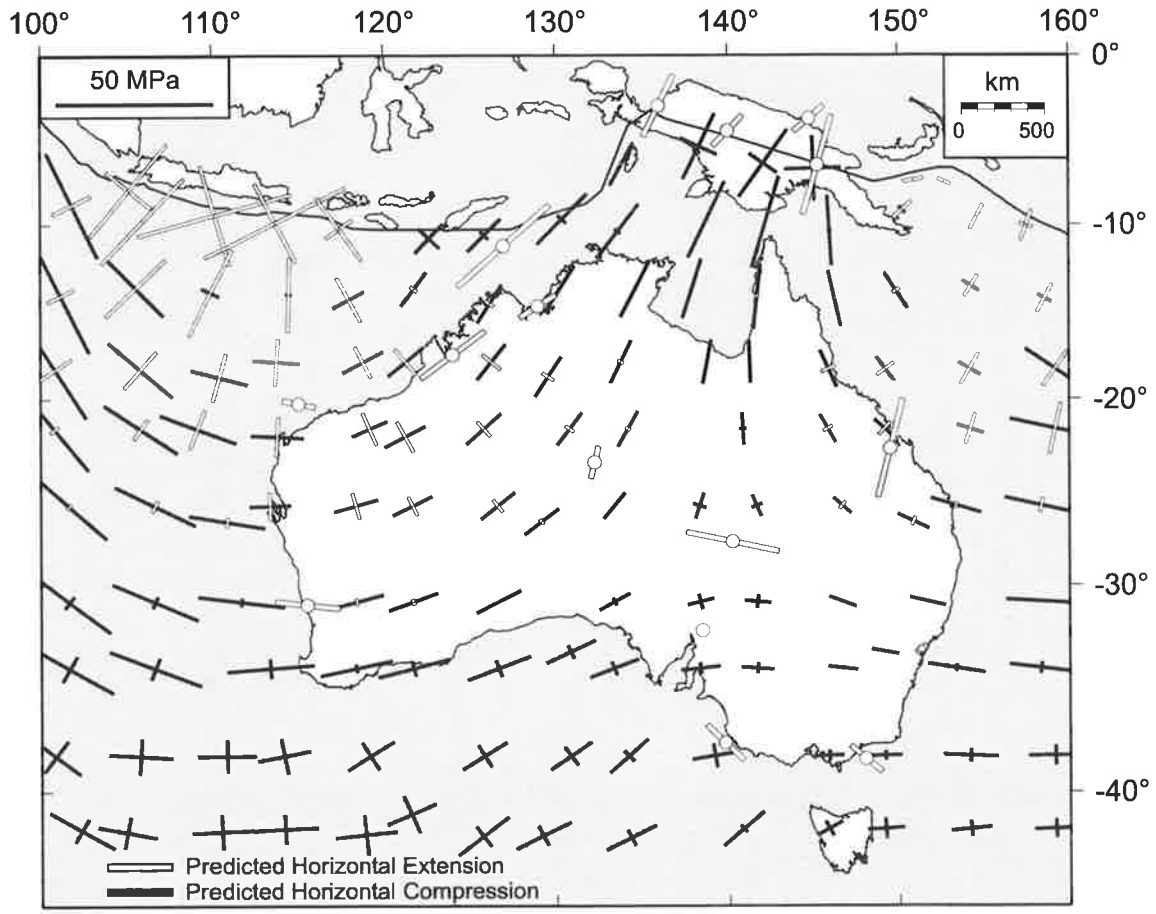

Figure 8.8 Model 4 from Coblentz *et al.* (1998) with the new stress province data.

The best fitting model present herein, differs significantly from that of Cloetingh and Wortel (1986) with regards to the force acting along the Tonga-Kermadec subduction zone. Whereas Cloetingh and Wortel (1986) applied extensional forces along this boundary, current modelling indicates that moderate compression best fits the observed stress field (Table 8.4). The large extensional force proposed by Cloetingh and Wortel (1986) resulted in significant east-west extension and a north-south σ_{Hmax} orientation in eastern Australia. In the present study, the average force applied in the top 100 models at the Tonga-Kermadec subduction zone was approximately 1×10^{12} Nm^{-1} (Table 8.4). A force of this magnitude is required along the Tonga-Kermadec boundary in order to produce a strong east-west σ_{Hmax} orientation in the Cooper Basin stress province (Figure 8.1). The existence of E-W compression throughout SE Australia is further substantiated by several characteristics of the observed stress field that were not used as a modelling constraint, but nevertheless support these modelling results, including:

(1) A very weak east-west σ_{Hmax} orientation in the Flinders Ranges to the south of the Cooper Basin (Figure 7.2).

(2) A large number of east-west reverse focal mechanisms exist in southeastern Australian (Denham, 1980; Everingham and Smith, 1979; McCue *et al.*, 1990a).

(3) The Bowen Basin and Sydney Basin stress provinces on the eastern side of Australia also show reverse faulting condition from hydraulic fracturing and overcoring measurements (Chapters 4 and 5).

Current and also previous modelling results indicate that extensional forces associated with the subduction zone along the Tonga-Kermadec boundary would result in a north-south oriented σ_{Hmax}, which is at odds with the observations listed above.

8.5.2 Stress Provinces in the Western Half of Australia

The stress provinces in the western half of Australia include the Perth region, the Carnarvon Basin, the Canning Basin, the Amadeus Basin and the south and north Bonaparte Basins. The fit between the predicted and observed stress fields is excellent in all of these stress provinces with the exception of the Amadeus Basin. The stress data in the Amadeus Basin indicate an approximately north-south σ_{Hmax} orientation. However, the predicted σ_{Hmax} orientation from the best fitting model is northeast-southwest, which corresponds closely to the stress trajectories in the region (Figure 8.7). Hence, the misfit between the observed and predicted stress field in the Amadeus Basin is not seen as significant.

The fit achieved here for the western half of Australia is similar to that of previous studies (Cloetingh and Wortel, 1986; Coblentz *et al.*, 1995; Coblentz *et al.*, 1998). The modelling results herein are in agreement with the conclusions of these previous studies in that the stress field in the western half of Australia is controlled by the Himalayan and Papua New Guinea boundaries. When both of these boundaries are compressional, the stress field is focussed between the two boundaries, with σ_{Hmax} oriented east-west in extreme western Australia, rotating through a north-south orientation in central Australia, to a northeast-southwest orientation along the North West shelf. The fit between the predicted and observed stress fields is further improved in the western half of Australia by compression along the Banda boundary segment. This compression results in a more northerly σ_{Hmax} orientation in the northern Bonaparte Basin than that produced by compression along the Papua New Guinea and Himalayan boundaries alone. The results from modelling herein and previous studies suggest the stress field throughout the western half of Australia is controlled by large-scale tectonic forces. However, areas still exist where local stress rotations occur, such as those explained in Chapter 6 of this thesis.

8.5.3 Bowen Basin Stress Province

The observed stress field in the Bowen Basin is described in Chapter 4 and shows a consistent north-northeast trend over some 500 km that is believed to represent the first order stress field. Due to their proximity, the plate boundaries with the greatest influence on the stress field in the Bowen Basin are Papua New Guinea, Solomon, New Hebrides and Tonga-Kermadec. Current modelling results indicate that a good fit to the observed stress orientations in the Bowen Basin requires compression along both the Solomon and New Hebrides boundaries. Forces acting on the Solomon and New Hebrides boundaries display only small variation in magnitude within the top 100 models (Table 8.4). On average within the top 100 models, both the Solomon and New Hebrides boundaries exert a greater force than along either Papua New Guinea or the Tonga-Kermadec boundaries.

As previously mentioned, modelling herein requires a compressional force along the Tonga-Kermadec boundary. However, the magnitude of this compression is limited by the orientation of σ_{Hmax} in the Bowen Basin, which would be east-west in the case of a large compressive force acting along the Tonga-Kermadec Trench. Moreover, if the force on the Papua New Guinea boundary exceeds the force along the Solomon boundary, the predicted σ_{Hmax} orientation in the Bowen Basin would rotate in a northwest orientation. A small relative

change in the forces along the Papua New Guinea and Solomon boundaries results in a change in the predicted σ_{Hmax} orientation for the Bowen Basin. This observation suggests that the observed stress field in the Bowen Basin stress province plays a critical role in determining the relative force magnitude along the Papua New Guinea and Solomon boundaries.

An attempt was made to fit the observed stress field in the Bowen Basin without requiring a compressive force along the Solomon subduction zone. In this case, the applied force acting perpendicular to the Papua New Guinea plate boundary was rotated by 20° to the east to compensate for the lack of compression along the Solomon boundary. Nonetheless, even with this rotation the predicted stress field could not be made to match the observed stress field. It is therefore concluded that if the north-northeast σ_{Hmax} orientation in the Bowen Basin is a first order trend, then a compressive force must act along the Solomon subduction zone, which is contrary to the conclusion of the previous modelling studies (Cloetingh and Wortel, 1986; Coblentz *et al.*, 1995; Coblentz *et al.*, 1998).

8.5.4 Sydney Basin Stress Province

The observed stress field in the Sydney Basin is described in Chapter 5 and shows a poorly defined northeast-southwest trend, approximately parallel to the coastline. Due to the large degree of scatter in the data, the Sydney Basin was assigned a low weighting for constraining the predicted stress field. Closer examination of individual stress measurements within the Sydney Basin shows that σ_{Hmax} orientations vary from east-west in the western section of the basin to approimately north-south in the eastern section (Chapter 5). The high degree of scatter exhibited by the stress indicators in the Sydney Basin may be due to a larger influence by local sources of stress rather than by regional tectonic sources (Chapter 5). This suggestion is consistent with the fact that predicted stresses for eastern Australia are relatively isotropic. The difference between the two modelled horizontal stresses in eastern Australia ranges from 1-10 MPa (Figure 8.6). If the regional (plate boundary force related) horizontal stress anisotropy is low the orientation of σ_{Hmax} tends to be influenced by local sources of stress, such as topography, density heterogeneities and sediment loading on the continent margin (e.g. Zoback, 1992). Plate boundary forces acting along the Tonga-Kermadec, New Zealand and southern New Zealand boundary segments would be expected to exert the principal control on the stresses in the Sydney Basin due to their proximity. This assumption is supported by the results of the modelling which demonstrate that if the boundary forces acting along the Tonga-Kermadec Trench are dominant then an east-west oriented σ_{Hmax} in the

Sydney Basin results, while southeast-northwest oriented σ_{Hmax} is generated if the boundary forces acting along New Zealand are dominant. These results demonstrate that east-west σ_{Hmax} orientation in eastern Australia can be attributed to plate boundary forces and thus there is no need to appeal to other sources such as variation in the lithospheric density structure (e.g. Zhang *et al.*, 1996). It should be noted that the model predictions for the Sydney Basin stress field are relatively robust with a circular standard deviation of less than 8° for the top 100 models (Figure 8.5). Moreover, the stress trajectories in the vicinity of the Sydney Basin are consistent with the southeast-northwest predicted σ_{Hmax} orientation exhibited by the best fitting model (Figure 8.7).

8.5.5 Southeastern Australia Stress Provinces

The forces acting along the eastern plate boundaries, including the strike-slip collisional boundary at New Zealand and the boundary south of New Zealand, primarily control the stress field of southeastern Australia. The southeast-northwest orientation of σ_{Hmax} in the Otway and Gippsland Basins requires a force of approximately 1.4×10^{12} Nm^{-1} along the strike-slip collisional boundary in New Zealand, with a substantially greater force of approximately 3×10^{12} Nm^{-1} acting along the margin south of New Zealand. A trade-off exists between the amount of compression acting on the plate from the southeastern boundaries (New Zealand and south of New Zealand) with the compressional forces acting along the northern boundaries (Banda, Papua New Guinea, Solomon and New Hebrides). An increase in the force applied to the northern boundaries would require an increase in force along the southeastern boundaries to rotate the predicted stress field back towards the south. Hence, a balance between the northern and southeastern boundaries is required to adequately fit the entire observed stress field.

The boundary south of New Zealand, which consists of the Puysegur Trench and the Macquarie Ridge Complex (Sutherland, 1995) was required to exert a substantially greater force on the IAP than was initially expected. The total torque produced by this boundary on the IAP was approximately the same magnitude as the total torque produced by the Himalayan boundary (Table 8.4). A large force on the boundary south of New Zealand is supported by other geophysical data, with a number of studies proposing the area is experiencing regional deformation (DeMets *et al.*, 1988; Valenzuela and Wysession, 1993; Spitzak and DeMets, 1996). The southern Tasman Sea, an area to the west of the Macquarie Ridge Complex, appears to be undergoing significant regional deformation with diffuse

intraplate seismicity and the presence of three parallel southeast trending gravity undulations (Valenzuela and Wysession, 1993). The tectonics of the area has been likened to the internally deforming area of the Indian Ocean (Valenzuela and Wysession, 1993). Thus the large force predicted to be acting on the boundary south of New Zealand is tectonically plausible.

8.6 Conclusions

This study has found that the regional stress field of continental Australia, as characterised by 12 stress provinces, can be modelled using a combination of the principal tectonic forces acting on the plate. The modelled stress orientations are also consistent with information about the regional stress field from other sources such as the stress trajectory map. The new basis-set approach provides a method of evaluating a very large number of boundary force combinations and of quantitatively assessing the fit between the observed and predicted stress fields. In this study the regional stress field was better constrained than in previous studies by the inclusion of a substantial amount of new data particularly in central and eastern Australia. However, the study finds, as discussed in the previous investigations, that a number of different boundary force combinations can produce similar predicted stress fields and thus it is not possible to uniquely define the plate boundary forces acting on the IAP. Despite this limitation, results indicate the following key points:

1. Compressional forces act along the Himalaya and Papua New Guinea boundaries to produce stress focussing normal to those boundaries and stress rotation between them.
2. The observed stress field in the Bowen Basin requires compressional forces along the Solomon and New Hebrides subduction zones.
3. East-west compression in eastern Australia requires moderate compression acting along the Tonga-Kermadec subduction zone. The fit between the predicted and observed stress field degrades with the application of extensional force along this boundary.
4. Modelling stresses in southeastern Australian (specifically in the Otway and Gippsland Basin stress provinces) requires compressional forces along the New Zealand, Puysegur Trench and Macquarie Ridge boundary segments.
5. Extensional forces act along the Java subduction zone. The Australian stress field is not sensitive to the forces acting along the Sumatran boundary segment.

The orientation of the modelled stress field over most of Australia is robust for the top 100 models, with predicted stresses in northeastern and southern Australia the most sensitive to variations in the plate boundary force combination. The forces on each boundary that produce the best fitting model are consistent with predicted force magnitudes from other plates (Meijer and Wortel, 1992; Coblentz and Richardson, 1996; Gölke and Coblentz, 1996). While the magnitude of plate boundary forces remain poorly understood (with the exception of the "ridge push" force), the force magnitudes predicted by this modelling fall within the magnitude range of plate driving forces (e.g. Harper, 1974; Forsyth and Uyeda, 1975; England and Wortel, 1980; Bott *et al.*, 1989). Low tectonic stress magnitudes, between 20 MPa and 45 MPa (averaged over the thickness of the lithosphere) are predicted throughout the Australian continent by the top 100 models. Large sections of eastern Australia have an isotropic stress field resulting in the stress field being dominated by local sources of stress that cause the observed stress field to be highly variable (e.g. Sydney Basin).

Although the modelling results presented in this chapter provide a significant advancement in our understanding of the dynamics of the IAP, the potential exists for further modelling work. In particular, a more detailed exploration of the nature of the solution space about the best fitting force ensemble could provide valuable information in constraining the forces acting at the plate boundaries of the IAP. Also, more detailed modelling using a variable elastic plate thickness would provide valuable insight into the effect different geological and tectonic domains have on the *in situ* stress field (e.g. Zhao and Müller, under review). Further constrainment of the current modelling can be achieved by the addition of observed stress data, particularly in northeastern and central Australia.

Concluding Statement

The aims of this thesis, as stated in Chapter 1, were (1) to improve knowledge of the *in situ* stress field of the Bowen, Sydney and Perth Basin areas of Australia, (2) to evaluate and define the regional *in situ* stress field of continental Australia using the new *in situ* stress measurements presented for the Bowen, Sydney and Perth Basins in this thesis and the additional stress measurements available in the ASM database and (3) to use the regional *in situ* stress field to constrain new finite element models of the plate boundary and topographic forces acting on the IAP.

This thesis has indeed provided a significant advancement in our knowledge of the *in situ* stress field of the Bowen, Sydney and Perth Basins. Furthermore, the regional stress field of continental Australia has been defined using stress provinces and stress trajectory mapping and provides valuable additional constraints to the new finite element modelling of the plate boundary and topographic forces acting on the IAP. Modelling results indicate that the major features of the regional stress field in continental Australia can be explained in terms of a geologically plausible array of tectonic boundary and potential energy forces. This thesis employed the new, 'basis-set' approach to modelling the intraplate stress field of continental Australia, which has allowed an important advancement in the understanding of the dynamics of the IAP.

References

Aadnoy, B.S. and Bell, J.S., 1998. Classification of drill-induce fractures and their relationship to in-situ stress directions. *The Log Analyst*, **39,** 27-42.

Aamodt, L. and Kuriyagawa, M., 1983. Measurement of instantaneous shut-in pressure in crystalline rock, Proc. Hydraulic Fracturing Stress Measurements, Monterey. National Academy Press, 139-142.

Alder, J., Hawley, S., Mullard, B. and Shaw, R., 1998. Origin of the Sydney Basin: A new structural model. In: *Proceedings of the Thirty Second Newcastle Symposium on "Advances in the study of the Sydney Basin"*, 1-11. The University of Newcastle, Newcastle.

Aleksandroski, P., Inderhaug, O.H. and Knapstad, B., 1992. Tectonic structures and wellbore breakout orientation. In: *33rd US Symposium on Rock Mechanics*, 29-37. Santa Fe, Balkema, Rotterdam.

Allen, C.M. and Chappell, B.W., 1993. Contrasting Carboniferous-Permian and Cretaceous plutonism in the Urannah batholith, northern New England Fold Belt. In: *New England Orogen, eastern Australia*, 573-579. Proceedings of the 1993 Conference, University of New England, Armidale.

Amadei, B. and Stephansson, O., 1997. Rock Stress and its Measurement. Chapman & Hall, 490.

Anderson, E.M., 1951. The Dynamics of Faulting and Dike Formation With Application in Britian. Oliver and Boyd, Edinburgh.

Anderson, H., 1988. Comparison of centroid-moment tensor and first motion solutions for western Mediterranean earthquakes. *Physics of the Earth and Planetary Interiors*, **52,** 1-7.

Angelier, J., 1984. Tectonic analysis of fault slip data sets. *Journal of Geophysical Research*, **89,** 5835-5848.

Artyushkov, E.V., 1973. Stresses in the lithosphere caused by crustal thickness inhomogeneities. *Journal of Geophysical Research*, **78,** 7675-7708.

Ask, M.V.S., 1997. In situ stress from breakouts in the Danish Sector of the North Sea. *Marine and Petroleum Geology*, **14,** 0-13.

Assameur, D.M. and Mareschal, J-C., 1995. Stress induced by topography and crustal density heterogeneities: Implications for the seismicity of southeastern Canada. *Tectonophysics*, **241,** 179-192.

Babcock, E.A., 1978. Measurement of subsurface fractures from dipmeter logs. *AAPG Bulletin*, **62,** 1111-1126.

Baker, J.C., Fielding, C.R., Caritat, P.D. and Wilkinson, M.M., 1993. Permian evolution of sandstone composition in a complex back-arc extensional to foreland basin: the Bowen Basin, eastern Australia. *Journal of Sedimentary Petrology*, **63,** 881-893.

Barton, C.A., 2000. Discrimination of natural fractures from drilling-induced wellbore failures in wellbore image data - Implications for reservoir permeability. In: *SPE International Petroleum Conference and Exhibition*. Villahermosa.

Barton, C.A., Castillo, D.A., Moos, D., Peska, P. and Zoback, M.D., 1998. Characterising the full stress tensor based on observations of drilling-induced wellbore failures in vertical and inclined boreholes leading to improved wellbore stability and permeability prediction. *APPEA Journal*, 466-487.

Barton, C.A. and Zoback, M.D., 1994. Stress perturbations associated with active faults penetrated by boreholes: Possible evidence for near-complete stress drop and a new technique for stress magnitude measurement. *Journal of Geophysical Research*, **99,** 9373-9390.

Barton, C.A., Zoback, M.D. and Burns, K.L., 1988. In-situ stress orientation and magnitude at the Fenton geothermal site, New Mexico, determined from wellbore breakouts. *Geophysical Research Letters*, **15,** 467-470.

Bell, J.S., 1990. Investigating stress regimes in sedimentary basins using information from oil industry wireline logs and drilling records. In: Hurst, A., Lovell, M.A. and Morton, A.C. (Eds), Geological applications of Wireline Logs geological Society Special Publication No. 48, 305-325.

Bell, J.S., 1996. Petro Geoscience 1. In situ stresses in sedimentary rocks (part 1): measurement techniques. *Geoscience Canada*, **23,** 85-100.

Bell, J.S., Caillet, G. and Adams, J., 1992. Attempts to detect open fractures and non-sealing faults with dipmeter logs. In: Hurst, A., Griffiths, C.M. and Worthington, P.F. (Eds), Geological Applications of Wireline Logs II. Geological Society Special Publications, 211-220.

Bell, J.S. and Gough, D.I., 1979. Northeast-southwest compressive stress in Alberta - evidence from oil wells. *Earth and Planetary Science Letters*, **45,** 475-482.

Bemebrick, C., Herbert, C., Scheibner, E. and Stuntz, J., 1980. Structural subdivison of the Sydney Basin. In: Herbert, C. and Helby, R. (Eds), A Guide to the Sydney Basin, 2-9.

Bird, P. and Kong, X., 1994. Computer simulations of California tectonics confirm very low strength of major faults. *Geological Society of America Bulletin*, **106,** 159-174.

Bird, P. and Piper, K., 1980. Plane-stress finite-element models of tectonic flow in southern California. *Physics of the Earth and Planetary Interiors*, **21,** 158-175.

Bjarnason, B., Ljunggren, C. and Stephansson, O., 1989. New developments in hydrofracturing stress measurements at Luleå University of Technology. *International Journal of Rock Mechanics, Mining Science and Geomechanical Abstracts*, **26,** 579-586.

Blümling, P., Fuchs, K. and Schneider, T., 1983. Orientation of the stress field from borehole breakouts in a crystalline well in a seismic active area. *Physics of the Earth and Planetary Interiors*, **33,** 250-254.

Bott, M.H.P., 1959. The mechanics of oblique slip faulting. *Geological Magazine*, **46,** 109-117.

Bott, M.H.P., 1991. Ridge push and associated plate interior stress in normal and hot spot regions. *Tectonophysics*, **200,** 17-32.

Bott, M.H.P. and Dean, D.S., 1972. Stress systems at young continental margins. *Nature*, **235,** 23-25.

Bott, M.H.P., Waghorn, G.D. and Whittaker, A., 1989. Plate boundary forces at subduction zones and trench-arc compression. *Tectonophysics*, **170,** 1-15.

Bowman, F., 1958. Introduction to Bessel Functions. Dover Publications Inc., New York.

Branagan, D.F., Mills, K.J. and Norman, A.R., 1988. Sydney faults: Facts of fantasies. In: *Proceedings of the Twenty Second Newcastle Symposium on "Advances in the study of the Sydney Basin"*, 111-118. Newcastle.

Bredehoeft, J.D., Wolff, R.G., Keys, W.S. and Shuter, E., 1976. Hydraulic fracturing to determine the regional in situ stress field, Piceance Basin, Colorado. *Geological Society of America Bulletin*, **87,** 250-258.

Brudy, M. and Zoback, M.D., 1993. Compressive and tensile failure of borehole arbitrarily inclined to principal stress axes: Application to KTB boreholes, Germany. *International Journal of Rock Mechanics and Mining Sciences*, **30,** 1035-1038.

Brudy, M. and Zoback, M.D., 1999. Drilling-induced tensile wall-fractures: implications for determination of in-situ stress orientation and magnitude. *International Journal of Rock Mechanics and Minning Sciences*, **36,** 191-215.

Byerlee, J., 1978. Friction of rocks. *Pure and Applied Geophysics*, **116,** 615-626.

Carey, E. and Mercier, J.L., 1987. A numerical method for determining the state of stress using focal mechanisms of earthquake populations. Application to Tibetan teleseisms and microseismicity of Southern Peru. *Earth and Planetary Science Letters*, **82,** 165-179.

Caritat, P.D. and Braun, J., 1992. Cyclic development of sedimentary basins at convergent plate margins - 1. structural and tectono-thermal evolution of some Gondwana basins of eastern Australia. *Journal of Geodynamics*, **16,** 241-282.

Chinnery, M.A., 1964. The strength of the Earth's crust under horizontal shear stress. *Journal of Geophysical Research*, **69,** 2085-2089.

Cloetingh, S. and Wortel, R., 1985. Regional stress field of the Indian plate. *Geophysical Research Letters*, **12,** 77-80.

Cloetingh, S. and Wortel, R., 1986. Stress in the Indo-Australia plate. *Tectonophysics*, **132,** 49-67.

Coblentz, D.D. and Richardson, R.M., 1995. Statistical trends in the intraplate stress field. *Journal of Geophysical Research*, **100,** 20245-20255.

Coblentz, D.D. and Richardson, R.M., 1996. Analysis of the South American intraplate stress field. *Journal of Geophysical Research*, **101,** 8643-8657.

Coblentz, D.D., Richardson, R.M. and Sandiford, M., 1994. On the gravitational potential of the Earth's lithosphere. *Tectonics*, **13,** 929-945.

Coblentz, D.D. and Sandiford, M., 1994. Tectonic stresses in the African plate: Constraints on the ambient lithosphere stress state. *Geology*, **22,** 831-834.

Coblentz, D.D., Sandiford, M., Richardson, R.M., Zhou, S. and Hillis, R.R., 1995. The origins of the intraplate stress field in continental Australia. *Earth and Planetary Science Letters*, **133,** 299-309.

Coblentz, D.D., Zhou, S., Hillis, R.R., Richardson, R.M. and Sandiford, M., 1998. Topography, boundary forces, and the Indo-Australian intraplate stress field. *Journal of Geophysical Research*, **103,** 919-931.

Conolly, J.R., 1969. Western Tasman sea floor. *New Zealand Journal of Geology and Geophysics*, **12,** 310-343.

Cox, J.W., 1970. The high resolution dipmeter reveals dip-related borehole and formation characteristics. In: *11th Annual Logging Symposium Transactions: Society of Professional Well Log Analysts*, 26. Los Angeles, California.

Dart, C.J., Inderhaug, O.H., Klovjan, O. and Ottesen, C., 1995. The present day stress regime in the barents sea from borehole breakout. *Workshop on Rock Stresses in the North Sea, Trondheim, Norway*, 179-190.

Dart, R.L. and Zoback, M.L., 1989. Wellbore breakout stress analysis within the Central and Eastern Continental United States. *The Log Analyst*, **30,** 12-25.

Davis, J.C., 1986. Statistics and Data Analysis in Geology. John Wiley, New York, 646.

de Bree, P. and Walters, J.V., 1989. Micro/Minifrac test procedures and interpretation for in situ stress determination. *International Journal of Rock Mechanics, Mineral Science and Geomechanical Abstracts*, **26,** 515-521.

DeMets, C., Gordon, R.G. and Argus, D.F., 1988. Intraplate deformation and closure of the Australia-Antarctica-Africa plate circuit. *Journal of Geophysical Research*, **93,** 11877-11897.

Denham, D., Alexander, L.G. and Worotnicki, G., 1979. Stresses in the Australian crust; evidence from earthquake and in-situ stress measurements. *BMR Journal of Australian Geology and Geophysics*, **4,** 289-295.

Denham, D., 1980. The 1961 Robertson earthquake - more evidence for compressive stress in southeast Australia. *BMR Journal of Australian Geology and Geophysics*, **5,** 153-156.

Dentith, M.C., Long, A., Scott, J., Harris, L.B. and Wilde, S.A., 1994. The influence of basement on faulting within the Perth Basin, Western Australia. In: *The Sedimentary Basins of Western Australia: Proceedings of Petroleum Exploration Society of Australia Symposium*, 791-799. Perth, Western Australia.

Desroches, J. and Kurkjian, A.L., 1998. Applications of Wireline Stress Measurements. In: *SPE Annual Technical Conference and Exhibition*. New Orleans, Louisiana.

Detournay, E. and Roegiers, J.C., 1986. Comment on "Wellbore breakouts and in situ stress" by M. D. Zoback, D. Moos, L. Mastin, R. N. Anderson. *Journal of Geophysical Research*, **91,** 14161-14162.

Dziewonski, A.M., Chou, T.A. and Woodhouse, J.H., 1981. Determination of earthquake source parameters from waveform data for studies of global and regional seismicity. *Journal of Geophysical Research*, **86,** 2825-2852.

Ekstrom, M.P., Dahan, C.A., Chen, M.Y., Lloyd, P.M. and Rossi, D.J., 1987. Formation imaging with microelectrical scanning arrays. *Log Analyst*, **28,** 294-306.

Elliott, L., 1989. The Surat and Bowen Basins. *The APEA Jounal*, **29,** 398-416.

Elliott, L.G., 1993. Post-Carboniferous tectonic evolution of eastern Australia. *The APEA Journal*, **33,** 215-236.

Ellis, G.K. and Bruce, R.H., 1998. Dongara oil and gas field, Perth Basin. In: *The Sedimentary Basins of Western Australia 2: Proceedings of Petroleum Exploration Society of Australia Symposium*, 625-635. Perth, Western Australia.

Enever, J., 1999. The contemporary stress field in the Newcastle coal measures. In: *Proceedings of the Thirty Third Newcastle Symposium on "Advances in the study of the Sydney Basin"*, 1-8. The University of Newcastle, Newcastle.

Enever, J.R., 1993. Case studies of hydraulic fracture stress measurement in Australia. In: Hudson, J.A. (Ed), Comprehensive Rock Engineering, Rock Testing and Site Characterization. *Comprehensive rock engineering : principles, practice, and projects*. Pergamon Press, 497-532.

Enever, J.R. and Chopra, P.N., 1986. Experience with hydraulic fracture stress measurements in granites, Proceedings of the International Symposium on Rock Stress and Rock Stress Measurements. Centek Publications, 411-420.

Enever, J.R. and Clark, I., 1997. The current stress state in the Sydney Basin. In: *Proceedings of the Thirty First Newcastle Symposium on "Advances in the Study of the Sydney Basin"*, 91-98. Newcastle, Australia.

Enever, J.R., Glen, R.A. and Beckett, J., 1998. The stress field and structural environment of the Hunter Valley, Geotechnical Engineering and Engineering Geology in the Hunter Valley.

Enever, J.R., Mallet, C. and Lohe, E., 1989. Summary of the in-situ stress state derived from the direct stress measurements in the Sydney Basin, and the relationship to major structures. In: *Proceedings of the Newcastle Symposium on "Advances in the Study of the Sydney Basin"*, 157-161. Newcastle, Australia.

Enever, J.R. and Walton, R.J., 1995. Assessment of ground stresses. In: Krzyszton, D. (Ed), Geomechanical Criteria for Underground Coal Mines Design. International Bureau of Strata Mechanics, 7-34.

Engelder, T., 1981. General characteristics of strain relaxation: A note on sample preparation for large-scale tests. *Geophysical Research Letters*, **8,** 687-689.

Engelder, T., 1993. Stress Regimes in the Lithosphere. Princeton University Press, New Jersey, 457.

Engelder, T. and Sbar, M.L., 1984. Near-surface in situ stress: Introduction. *Journal of Geophysical Research*, **89,** 9321-9322.

England, P. and Wortel, R., 1980. Some consequences of the subduction of young slabs. *Earth and Planetary Science Letters*, **47,** 403-415.

Everingham, I.B. and Smith, R.S., 1979. Implications of fault-plane solutions for Australian earthquakes on 4 July 1977, 6 May 1978 and 25 November 1978. *BMR Journal of Australian Geology and Geophysics*, **4,** 297-301.

Fielding, C.R., Gray, A.R.G., Harris, G.I. and Salomon, J.A., 1990. The Bowen Basin and overlying Surat Basin. In: Finlayson, D.M. (Ed), The Eromanga-Brisbane Geoscience Transect: a guide to basin development across Phanerozoic Australia in southern

Queensland. Bureau of Mineral Resources, Geology and Geophysics, Australia, Bulletin, 105-116.

Fielding, C.R., Kassan, J. and Craper, J.J., 1996. Geology of the Bowen and Surat Basins, Eastern Queensland, Australasian Sedimentologists Group Field Guide Series No. 8. Geological Society of Australia, Sydney.

Fjær, E., Holt, R.M., Horsrud, P., Raaen, A.R. and Risnes, R., 1992. Petroleum Related Rock Mechanics. In: Chilingarian, G.V. (Ed), Developments in Petroleum Science. Elsevier, Amsterdam, 338.

Fleitout, L. and Froidevaux, C., 1982. Tectonics and topography for a lithosphere containing density heterogeneities. *Tectonics*, **1,** 21-56.

Fordjor, C.K., Bell, J.S. and Gough, D.I., 1983. Breakouts in Alberta and stress in the North American plate. *Canadian Journal of Earth Science*, **20,** 1445-1455.

Forsyth, D. and Uyeda, S., 1975. On the relative importance of the driving forces of plate motion. *The Geophysical Journal of the Royal Astronomical Society*, **43,** 163-200.

Gaina, C., Muller, D.R., Royer, J.-Y., Stock, J., Hardebeck, J. and Symonds, P., 1998. The tectonic history of the Tasman Sea: A puzzle with 13 pieces. *Journal of Geophysical Research*, **103,** 12413-12433.

Gallagher, K., 1990. Permian to Cretaceous subsidence history along the Eromanga-Brisbane Geoscience Transect. In: Finlayson, D.M. (Ed), The Eromanga-Brisbane Geoscience Transect: a guide to basin development across Phanerozoic Australia in southern Queensland. Bureau of Mineral Resources, Geology and Geophysics, Australia, Bulletin, 133-151.

Gephart, J.W. and Forsyth, D., 1984. An improved method for determining the regional stress tensor using earthquake focal mechanism data: Application to the San Fernando earthquake sequence. *Journal of Geophysical Research*, **89,** 9305-9320.

Gölke, M. and Brudy, M., 1996. Orientation of crustal stresses in the North Sea and Barents Sea inferred from borehole breakouts. *Tectonophysics*, **266,** 25-32.

Gölke, M. and Coblentz, D., 1996. Origins of the European regional stress field. *Tectonophysics*, **266,** 11-24.

Gough, D.I. and Bell, J.S., 1982. Stress orientations from borehole wall fractures with examples from Colorado, east Texas, and northern Canada. *Canadian Journal of Earth Sciences*, **19,** 1358-1370.

Gronseth, J.M. and Kry, P.R., 1983. Instantaneous shut-in pressure and its relationship to the minimum in-situ stress, Proc. Hydraulic Fracturing Stress Measurements, Monterey. National Academy Press, 55-60.

Gust, D.A., Stephens, C.J. and Grenfell, A.T., 1993. Granitoids of the northern New England Orogen: their distribution in time and space and their tectonic implications. In: *New England Orogen, eastern Australia*, 565-571. Proceedings of the 1993 Conference, University of New England, Armidale.

Haimson, B. and Fairhurst, C., 1967. Initiation and extension of hydraulic fractures in rocks. *Society of Petroleum Engineers Journal*, 310-318.

Haimson, B.C., 1968. Hydraulic fracturing in porous and nonporous rock and it potential for determining in-situ stress at great depth. PhD Thesis, University of Minnesota.

Haimson, B.C., 1978a. The hydrofracturing stress measuring method and recent field results. *International Journal of Rock Mechanics, Mining Science and Geomechanical Abstracts*, **15,** 167-178.

Haimson, B.C., 1978b. Near-surface and deep hydrofracturing stress measurements in the Waterloo Quartzite. In: *Proceedings of the U.S. Symposium on Rock Mechanics, 19th*, 345-361.

Haimson, B.C., 1980. Near-surface and deep hyrofracturing stress measurements in the Waterloo quartzite. *International Journal of Rock Mechanics, Mining Science and Geomechanical Abstracts*, **17,** 81-88.

Haimson, B.C., 1993. The hydraulic fracturing method of stress measurement: theory and practice. In: Hudson, J.A. (Ed), Comprehensive Rock Engineering: Principles, Practice and Projects. *Comprehensive Rock Engineering: Principles, Practice and Projects.* Pergamon Press, 395-412.

Hansen, K.M. and Mount, V.S., 1990. Smoothing and extrapolation of crustal stress orientation measurements. *Journal of Geophysical Research*, **95,** 1155-1165.

Hardy, M.P., 1973. Fracture mechanics applied to rock. PhD Thesis, University of Minnesota.

Harper, J.F., 1974. On the driving forces of plate tectonics. *The Geophysical Journal of the Royal Astronomical Society*, **40,** 465-474.

Harris, L.B., 1994. Structural and tectonic synthesis for the Perth Basin, Western Australia. *Journal of Petroleum Geology*, **17,** 129-156.

Herbert, C., 1980. Depositional Development of the Sydney Basin. In: Herbert, C. and Helby, R. (Eds), A Guide to the Sydney Basin. New South Wales Geological Survey - Bulletin No.26, 11-52.

Hickman, S.H., Healy, J.H. and Zoback, M.D., 1985. In situ stress, natural fracture distribution, and borehole elongation in the Aurburn geothermal well, Auburn, New York. *Journal of Geophysical Research*, **90,** 5497-5512.

Hillis, R., 1991. Australia-Banda Arc collision and in situ stress in the Vulcan Sub-basin (Timor Sea) as revealed by borehole breakout data. *Exploration Geophysics*, **22,** 189-194.

Hillis, R.R., Enever, J.R. and Reynolds, S.D., 1999. In situ field of eastern Australia. *Australian Journal of Earth Sciences*, **46,** 813-825.

Hillis, R.R., Meyer, J.J. and Reynolds, S.D., 1998. The Australian stress map. *Exploration Geophysics*, **29,** 420-427.

Hillis, R.R., Mildren, S.D., Pigram, C.J. and Willoughby, D.R., 1997. Rotation of horizontal stresses in the Australian North West continental shelf due to the collision of the Indo-Australian and Eurasian Plates. *Tectonics*, **16,** 323-335.

Hillis, R.R. and Reynolds, S.D., 2000. The Australian Stress Map. *Journal of the Geological Society, London*, **157,** 915-921.

Homberg, C., Hu, J.C., Angelier, J., Bergerat, F. and Lacombe, O., 1997. Characterization of stress pertubations near fault zones: insights from 2-D distinct-element numerical modelling and field studies (Jura mountains). *Journal of Structural Geology*, **19,** 703-718.

Hubbert, M.K. and Rubey, W.W., 1959. Role of fluid pressure in mechanics of overthrust faulting. *Bulletin of the Geological Society of America*, **70,** 115-166.

Hubbert, M.K. and Willis, D.G., 1957. Mechanics of hydraulic fracturing. *AIME Petroleum Transactions*, **210,** 153-166.

Isacks, B.L. and Molnar, P., 1971. Distribution of stresses in the decending lithosphere from a global survey of focal-mechanism solutions of mantle earthquakes. *Reviews of Geophysics and Space Physics*, **9,** 103-174.

Jaeger, J.C., 1962. Elasticity, Fracture and Flow. Wiley, London, 212.

Jaeger, J.C. and Cook, N.G.W., 1979. Fundamentals of rock mechanics. Chapman and Hall, London, United Kingdom, 593.

Jones, C. and Sargeant, J.P., 1993. Obtaining the minimum horizontal stress from microfracture test data: A new approach using a derivative algorithm. *Society of Petroleum Engineers Production & Facilities*, February, 39-44.

Kasahara, K., 1981. Earthquake Mechanics. Cambridge University Press, Cambridge.

Kim, K. and Franklin, J.A., 1987. Suggested methods for rock stress determination. *International Journal of Rock Mechanics, Mining Science and Geomechanical Abstracts*, **24,** 53-73.

Kirby, S.H., 1983. Rheology of the lithosphere. *Reviews of Geophysics and Space Physics*, **21,** 1458-1487.

Kirsch, G., 1898. Die Theorie der Elastizitat und die Beaurforisse der Festigkeitslehre. *Zeitschrift des Vereines Deutscher Ingenieure*, **42,** 797-807.

Kong, X. and Bird, P., 1995. SHELLS: A thin-shell program for modeling neotectonics of regional or global lithosphere with faults. *Journal of Geophysical Research*, **100,** 22129-22131.

Korsch, R.J. and Totterdell, J.M., 1995. Structural events and deformation styles in the Bowen Basin. In: *Bowen Basin Symposium*, 27-35.

Leach, J.H.J., Mallett, C.W. and Hobbs, B.E., 1986. Structure of the Bowen Basin, Queensland, Australia. In: Berkman, D.A. (Ed), 13th CMMI Congress Geology and Exploration, 73-78.

Lee, J. and Angelier, J., 1994. Paleostress trajectory maps based on the results of local determinations: The "Lissage" program. *Computers and Geoscience*, **20,** 161-191.

Lee, M.Y. and Haimson, B.C., 1989. Statistical evaluation of hydraulic fracturing stress measurement parameters. *International Journal of Rock Mechanics, Mineral Science and Geomechanical Abstracts*, **26,** 447-456.

Lister, C.R., 1975. Gravitational drive on oceanic plates caused by thermal contraction. *Nature*, **257,** 663-665.

Lohe, E.M. and McLennan, T.P.T., 1989. Structural setting of Hunter Valley coalmines - A regional review. In: *Proceedings of the Twenty Third Newcastle Symposium on "Advances in the study of the Sydney Basin"*, 21-27. Newcastle.

Lohe, E.M. and McLennan, T.P.T., 1991. An overview of the structural fabrics of the Sydney Basin, and a comparison with the Bowen Basin. In: *Proceedings of the Twenty Fifth Newcastle Symposium on "Advances in the study of the Sydney Basin"*, 12-21. Newcastle.

Mallet, C.W., Hammond, R.L. and Sullivan, T.D., 1988. The implications for the Sydney Basin of upper crustal extension in the Bowen Basin. In: *Advances in the Study of the Sydney Basin, 22nd Newcastle Symposium*, 1-8. Newcastle.

Mardia, K.V., 1972. Statistics of Directional Data. Academic Press, New York.

Mareschal, J.C. and Kuang, J., 1986. Intraplate stresses and seismicity: the role of topography and density heterogeneities. *Tectonophysics*, **132,** 153-162.

Mastin, L., 1988. Effect of borehole deviation on breakout orientations. *Journal of Geophysical Research*, **93,** 9187-9195.

Mayne, S.J., Nicholas, E., Bigg-Wither, A.L., Raside, J.S. and Raine, M.J., 1974. Geology of the Sydney Basin - A review, Australian Bureau of Mineral Resources Geology and Geophysics Bulletin, 229.

McCue, K., Gibson, G. and Wesson, V., 1990a. The earthquake near Nhill, western Victoria, on 22 December 1987 and the seismicity of eastern Australia. *BMR Journal of Australian Geology and Geophysics*, **11,** 415-420.

McCue, K., Kennett, B.L.N., Gaull, B.A., Michael-Leiba, M.O., Weekes, J. and Krayshek, C., 1989. A century of earthquakes in the Dalton-Gunning region of New South Wales. *BMR Journal of Australian Geology and Geophysics*, **11,** 1-9.

McCue, K., Wesson, V. and Gibson, G., 1990b. The Newcastle, New South Wales, earthquake of 28 December 1989. *BMR Journal of Australian Geology and Geophysics*, **11,** 559-567.

McGarr, A., 1988. On the state of lithospheric stress in the absence of applied tectonic forces. *Journal of Geophysical Research*, **93,** 13,609-13,617.

McGarr, A. and Gay, N.C., 1978. State of stress in the Earth's crust. *Annual Review of Earth and Planetary Sciences*, **6,** 405-436.

McKenzie, D.P., 1969a. The relation between fault plane solutions for earthquakes and the directions of the principal stresses. *Bulletin of the Seismological Society of America*, **59,** 591-601.

McKenzie, D.P., 1969b. Speculations on the consequences and causes of plate motions. *Geophysical Journal of the Royal Astronomical Society*, **18,** 1-32.

Meijer, P.T., Govers, R. and Wortel, M.J.R., 1997. Forces controlling the present-day state of stress in the Andes. *Earth and Planetary Science Letters*, **148,** 157-170.

Meijer, P.T. and Wortel, M.J.R., 1992. The dynamics of motion of the South American plate. *Journal of Geophysical Research*, **97,** 11,915-11,931.

Michael, A.J., 1987. Use of focal mechanisms to determine stress: A control study. *Journal of Geophysical Research*, **92,** 357-368.

Mildren, S.D. and Hillis, R.R., 2000. In situ stresses in the southern Bonaparte Basin, Australia: Implications for first- and second-order controls on stress orientation. *Geophysical Research Letters*, **27,** 3413-3416.

Moos, D. and Zoback, M.D., 1990. Utilization of Observations of Well Bore Failure to Constrain the Orientation and Magnitude of Crustal Stresses: Application to Continental, Deep Sea Drilling Project and Ocean Drilling Program Boreholes. *Journal of Geophysical Research*, **95,** 9305-9325.

Müller, B., Reinecker, J. and Fuchs, K., 1997. The 1997 release of the World Stress Map. Heidelberg Academy of Science and Humanities, University of Karlsruhe/International Lithosphere Program (available online at www.world-stress-map.org). .

Müller, B., Reinecker, J. and Fuchs, K., 2000. The 2000 release of the World Stress Map. Heidelberg Academy of Science and Humanities, University of Karlsruhe/International Lithosphere Program (available online at www.world-stress-map.org). .

Murray, C.G., 1990. Tectonic evolution and metallogenesis of the Bowen Basin. In: *Proceedings of Bowen Basin Symposium*, 201-212. Mackay, Queensland.

Parsons, B. and Richter, F.M., 1980. A relation between driving force and geoid anomaly associated with the mid-ocean ridges. *Earth and Planetary Science Letters*, **51,** 445-450.

Peltzer, G. and Saucier, F., 1996. Present-day kinematics of Asia derived from geologic slip rates. *Journal of Geophysical Research*, **101,** 27943-2756

Peska, P. and Zoback, M.D., 1995. Compressive and tensile failure of inclined well bores and determination of in situ and rock strength. .

Playford, P.E., Cockbain, A.E. and Low, G.H., 1976. Geology of the Perth Basin, Western Australia. *Geological Survey of Western Australia Bulletin*, **124**.

Plumb, R.A. and Cox, J.W., 1987. Stress directions in eastern North America determined to 4.5 km from borehole elongation measurements. *Journal of Geophysical Research*, **92,** 4805-4816.

Plumb, R.A. and Hickman, S.H., 1985. Stress-induced borehole elongation: A comparison between the Four-Arm Dipmeter and the Borehole Televiewer in the Auburn Geothermal Well. *Journal of Geophysical Research*, **90,** 5513-5521.

Prensky, S., 1992. Borehole breakouts and in-situ rock stress - A review. *The Log Analyst*, **33,** 304-312.

Rebai, S., Philip, H. and Taboada, A., 1992. Modern tectonic stress field in the Mediterranean region: evidence for variation in stress directions at different scales. *Geophysical Journal International*, **110,** 106-140.

Reynolds, S.D. and Hillis, R.R., 2000. The in situ stress field of the Perth Basin, Australia. *Geophysical Research Letters*, **27,** 3421-3424.

Richardson, R.M., 1992. Ridge forces, absolute plate motions, and the intraplate stress field. *Journal of Geophysical Research*, **97,** 11739-11748.

Richardson, R.M. and Reding, L.M., 1991. North American plate dynamics. *Journal of Geophysical Research*, **96,** 12201-12223.

Richardson, R.M., Solomon, S.C. and Sleep, N.H., 1979. Tectonic stress in the plates. *Reviews of Geophysics and Space Physics*, **17,** 981-1019.

Ringis, J., 1972. The structure and history of the Tasman Sea and southeast Australian margin. Ph.D. Thesis, University of N.S.W., 338.

Rivera, L. and Cisternas, A., 1990. Stress tensor and fault plane solutions for population of earthquakes. *Bulletin of the Seismological Society of America*, **80,** 600-614.

Saucier, F., Humphreys, E. and II, R.W., 1992. Stress near geometrically complex strike-slip faults: Application to the San Andreas Fault at Cajon Pass, Southern California. *Journal of Geophysical Research*, **97,** 5081-5094.

Sbar, M.L., 1982. Delineation and interpretation of seismotectonic domains in western North America. *Journal of Geophysical Research*, **87,** 3919-3928.

Sbar, M.L., Armbruster, J. and Aggarwal, Y.P., 1972. The Adirondack, New York, earthquake swarm of 1971 and tectonic implications. *Seismological Society of America Bulletin*, **62,** 1303-1318.

Sbar, M.L. and Sykes, L.R., 1973. Contemporary compressive stress and seismicity in eastern North America: An example of intra-plate tectonics. *Geological Society of America Bulletin*, **80,** 1231-1264.

Scheibner, E., 1993. Structural framework of New South Wales. *Geological Survey of New South Wales, Quaterly Notes*, **93,** 1-36.

Shepherd, J. and Huntington, J.F., 1981. Geological fracture mapping in coalfields and the stress fields of the Sydney Basin. *Journal of the Geological Society of Australia*, **28,** 299-309.

Solomon, S.C. and Sleep, N.H., 1974. Some simple physical models for absolute plate motions. *Journal of Geophysical Research*, **79,** 2557-2567.

Solomon, S.C., Sleep, N.H. and Richardson, R.M., 1975. On the forces driving plate tectonics: inferences from absolute plate velocities and intraplate stresses. *The Geophysical Journal of the Royal Astronomical Society*, **42,** 769-801.

Sonder, L.J., 1990. Effects of density contrasts on the orientation of stresses in the lithosphere: relation to principal stress direction in the Transverse Ranges, California. *Tectonics*, **9,** 761-771.

Spassov, E. and Kennett, B.L.N., 2000. Stress and faulting in southeast Australia as derived from the strongest earthquakes in the region. *Journal of Asian Earth Sciences*, **18,** 17-23.

Spitzak, S. and DeMets, C., 1996. Constraints on present-day motions south of 30°S from satellite altimetry. *Tectonophysics*, **253,** 167-208.

Stefanick, M. and Jurdy, D.M., 1992. Stress observations and driving force models for the South American plate. *Journal of Geophysical Research*, **97,** 11905-11913.

Stein, S.S., Cloetingh, S., Sleep, N.H. and Wortel, R., 1989. Passive margin earthquakes, stresses and rheology. In: Gregersen, S. and Basham, P. (Eds), Earthquakes at North Atlantic Passive Margins: Neotectonics and Postglacial Rebound, NATO ASI Series C. Kluwer Academic, 231-259.

Sullivan, P.B., Coyle, D.A., Gleadow, A.J. and Kohn, B.P., 1995. Late Mesozoic to Early Cenozoic thermotectonic history of the Sydney Basin and the eastern Lachlan Fold Belt, Australia. In: *Mesozoic Geology of the Eastern Australia Plate Conference*, 424-432. Brisbane.

Sutherland, R., 1995. The Australia-Pacific boundary and Cenozoic plate motions in the SW Pacific: Some constraints from Geosat data. *Tectonics*, **14,** 819-831.

Terzaghi, K., 1943. Theoretical Soil Mechanics. John Wiley and Sons, New York, 51.

Turcotte, D.L. and Schubert, G.C., 1971. Structure of the olivine-spinel phase boundary in the descending lithosphere. *Journal of Geophysical Research*, 7980-7987.

Turnbridge, L.W., 1989. Interpretation of the shut-in pressure from the rate of pressure decay. *International Journal of Rock Mechanics, Mineral Science and Geomechanical Abstracts*, **26,** 457-459.

Valenzuela, R.W. and Wysession, M.E., 1993. Intraplate earthquakes in the southwest Pacific Ocean Basin and the seismotectonics of the southern Tasman Sea. *Geophysical Research Letters*, **20,** 2467-2470.

Veevers, J.J. and Powell, C.M., 1994. Permian-Triassic Pangean Basins and Foldbelts along the Panthalassan Margin of Gondwanaland, Memoir 184, Geological Society of America.

Vernik, L. and Zoback, M.D., 1992. Estimation of maximum horizontal principal magnitude from stress-induced well bore breakouts in the Cajon Pass Scientific Research Borehole. *Journal of Geophysical Research*, **97,** 5109-5119.

Wiley, R., 1981. The borehole televiewers: An update on application, World Oil, 47-53.

Woodland, D.C. and Bell, J.S., 1989. In situ stress magnitudes from mini-frac records in western Canada. *The Journal of Canadian Petroleum Technology*, **28,** 22-31.

Wright, C.A., Weijers, L., Minner, W.A. and Snow, D.M., 1996. Robust technique for real-time closure stress determination. *Society of Petroleum Engineers Production & Facilities*, 150-155.

Wyss, M. and Brune, J.N., 1968. Seismic moment, stress, and source dimensions for earthquakes in the California-Nevada region. *Journal of Geophysical Research*, **73,** 4681-4694.

Zajac, B.J. and Stock, J.M., 1997. Using borehole breakouts to constrain the complete stress tensor: Results from the Sijan Deep Drilling Project and offshore Santa Maria Basin, California. *Journal of Geophysical Research*, **102,** 10083-10100.

Zhang, Y., Scheibner, E., Ord, A. and Hobbs, B.E., 1996. Numerical modelling of crustal stresses in the eastern Australian passive margin. *Australian Journal of Earth Sciences*, **43,** 161-175.

Zhao, S and Müller, R.D., under review. Three-dimensional finite element modelling of the tectonic stress field in continental Australia. The Evolution and Dynamics of the Australian Plate, *Special Publication of the Geological Society of Australia and the Geological Society of America.*

Ziolkowski, V. and Taylor, R., 1985. Regional structure of the north Denison Trough. *Geological Society of Australia Abstracts*, **17,** 129-135.

Zoback, M.D. and Healy, J., 1984. Friction, faulting and in situ stress. *Annales Geophysicae*, **2,** 689-698.

Zoback, M.D. and Healy, J.H., 1992. In situ stress measurements to 3.5 km depth in the Cajon Pass Scientific Research Borehole: Implications for the mechanics of crustal faulting. *Journal of Geophysical Research*, **97,** 5039-5057.

Zoback, M.D., Moos, D., Mastin, L. and Anderson, R.N., 1985. Well bore breakouts and in situ stress. *Journal of Geophysical Research*, **90,** 5523-5530.

Zoback, M.D. and Zoback, M.L., 1991. Tectonic stress field of North America and relative plate motion. In: Slemmons, D.B., Engdahl, E.R., Zoback, M.D. and Blackwell, D.D. (Eds), Neotectonics of North America. Geological Society of America, 339-366.

Zoback, M.L., 1992. First- and second-order patterns of stress in the lithosphere: The world stress map project. *Journal of Geophysical Research*, **97,** 11703-11728.

Zoback, M.L. and Magee, M., 1991. Stress magnitudes in the crust: Constraints from stress orientation and relative magnitude data. *Philosophical Transactions of the Royal Society of London, Series A: Mathematical and Physical Sciences*, **337,** 181-194.

Zoback, M.L. and Zoback, M.D., 1980. Sate of stress in the conterminous United States. *Journal of Geophysical Research*, **85,** 6113-6156.

Zoback, M.L., Zoback, M.D., Adams, J., Assumpcao, M., Bell, S., Bergman, E.A., Blumling, P., Bereton, N.R., Denham, D., Ding, J., Fuchs, K., Gay, N., Gregersen, S., Gupta, H.K., Gvishiani, A., Jacob, K., Klein, R., Knoll, P., Magee, M., Mercier, J.L., Muller, B.C., Paquin, C., Rajendran, K., Stephansson, O., Suarez, G., Suter, M., Udias, A., Xu, Z.H. and Zhizhin, M., 1989. Global patterns of tectonic stress. *Nature*, **341,** 291-298.

Appendix A

Australian Stress Map Web Site

The current ASM web site has been designed and created by the author of this thesis. The front page of the current ASM web site is shown in Figure A.1. The entire web site is located on the accompanying CDROM under the directory labelled 'web page'. The latest update of the ASM web site is located at http://www.ncpgg.adelaide.edu.au/asm.

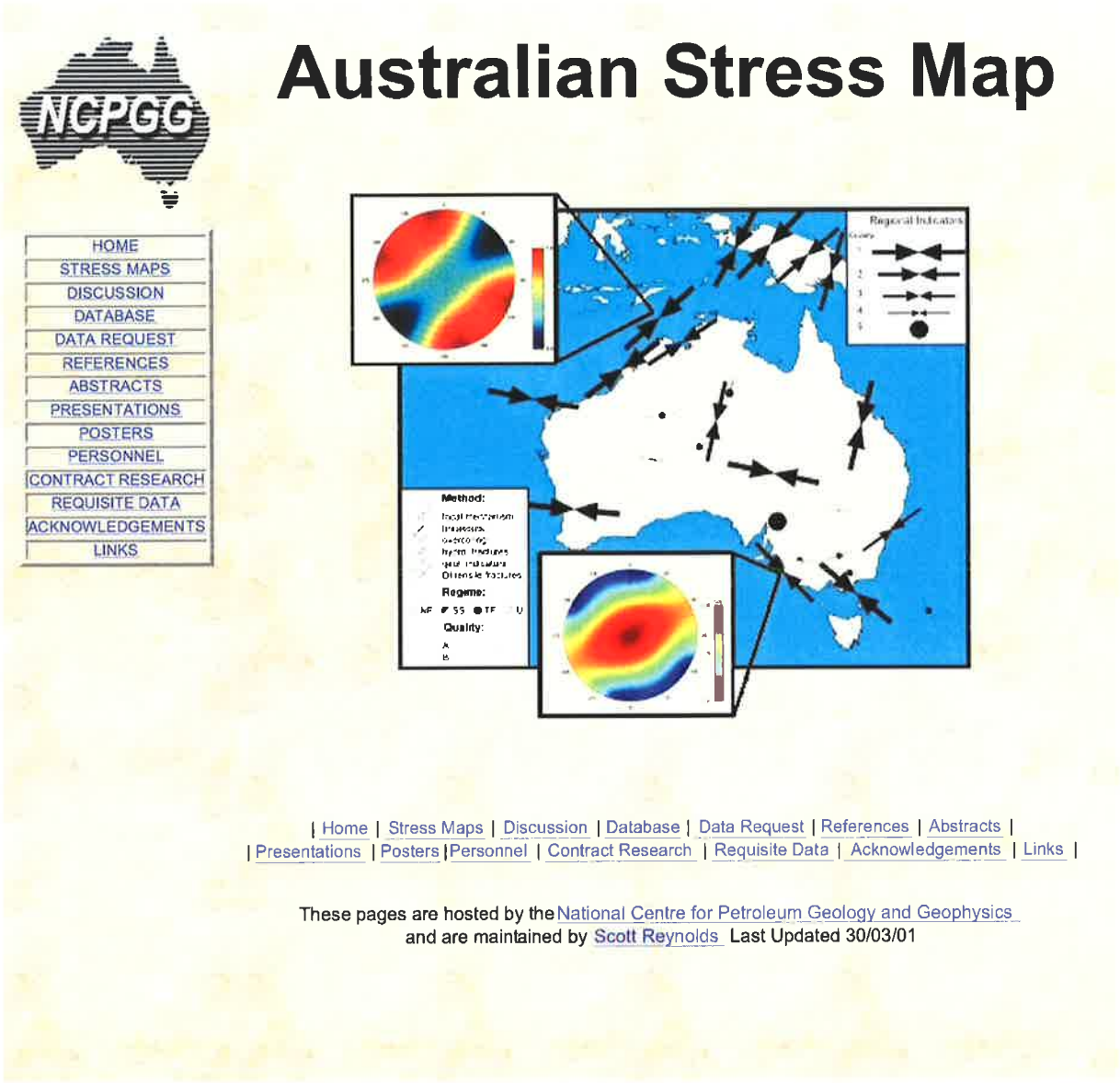

Figure A.1 Front page of the current ASM web site (http://www.ncpgg.adelaide.edu.au/asm).

Appendix B

Mohr-Coulomb Analysis

This appendix explores 3D Mohr's circles of stress as discussed in stress and rock failure (Section 2.3) and the procedure for the Mohr-Coulomb analysis used in Chapters 4 and 5 of this thesis. The procedure has been adapted from Jaeger and Cook (1979).

Three-Dimensional Mohr Circles

The state of stress at any point can be represent on a 3D Mohr circle diagram (Figure B.1). A Mohr diagram plots normal stress versus shear stress. Three semi-circles span between the three principal stresses that are located along the normal stress axis (Figure B.1). The shaded area in Figure B.1 indicates the shear and normal stresses acting on all arbitrary plane in the particular stress field. The next section explains the computations used to calculate the shear and normal stresses on an arbitrary plane from the dip and strike of the plane.

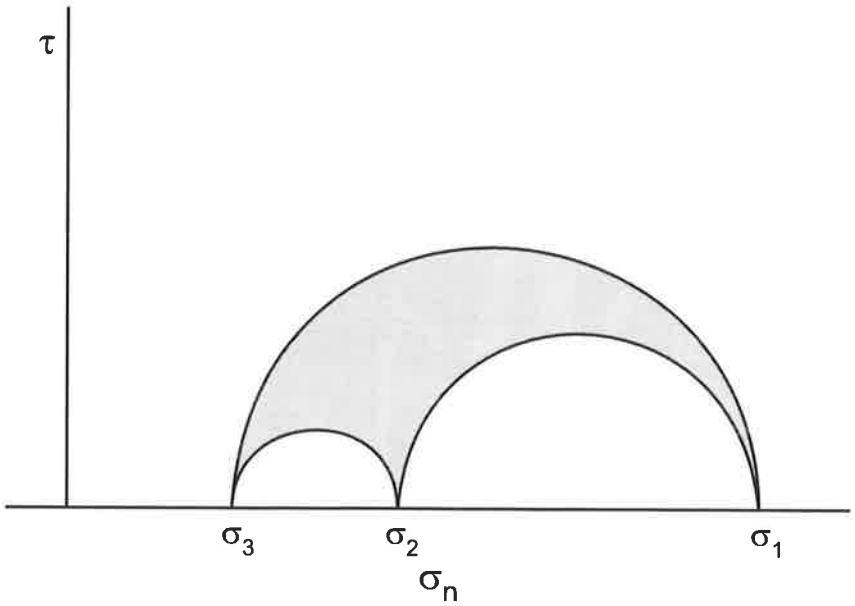

Figure B.1 Three-dimensional Mohr circle of stress.

Shear and Normal Stresses on an Arbitrary Plane

For a plane with dip α and strike β, relative to the maximum horizontal stress orientation, the following relationships can be derived for ϕ, λ and θ which are the angles between the normal to the plane and the σ_1, σ_2, and σ_3 directions respectively (Figure B.2).

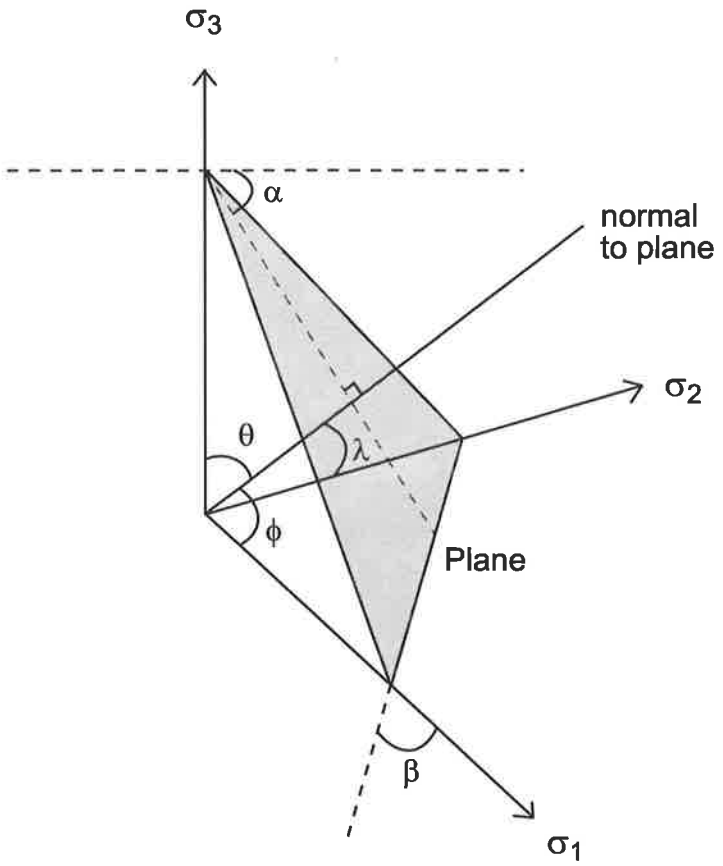

Figure B.2 Relationship between a plane, with dip α and strike β, with the three angles, ϕ, λ and θ which are the angles between the normal to the plane and the σ_1, σ_2, and σ_3 directions respectively.

Reverse Faulting Stress Regime ($\sigma_{Hmax}>\sigma_{hmin}>\sigma_v$),

$\theta = \alpha$ (Eq. B.1)

$\phi = \cos^{-1}(\sin\alpha\sin\beta)$ (Eq. B.2)

$\lambda = \cos^{-1}(\sin\alpha\sin(90-\beta))$ (Eq. B.3)

Strike-Slip Faulting Stress Regime ($\sigma_{Hmax}>\sigma_v>\sigma_{hmin}$),

$\theta = \cos^{-1}(\sin\alpha\sin(90-\beta))$ (Eq. B.4)

$\phi = \cos^{-1}(\sin\alpha\sin\beta)$ (Eq. B.5)

$\lambda = \alpha$ (Eq. B.6)

Normal Faulting Stress Regime ($\sigma_v>\sigma_{Hmax}>\sigma_{hmin}$),

$\theta = \cos^{-1}(\sin\alpha\sin(90-\beta))$ (Eq. B.7)

$\phi = \alpha$ (Eq. B.8)

$\lambda = \cos^{-1}(\sin\alpha\sin\beta)$ (Eq. B.9)

The following three relationships (Equations B.10, B.11 and B.12) can be found in Jaeger and Cook (1979) pages 27 and 28. The values n, l and m are the directional cosines of angles θ, ϕ and λ respectively.

$$\tau^2 + [\sigma - \tfrac{1}{2}(\sigma_1 + \sigma_2)]^2 = \tfrac{1}{4}(\sigma_1 - \sigma_2)^2 + n^2(\sigma_1 - \sigma_3)(\sigma_2 - \sigma_3) \qquad \text{(Eq. B.10)}$$

$$\tau^2 + [\sigma - \tfrac{1}{2}(\sigma_2 + \sigma_3)]^2 = \tfrac{1}{4}(\sigma_2 - \sigma_3)^2 + l^2(\sigma_2 - \sigma_1)(\sigma_3 - \sigma_1) \qquad \text{(Eq. B.11)}$$

$$\tau^2 + [\sigma - \tfrac{1}{2}(\sigma_1 + \sigma_3)]^2 = \tfrac{1}{4}(\sigma_1 - \sigma_3)^2 + m^2(\sigma_3 - \sigma_2)(\sigma_1 - \sigma_2) \qquad \text{(Eq. B.12)}$$

Expanding Equations B.10 and B.11 and then subtracting the two equations produces the following equation for the normal stress acting on a plane:

$$\sigma = (\tfrac{1}{4}(\sigma_1 - \sigma_2)^2 + n^2(\sigma_1 - \sigma_3)(\sigma_2 - \sigma_3) - \tfrac{1}{4}(\sigma_1 + \sigma_2)^2 - \tfrac{1}{4}(\sigma_2 - \sigma_3)^2 + l^2(\sigma_2 - \sigma_1)(\sigma_3 - \sigma_1) + \tfrac{1}{4}(\sigma_2 + \sigma_3)^2)/(\sigma_3 - \sigma_1)\,. \qquad \text{(Eq. B.13)}$$

The corresponding shear stress can then be calculated by substituting the appropriate values into Equation B.10, B.11 or B.12.

Coulomb Failure Criterion

Throughout this thesis the Coulomb criterion is used as the failure envelope (Figure 2.2). For intact rock the Coulomb failure criterion for frictional sliding is defined by (Figure 2.2):

$$\tau = C + \mu\,(\sigma_n - P_o)\,, \qquad \text{(Eq. B.14)}$$

where σ_n and τ are, respectively, the components of normal and shear stress acting on the failure plane, C is the cohesive or shear strength of the rock and μ is the coefficient of internal friction. For pre-existing planes of weakness with no cohesive strength the Coulomb failure envelope is represented by a straight line passing through zero shear stress (Figure 2.2):

$$\tau = \mu\,(\sigma_n - P_o)\,, \qquad \text{(Eq. B.15)}$$

Laboratory experiments on a wide variety of rock types have suggested that the coeffiecient of internal friction, μ, lies between 0.6 and 1.0 (Byerlee, 1978). Planes that are represented by

points lying above the failure line are relatively unstable and prone to failure. Planes represented by points below the failure are stable. For $\mu = 0.6$ planes optimally oriented for reactivation are inclined at 29.5° to the maximum principal stress, and for $\mu = 1.0$ planes optimally oriented for reactivation are inclined at 22.5° to the maximum principal stress.

Throughout this thesis Mohr-Coulomb analysis was undertaken assuming Byerlee's (1978) Law, which states that at normal stresses up to 200 MPa the shear stress to cause sliding on a pre-existing fault is approximately 0.85 times the normal stress. Thus the coefficient of frictional sliding along an optimally oriented plane of weakness, μ, is 0.85.

Propensity for Failure

The propensity for failure was calculated for both the Bowen and Sydney Basins in Chapters 4 and 5 respectively. This process assumed the horizontal and vertical stresses were the principal stresses. The shear stress (τ) and effective normal stress (σ_n-P_p) were normalised with respect to the vertical stress in order that data from different depths could be compared. A particular point from each 3D Mohr circle, corresponding to an actual plane, was plotted to allow the comparison of all locations on the same diagram (Figure B.3). This reduced the cluster of plotting the 3D Mohr circle from each measurement on the same diagram.

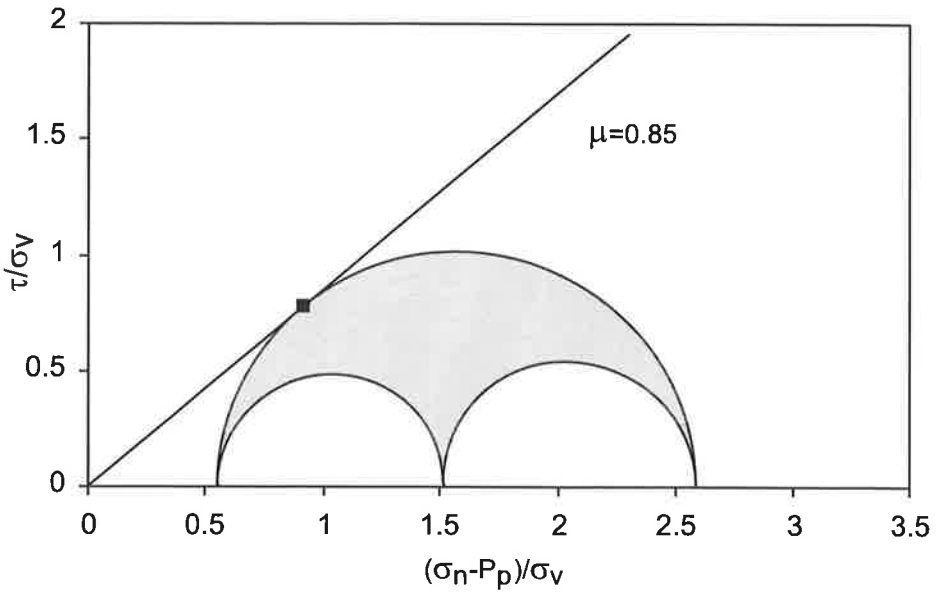

Figure B.3 Example of a 3D Mohr diagram. Shear stress (τ) and effective normal stress (σ_n-P_p) have both been normalised with respect to vertical stress in order that data from different depths can be compared. In this example the point representing the most critically stressed plane, which is on the threshold of failure assuming $\mu = 0.85$, is shown. The normal to this plane is oriented 65.2° to the maximum principal stress. Planes in all other directions, which all lie beneath the failure line, are stable.

The shear and normal stresses were calculated on an optimally oriented plane of no cohesion for each region. The optimally oriented plane, assuming $\mu = 0.85$, has a normal oriented at 65.2° to the maximum principal stress. This plane represents the most critically stressed point on the Mohr circle when Byerlee's Law is assumed (Figure B.3). However, the structural history of the each region has resulted in pre-existing planes of weakness with a preferential orientation that may not be optimal for faulting with respect to the *in situ* stress field. Hence the shear and normal stresses were also calculated on the plane that represents the predominant structural grains for both the Bowen and Sydney Basins. The propensity for failure was then assessed for each of the structural grains.

Appendix C

Directional Statistical Methods

C1 Unimodal Analysis of Directional Data

Orientation data, such as those determined through stress measurements, cannot be analysed using conventional linear statistics. Circular statistics developed by Mardia (1972) must be used when attempting to analyse the data. Since the azimuthal range lies between 0 and π, azimuths should be doubled before calculating the mean. The subsequent mean must then be halved to give the correct mean azimuth.

The mean is calculated using the following equations:

$$\bar{x} = \begin{cases} \bar{x}' & \text{if } \bar{S} > 0,\ \bar{C} > 0 \\ \bar{x}' + \pi & \text{if } \bar{C} < 0 \\ \bar{x}' + 2\pi & \text{if } \bar{S} < 0,\ \bar{C} > 0 \end{cases} \qquad \text{(Eq. C.1)}$$

where $\bar{x}' = \arctan(\bar{S} / \bar{C})$ (Eq. C.2)

$$\bar{C} = 1/n \sum fi \cos\theta i \qquad \text{(Eq. C.3)}$$

$$\bar{S} = 1/n \sum fi \sin\theta i \qquad \text{(Eq. C.4)}$$

$$\bar{R} = (\bar{C}^2 + \bar{S}^2)^{1/2} \qquad \text{(Eq. C.5)}$$

In the above equations θ is the azimuth of the observation, f is the frequency of a given azimuth and n is the total number of observations in the population.

The standard deviation about the mean azimuth is given by:

$$Stdev = [(-2 \ln \bar{R})^{1/2}] / l \qquad \text{(Eq. C.6)}$$

where azimuths are of range (periodicity) $(0, 2\pi/l)$.

The mean of a data set will only be useful if the data are not random. The Rayleigh test can be used to determine if a significant trend is present in the data (Section C3). This involved the comparison of the $\overline{R}$ value against statistical tables giving critical values of $\overline{R}$. The null hypothesis is that there is no single preferred direction. If the null hypothesis was rejected at a 99% confidence level or above, then the data were considered unimodal. Data that is not considered unimodal were analysed for bimodal trends using the technique outlined in Section C2.

A semi-circular normal distribution curve was used to approximate the orientation data in Chapters 4 and 5 to highlight the unimodal nature of the data:

$$f(x_j) = \frac{1}{2\pi I_0(\theta)} \exp[\theta \cos(x_j - \gamma)], \qquad \text{Eq. C.7}$$

where γ is the mean of the distribution, θ is the concentration parameter of the distribution and $I_0(x)$ is the bessel function. The Bessel function can be approximated by (Bowman, 1958):

$$I_0(x) = 1 + \frac{x^2}{2^2} + \frac{x^4}{2^2 4^2} + \frac{x^6}{2^2 4^2 6^2} + \ldots\ldots \qquad \text{Eq. C.8}$$

A 25 term approximation was used during the analysis.

The semi-circular normal distribution can be optimised to the data by maximising the maximum likelihood function $L(\phi)$:

$$\lambda(\phi) = \log_e L(\phi) = \sum_{j=1}^{n} \log_e f(x_j, \phi), \qquad \text{Eq. C.9}$$

where $\phi = (\gamma, \theta)$. The set of optimal parameters are used in the semi-circular normal distribution to produce the theoretical curve that best fits the data.

C2 Bimodal Analysis of Directional Data

A bimodal analysis was performed on each data set not considered unimodal using two semi-circular normal distributions to approximate the data:

$$f(x_j) = \frac{\alpha}{2\pi I_0(\theta_1)} \exp[\theta_1 \cos(x_j - \gamma_1)] + \frac{(1-\alpha)}{2\pi I_0(\theta_2)} \exp[\theta_2 \cos(x_j - \gamma_2)], \qquad \text{Eq. C.10}$$

where γ_1 is the mean of distribution 1, γ_2 is the mean of distribution 2, θ_1 is the concentration parameter for distribution 1, θ_2 is the concentration parameter for distribution 2, α is the proportion of distribution 1 and $I_0(x)$ is the bessel function (Equation C.8).

The semi-circular normal distribution can be optimised for each data set by maximising the maximum likelihood function $L(\phi)$:

$$\lambda(\phi) = \log_e L(\phi) = \sum_{j=1}^{n} \log_e f(x_j, \phi), \qquad \text{Eq. C.11}$$

where $\phi = (\alpha, \gamma_1, \gamma_2, \theta_1, \theta_2)$.

Once the optimal set of parameters has been determined, the Rayleigh test is performed on both semi-circular normal distributions to determine whether they are significant. If the null hypothesis for both distributions is rejected at a 99% confidence level or above, then the data are considered bimodal. The optimal parameters are then used to produce the best fitting theoretical distribution.

C3 Rayleigh Test

The Rayleigh test (Mardia, 1972; Davis, 1986) is a statistical test to determine whether the average orientation from a dataset is significant. The test is based on the assumption that random orientations approximate a von Mises distribution, the circular equivalent of the normal distribution (Mardia, 1972). The length of the mean resultant vector, $\overline{R}$ (Equation C.5), of the σ_{Hmax} orientations is compared to critical values in Table C.1. If the $\overline{R}$ value is greater than the critical value then the null hypothesis that the distribution is random can be rejected at a specific confidence level. The $\overline{R}$ value is comparable to the standard

deviation of the distribution but in the opposite sense. Values for $\overline{R}$ lie between 1 and 0. A large value for $\overline{R}$ indicates the vectors are tightly bunched while a low value near zero indicates the vectors are dispersed.

Table C.1 Critical values used in the Rayleigh test

Number of Values	$\overline{R}$ Value at Confidence Level				
	90 %	95 %	97.5 %	99 %	99.9 %
4	0.768	0.847	0.905	0.960	-
5	0.677	0.754	0.816	0.879	0.991
6	0.618	0.690	0.753	0.825	0.940
7	0.572	0.642	0.702	0.771	0.891
8	0.535	0.602	0.660	0.725	0.847
9	0.504	0.569	0.624	0.687	0.808
10	0.478	0.540	0.594	0.655	0.775
11	0.456	0.516	0.567	0.627	0.743
12	0.437	0.494	0.544	0.602	0.716
13	0.420	0.475	0.524	0.580	0.692
14	0.405	0.458	0.505	0.560	0.669
15	0.391	0.443	0.489	0.542	0.649
16	0.379	0.429	0.474	0.525	0.630
17	0.367	0.417	0.460	0.510	0.613
18	0.357	0.405	0.447	0.496	0.597
19	0.348	0.394	0.436	0.484	0.583
20	0.339	0.385	0.425	0.472	0.569
21	0.331	0.375	0.415	0.461	0.556
22	0.323	0.367	0.405	0.451	0.544
23	0.316	0.359	0.397	0.441	0.533
24	0.309	0.351	0.389	0.432	0.522
25	0.303	0.344	0.381	0.423	0.512
30	0.277	0.315	0.348	0.387	0.470
35	0.256	0.292	0.323	0.359	0.436
40	0.240	0.273	0.302	0.336	0.409
45	0.226	0.257	0.285	0.318	0.386
50	0.214	0.244	0.270	0.301	0.367
100	0.150	0.170	0.190	0.210	0.260
200	0.110	0.120	0.140	0.160	0.200

Appendix D

Raw Data

This appendix contains the individual hydraulic fracture (HF) and overcoring (OC) measurements for both the Bowen (Table D.1) and Sydney Basins (Table D.2) from the CSIRO database. The regime at each test depth has been defined as either reverse fault conditions (TF), strike-slip fault conditions (SS), normal fault conditions (NF) or unknown (U). These regimes have been determined by the relative magnitudes of σ_{Hmax}, σ_{hmin} and σ_v. The overburden density used in the calculation of σ_v was 2308 kgm^{-3} (equivalent to an overburden stress of 22.6 MPa/km or 1 psi/ft) for the two basins, on the basis of density log data. The individual breakouts determined for the wells within the Perth Basin (Table D.3) are also included in this Appendix. All depths and distances relating to the breakouts are in metres.

Table D.1 Individual hydraulic fracturing and overcoring in situ stress measurements from the Bowen Basin.

Site	Latitude	Longitude	Type	Depth (m)	σ_{Hmax} Orientation	σ_{Hmax} (MPa)	σ_{hmin} (MPa)	σ_v (MPa)	Regime
AU122	-23.094	148.502	HF	62	061	4.1	2.6	1.4	TF
				67	043	4.1	2.6	1.52	TF
				69	038	4.1	2.6	1.56	TF
				122	066	5.8	4	2.76	TF
				149	054	6	4.2	3.37	TF
				171	030	7	4.7	3.87	TF
AU125	-21.592	148.173	HF	90	022	5.5	1.5	2.04	SS
				110	090	5.6	1.5	2.49	SS
				130	170	6	3.5	2.94	TF
				174	016	7	3	3.94	SS
				210	018	7.1	3.2	4.75	SS
				250	010	13	5	5.66	SS
				235	175	5.2	4.7	5.32	NF
				88	018	5.5	1.8	1.99	SS
				170	063	5.5	2.5	3.85	SS
				452	-	13.6	9.7	10.23	SS
				455	-	16.6	10.7	10.3	TF
				465	-	17.5	11.4	10.52	TF
				470	-	17.5	11.4	10.64	TF
				486	-	14.4	9.6	11	SS
				489	008	15.6	10.7	11.07	SS
				494	008	19	12.4	11.18	TF
				579	158	22.1	13.8	13.1	TF
				583	-	22.8	14.1	13.19	TF
				590	038	31.8	18.3	13.35	TF
				625	003	22.9	14.5	14.15	TF
				627	-	23.9	14.9	14.19	TF
				632	018	26.1	16.5	14.3	TF

Table D.1 continued...

Site	Latitude	Longitude	Type	Depth (m)	σ_{Hmax} Orientation	σ_{Hmax} (MPa)	σ_{hmin} (MPa)	σ_v (MPa)	Regime
AU196	-21.602	147.957	HF	673	-	25.8	16.5	15.23	TF
				681	024	28.5	17.6	15.41	TF
				684	015	28.2	17.6	15.48	TF
AU197	-21.592	147.966	HF	275	038	8.6	5.5	6.22	SS
				278	008	9.6	6.2	6.29	SS
				281	-	13.1	7.6	6.36	TF
				300	003	17.1	9.6	6.79	TF
				462	014	18.6	11.4	10.46	TF
				465	-	18.1	11.7	10.52	TF
				469	014	22.9	13.8	10.61	TF
AU198	-21.833	148.058	HF	245	-	10	6.6	5.54	TF
				310	033	9.3	7.6	7.02	TF
				359	024	14.3	9.3	8.13	TF
				361	008	13.4	9.3	8.17	TF
				383	017	18.6	10.3	8.67	TF
				436	-	16.9	10.7	9.87	TF
				458	031	19.2	12.8	10.37	TF
				485	051	20	12.4	10.98	TF
				491	-	17.2	11.4	11.11	TF
AU199	-21.51	148	HF	85	023	2.6	2.3	1.92	TF
				86	000	2.9	2.7	1.95	TF
				124	018	5.6	3.8	2.81	TF
				152	013	7	5.5	3.44	TF
				175	008	9.2	6.1	3.96	TF
AU200	-21.866	148.009	HF	327	018	20	15.8	7.4	TF
				316	023	-	13.1	7.15	TF
				282	013	15.9	12.4	6.38	TF
				232	013	13.8	9.6	5.25	TF
				198	008	12.4	6.9	4.48	TF
				196	023	8.5	5.5	4.44	TF
AU201	-21.264	147.914	HF	107	010	6.6	1.05	2.42	SS
				118	008	8.3	3.5	2.67	TF
				125	004	5.8	3.5	2.83	TF
				145	013	8.8	5.3	3.28	TF
				162	000	8.7	4.6	3.67	TF
				165	172	8.2	6	3.73	TF
AU202	-21.54	148.25	HF	50	128	0.9	0.7	1.13	NF
				54	148	1.37	0.86	1.22	SS
				58	008	3.1	1.72	1.31	TF
				87	158	3.8	2.8	1.97	TF
				89	133	2.8	2.4	2.01	TF
AU203	-21.592	148.173	HF	277	168	11.4	7.2	6.27	TF
				281	140	12.5	7.9	6.36	TF
				300	163	14.4	8.6	6.79	TF
				315	158	12.2	7.8	7.13	TF
AU204	-23.043	148.564	HF	151	008	13.1	5.6	3.42	TF
				159	013	15.3	5.3	3.6	TF
				170	013	17.3	5.6	3.85	TF
				175	013	17.7	5.6	3.96	TF
AU205	-23.051	148.542	HF	67	143	4.1	3.2	1.52	TF
				71	146	4.3	3.2	1.61	TF
				80	008	10.3	3.5	1.81	TF
				109	008	5.5	3.9	2.47	TF

Table D.1 continued...

Site	Latitude	Longitude	Type	Depth (m)	σ_{Hmax} Orientation	σ_{Hmax} (MPa)	σ_{hmin} (MPa)	σ_v (MPa)	Regime
AU205	-23.051	148.542	HF	123	008	15.5	4.6	2.78	TF
AU206	-23.058	148.563	HF	186	-	-	17.5	4.21	TF
				192	008	28.2	15.8	4.35	TF
				196	008	17	10.9	4.44	TF
AU207	-21.592	148.173	HF	163	013	5.8	3.8	3.69	TF
				165	008	4.6	3.1	3.73	SS
				188	148	8.7	5.2	4.25	TF
				218	122	8.3	4.8	4.93	SS
AU208	-23.078	148.528	HF	88	061	5.5	3.2	1.99	TF
				93	065	5.9	3.4	2.1	TF
				101	030	7	4.2	2.29	TF
				110	036	6	3.6	2.49	TF
				112	054	5.5	3.6	2.53	TF
				115	043	4.9	3.65	2.6	TF
AU209	-23.012	148.56	HF	110	003	7.5	4.8	2.49	TF
				127	020	9	5.8	2.87	TF
				130	051	7.8	5.3	2.94	TF
				175	013	12.5	7	3.96	TF
AU210	-22.946	148.586	HF	54	150	4	2.5	1.22	TF
				85	013	7	3.5	1.92	TF
				95	021	5	3.3	2.15	TF
				102	167	5.1	4	2.31	TF
AU211	-22.995	148.554	HF	138	030	9.1	5.9	3.12	TF
				157	068	9.6	6.2	3.55	TF
				200	048	10.7	6.8	4.53	TF
AU212	-24.033	148.614	HF	81	023	3.1	2.17	1.83	TF
				84	-	3.62	2.24	1.9	TF
				166	145	5.72	3.79	3.76	TF
				178	168	6.34	5.51	4.03	TF
				180	158	15.6	10.34	4.07	TF
				183	145	5.62	5.17	4.14	TF
				185	018	12.44	7.92	4.19	TF
				188	145	-	-	-	U
				193	018	-	-	-	U
				210	004	7.68	6.06	4.75	TF
				212	008	6.03	5.51	4.8	TF
				218	012	-	7.23	4.93	TF
AU213	-24.014	148.646	HF	87	098	-	3.1	1.97	TF
				89	048	2.58	2.41	2.01	TF
				92	038	9.41	6.89	2.08	TF
				95	-	9.41	6.89	2.15	TF
				100	008	-	-	2.26	U
				121	023	6.37	3.79	2.74	TF
				123	048	3.93	3.1	2.78	TF
				125	028	4.96	3.1	2.83	TF
AU214	-24.673	149.911	HF	328	023	13.8	8.3	7.42	TF
				385	048	27.1	17.2	8.71	TF
				416	008	40	22.4	9.42	TF
				466	031	22.1	13.8	10.55	TF
				499	038	40.5	22.7	11.29	TF
AU215	-24.621	149.882	HF	561	058	35	20	12.7	TF
				587	028	24.1	15.2	13.29	TF
				589	-	25.8	15.9	13.33	TF

Table D.1 continued...

Site	Latitude	Longitude	Type	Depth (m)	σ_{Hmax} Orientation	σ_{Hmax} (MPa)	σ_{hmin} (MPa)	σ_v (MPa)	Regime
AU215	-24.621	149.882	HF	592	-	29.5	17.9	13.4	TF
				595	-	28	17.2	13.47	TF
				624	-	40.2	23.1	14.12	TF
				633	018	43.3	24.5	14.33	TF
				689	-	32.6	20	15.59	TF
				707	-	35.4	21.4	16	TF
AU216	-24.585	149.914	HF	320	000	13.8	8.6	7.24	TF
				323	016	19.3	11.4	7.31	TF
				334	-	12.8	9	7.56	TF
				352	006	11.7	9.3	7.97	TF
				393	013	11.7	10	8.89	TF
				402	030	34.5	17.9	9.1	TF
				456	008	18.6	11	10.32	TF
				459	-	19.3	11.7	10.39	TF
				503	-	39.3	22.7	11.38	TF
AU217	-24.684	149.9	HF	407	013	16.5	10.3	9.21	TF
				433	043	20	11.7	9.8	TF
				437	058	25.5	14.5	9.89	TF
				468	-	20.3	12.4	10.59	TF
				504	043	20	13.1	11.41	TF
				515	043	22.1	13.8	11.66	TF
				537	043	22.7	14.5	12.15	TF
				550	038	28.6	17.2	12.45	TF
				569	033	25	15.9	12.88	TF
				574	053	34.5	20.7	12.99	TF
				620	035	37.9	22.1	14.03	TF
AU218	-24.644	149.908	HF	348	000	12.4	8.6	7.88	TF
				383	028	11	7.2	8.67	SS
				429	002	13.4	9	9.71	SS
				477	001	13.1	9	10.8	SS
				482	-	16.8	11	10.91	TF
				509	-	12.1	8.6	11.52	SS
AU219	-24.31	149.882	HF	533	058	23.8	15.2	12.06	TF
				550	053	29.3	18.6	12.45	TF
				566	098	34.5	20	12.81	TF
				601	138	34.8	22.7	13.6	TF
				617	098	8.3	8.3	13.96	NF
				637	068	40	24.1	14.42	TF
				645	-	22.4	16.5	14.6	TF
				661	058	21.7	13.8	14.96	SS
				666	-	22.1	13.8	15.07	SS
AU220	-24.47	150.031	HF	531	006	19.3	12.8	12.02	TF
				536	007	19	12.1	12.13	SS
				547	000	16.2	11	12.38	SS
				558	173	15.5	11	12.63	SS
				578	033	26.9	15.5	13.08	TF
				587	000	19	12.8	13.29	SS
				594	-	20	13.4	13.44	SS
				615	028	31.7	18.6	13.92	TF
				620	-	29.6	17.9	14.03	TF
				637	-	29.9	19.3	14.42	TF
AU221	-24.528	149.954	HF	583	058	26.7	16.6	13.19	TF
				603	098	38.1	22.4	13.65	TF

Table D.1 continued...

Site	Latitude	Longitude	Type	Depth (m)	σ_{Hmax} Orientation	σ_{Hmax} (MPa)	σ_{hmin} (MPa)	σ_v (MPa)	Regime
AU221	-24.528	149.954	HF	629	024	28.5	19.3	14.24	TF
				694	018	26.9	19.3	15.71	TF
				725	-	32.9	19.6	16.41	TF
				749	033	30.6	20.7	16.95	TF
				792	025	31.8	19.6	17.93	TF
AU252	-21.592	148.173	HF	186	168	4.96	3.45	4.21	SS
				191	171	4.9	3.45	4.32	SS
				194	008	5.34	3.27	4.39	SS
				206	178	7.06	4.48	4.66	SS
AU253	-21.592	148.173	HF	227	008	9.7	5.2	5.14	TF
				238	151	6.1	4.1	5.39	SS
				263	173	7.4	5	5.95	SS
				281	028	3.4	2.9	6.36	NF
AU274	-24.76	150.045	HF	382	000	9.1	7.2	8.65	SS
				386	173	13.5	9	8.74	TF
				390	018	17.3	11	8.83	TF
				404	-	17.9	11.4	9.14	TF
				439	-	18.8	12.8	9.94	TF
				451	-	9	7.8	10.21	NF
				463	-	11.7	9.3	10.48	SS
AU275	-24.76	150.045	HF	392	-	-	5.2	8.87	U
				396	-	-	5.2	8.96	U
				402	-	21.8	12.4	9.1	TF
				422	-	22.7	13.4	9.55	TF
				433	-	22.3	13.1	9.8	TF
				436	-	18.2	11	9.87	TF
AU276	-24.76	150.045	HF	398	-	21	12.1	9.01	TF
				403	030	17.3	10.5	9.12	TF
				409	025	13.1	8.6	9.26	SS
				437	015	24	17.5	9.89	TF
AU277	-23.8	148.894	OC	230	000	8.7	7	5.21	TF
AU278	-23.867	148.833	OC	120	015	1.3	0.42	2.72	NF
AU279	-21.24	147.947	OC	110	004	6.5	4.1	2.49	TF
AU280	-23.08	148.41	OC	90	007	4.5	2	2.04	SS
AU281	-21.764	148.038	OC	170	005	5.1	2.8	3.85	SS
AU282	-23.24	148.082	OC	230	178	13	12	5.21	TF
AU283	-23.707	148.864	OC	400	020	22	12	9.05	TF

Table D.2 Individual hydraulic fracturing and overcoring in situ stress measurements from the Sydney Basin.

Site	Latitude	Longitude	Type	Depth (m)	σ_{Hmax} Orientation	σ_{Hmax} (MPa)	σ_{hmin} (MPa)	σ_v (MPa)	Regime
AU113	-34.318	150.88	OC	430	033	27.1	13.4	9.73	TF
AU114	-32.373	150.978	OC	180	088	9.6	4.6	4.07	TF
AU115	-32.591	151.044	HF	112	158	8	3.6	2.53	TF
				100	154	5.4	2.7	2.26	TF
				96	124	5.2	2.6	2.17	TF
AU116	-32.661	151.147	HF	75	136	7	4.4	1.7	TF
				68	134	7.6	3.8	1.54	TF
				66	129	7.5	4.1	1.49	TF
				47	013	2.8	1.5	1.06	TF
				86	152	5.4	2.7	1.95	TF
AU117	-33.173	151.5	OC	90	005	7.8	5.7	2.04	TF
AU118	-34.2	150.772	OC	480	086	26	15.2	10.86	TF
AU119	-33.959	151.25	HF	71	-	5.1	2.6	1.61	TF
				73.3	-	5.1	2.6	1.66	TF
				90	-	7.4	3.5	2.04	TF
				102.5	028	6.4	3.1	2.32	TF
				106.6	-	6.4	3.1	2.41	TF
				117.4	-	5.7	2.9	2.66	TF
				122.5	017	7.8	3.7	2.77	TF
				76	-	7.1	3.4	1.72	TF
AU120 #	-33.892	151.261	HF	81	048	2.9	1.5	1.83	SS
				104.7	048	5.9	3	2.37	TF
AU240	-33.366	150.14	HF	220	138	11.1	7.2	4.98	TF
				277	158	36.2	18.6	6.27	TF
				322	178	-	-	7.29	U
				323	048	-	-	7.31	U
				335	158	-	-	7.58	U
				346	003	-	-	7.83	U
				358	178	22.9	14.1	8.1	TF
AU241	-33.385	150.14	HF	271	073	23.7	11.4	6.13	TF
				288	073	25.3	15.5	6.52	TF
				301	085	29.7	17.9	6.81	TF
				342	088	26.6	17.2	7.74	TF
				345	113	20.1	12.4	7.81	TF
				337	138	29.7	13.8	7.63	TF
AU242	-33.384	150.145	HF	291	074	26.1	12.4	6.59	TF
				305	096	16.2	12.4	6.9	TF
				308	-	33.6	20.7	6.97	TF
				323	-	-	9.3	7.31	TF
				344	100	19	12.4	7.79	TF
				353	048	26.2	13.1	7.99	TF
AU243	-33.392	150.145	HF	307	068	10.7	6.9	6.95	SS
				311	103	10.7	7.2	7.04	TF
				312	078	-	7.9	7.06	TF
				318	033	20	17.2	7.2	TF
				321	070	31.6	19.6	7.27	TF
				322	108	25.4	15.9	7.29	TF
				362	100	25.2	19	8.19	TF
				364	154	16.8	13.4	8.24	TF
AU244	-33.394	150.149	HF	326	098	-	-	7.38	U
				343	098	15.9	9	7.76	TF
				352	157	40.9	22.7	7.97	TF
				360	008	17.7	11.7	8.15	TF

Table D.2 continued...

Site	Latitude	Longitude	Type	Depth (m)	σ_{Hmax} Orientation	σ_{Hmax} (MPa)	σ_{hmin} (MPa)	σ_{v} (MPa)	Regime
AU244	-33.394	150.149	HF	375	098	10	7.2	8.49	SS
				379	098	31.1	17.9	8.58	TF
				382	098	20.4	13.1	8.65	TF
				384	148	16.2	13.8	8.69	TF
				386	-	12.7	8.3	8.74	SS
AU245	-33.382	150.145	HF	240	123	-	15	5.43	TF
				244	109	22.9	13.8	5.52	TF
				261	086	14	10.7	5.91	TF
				256	081	-	-	5.79	U
				265	-	-	-	6	U
				274	-	-	6.9	6.2	TF
				276	008	11	7.6	6.25	TF
				267	-	17.3	10.9	6.04	TF
AU246	-33.386	150.15	HF	309	098	16.3	11	6.99	TF
				330	083	15.7	12.4	7.47	TF
				343	068	53.8	29.6	7.76	TF
				345	063	34.5	21.4	7.81	TF
				370	083	14	8.6	8.37	TF
				372	103	24.5	13.8	8.42	TF
				375	061	14.1	8.3	8.49	SS
AU247	-33.392	150.16	HF	330	158	19.4	10.3	7.47	TF
				335	158	-	-	7.58	U
				338	114	15.8	11	7.65	TF
				343	110	15.1	13.8	7.76	TF
				383	122	18.2	15.2	8.67	TF
				395	120	-	-	8.94	U
AU248	-33.396	150.158	HF	315	138	17.2	13.1	7.13	TF
				334	148	29.2	20.7	7.56	TF
				333	138	21	17.9	7.54	TF
				336	156	37.4	22.1	7.6	TF
				342	028	14	9.7	7.74	TF
				348	108	-	-	7.88	U
				374	028	17.3	11.4	8.46	TF
				383	148	19.2	11.7	8.67	TF
AU249	-33.391	150.162	HF	271	-	26.7	15.2	6.13	TF
				273	133	22	10.8	6.18	TF
				321	118	-	-	7.27	U
AU250	-33.363	150.163	HF	323	076	21.3	12.8	7.31	TF
				350	008	-	-	7.92	U
				353	133	21.3	12.8	7.99	TF
				355	068	-	-	8.03	U
				356	113	25.7	15.5	8.06	TF
AU251	-33.361	150.161	HF	311	138	30.5	17.2	7.04	TF
				314	108	-	-	7.11	U
				323	008	9.5	6.9	7.31	SS
				340	143	-	13.8	7.7	TF
AU254	-32.188	150.849	HF	156	138	8.2	4.5	3.53	TF
				158	128	5.9	3.8	3.58	TF
				243.5	108	-	24.8	5.51	TF
				248.5	078	-	22.1	5.62	TF
				260	118	9.1	6.9	5.88	TF
				268	103	16	9.6	6.07	TF
				60	145	1.3	1	1.36	NF

Table D.2 continued...

Site	Latitude	Longitude	Type	Depth (m)	σ_{Hmax} Orientation	σ_{Hmax} (MPa)	σ_{hmin} (MPa)	σ_v (MPa)	Regime
AU254	-32.188	150.849	HF	120	078	3.5	2.4	2.72	SS
				181	-	11	8.3	4.1	TF
				326	076	27.7	17.9	7.38	TF
				334	064	33.4	19	7.56	TF
AU255	-32.441	150.802	HF	171	053	16.4	3.5	3.87	SS
				198	064	26.2	7.9	4.48	TF
				237	057	15.5	8.3	5.36	TF
				278	060	10	6.2	6.29	SS
				318	066	26.7	13.8	7.2	TF
				385	-	34.8	19.3	8.71	TF
				465	-	12.5	9.7	10.52	SS
AU256	-32.438	150.835	HF	270	078	11	7.9	6.11	TF
				275	048	17.4	9.7	6.22	TF
				341	052	18.9	11	7.72	TF
				345	058	20	11.4	7.81	TF
				372	068	24.1	13.8	8.42	TF
				441	-	26.9	16.2	9.98	TF
				547	-	34.2	22.1	12.38	TF
AU257	-33.825	151.264	HF	105	-	6	2.9	2.38	TF
				109.5	020	5.1	2.6	2.48	TF
				124.7	022	5.9	2.9	2.82	TF
				102.1	078	12.2	5.2	2.31	TF
AU258	-33.972	151.247	HF	92	011	5.8	3.8	2.08	TF
				108	017	7.9	4.5	2.44	TF
				122	028	4.1	3.8	2.76	TF
				123	065	3.6	3.2	2.78	TF
				131	019	4.6	4.2	2.96	TF
				139	021	9	5.5	3.15	TF
AU259	-33.377	151.383	HF	640	071	34	27	14.48	TF
				612	068	29	25	13.84	TF
				653	070	-	-	14.77	U
AU260	-33.082	151.4	HF	208	176	11.5	7	4.7	TF
				209	027	13.5	7.5	4.73	TF
				212	029	11.5	7	4.8	TF
				228	152	-	9	5.16	TF
				234	054	-	7	5.29	TF
AU261	-33.082	151.4	HF	45	155	-	3.5	1.02	TF
				247	172	-	7	5.59	TF
AU262	-33.082	151.4	HF	29	160	3.5	1.9	0.66	TF
				184	045	9.6	6.3	4.16	TF
				209	045	10.3	5.5	4.73	TF
				228	040	-	3.1	5.16	SS
AU263	-33.241	151.196	HF	694	068	13.3	9.9	15.7	NF
				722	092	21.4	14.5	16.33	SS
				821	-	17.6	12.8	18.57	NF
				825	079	19.8	14	18.66	SS
				851	068	20.4	14.5	19.25	SS
				889	081	32.4	20.7	20.11	TF
				902	080	34.4	21.7	20.4	TF
				936	088	55	31	21.17	TF
				985	-	54	28.9	22.28	TF
AU264	-32.9	151.244	HF	198	036	53	28.3	4.48	TF
				187	098	33.5	17.2	4.23	TF

Table D.2 continued…

Site	Latitude	Longitude	Type	Depth (m)	σ_{Hmax} Orientation	σ_{Hmax} (MPa)	σ_{hmin} (MPa)	σ_v (MPa)	Regime
AU264	-32.9	151.244	HF	204	073	33	20	4.61	TF
				211	080	16.8	11.7	4.77	TF
				328	092	30	22.4	7.42	TF
AU265	-32.355	151.256	HF	492	055	39	23.4	11.13	TF
				491	049	37	23.3	11.11	TF
AU266	-33.897	151.193	HF	143	018	10.9	7.9	3.24	TF
				337	042	16.2	11	7.63	TF
				576	053	-	-	13.04	U
				602	053	-	-	13.62	U
				605	046	-	-	13.69	U
				775	080	-	-	17.54	U
				959	014	40.4	24.1	21.7	TF
				1046	026	30.3	19.3	23.67	SS
AU267	-33.972	151.229	HF	407	058	24.4	16.2	9.21	TF
				429	043	17.6	11	9.71	TF
				499	033	17.8	12.1	11.29	TF
				525	018	22.1	13.8	11.88	TF
				554	033	20.3	12.9	12.54	TF
				583	035	23.5	15.2	13.19	TF
AU268	-33.892	151.249	HF	19.5	017	2.2	1.7	0.44	TF
				33	070	2.1	1.7	0.75	TF
				43	036	7.9	5.1	0.97	TF
				44.5	025	3.3	2.6	1.01	TF
				47	022	3.8	2.8	1.06	TF
				50	108	7.1	4.5	1.13	TF
AU269	-33.872	151.2	HF	2	020	2.1	1.2	0.05	TF
				4.7	160	3.9	2.3	0.11	TF
				7.9	010	2.1	1.2	0.18	TF
				17.2	020	2.9	1.8	0.39	TF
				1.5	040	2	1.1	0.03	TF
				5.1	005	2.5	1.5	0.12	TF
				8.4	170	1.6	1.1	0.19	TF
				16.1	003	2.5	1.6	0.36	TF
				6	000	0.8	0.7	0.14	TF
				11.7	000	1.6	1	0.26	TF
				14	025	2.5	1.3	0.32	TF
AU270	-33.882	151.197	HF	4.5	012	1.3	0.8	0.1	TF
				5.5	012	2.5	1.7	0.12	TF
				7.2	008	1.2	0.9	0.16	TF
AU271	-33.88	151.196	HF	3	108	1.3	0.7	0.07	TF
				8.5	150	1	1	0.19	TF
				9.5	032	-	1.2	0.22	TF
				10	080	-	2.2	0.23	TF
				13	168	1	0.9	0.29	TF
				14	018	-	-	0.32	U
AU272	-33.83	151.226	HF	89	133	-	-	2.01	U
				98	147	4	2.6	2.22	TF
AU273	-33.819	151.251	HF	67	008	4.2	2.8	1.52	TF
				69	158	5.6	2.9	1.56	TF
				71	003	4.1	2.8	1.61	TF
				94	053	3.9	2.8	2.13	TF
				97	153	3.1	2.8	2.2	TF
				99	-	6.1	4.1	2.24	TF

Table D.2 continued…

Site	Latitude	Longitude	Type	Depth (m)	σ_{Hmax} Orientation	σ_{Hmax} (MPa)	σ_{hmin} (MPa)	σ_v (MPa)	Regime
AU284	-32.109	150.745	OC	190	084	5	4.2	4.3	SS
AU285	-32.5	150.952	OC	80	086	10	6.7	1.81	TF
AU286	-32.9	151.211	OC	550	059	35	25	12.44	TF
AU287	-32.909	151.5	OC	190	016	29	19.8	4.3	TF
AU288	-32.9	151.6	OC	100	000	13.3	9.6	2.26	TF
AU289	-33.182	151.228	OC	250	066	12.4	9.4	5.65	TF
AU290	-33.959	151.25	OC	125	029	6.8	3.8	2.83	TF
AU291	-33.982	150.473	OC	173	104	10.1	4.9	3.92	TF
AU292	-34.018	150.457	OC	472	074	19.7	13.5	10.68	TF
AU293	-34.182	150.755	OC	450	075	25	14.7	10.18	TF
AU294	-34.2	150.554	OC	430	038	17	15.5	9.73	TF
AU295	-34.236	150.707	OC	500	072	44	31	11.32	TF
AU296	-34.2	150.88	OC	500	060	27	19.3	11.32	TF
AU297	-34.168	150.951	OC	500	048	14	10.8	11.32	SS
AU298	-34.255	150.913	OC	350	000	20	11.5	7.92	TF
AU299	-34.473	150.701	OC	400	107	15	13.6	9.05	TF
AU300	-33.436	150.239	OC	200	063	5	2	4.53	SS

Table D.3 Individual borehole breakouts recorded from Perth Basin wells.

Site	Well	Latitude	Longitude	Quality	Breakout Data				
					Length	Orientation	Top	Bottom	Aver. Depth
AU302	Batavia 1	-28.899	114.26	D	28.5	090	2320.5	2349	2334.75
AU303	Beekeeper 1	-29.714	115.185	B	37.0	025	2963	3000	2981.5
					10.0	008	2893	2903	2898
					132.0	010	2675	2807	2741
					85.0	027	2590	2675	2632.5
AU304	Coomallo 1	-30.248	115.415	B	5.0	095	2941	2945	2943
					5.0	100	2565	2570	2567.5
					95.0	100	3090	3185	3137.5
AU305	Dongara 24	-29.237	115.016	D	6.0	150	1189	1195	1192
					23.0	137	1142	1165	1153.5
AU306	Indoon 1	-29.883	115.151	D	3.5	005	2132.5	2136	2134.25
					25.0	160	1377	1402	1389.5
AU307	Lake Preston 1	-32.92	115.66	B	26.2	086	4123.3	4149.5	4136.4
					162.8	088	3907.5	4070.3	3988.9
					105.8	110	3795.7	3901.4	3848.6
					62.2	114	3706.4	3761.2	3733.8
					54.9	080	3632.0	3686.9	3659.4
					2.4	050	3566.2	3568.6	3567.4
					4.3	050	3545.4	3549.7	3547.6
					11.6	045	3530.8	3542.4	3536.6
					26.2	080	3500.9	3527.1	3514.0
					25.0	110	3418.6	3443.6	3431.1
					13.4	090	3388.2	3401.6	3394.9
					18.3	070	3361.9	3380.2	3371.1
					10.4	080	3341.2	3351.6	3346.4
					22.6	065	3314.4	3337.0	3325.7
					163.4	070	3110.2	3273.6	3191.9
					58.5	065	3037.0	3095.5	3066.3
					95.7	070	2941.3	3037.0	2989.2
AU308	Sugarloaf 1	-32.915	115.052	C	3.7	060	3519.8	3523.5	3521.7
					7.9	065	3482.6	3490.6	3486.6
					5.5	077	3398.5	3404.0	3401.3
					3.0	067	3383.3	3386.3	3384.8
					7.3	054	3370.5	3377.8	3374.1
AU309	Walyering 2	-30.701	115.472	B	3.7	118	3706.4	3710.0	3708.2
					3.0	116	3697.2	3700.3	3698.7
					26.2	115	3658.2	3684.4	3671.3
					48.8	115	3596.6	3645.4	3621.0
					25.0	116	3497.9	3522.9	3510.4
					6.7	116	3405.2	3411.9	3408.6
					30.5	113	3363.8	3395.5	3379.6
					8.5	108	3107.7	3116.3	3112.0
AU310	Walyering 3	-30.666	115.492	B	14.0	105	2976	2980	2978
					14.5	105	2952	2976.5	2964.25
					51	116	2844	2895	2869.5
					26	112	2802	2828	2815
					12	102	2718	2730	2724
					26	138	2686	2712	2699
					46	144	2640	2686	2663
					10	105	2622	2632	2627

Table D.3 continued...

Site	Well	Latitude	Longitude	Quality	Breakout Data				
					Length	Orientation	Top	Bottom	Aver. Depth
AU310	Walyering 3	-30.666	115.492	B	64	093	2554	2618	2586
					4	140	2540	2544	2542
					6	147	2528	2534	2531
					9	140	2513	2522	2517.5
					12	093	2497	2509	2503
					7	147	2477	2484	2480.5
					54	100	2418	2472	2445
					88	095	2324	2412	2368
					16	105	2280	2296	2288
					8	107	2248	2256	2252
					5	115	2233	2238	2235.5
					46	102	1982	2228	2105
					12	108	2164	2176	2170
					30	105	2068	2098	2083
					9	100	2024	2033	2028.5
					8	105	2010	2018	2014
					17	110	1986	2003	1994.5
					6	104	2062	2068	2065
					23	105	1933	1956	1944.5
					17	106	1880	1897	1888.5
AU311	Warradong 1	-29.301	115.171	C	1.5	105	3585	3586.5	3585.75
					2	140	3576	3578	3577
					15	140	3390	3405	3397.5
					35	130	3213	3248	3230.5
AU312	Georgina 1	-29.145	115.074	C	5.0	117	1544	1549	1546.5
					10.0	110	1435	1445	1440
					18.0	090	1270	1288	1279
					12.0	090	1109	1121	1115
AU313	Dongara 20	-29.266	115.022	A	4.0	078	1781	1785	1783
					32.0	097	1660	1692	1676
					5.0	095	1639	1644	1641.5
					20.0	110	1505	1525	1515
					7.5	105	1436	1443.5	1439.75
					7.0	095	1242	1249	1245.5
					11.0	090	1223	1234	1228.5
					8.0	090	1040	1048	1044
					8.0	095	1028	1036	1032
					8.0	100	848	856	852
					3.0	100	776	779	777.5
					17.0	096	742	759	750.5
					19.0	080	719	738	728.5
AU314	Woodada 4	-29.835	115.141	C	41	124	1894	1935	1914.5
					37	092	1798	1835	1816.5
					12	132	1740	1752	1746
AU315	South Turtle Dove 1	-30.13	114.636	C	29.0	126	1242	1271	1256.5
					22.0	080	1215	1237	1226
					43.0	130	1151	1194	1172.5
AU316	Warro 1	-30.168	115.736	B	64	125	3920	3984	3952
					7	100	3894	3901	3897.5
					13	100	3875	3888	3881.5

Table D.3 continued...

Site	Well	Latitude	Longitude	Quality	Breakout Data				
					Length	Orientation	Top	Bottom	Aver. Depth
AU316	Warro 1	-30.168	115.736	B	18	100	3856	3874	3865
					22	105	3818	3840	3829
					20	085	3794	3814	3804
AU316	Warro 1	-30.168	115.736	B	28	095	3766	3794	3780
AU317	Mullaloo 1	-31.867	115.462	C	80.0	140	1915	1995	1955
					151.0	130	1764	1915	1839.5
					5.0	087	1625	1630	1627.5
					35.0	070	1395	1430	1412.5
					82.0	110	1205	1287	1246
					25.0	090	1157	1172	1164.5
					35.0	162	940	975	957.5
AU318	Geelvink 1A	-29.096	114.298	C	10.0	130	3085	3095	3090
					19.0	142	2927	2946	2936.5
					8.0	135	2919	2927	2923

Appendix E

Australian Stress Map Database

This appendix contains a subsection of the Australian Stress Map database (Table E.1). The first nine fields have been displayed containing the relevant information to reproduce all stress maps seen within this thesis. A total of 538 measurements have been listed below. A complete list of all the fields in the ASM database can be found in digital format on the attached CDROM under the database directory. A description of the abbreviations used in this table is listed at the end of the table and also on the ASM web page on the attached CDROM.

Table E.1 Subsection of the Australian Stress Map database.

Site	Lat.	Lon.	σ_{Hmax} Orientation	Type	Depth (km)	Quality	Regime	Locality
AU001	-19.582	113.533	100	BO	0	A	U	Jupiter 1
AU002	-17.624	124.501	055	BO	0.32	C	U	Bilna 1
AU003	-30.870	116.930	066	OC	0.006	C	TS	Wongan Hills Cousins
AU004	-31.390	116.350	093	OC	0.006	D	U	Goomalling
AU005	-31.690	116.350	149	OC	0.007	D	TS	Meckering
AU006	-32.210	117.200	097	OC	0.005	D	TS	Quajabin Peak
AU007	-32.370	117.200	034	OC	0.005	D	TS	Brookton
AU008	-32.660	117.170	079	OC	0.006	C	TS	Popanyinning
AU009	-31.110	116.470	102	FMS	1	C	SS	Calingri
AU010	-22.080	126.650	078	FMS	8	B	TF	E. Canning Basin
AU011	-25.010	136.370	145	FMS	12	D	TF	Simpson Desert
AU012	-34.170	150.320	073	FMS	21	C	TF	Picton
AU013	-19.694	115.848	145	BOC	2.5	B	U	Goodwyn #4
AU014	-19.572	116.137	126	BOC	2.875	B	U	North Rankin #5
AU015	-14.101	121.514	067	BOC	4.705	D	U	Scott Reef #2A
AU016	-35.410	150.360	012	OC	0.007	D	TF	Milton
AU017	-35.910	150.360	008	OC	0.004	D	TF	Moruya
AU018	-34.200	146.800	102	OC	0.009	D	TF	Ardlethon
AU019	-36.430	148.620	003	OC	0.009	D	TF	Jindabyne
AU020	-40.040	144.050	159	OC	0.075	D	U	Dolphin mine
AU021	-31.500	145.820	098	OC	0.439	B	TS	Cobar, NSW
AU022	-35.070	139.020	173	OC	0.058	D	U	Kanmantoo mine
AU023	-31.970	141.430	089	OC	1.258	D	U	North Broken Hill
AU024	-31.950	141.150	077	OC	0.743	D	U	ZC, New Broken Hill
AU025	-20.780	139.480	095	OC	0.864	C	TS	Mt. Isa, QLD
AU026	-19.450	133.950	032	OC	0.282	B	TS	Warrego mines
AU027	-31.200	121.670	098	OC	0.085	D	U	Durkin mine Kambalda
AU028	-20.215	115.066	139	BO	0	A	U	West Tryal Rocks #2
AU029	-20.000	145.000	045	GVA	0	E	U	Nulla Basalt prov.
AU030	-19.097	116.136	140	BO	3.028	C	U	Brigadier #1
AU031	-18.500	144.700	045	GVA	0	E	U	McBride volc. prov.
AU032	-12.195	124.496	090	BOC	3.638	E	U	Swan 2

Table E.1 continued...

Site	Lat.	Lon.	σ_{Hmax} Orientation	Type	Depth (km)	Quality	Regime	Locality
AU033	-18.277	122.401	055	BOC	1.025	C	U	Hedonia 1
AU034	-17.969	122.724	028	BOC	1.588	C	U	Cow Bore 1
AU035	-18.017	122.608	056	BOC	1.913	A	U	East Crab Creek
AU036	-17.260	123.829	048	BOC	2.238	B	U	Kora 1
AU037	-17.758	124.572	040	BOC	2.799	A	U	Boronia 1
AU038	-17.626	124.463	060	BOC	1.095	C	U	Hakea 1
AU039	-26.528	125.614	100	BOC	2.181	B	U	Kanpa 1A
AU040	-22.250	131.080	006	BOC	1.44	B	U	Davis 1
AU041	-24.227	133.896	004	BOC	2.5	D	U	Dingo 1
AU042	-25.572	143.058	065	BOC	2.16	C	U	Moothandella
AU043	-26.805	149.322	162	BOC	2.508	C	U	Lorelle 2
AU044	-27.550	149.661	136	BOC	2.923	C	U	Inglestone 1
AU045	-27.663	149.458	143	BOC	2	C	U	Waggamba 1
AU046	-38.319	148.436	122	BOC	2.537	D	U	Flounders
AU047	-38.555	148.549	135	BOC	2.537	C	U	Hapuku 1
AU048	-37.502	139.235	155	BOC	2.196	A	U	Morum 1
AU049	-38.374	148.239	080	BO	1.93	B	U	Fortescue 1
AU050	-38.251	147.854	127	BO	2.642	A	U	Whiting 2
AU051	-38.437	148.437	123	BOC	2.61	D	U	Selene 1
AU052	-38.613	147.717	116	BO	3.103	D	U	Omeo #1
AU053	-38.602	148.298	130	BOC	4.412	C	U	Hermes #1
AU054	-38.695	148.276	151	BOC	2.5	B	U	Helios #1
AU055	-38.197	147.808	138	BOC	2.8	C	U	Wirrah #3
AU056	-38.189	147.816	131	BO	2.538	A	U	Wirrah #1
AU057	-38.068	141.515	141	BOC	2.27	A	U	Break Sea Reef #1
AU058	-21.299	113.690	000	BOC	1.785	E	U	Resolution #1
AU059	-35.680	145.820	072	HFM	0.119	B	TF	Berrigan
AU060	-37.180	144.750	073	HFM	0.011	C	TS	Lancefield
AU061	-34.370	147.070	081	OC	0.007	D	TS	Mirrool
AU062	-30.800	117.030	060	OC	0.006	C	TS	Cadoux(Jones,Walker)
AU063	-30.700	117.150	101	OC	0.009	D	TF	Cadoux(Tank,FlatRock
AU064	-31.140	116.880	014	OC	0.007	D	TS	Oak Park
AU065	-33.330	117.400	179	OC	0.007	D	TS	Wagin
AU066	-32.970	117.380	068	OC	0.007	D	TS	Narrogin
AU067	-32.540	117.190	144	OC	0.007	D	TS	Pingelly
AU068	-30.670	117.160	174	OC	0.009	D	TF	Cadoux(Flat Rocks)
AU069	-26.190	132.770	066	FMS	1.5	C	TF	Marryat Creek, SA
AU070	-30.794	138.405	097	FMS	20	C	SS	Beltana, SA
AU072	-37.205	146.956	119	FMS	17	B	TF	Wonnangatta
AU073	-34.020	147.330	124	FMS	4	C	TF	West Wyalong
AU074	-36.690	148.330	095	FMS	6	D	SS	Suggan Buggan
AU075	-34.240	150.900	098	FMS	12	D	TF	Appin
AU076	-32.476	138.878	076	FMS	6.8	D	SS	Carrieton, SA
AU077	-30.730	117.210	075	FMS	2	B	TF	Cadoux, WA
AU079	-25.880	137.460	125	FMS	15	C	TF	Simpson Desert
AU080	-19.550	126.560	145	FMS	17	C	TF	Halls Creek
AU081	-32.389	138.923	153	FMS	16.4	D	SS	Yalpara, SA
AU082	-37.880	144.270	112	FMS	21	D	TF	Balliang
AU083	-32.300	139.310	059	FMS	15	C	SS	Melton, SA
AU084	-31.060	138.470	041	FMS	10	C	SS	Blinman, SA

Table E.1 continued...

Site	Lat.	Lon.	σ_{Hmax} Orientation	Type	Depth (km)	Quality	Regime	Locality
AU085	-34.660	148.880	154	FMA	12.5	D	SS	Bowning
AU086	-32.440	137.960	074	FMS	5	C	SS	Quorn, SA
AU087	-35.030	149.020	091	FMS	5	C	SS	Dalton Gunning
AU089	-34.220	147.470	003	FMS	4	C	SS	Temora
AU090	-36.220	148.780	136	FMC	5	D	SS	Middlingbank
AU092	-31.540	117.000	093	FMS	3	B	TF	Meckering, WA
AU093	-37.042	147.168	146	FMS	15	D	TF	Mt. Hotham,Vic.
AU094	-34.550	150.500	046	FMS	9	C	TF	Robertson
AU095	-36.220	149.640	147	FMS	15	D	TF	Berridale, NSW
AU096	-27.000	152.500	045	FMC	10	D	TF	Wivenhoe Dam
AU097	-34.750	149.190	140	FMS	4	D	TS	Dalton Gunning, NSW
AU098	-42.000	146.800	155	OC	0	E	U	Tasmania
AU099	-35.680	145.820	077	OC	0.004	D	TS	Berrigan
AU100	-34.780	149.170	082	FMS	3	C	TS	Dalton Gunning, NSW
AU101	-36.720	148.240	146	FMS	6	D	TF	Pilot
AU102	-30.370	116.940	070	HFM	0.064	C	TF	Wogan Hills Cousins
AU103	-19.810	133.980	017	FMA	6.5	A	TF	Tennant Creek, NT
AU104	-12.195	124.496	146	BOC	3.95	E	U	Swan 2
AU105	-38.632	143.143	000	BOC	2.73	E	U	Ross creek 1
AU106	-11.120	125.150	011	FMS	0	E	NF	NW shelf
AU107	-16.680	124.660	068	FMS	10	C	SS	Western Australia
AU108	-25.250	130.650	064	FMS	31	B	TF	Uluru, NT
AU109	-34.890	149.340	077	FMS	2	D	SS	Dalton-Gunning, NSW
AU110	-34.780	149.190	164	FMS	1	C	TF	Dalton-Gunning, NSW
AU111	-34.740	149.180	144	FMS	0	D	SS	Dalton-Gunning, NSW
AU112	-31.190	121.780	050	HFM	0.6	C	SS	Longshaft Mine, WA
AU113	-34.318	150.880	033	OC	0.43	D	TF	Corrimal Coll., NSW
AU114	-32.280	151.000	088	OC	0.18	D	SS	Liddell Coll., NSW
AU115	-32.591	151.044	146	HFM	0.103	B	TF	Wambo Colliery, NSW
AU116	-32.661	151.147	145	HFM	0.068	C	TF	Saxonvale Coll., NSW
AU117	-33.173	151.500	005	OC	0.09	D	TF	Moonee Colliery, NSW
AU118	-34.200	150.772	086	OC	0.48	D	SS	West Cliff Coll, NSW
AU119	-33.959	151.250	023	HFM	0.113	C	TF	Malabar, NSW
AU120	-33.892	151.261	048	HFM	0.093	C	TF	Bondi, NSW
AU121	-24.520	150.050	010	HFM	0.197	B	TF	Moura Mine, QLD
AU122	-23.250	148.540	048	HFM	0.131	B	TF	Oakey Ck Mine, QLD
AU123	-22.920	148.610	029	HFM	0.131	C	TF	German Ck Mine, QLD
AU124	-21.740	148.050	001	HFM	0.123	C	TF	Goonyella Mine, QLD
AU125	-21.593	148.173	017	HFM	0.169	D	SS	Burton Downs, QLD
AU126	-38.159	140.612	118	BO	1.717	D	U	Break Sea Reef 1
AU127	-37.228	140.161	116	BO	1.375	D	U	Greenways 1
AU128	-37.486	140.253	-	BO	1.651	E	U	Hatherleigh 1
AU129	-37.454	140.781	119	BO	1.575	C	U	Katnook 1
AU130	-37.451	140.789	013	BO	2.106	E	U	Katnook 2
AU131	-37.450	140.774	164	BO	1.822	D	U	Katnook 3
AU132	-37.468	140.781	119	BO	2.076	C	U	Ladbroke Grove 1
AU133	-37.323	140.155	-	BO	-	E	U	Reedy Creek 1
AU134	-38.349	140.873	121	BO	1.923	E	U	Sawpit 1
AU135	-37.404	140.033	143	BO	2.486	D	U	St. Clair 1
AU136	-37.414	140.666	131	BO	1.779	D	U	Zema 1

Table E.1 continued...

Site	Lat.	Lon.	σ_{Hmax} Orientation	Type	Depth (km)	Quality	Regime	Locality
AU137	-37.426	140.675	-	BO	-	E	U	Laira 1
AU138	-30.770	117.090	116	FMS	5	C	TF	Cadoux, WA
AU139	-34.810	149.170	094	FMS	5.3	C	TF	Oolong, NSW
AU140	-33.330	150.604	173	FMS	2	C	SS	Upper Colo, NSW
AU141	-31.500	138.350	130	FMC	3	C	TF	Moralana, SA
AU142	-31.370	138.640	120	FMS	3	D	U	Wilpena, SA
AU143	-33.432	150.149	066	FMS	5	C	SS	Lithgow, NSW
AU144	-36.107	141.539	098	FMS	6	B	SS	Nhill, VIC
AU145	-16.180	124.510	168	FMS	5	D	SS	Doubtful Bay, WA
AU146	-35.730	144.490	116	FMS	10	D	SS	Bunnaloo, NSW
AU147	-32.950	151.610	044	FMS	11.5	B	TF	Newcastle, NSW
AU149	-23.590	150.700	040	FMS	6	D	TF	Bajool, QLD
AU150	-31.760	139.420	086	FMS	5	D	SS	Lake Frome, SA
AU151	-32.510	122.220	104	FMS	10	D	NF	Norseman, WA
AU152	-35.280	149.110	111	FMS	2	D	TF	Canberra, ACT
AU153	-24.017	131.600	019	BO	1.3	E	U	East Mereenie 14
AU154	-24.033	131.633	031	BO	1.3	D	U	East Mereenie 20
AU155	-24.001	131.595	096	BO	0.94	D	U	East Mereenie 31
AU156	-24.000	131.583	059	BO	1.14	B	U	East Mereenie 33
AU157	-24.002	131.600	035	BO	1.25	D	U	East Mereenie 35
AU158	-24.000	131.590	016	BO	1.3	C	U	East Mereenie 36
AU159	-24.004	131.610	018	BO	1.4	A	U	East Mereenie 37
AU160	-23.994	131.580	001	BO	1.13	E	U	West Mereenie 8
AU161	-23.990	131.570	104	BO	1.4	E	U	West Mereenie 10
AU162	-24.020	131.600	088	BO	0.8	D	U	East Mereenie 13
AU163	-24.034	131.608	029	BO	1.25	D	U	East Mereenie 30
AU164	-24.034	131.596	053	BO	1.25	E	U	East Mereenie 32
AU165	-24.020	131.583	102	BO	1.2	C	U	East Mereenie 34
AU166	-24.020	131.591	103	BO	1.25	D	U	East Mereenie 38
AU167	-23.960	131.417	177	BO	1.3	A	U	West Mereenie 1
AU168	-23.940	131.440	070	BO	1	D	U	West Mereenie 4
AU169	-23.970	131.470	034	BO	1.25	D	U	West Mereenie 9
AU170	-23.980	131.460	038	BO	1.25	B	U	West Mereenie 11
AU171	-24.000	132.770	-	BO	0	E	U	Palm Valley 1
AU172	-24.002	132.650	-	BO	0	E	U	Palm Valley 2
AU173	-24.007	132.617	-	BO	0	E	U	Palm Valley 3
AU174	-23.898	132.650	175	BO	2.228	B	U	Palm Valley 4
AU175	-24.070	132.854	175	BO	1.64	B	U	Palm Valley 5
AU176	-23.999	132.728	020	BO	1.329	B	U	Palm Valley 7
AU177	-24.012	132.794	005	BO	1.068	C	U	Palm Valley 8
AU178	-24.003	132.683	000	BO	1.168	E	U	Palm Valley 9
AU179	-24.003	132.706	000	BO	0	E	U	Palm Valley 6
AU180	-16.517	123.578	066	FMS	10	C	SS	Cockatoo Is., WA
AU181	-27.633	140.423	100	BO	2.626	B	U	Wantana 1
AU182	-28.115	140.875	100	BO	1.076	B	U	Dullingari 27
AU183	-27.570	140.136	144	BO	2.393	B	U	Moorari 7
AU184	-28.106	140.875	076	BO	1.384	C	U	Dullingari 13
AU185	-28.361	139.974	130	BO	1.933	D	U	Daralingie 10
AU186	-27.590	140.117	152	BO	2.1	D	U	Woolkina 1
AU187	-28.083	140.854	083	BO	1.41	E	U	Dullingari 33

Table E.1 continued...

Site	Lat.	Lon.	σ_{Hmax} Orientation	Type	Depth (km)	Quality	Regime	Locality
AU189	-28.111	140.893	088	BO	1.995	D	U	Dullingari 24
AU190	-27.839	140.577	089	BO	2.818	A	U	Bullyeroo 1
AU191	-28.018	140.256	098	BO	2.575	A	U	Moomba 73
AU192	-28.040	140.128	104	BO	2.53	A	U	Moomba 74
AU194	-28.026	140.781	105	BO	1.852	A	U	Nappacoongee East 1
AU195	-33.816	138.984	100	FMS	20.4	B	TF	Burra, SA
AU196	-21.602	147.957	012	HFM	0.597	B	TF	Bowen Basin
AU197	-21.592	147.967	015	HFM	0.357	B	TF	Bowen Basin
AU198	-21.833	148.058	027	HFM	0.393	B	TF	Bowen Basin
AU199	-21.510	148.000	012	HFM	0.124	B	TF	Bowen Basin
AU200	-21.866	148.009	016	HFM	0.259	B	TF	Bowen Basin
AU201	-21.264	147.914	005	HFM	0.137	B	TF	Bowen Basin
AU202	-21.540	148.250	149	HFM	0.068	C	TF	Bowen Basin
AU203	-21.592	148.173	157	HFM	0.293	B	TF	Bowen Basin
AU204	-23.043	148.564	012	HFM	0.164	B	TF	Bowen Basin
AU205	-23.051	148.542	172	HFM	0.09	C	TF	Bowen Basin
AU206	-23.058	148.563	008	HFM	0.194	C	TF	Bowen Basin
AU207	-21.592	148.173	165	HFM	0.184	D	SS	Bowen Basin
AU208	-23.078	148.528	048	HFM	0.103	B	TF	Bowen Basin
AU209	-23.012	148.560	021	HFM	0.136	C	TF	Bowen Basin
AU210	-22.946	148.586	178	HFM	0.084	C	TF	Bowen Basin
AU211	-22.995	148.554	049	HFM	0.165	C	TF	Bowen Basin
AU212	-24.033	148.614	176	HFM	0.176	C	TF	Bowen Basin
AU213	-24.014	148.646	037	HFM	0.105	C	TF	Bowen Basin
AU214	-24.673	149.911	030	HFM	0.419	B	TF	Bowen Basin
AU215	-24.621	149.882	034	HFM	0.594	B	TF	Bowen Basin
AU216	-24.585	149.914	012	HFM	0.374	A	TF	Bowen Basin
AU217	-24.684	149.900	040	HFM	0.515	A	TF	Bowen Basin
AU218	-24.644	149.908	007	HFM	0.409	A	SS	Bowen Basin
AU219	-24.310	149.882	076	HFM	0.595	D	TF	Bowen Basin
AU220	-24.470	150.031	009	HFM	0.565	B	TF	Bowen Basin
AU221	-24.528	149.954	036	HFM	0.675	D	TF	Bowen Basin
AU222	-39.792	145.448	152	BO	2.665	B	U	Aroo 1
AU223	-39.633	145.151	000	BO	2.676	B	U	Koorkah 1
AU224	-40.074	145.978	138	BO	2.151	D	U	Nangkero 1
AU225	-40.262	145.864	014	BO	2.446	D	U	Pelican 3
AU226	-40.361	145.872	041	BO	2.427	B	U	Pelican 4
AU227	-40.345	145.864	135	BO	2.756	D	U	Pelican 5
AU228	-40.386	145.696	094	BO	1.517	D	U	Pipipa 1
AU229	-40.138	145.917	163	BO	3.114	D	U	Poonboon 1
AU230	-39.894	145.978	086	BO	2.953	D	U	Tilana 1
AU231	-39.410	145.396	030	BO	2.026	D	U	Toolka 1
AU232	-39.921	146.267	056	BO	1.462	D	U	Yurongi 1
AU233	-39.839	145.806	146	BO	2.258	D	U	Yolla 1
AU234	-37.442	140.830	140	BO	2.47	C	U	Haselgrove 1
AU235	-37.450	140.615	147	BO	1.31	D	U	Hungerford 1
AU236	-37.432	140.762	143	BO	2.138	D	U	Redman 1
AU237	-37.563	140.234	147	BO	2.263	A	U	Rendelsham
AU238	-37.313	139.617	114	BO	2.038	D	U	Sophia Jane 1
AU239	-37.409	140.872	130	BO	2.393	D	U	Wynn 1

Table E.1 continued...

Site	Lat.	Lon.	σ_{Hmax} Orientation	Type	Depth (km)	Quality	Regime	Locality
AU240	-33.366	150.140	171	HFM	0.312	C	TF	Sydney Basin
AU241	-33.385	150.140	092	HFM	0.314	C	TF	Sydney Basin
AU242	-33.384	150.145	081	HFM	0.323	C	TF	Sydney Basin
AU243	-33.392	150.145	086	HFM	0.327	D	TF	Sydney Basin
AU244	-33.394	150.149	113	HFM	0.363	D	TF	Sydney Basin
AU245	-33.382	150.145	100	HFM	0.255	D	TF	Sydney Basin
AU246	-33.386	150.150	080	HFM	0.349	B	TF	Sydney Basin
AU247	-33.392	150.160	129	HFM	0.354	C	TF	Sydney Basin
AU248	-33.396	150.158	150	HFM	0.346	D	TF	Sydney Basin
AU249	-33.391	150.162	133	HFM	0.273	D	TF	Sydney Basin
AU250	-33.363	150.163	080	HFM	0.349	B	TF	Sydney Basin
AU251	-33.361	150.161	142	HFM	0.322	D	TF	Sydney Basin
AU252	-21.592	148.173	176	HFM	0.194	B	SS	Bowen Basin
AU253	-21.592	148.173	000	HFM	0.252	C	SS	Bowen Basin
AU254	-32.188	150.849	103	HFM	0.217	D	TF	Sydney Basin
AU255	-32.441	150.802	060	HFM	0.24	B	TF	Sydney Basin
AU256	-32.438	150.835	061	HFM	0.321	B	TF	Sydney Basin
AU257	-33.825	151.264	036	HFM	0.112	D	TF	Sydney Basin
AU258	-33.972	151.247	025	HFM	0.119	B	TF	Sydney Basin
AU259	-33.377	151.383	070	HFM	0.635	B	TF	Sydney Basin
AU260	-33.082	151.400	017	HFM	0.218	D	TF	Sydney Basin
AU261	-33.082	151.400	164	HFM	0.146	C	TF	Sydney Basin
AU262	-33.082	151.400	043	HFM	0.207	B	TF	Sydney Basin
AU263	-33.241	151.196	079	HFM	0.831	A	TF	Sydney Basin
AU264	-32.900	151.244	078	HFM	0.226	C	TF	Sydney Basin
AU265	-32.355	151.256	052	HFM	0.492	C	TF	Sydney Basin
AU266	-33.897	151.193	041	HFM	0.63	B	TF	Sydney Basin
AU267	-33.972	151.229	037	HFM	0.5	A	TF	Sydney Basin
AU268	-33.892	151.249	037	HFM	0.04	D	TF	Sydney Basin
AU269	-33.872	151.200	008	HFM	0.009	D	TF	Sydney Basin
AU270	-33.882	151.197	011	HFM	0.006	D	TF	Sydney Basin
AU271	-33.880	151.196	179	HFM	0.01	D	TF	Sydney Basin
AU272	-33.830	151.226	140	HFM	0.094	C	TF	Sydney Basin
AU273	-33.819	151.251	178	HFM	0.08	D	TF	Sydney Basin
AU274	-24.760	150.045	004	HFM	0.386	B	TF	Bowen Basin
AU275	-24.760	150.045	-	HFM	-	E	TF	Bowen Basin
AU276	-24.760	150.045	023	HFM	0.416	B	TF	Bowen Basin
AU277	-23.800	148.894	000	OC	0.23	D	TF	Bowen Basin
AU278	-23.867	148.833	015	OC	0.12	D	NF	Bowen Basin
AU279	-21.240	147.947	004	OC	0.11	D	TF	Bowen Basin
AU280	-23.080	148.410	007	OC	0.09	D	SS	Bowen Basin
AU281	-21.764	148.038	005	OC	0.17	D	SS	Bowen Basin
AU282	-23.240	148.082	178	OC	0.23	D	TF	Bowen Basin
AU283	-23.707	148.864	020	OC	0.4	D	TF	Bowen Basin
AU284	-32.109	150.745	084	OC	0.19	D	SS	Sydney Basin
AU285	-32.500	150.952	086	OC	0.08	D	TF	Sydney Basin
AU286	-32.900	151.211	059	OC	0.55	D	TF	Sydney Basin
AU287	-32.909	151.500	016	OC	0.19	D	TF	Sydney Basin
AU288	-32.900	151.600	000	OC	0.1	D	TF	Sydney Basin
AU289	-33.182	151.228	066	OC	0.25	D	TF	Sydney Basin

Table E.1 continued...

Site	Lat.	Lon.	σ_{Hmax} Orientation	Type	Depth (km)	Quality	Regime	Locality
AU290	-33.959	151.250	029	OC	0.125	D	TF	Sydney Basin
AU291	-33.982	150.473	104	OC	0.3	D	TF	Sydney Basin
AU292	-34.018	150.457	074	OC	0.472	D	TF	Sydney Basin
AU293	-34.182	150.755	075	OC	0.45	D	TF	Sydney Basin
AU294	-34.200	150.554	038	OC	0.43	D	TF	Sydney Basin
AU295	-34.236	150.706	005	OC	0.5	D	TF	Sydney Basin
AU296	-34.200	150.880	060	OC	0.5	D	TF	Sydney Basin
AU297	-34.168	150.951	048	OC	0.5	D	SS	Sydney Basin
AU298	-34.255	150.913	000	OC	0.35	D	TF	Sydney Basin
AU299	-34.473	150.701	107	OC	0.4	D	TF	Sydney Basin
AU300	-33.436	150.239	063	OC	0.2	D	SS	Sydney Basin
AU301	-34.191	150.770	018	BO	0.4	A	U	Appin 1
AU302	-28.899	114.260	088	BO	2.335	D	U	Batavia 1
AU303	-29.714	115.185	015	BO	2.813	B	U	Beekeeper 1
AU304	-30.248	115.415	096	BO	2.883	B	U	Coomallo 1
AU305	-29.237	115.016	142	BO	1.173	D	U	Dongara 24
AU306	-29.883	115.151	171	BO	1.762	D	U	Indoon 1
AU307	-32.920	115.660	074	BO	3.508	B	U	Lake Preston 1
AU308	-32.915	115.052	062	BO	3.434	C	U	Sugarloaf 1
AU309	-30.701	115.472	113	BO	3.514	B	U	Walyering 2
AU310	-30.666	115.492	110	BO	2.406	B	U	Walyering 3
AU311	-29.301	115.171	127	BO	3.448	C	U	Warradong 1
AU312	-29.145	115.074	095	BO	1.345	C	U	Georgina 1
AU313	-29.266	115.022	093	BO	1.211	A	U	Dongara 20
AU314	-29.835	115.414	110	BO	1.826	C	U	Woodada 4
AU315	-30.130	114.636	118	BO	1.218	C	U	South Turtle Dove 1B
AU316	-30.168	115.736	099	BO	1.176	B	U	Warro 1
AU317	-31.867	115.462	122	BO	1.458	C	U	Mullaloo 1
AU318	-29.096	114.298	135	BO	2.983	C	U	Geelvink 1A
AU319	-28.035	139.992	104	BO	1.885	B	U	Gidealpa 54
AU320	-27.563	140.651	118	BO	2.079	B	U	Pondrinie 9
AU321	-27.839	140.577	097	DTF	2.818	B	U	Bulyeroo 1
AU323	-28.018	140.256	104	DTF	2.75	B	U	Moomba 73
AU324	-28.026	140.781	102	DTF	1.852	B	U	Nappacoongee East 1
AU325	-27.563	140.651	102	DTF	2.079	C	U	Pondrinie 9
AU326	-28.038	140.001	080	DTF	-	D	U	Gidealpa 55
AU327	-37.212	140.667	124	BO	0.659	A	U	Killanoola DW1
AU328	-35.479	134.930	133	BO	4.275	A	U	Greenly 1
AU329	-35.845	135.687	147	BO	2.593	C	U	Borda 1
IS077	-4.500	140.030	175	FMS	19.6	B	TF	E. Irian Jaya
IS078	-4.580	140.140	069	FMS	16.3	B	SS	E. Irian Jaya
IS079	-4.580	140.140	119	FMS	13.4	B	NF	E. Irian Jaya
IS080	-4.520	140.240	033	FMS	23	B	SS	E. Irian Jaya
IS081	-4.560	139.950	048	FMS	22.6	B	TF	E. Irian Jaya
IS082	-4.540	139.930	047	FMS	8.1	B	SS	E. Irian Jaya
IS083	-4.560	139.280	056	FMS	10.2	B	SS	E. Irian Jaya
IS084	-4.550	138.950	042	FMS	44.6	B	TF	E. Irian Jaya
IS085	-4.100	135.650	178	FMS	7.4	B	SS	W. Irian Jaya
IS086	-4.320	134.260	018	FMS	9.8	B	SS	W. Irian Jaya
IS087	-4.250	135.140	036	FMS	19.2	E	U	W. Irian Jaya

Table E.1 continued...

Site	Lat.	Lon.	σ_{Hmax} Orientation	Type	Depth (km)	Quality	Regime	Locality
IS088	-4.150	135.990	045	FMS	15.4	B	TF	W. Irian Jaya
IS089	-4.100	136.280	065	FMS	6.8	B	SS	W. Irian Jaya
IS090	-4.120	136.250	043	FMS	11.3	B	SS	W. Irian Jaya
IS091	-4.090	136.070	050	FMS	9.6	B	SS	W. Irian Jaya
IS142	-4.680	133.920	022	FMS	15	C	NF	West Irian Region
IS147	-3.360	136.080	160	FMS	15	C	SS	West Irian Region
IS148	-2.970	137.140	173	FMS	18.1	C	TF	West Irian
IS149	-0.820	135.570	076	FMS	21.4	C	NF	West Irian Region
IS151	-3.530	143.760	059	FMS	15	C	TF	Near N Coast of PNG
IS155	-3.550	143.030	040	FMS	15	C	SS	Near N Coast of PNG
IS157	-2.760	139.460	026	FMS	28.6	C	TF	Coast of PNG
IS158	-2.730	139.390	023	FMS	22.7	C	TF	Coast of PNG
IS170	-0.880	136.360	100	FMS	15	C	NF	West Irian Region
IS171	-0.900	136.100	-	FMS	33.2	E	U	West Irian Region
IS173	-0.700	136.420	057	FMS	15	C	NS	West Irian Region
IS174	-1.280	136.520	040	FMS	15	C	SS	West Irian Region
IS176	-0.850	136.150	027	FMS	15	C	NF	West Irian Region
IS177	-0.510	135.740	065	FMS	15	C	NF	West Irian Region
IS178	-1.010	135.990	078	FMS	15	C	NF	West Irian Region
IS179	-0.640	135.890	032	FMS	15	C	TF	West Irian Region
IS180	-0.670	136.620	031	FMS	15	C	TF	West Irian Region
IS182	-0.690	136.120	028	FMS	27.2	C	TF	West Irian Region
IS183	-0.420	135.480	038	FMS	15	C	SS	West Irian Region
IS184	-1.110	136.380	045	FMS	33	C	SS	West Irian Region
IS186	-3.020	139.430	058	FMS	20.3	C	TF	West Irian
IS187	-1.110	136.870	-	FMS	15	E	U	West Irian Region
IS188	-1.590	136.540	067	FMS	16.5	C	SS	West Irian Region
IS190	-1.490	136.860	-	FMS	15	E	U	West Irian Region
IS196	-0.890	137.280	026	FMS	15	C	TF	West Irian Region
IS197	-0.960	137.790	020	FMS	28.5	C	TF	West Irian Region
IU039	-11.160	118.410	076	FMS	29	B	NF	Sumba
IU040	-15.970	117.570	122	BOT	1.054	C	U	ODP Hole 765D
IU047	-40.450	155.610	155	FMS	20	B	TF	Tasman Sea
PG001	-6.870	144.270	010	FMS	11.3	B	TF	central
PG002	-6.290	144.450	166	FMS	22.9	B	TF	central
PG003	-6.350	144.410	177	FMS	21	B	TF	central
PG004	-6.110	143.200	073	FMS	0.5	B	TF	central
PI050	-1.400	137.950	178	FMS	16.7	C	TF	Coast of PNG
PP072	-6.170	146.890	034	FMS	26.4	C	TF	East PNG
PP080	-3.620	146.330	049	FMS	23.4	C	SS	Near N Coast of PNG
PP097	-6.070	147.640	011	FMS	57	E	TF	East PNG
PP140	-6.030	146.740	-	FMS	23.3	E	U	East PNG
PP155	-2.060	140.380	071	FMS	15	C	NF	Coast of PNG
PP183	-6.490	146.570	026	FMS	15	C	TF	East PNG
PP185	-6.010	146.740	-	FMS	25.2	E	U	East PNG
PP191	-3.540	146.890	049	FMS	15	C	SS	Bismarck Sea
PP198	-6.510	146.240	017	FMS	26.4	C	SS	East PNG
PP199	-6.460	147.890	010	FMS	35	C	TF	East PNG
XA001	-20.533	115.633	094	BO	2.225	B	U	Bambra 1
XA002	-20.417	115.717	092	BO	1.967	A	U	Campbell 2

Table E.1 continued...

Site	Lat.	Lon.	σ_{Hmax} Orientation	Type	Depth (km)	Quality	Regime	Locality
XA003	-21.300	115.233	105	BO	1.308	D	U	Chervil 1
XA004	-21.167	114.683	110	BO	2.563	B	U	Chinook
XA005	-20.017	116.550	162	BO	0.651	D	U	Coojong 1
XA006	-19.567	116.500	116	BO	2.927	C	U	Cossack 1
XA007	-21.383	115.183	139	BO	2.028	D	U	Dillson 1
XA008	-20.533	115.783	101	BO	1.955	B	U	Emma 1
XA009	-20.767	115.583	093	BO	1.492	D	U	Flores 1
XA010	-19.683	115.883	108	BO	2.327	E	U	Goodwyn 1
XA011	-19.733	115.867	048	BO	0.702	C	U	Goodwyn 3A
XA012	-19.633	115.900	050	BO	2.897	B	U	Goodwyn 8B
XA013	-19.600	115.967	039	BO	3.016	C	U	Goodwyn 9A
XA014	-21.233	114.617	107	BO	2.943	B	U	Griffin 1
XA015	-21.217	114.617	114	BO	2.425	D	U	Griffin 2
XA016	-21.233	114.617	033	BO	2.631	C	U	Griffin 3
XA017	-21.217	114.633	113	BO	2.045	C	U	Griffin 4
XA018	-20.033	116.833	107	BO	0.818	E	U	Kanji 1
XA019	-20.500	115.167	105	BO	1.088	A	U	Maitland 1
XA020	-20.600	115.633	080	BO	1.696	B	U	Marra 1
XA021	-20.083	116.283	034	BO	2.248	E	U	Montebello 1
XA022	-21.550	114.317	100	BO	1.376	B	U	Santo 1
XA023	-21.183	114.700	110	BO	2.732	D	U	Scindian 1A
XA024	-21.217	114.683	110	BO	2.166	D	U	Scindian 2
XA025	-21.333	115.200	055	BO	1.542	B	U	South Chervil 1
XA026	-21.117	115.267	046	BO	2.197	E	U	South Pepper 1
XA027	-20.683	115.600	056	BO	1.838	D	U	Tanami 2
XA028	-20.167	116.467	149	BO	0.689	B	U	Tingle 1
XA029	-19.167	117.317	002	BO	2.449	D	U	Trafalgar 1
XA030	-22.283	114.067	057	BO	1.401	D	U	Trealla 1A
XA031	-20.517	115.717	102	BO	1.679	D	U	Ulidia 1
XA032	-19.583	116.433	094	BO	3.037	A	U	Wanaea 1
XA033	-19.617	116.417	099	BO	2.944	A	U	Wanaea 2
XA034	-19.567	116.433	099	BO	2.892	C	U	Wanaea 3
XA035	-20.133	116.417	055	BO	0.948	D	U	Wandoo 1
XA036	-20.117	116.433	053	BO	0.814	E	U	Wandoo 2
XA037	-20.133	116.433	160	BO	0.594	B	U	Wandoo 3
XA038	-20.150	116.433	025	BO	0.56	D	U	Wandoo 5
XA039	-20.117	116.433	041	BO	0.69	B	U	Wandoo 7
XA040	-20.883	114.917	094	BO	2.868	A	U	West Barrow 1A
XA041	-21.567	114.217	085	BO	0.96	E	U	West Muiron 3
XA042	-21.533	114.200	084	BO	1.175	D	U	West Muiron 4
XA043	-16.660	120.160	091	FMS	26	B	SS	Broome
XA044	-3.740	140.360	028	FMS	29.3	C	TF	West Irian
XA045	-2.610	134.210	022	FMS	53.5	E	NF	West Irian Region
XA046	-4.370	134.390	011	FMS	15	C	SS	West Irian Region
XA047	-3.470	135.600	001	FMS	33.2	C	TF	West Irian Region
XA048	-2.900	134.280	019	FMS	15	C	NF	West Irian Region
XA049	-4.230	135.130	036	FMS	24.8	C	SS	West Irian Region
XA050	-4.180	135.100	032	FMS	19	C	SS	West Irian Region
XA051	-4.230	134.850	012	FMS	15	C	TF	West Irian Region
XA052	-3.950	135.220	178	FMS	16.7	C	SS	West Irian Region

Table E.1 continued...

Site	Lat.	Lon.	σ_{Hmax} Orientation	Type	Depth (km)	Quality	Regime	Locality
XA053	-3.810	135.500	000	FMS	30.3	C	SS	West Irian Region
XA054	-4.500	134.740	024	FMS	18.4	C	SS	West Irian Region
XA055	-3.580	134.770	165	FMS	15	C	SS	West Irian Region
XA056	-3.260	134.560	005	FMS	15	C	NF	West Irian Region
XA057	-3.800	135.180	159	FMS	15	C	SS	West Irian Region
XA058	-3.030	138.770	-	FMS	67.6	E	U	West Irian
XC001	-12.633	124.783	046	BO	2.681	D	U	Anderdon 1
XC002	-11.967	124.950	160	BO	2.127	E	U	Arunta 1
XC003	-11.367	125.767	045	BO	1.547	D	U	Avocet 2
XC004	-10.574	129.981	033	BO	2.678	D	U	Beluga 1
XC005	-12.133	124.933	059	BO	1.69	B	U	Cassini 2
XC006	-12.117	125.000	079	BO	1.57	D	U	Challis 1
XC007	-12.117	125.017	065	BO	1.442	D	U	Challis 3
XC008	-12.117	125.000	073	BO	1.362	B	U	Challis 5
XC009	-12.117	125.000	072	BO	1.394	C	U	Challis 8
XC010	-12.133	125.017	047	BO	1.775	C	U	Challis 10
XC011	-12.117	125.050	052	BO	1.417	B	U	Challis 11
XC012	-12.117	125.000	062	BO	1.428	B	U	Challis 12
XC013	-10.918	126.166	048	BO	2.322	E	U	Cleia 1
XC014	-12.767	124.667	000	BO	2.155	B	U	Conway 1
XC015	-11.133	125.267	052	BO	2.524	A	U	Dillon Shoals 1
XC016	-12.883	123.817	082	BO	3.475	D	U	Discorbis 1
XC017	-11.283	125.833	061	BO	1.89	C	U	Drake 1
XC018	-12.233	124.633	085	BO	2.44	D	U	Eclipse 2
XC019	-11.567	125.133	051	BO	2.542	C	U	Fagin 1
XC020	-11.367	125.917	058	BO	1.827	D	U	Garganey 1
XC021	-12.267	124.150	023	BO	2.094	D	U	Grebe 1
XC022	-12.317	126.917	097	BO	2.064	D	U	Harbinger 1
XC023	-11.283	126.550	133	BO	3.668	D	U	Iris 1
XC024	-11.933	125.000	061	BO	2.221	B	U	Jabiru 1A
XC025	-11.933	125.017	018	BO	1.618	D	U	Jabiru 6
XC026	-11.917	125.017	046	BO	1.573	B	U	Jabiru 7
XC027	-11.950	124.983	061	BO	1.585	B	U	Jabiru 9
XC028	-13.033	123.867	060	BO	2.72	D	U	Kalyptea 1
XC029	-12.017	124.533	046	BO	3.3	D	U	Maple 1
XC030	-12.683	124.533	091	BO	2.854	E	U	Montara 1
XC031	-11.650	125.217	056	BO	1.538	D	U	Nome 1
XC032	-12.183	124.200	044	BO	2.021	D	U	Puffin 1
XC033	-11.933	124.333	061	BO	2.188	C	U	Rainbow 1
XC034	-12.067	125.017	073	BO	1.797	D	U	Rainier 1
XC035	-12.483	124.383	067	BO	2.921	B	U	Rowan 1
XC036	-12.037	126.651	063	BO	2.431	D	U	Shalimar 1
XC037	-12.500	124.400	044	BO	2.265	E	U	Skua 2
XC038	-12.483	124.433	061	BO	2.354	D	U	Skua 4
XC039	-12.467	124.433	044	BO	2.363	D	U	Skua 5
XC040	-12.483	124.433	115	BO	2.113	C	U	Suka 6
XC041	-12.500	124.417	173	BO	2.254	D	U	Suka 9
XC042	-12.117	124.300	079	BO	3.63	D	U	Swan 2
XC043	-12.533	124.450	020	BO	2.121	D	U	Swift 1
XC044	-12.617	124.583	014	BO	2.924	E	U	Taltarni 1

Table E.1 continued...

Site	Lat.	Lon.	σ_{Hmax} Orientation	Type	Depth (km)	Quality	Regime	Locality
XC045	-12.150	124.333	122	BO	2.352	D	U	Vulcan 1B
XC046	-12.383	124.083	070	BO	2.559	B	U	Woodbine 1
XC047	-11.280	125.572	040	BO	1.459	D	U	Keppler 1
XC048	-11.193	125.332	039	BO	2.422	B	U	Voltaire 1
XC049	-11.000	127.150	053	BO	3.505	B	U	Fohn 1
XC050	-10.600	126.783	061	BO	2.346	D	U	Mandar 1
XC051	-10.574	129.981	034	DTF	2.778	A	U	Beluga 1
XC052	-10.569	126.111	014	BO	3.325	A	U	Jahal 1
XC053	-10.628	126.028	001	BO	3.09	B	U	Laminaria 1
XC054	-10.779	126.372	048	BO	2.934	A	U	Squilla 1
XC055	-10.852	126.470	030	BO	3.074	B	U	Kakatua 1
XC056	-10.926	126.509	066	BO	2.818	A	U	Sandang 1
XC057	-10.883	126.536	043	BO	3.139	A	U	Elang West 1
XC058	-10.884	126.600	062	BO	2.526	A	U	Elang 1
XC059	-10.880	126.586	063	BO	2.108	B	U	Elang 2
XC060	-10.883	126.619	057	BO	2.548	A	U	Elang 3
XC061	-11.043	126.604	062	BO	3.081	A	U	Undan 1
XC062	-11.076	126.572	050	BO	3.104	B	U	Undan 2
XC063	-11.068	126.646	042	BO	3.067	B	U	Undan 3
XC064	-11.046	126.549	045	BO	3.163	A	U	Undan 4
XC065	-11.095	126.675	049	BO	3.064	A	U	Bayu 1
XC066	-11.040	126.694	056	BO	3.074	B	U	Bayu 2
XC067	-11.059	126.739	038	BO	3.084	B	U	Bayu 3
XC068	-11.011	126.698	051	BO	3.249	B	U	Bayu 4
XC069	-11.057	126.792	061	BO	3.194	B	U	Mistral 1
XC070	-10.641	126.872	036	BO	2.418	A	U	Naga 1
XC071	-10.804	127.298	046	BO	2.473	A	U	Basillsk 1
XC072	-10.448	126.194	022	DTF	3.438	C	U	Barncle 1
XC073	-10.569	126.111	030	DTF	3.226	B	U	Jahal 1
XC074	-10.628	126.028	026	DTF	3.099	D	U	Laminaria 1
XC075	-10.779	126.372	022	DTF	3.236	C	U	Squilla 1
XC076	-10.844	126.468	046	DTF	2.931	B	U	Katatua North 1
XC077	-10.852	126.470	035	DTF	3.032	B	U	Kakatua 1
XC078	-10.926	126.509	045	DTF	3.095	A	U	Sandang 1
XC079	-10.883	126.536	045	DTF	3.034	A	U	Elang West 1
XC080	-10.884	126.600	042	DTF	2.808	A	U	Elang 1
XC081	-10.880	126.586	052	DTF	1.899	A	U	Elang 2
XC082	-10.883	126.619	052	DTF	2.576	B	U	Elang 3
XC083	-11.043	126.604	044	DTF	3.028	B	U	Undan 1
XC084	-11.076	126.572	039	DTF	2.998	B	U	Undan 2
XC085	-11.068	126.646	040	DTF	3.025	A	U	Undan 3
XC086	-11.046	126.549	039	DTF	3.033	A	U	Undan 4
XC087	-11.095	126.675	036	DTF	3.007	A	U	Bayu 1
XC088	-11.040	126.694	045	DTF	2.944	A	U	Bayu 2
XC089	-11.059	126.739	048	DTF	3.01	B	U	Bayu 3
XC090	-11.011	126.698	041	DTF	3.192	A	U	Bayu 4
XC091	-11.057	126.792	051	DTF	3.056	D	U	Mistril 1
XC092	-10.804	127.298	050	DTF	2.91	A	U	Basillsk 1
XC093	-14.532	129.052	053	BO	2.092	A	U	Barnett 2
XC094	-14.530	129.061	061	BO	1.635	A	U	Barnett 1

Table E.1 continued...

Site	Lat.	Lon.	σ_{Hmax} Orientation	Type	Depth (km)	Quality	Regime	Locality
XC095	-14.290	128.433	053	BO	1.252	B	U	Cambridge 1
XC096	-12.126	125.628	053	BO	2.554	E	U	Crane 1
XC097	-11.471	128.164	040	BO	3.137	A	U	Jacaranda 1
XC098	-10.104	126.993	047	BO	2.503	E	U	Kelp 1
XC099	-14.778	129.111	061	BO	2.675	A	U	Kingfisher 1
XC100	-14.573	129.421	050	BO	1.075	D	U	Sunbird 1

(1) Measurement type abbreviations are as follows: BO = borehole breakout orientation from analysis of individual breakouts; BOC = borehole breakout orientation from analysis of cross-sectional shape of entire well; BOT = borehole breakout orientation from televiewer-imaged shapes of individual breakouts; FMS = single focal mechanism; FMA = average or inversion of several focal mechanisms; FMC = composite focal mechanism; HF = hydraulic fracturing measurement, no magnitude information; HFM = Hydraulic fracturing measurement, magnitude reported for maximum depth; OC = overcoring or other strain-relief stress measurement; GVA = geologic-volcanic vent alignment.
(2) Stress regime abbreviations are as follows: TF = thrust/reverse faulting ($\sigma_{Hmax}>\sigma_{hmin}>\sigma_v$); TS = thrust/reverse with strike-slip component; SS = strike-slip faulting ($\sigma_{Hmax}>\sigma_v>\sigma_{hmin}$); NS = normal with strike-slip component; NF = normal faulting ($\sigma_v>\sigma_{Hmax}>\sigma_{hmin}$); U = unknown.

Appendix F

Stress Province Statistics and Maps

This appendix contains detailed stress maps of the 16 stress provinces combined with a statistical analysis for each province. The position of the 16 stress provinces in relation to continental Australia is shown in Figure F.1. The 16 stress provinces cover 90% of the A-C quality indicators within the ASM database. The more variable D quality indicators are also included in this analysis to demonstrate the consistency of the mean σ_{Hmax} orientation within each stress province.

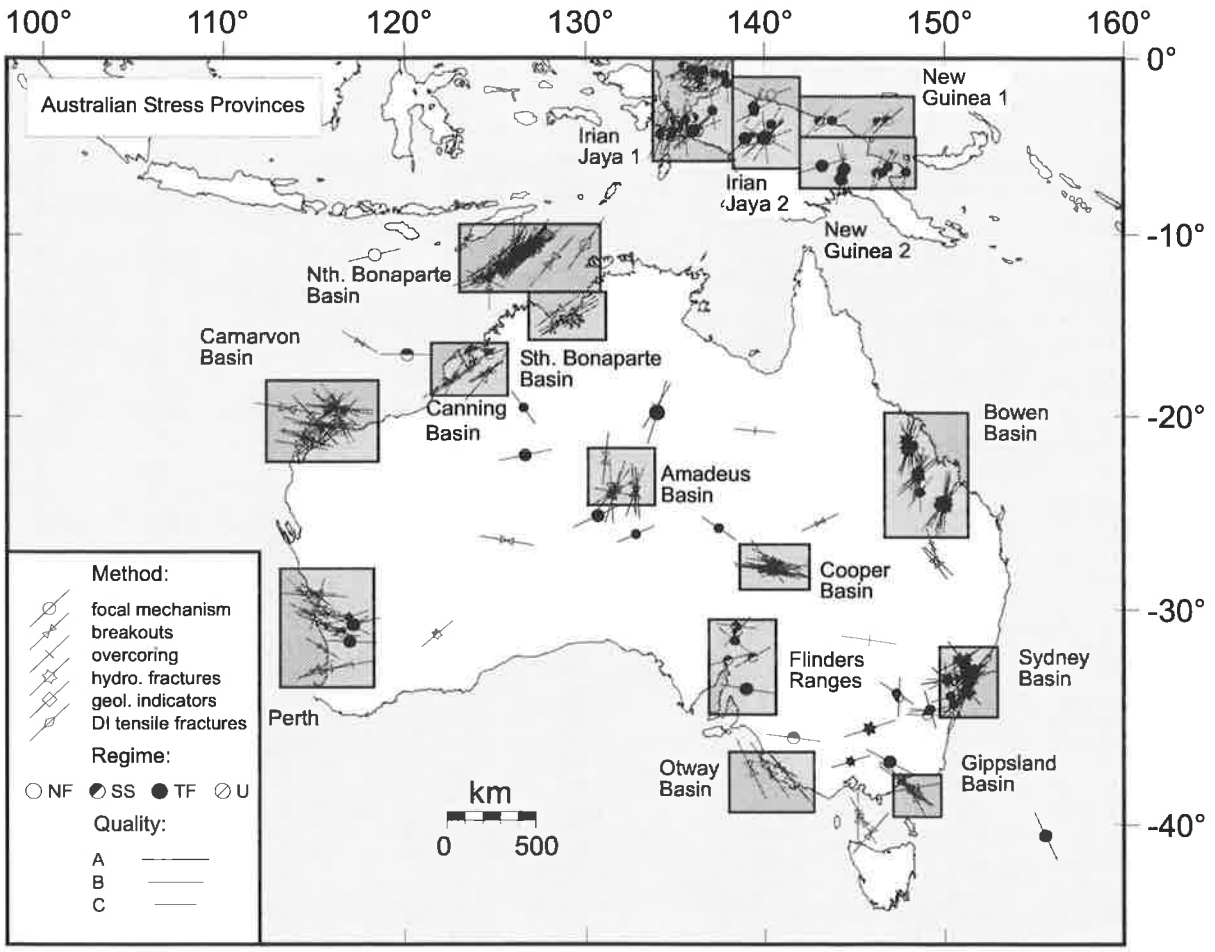

Figure F.1 Outline of the 16 stress provinces for the Australian continent using the A-C quality data. Details of all the stress data within each province are included in this appendix.

Amadeus Basin

The Amadeus Basin stress province is a sub-section of data from the ASM database bound by latitude –21.5° to –24.5° and longitude 131° to 133.5°.

Table F.1 Statistical analysis by indicator quality from data located in the Amadeus Basin stress province. N indicates number weighted and Q indicates quality weighted (A = 4, B = 3, C =2, D = 1).

	A	A-B N	A-B Q	A-C N	A-C Q	A-D N	A-D Q
Mean	008	014	013	013	013	029	019
Std.	11	22	21	27	25	38	31
$\overline{R}$	0.934	0.750	0.763	0.632	0.679	0.423	0.551
Number	2	8	8	11	11	19	19
% Pass	-	99	99	99	99	95	99

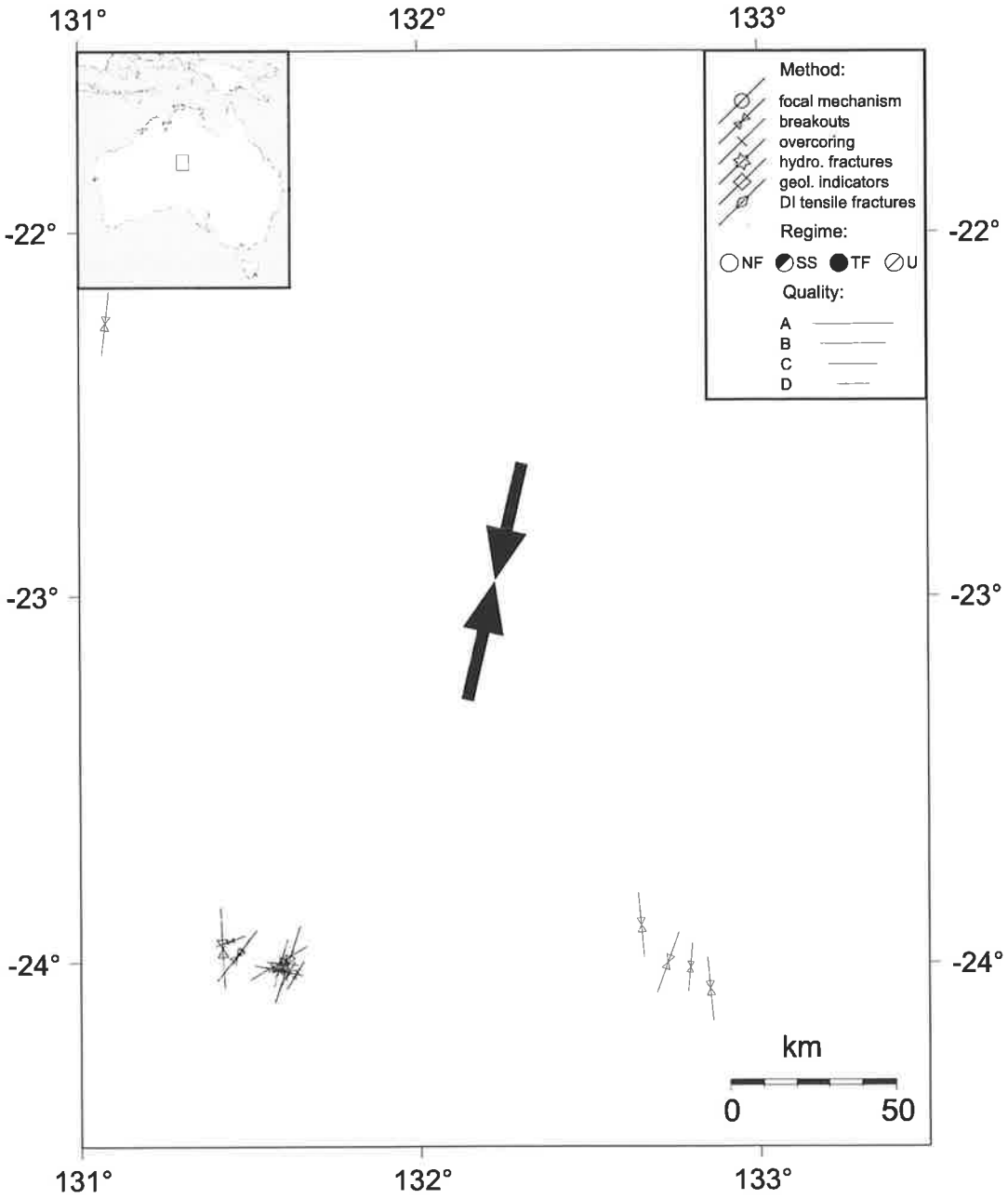

Figure F.2 Stress field of the Amadeus Basin stress province with the large arrow defining the average σ_{Hmax} orientation of the A-C quality data used in the analysis of the regional stress field.

Northern Bonaparte Basin

The Northern Bonaparte Basin stress province is a sub-section of data from the ASM database bound by latitude –9° to –13.5° and longitude 123° to 131°.

Table F.2 Statistical analysis by indicator quality from data located in the Northern Bonaparte Basin stress province. N indicates number weighted and Q indicates quality weighted (A = 4, B = 3, C =2, D = 1).

	A	A-B N	A-B Q	A-C N	A-C Q	A-D N	A-D Q
Mean	045	047	047	048	047	049	048
Std	10	14	14	16	15	21	17
$\overline{R}$	0.936	0.884	0.891	0.849	0.869	0.767	0.833
Number	24	52	52	60	60	88	88
% Pass	99.9	99.9	99.9	99.9	99.9	99.9	99.9

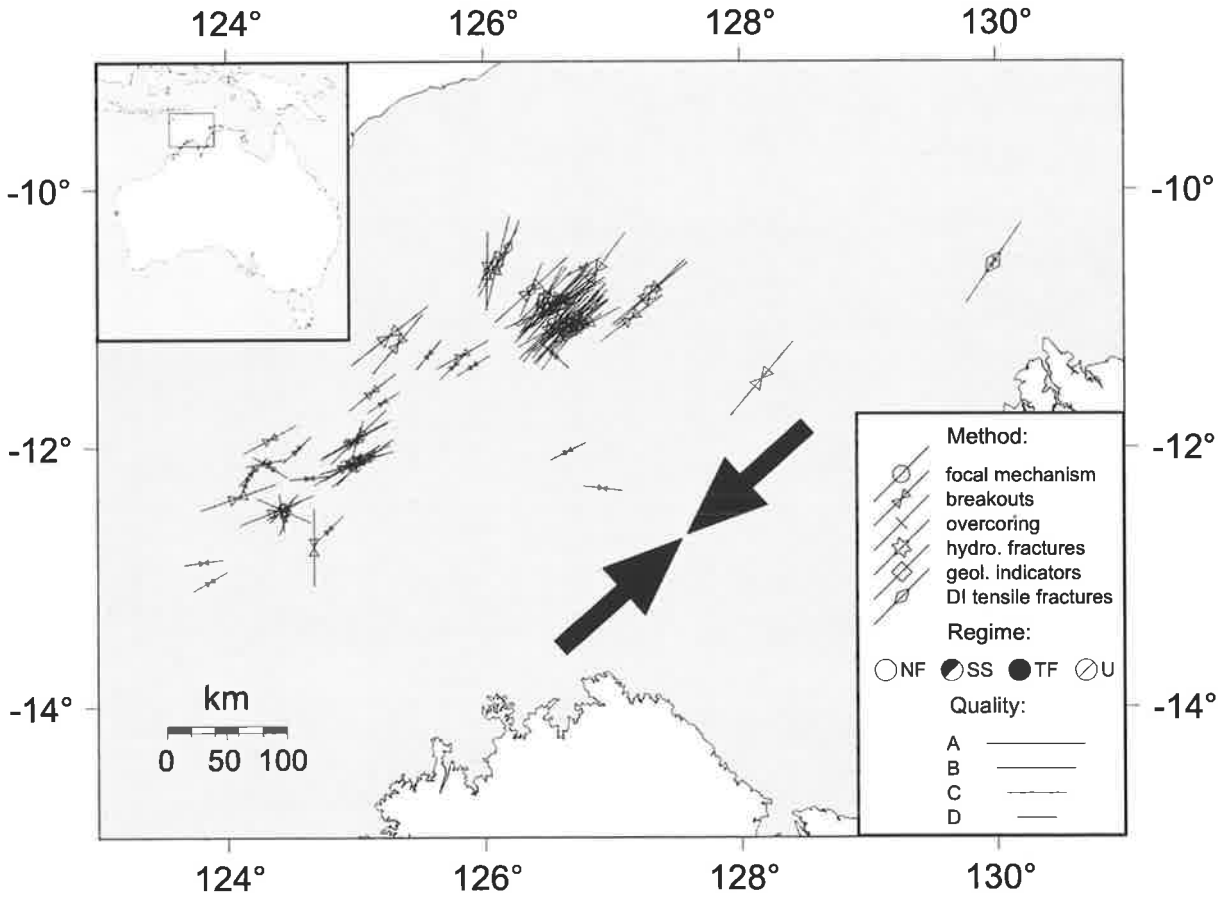

Figure F.3 Stress field of the Northern Bonaparte Basin stress province with the large arrow defining the average σ_{Hmax} orientation of the A-C quality data used in the analysis of the regional stress field.

Southern Bonaparte Basin

The Southern Bonaparte Basin stress province is a sub-section of data from the ASM database bound by latitude –13.5° to –16° and longitude 127° to 131°.

Table F.3 Statistical analysis by indicator quality from data located in the Southern Bonaparte Basin stress province. N indicates number weighted and Q indicates quality weighted (A = 4, B = 3, C =2, D = 1).

	A	A-B N	A-B Q	A-C N	A-C Q	A-D N	A-D Q
Mean	058	057	057	057	057	056	057
Std	4	4	4	4	4	5	4
$\overline{R}$	0.991	0.990	0.990	0.990	0.990	0.987	0.989
Number	3	4	4	4	4	5	5
% Pass	-	99	99	99	99	99	99

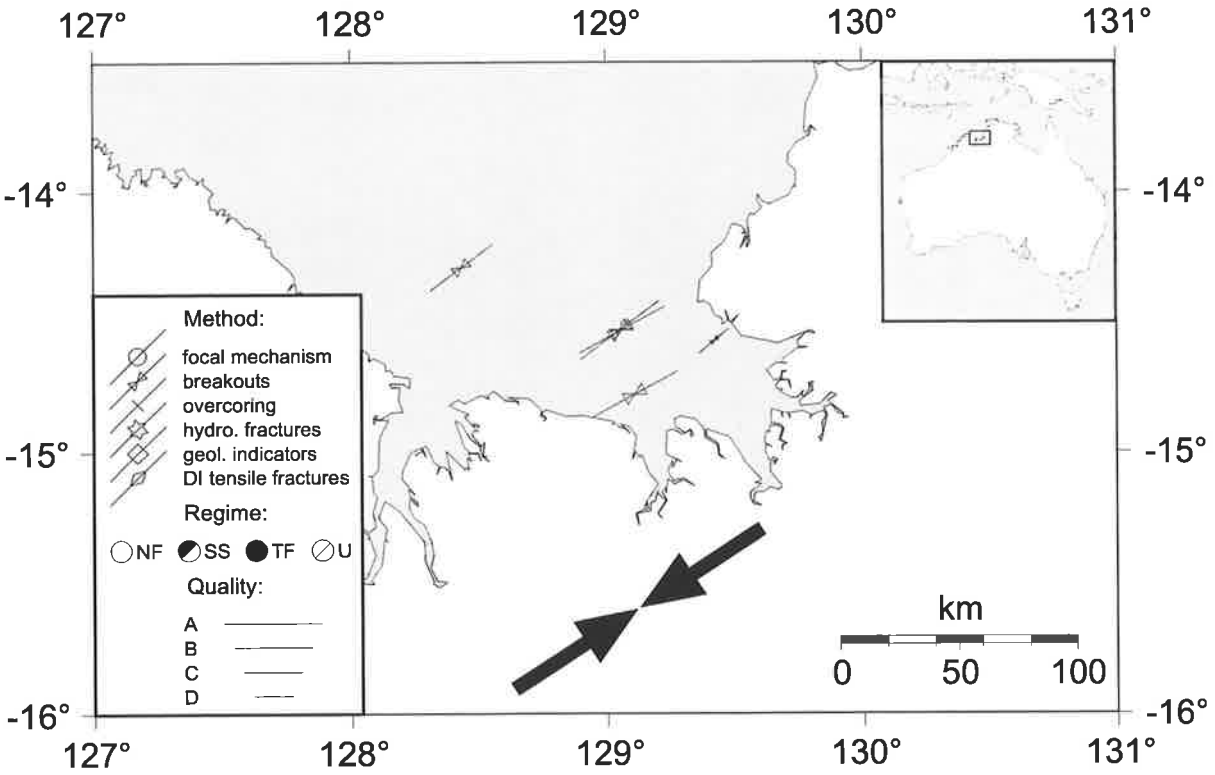

Figure F.4 Stress field of the Southern Bonaparte Basin stress province with the large arrow defining the average σ_{Hmax} orientation of the A-C quality data used in the analysis of the regional stress field.

Bowen Basin

The Bowen Basin stress province is a sub-section of data from the ASM database bound by latitude –20° to –25.5° and longitude 14° to 152°.

Table F.4 Statistical analysis by indicator quality from data located in the Bowen Basin stress province. N indicates number weighted and Q indicates quality weighted (A = 4, B = 3, C =2, D = 1).

	A	A-B N	A-B Q	A-C N	A-C Q	A-D N	A-D Q
Mean	019	017	017	014	015	014	015
Std	15	17	17	19	19	20	19
$\overline{R}$	0.876	0.841	0.842	0.798	0.810	0.782	0.801
Number	3	20	20	31	31	43	43
% Pass	-	99.9	99.9	99.9	99.9	99.9	99.9

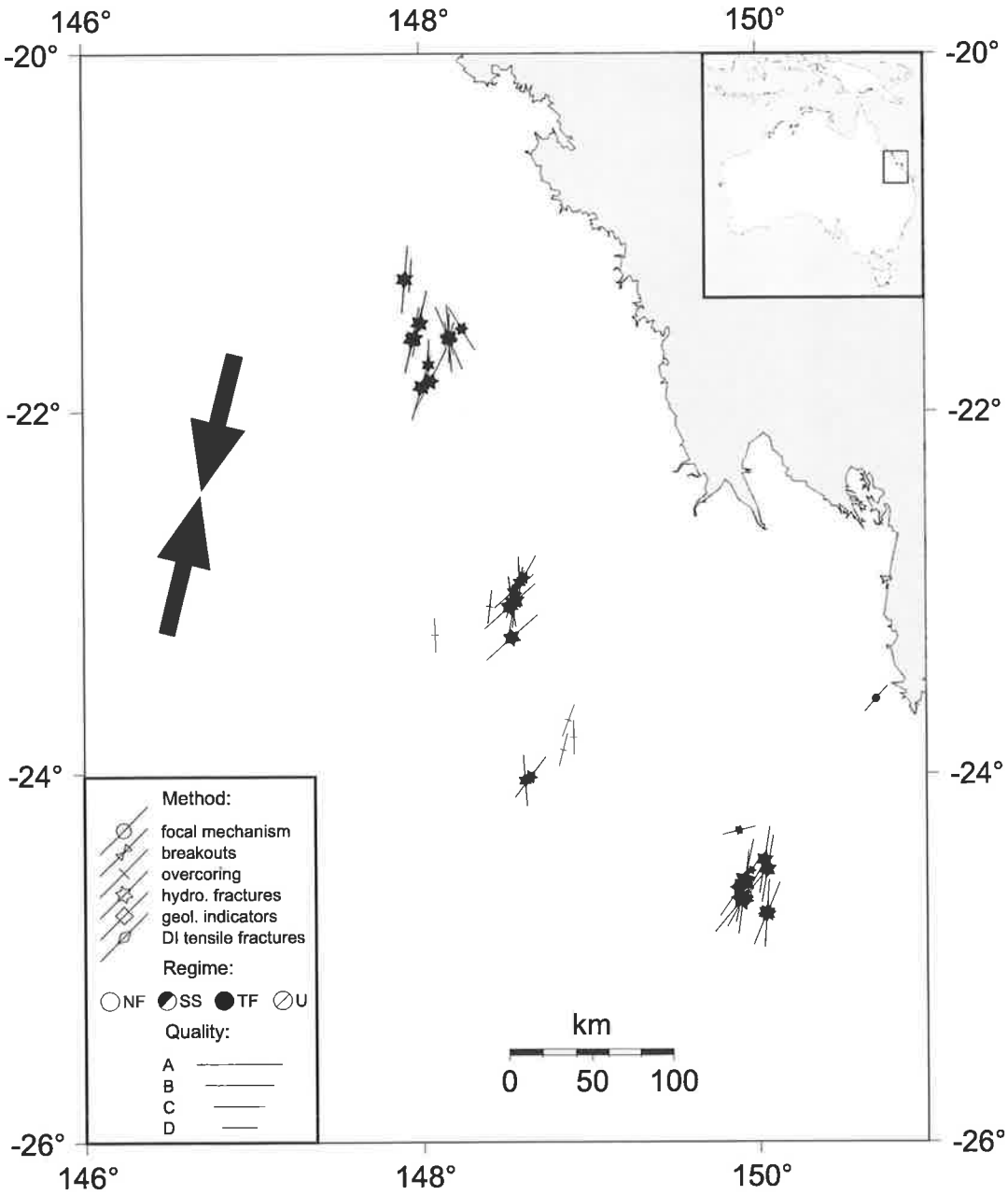

Figure F.5 Stress field of the Bowen Basin stress province with the large arrow defining the average σ_{Hmax} orientation of the A-C quality data used in the analysis of the regional stress field.

Canning Basin

The Canning Basin stress province is a sub-section of data from the ASM database bound by latitude –16° to –19° and longitude 122° to 126°.

Table F.5 Statistical analysis by indicator quality from data located in the Canning Basin stress province. N indicates number weighted and Q indicates quality weighted (A = 4, B = 3, C =2, D = 1).

	A	A-B N	A-B Q	A-C N	A-C Q	A-D N	A-D Q
Mean	048	048	048	053	052	050	051
Std	8	7	7	12	11	21	16
$\overline{R}$	0.961	0.974	0.972	0.917	0.926	0.764	0.862
Number	2	3	3	9	9	10	10
% Pass	-	-	-	99.9	99.9	99	99.9

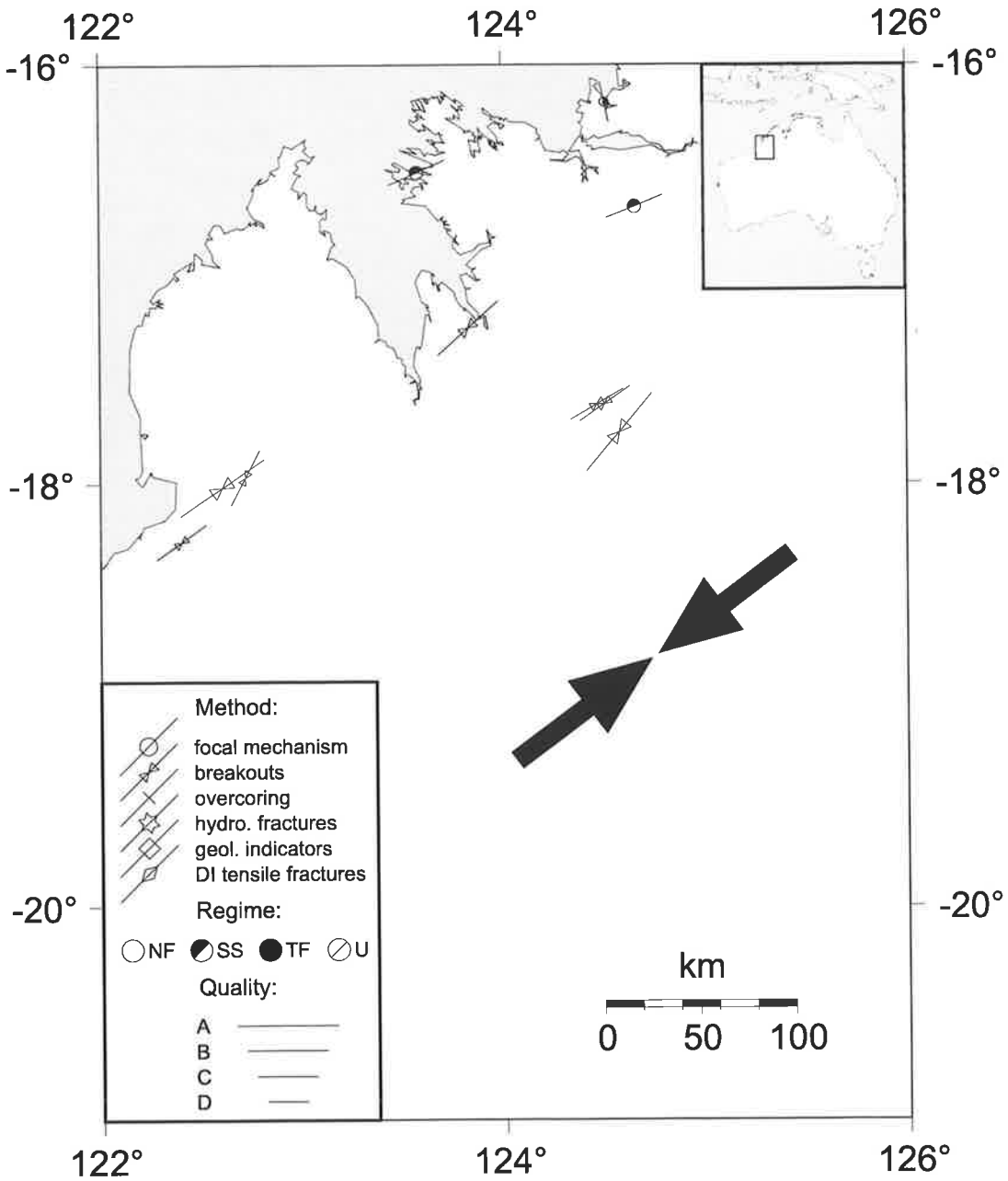

Figure F.6 Stress field of the Canning Basin stress province with the large arrow defining the average σ_{Hmax} orientation of the A-C quality data used in the analysis of the regional stress field.

Carnarvon Basin

The Carnarvon Basin stress province is a sub-section of data from the ASM database bound by latitude –18° to –22.5° and longitude 112.5° to 117.5°.

Table F.6 Statistical analysis by indicator quality from data located in the Carnarvon Basin stress province. N indicates number weighted and Q indicates quality weighted (A = 4, B = 3, C =2, D = 1).

	A	A-B N	A-B Q	A-C N	A-C Q	A-D N	A-D Q
Mean	102	102	102	101	101	099	101
Std	15	31	29	35	33	38	34
$\overline{R}$	0.875	0.557	0.590	0.465	0.523	0.416	0.493
Number	7	20	20	27	27	41	41
% Pass	99	99	99.9	99	99.9	99.9	99.9

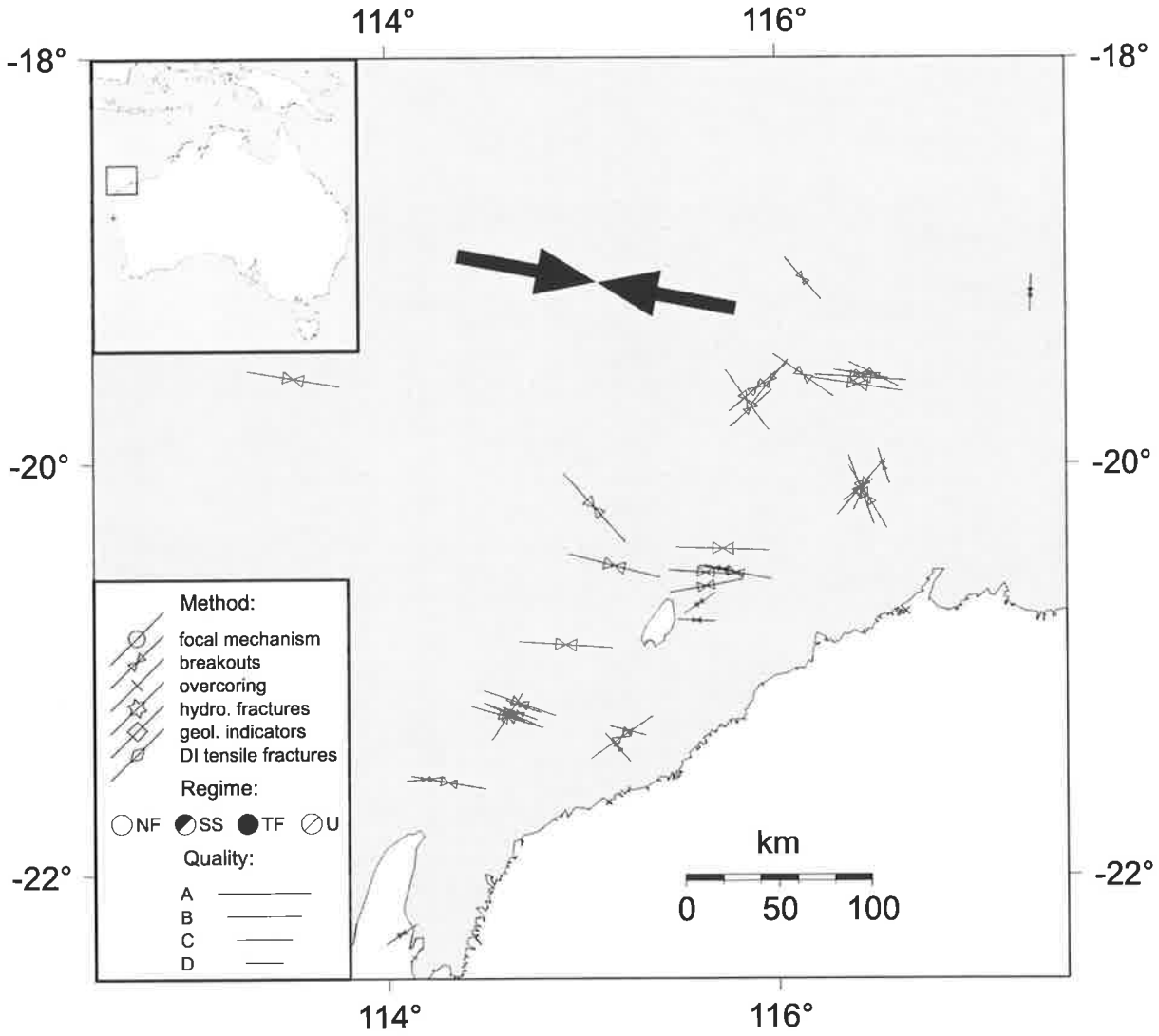

Figure F.7 Stress field of the Carnarvon Basin stress province with the large arrow defining the average σ_{Hmax} orientation of the A-C quality data used in the analysis of the regional stress field.

Cooper Basin

The Cooper Basin stress province is a sub-section of data from the ASM database bound by latitude –26.5° to –29° and longitude 138.5° to 142°.

Table F.7 Statistical analysis by indicator quality from data located in the Cooper Basin stress province. N indicates number weighted and Q indicates quality weighted (A = 4, B = 3, C =2, D = 1).

	A	A-B N	A-B Q	A-C N	A-C Q	A-D N	A-D Q
Mean	099	105	104	102	103	104	103
Std	6	13	12	14	13	19	15
$\overline{R}$	0.976	0.904	0.910	0.888	0.899	0.802	0.866
Number	4	12	12	14	14	18	18
% Pass	99	99.9	99.9	99.9	99.9	99.9	99.9

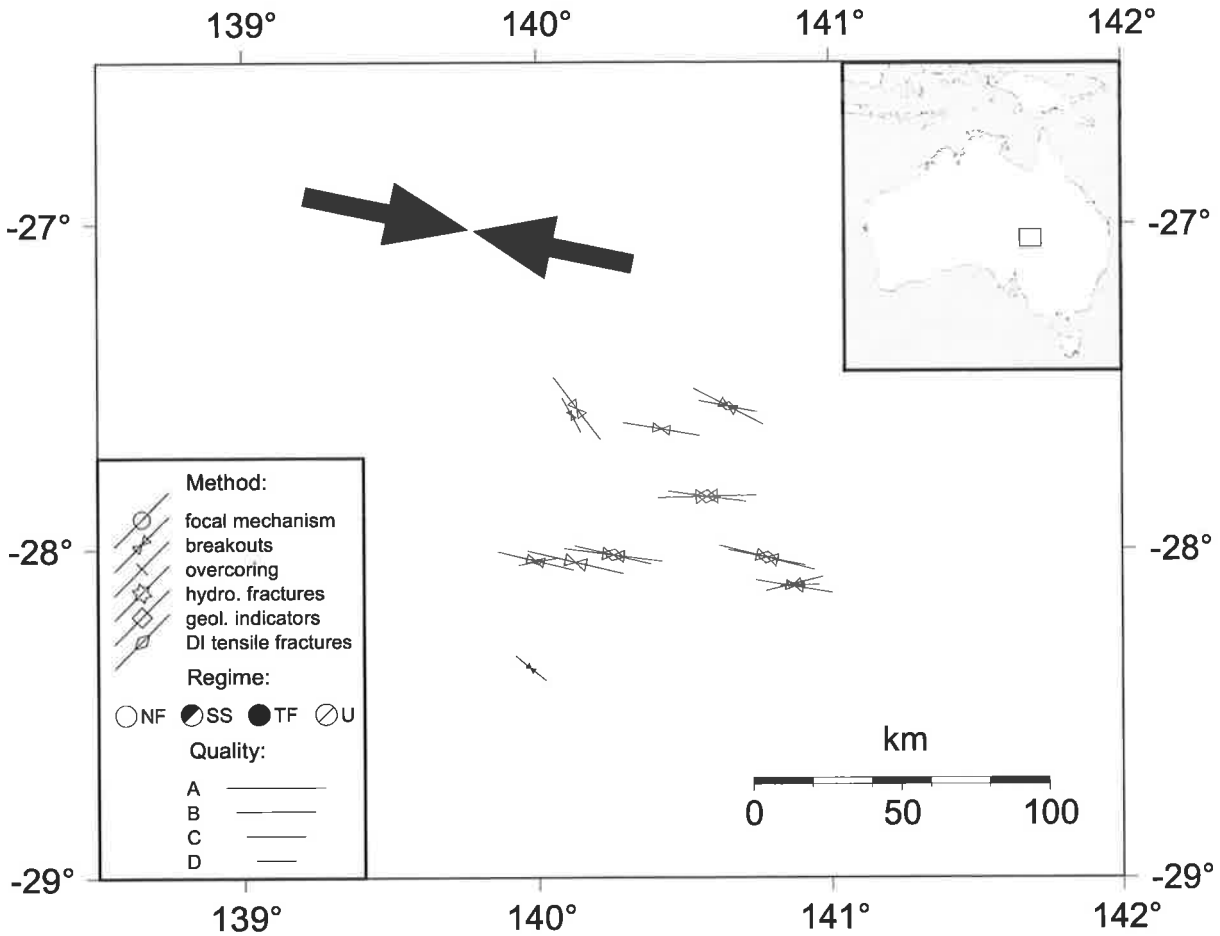

Figure F.8 Stress field of the Cooper Basin stress province with the large arrow defining the average σ_{Hmax} orientation of the A-C quality data used in the analysis of the regional stress field.

Flinders Ranges

The Flinders Ranges stress province is a sub-section of data from the ASM database bound by latitude –30° to –34.5° and longitude 137° to 140°.

Table F.8 Statistical analysis by indicator quality from data located in the Flinders Ranges stress province. N indicates number weighted and Q indicates quality weighted (A = 4, B = 3, C =2, D = 1).

	A	A-B N	A-B Q	A-C N	A-C Q	A-D N	A-D Q
Mean	-	100	100	083	085	091	089
Std	-	0	0	31	30	33	32
$\overline{R}$	-	1.000	1.000	0.561	0.583	0.505	0.544
Number	0	1	1	6	6	10	10
% Pass	-	-	-	fail	fail	90	95

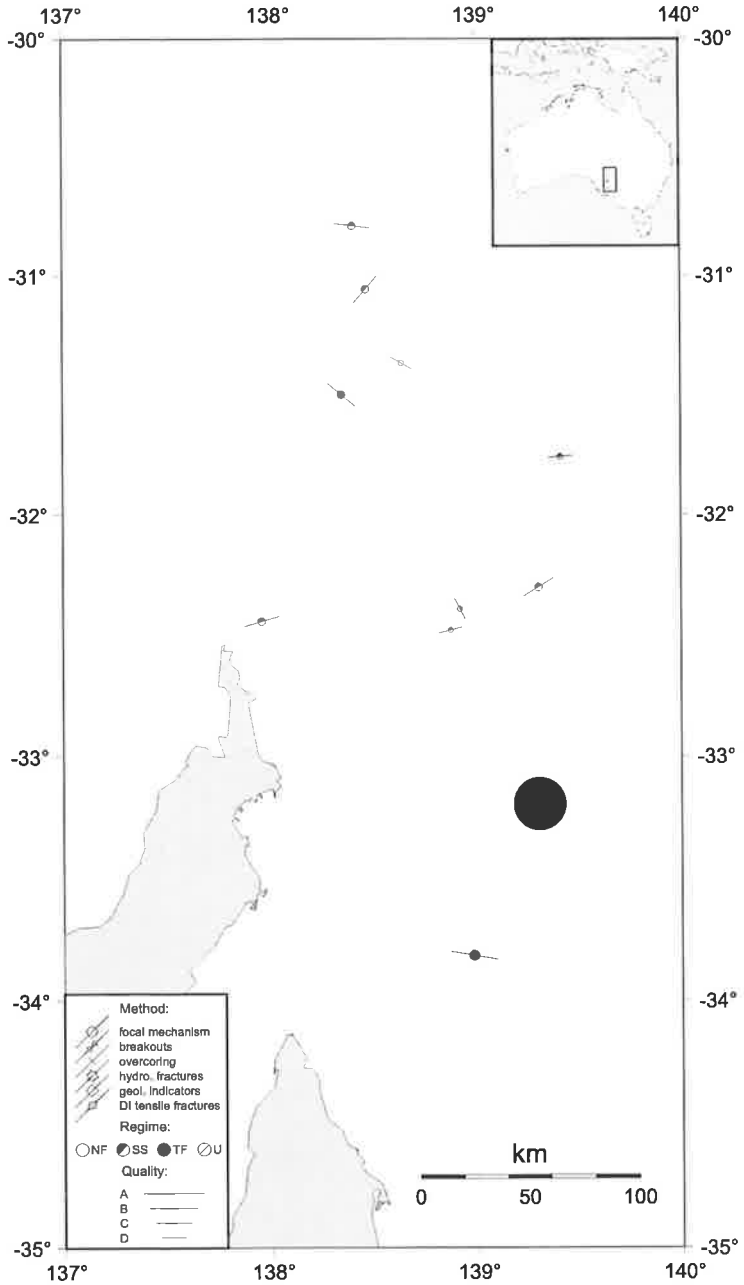

Figure F.9 Stress field of the Flinders Ranges stress province with the large circle indicating a random σ_{Hmax} orientation of the A-C quality data used in the analysis of the regional stress field.

Gippsland Basin

The Gippsland Basin stress province is a sub-section of data from the ASM database bound by latitude –37.5° to –39.5° and longitude 147° to 149°.

Table F.9 Statistical analysis by indicator quality from data located in the Gippsland Basin stress province. N indicates number weighted and Q indicates quality weighted (A = 4, B = 3, C =2, D = 1).

	A	A-B N	A-B Q	A-C N	A-C Q	A-D N	A-D Q
Mean	129	126	126	130	129	127	128
Std	2	27	24	20	20	17	19
$\overline{R}$	0.998	0.648	0.697	0.787	0.779	0.838	0.802
Number	2	4	4	7	7	10	10
% Pass	-	fail	fail	99	99	99.9	99.9

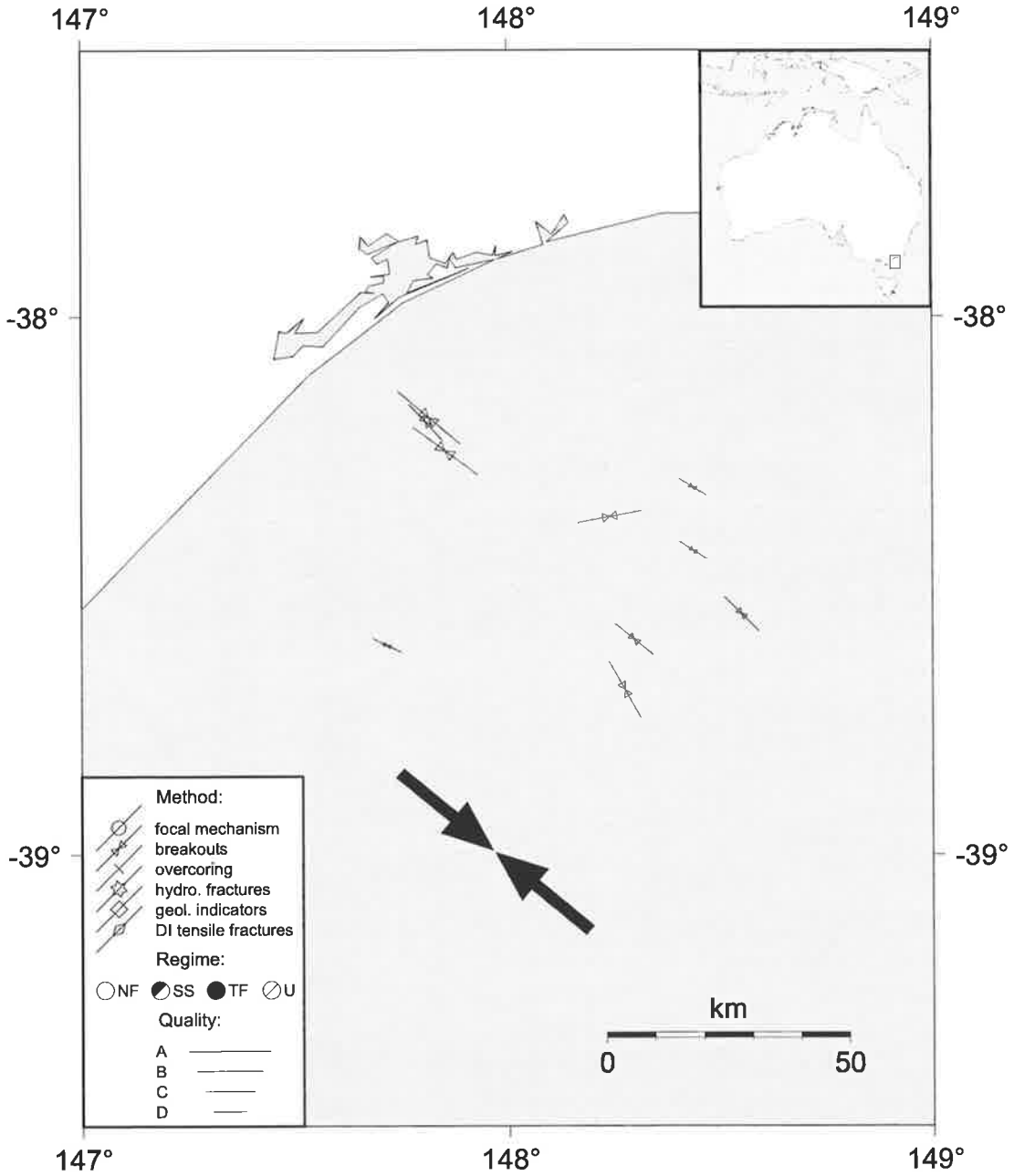

Figure F.10 Stress field of the Gippsland Basin stress province with the large arrow defining the average σ_{Hmax} orientation of the A-C quality data used in the analysis of the regional stress field.

Irian Jaya 1

The Irian Jaya 1 stress province is a sub-section of data from the ASM database bound by latitude 0° to –6° and longitude 133.5° to 138.5°.

Table F.10 Statistical analysis by indicator quality from data located in the Irian Jaya 1 stress province. N indicates number weighted and Q indicates quality weighted (A = 4, B = 3, C =2, D = 1).

	A	A-B N	A-B Q	A-C N	A-C Q	A-D N	A-D Q
Mean	-	038	038	026	027	026	027
Std	-	23	23	29	29	29	29
$\overline{R}$	-	0.733	0.733	0.602	0.608	0.602	0.608
Number	0	6	6	37	37	37	37
% Pass	-	95	95	99.9	99.9	99.9	99.9

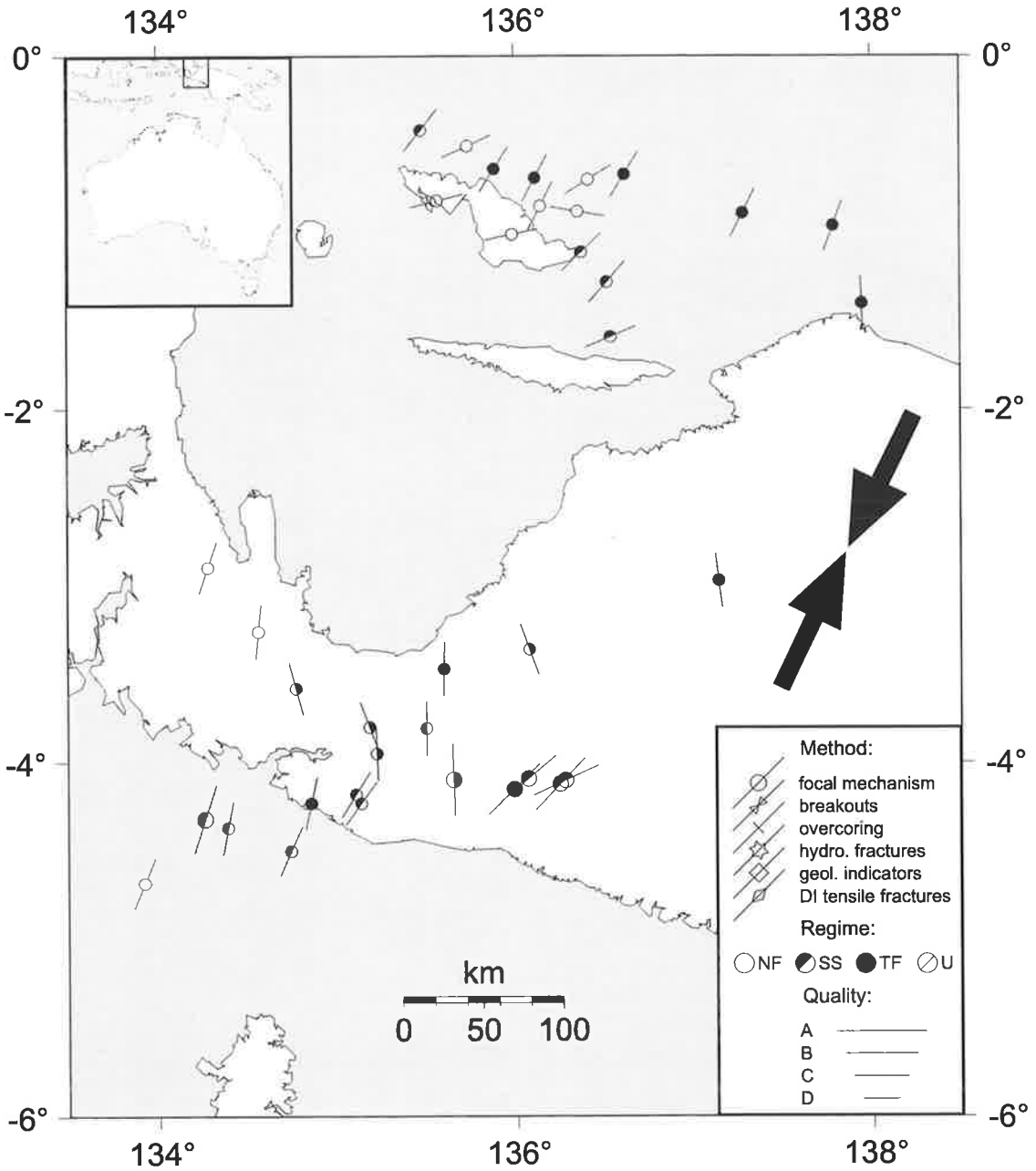

Figure F.11 Stress field of the Irian Jaya 1 stress province with the large arrow defining the average σ_{Hmax} orientation of the A-C quality data used in the analysis of the regional stress field.

Irian Jaya 2

The Irian Jaya 2 stress province is a sub-section of data from the ASM database bound by latitude –2° to –7° and longitude 138.5° to 141.5°.

Table F.11 Statistical analysis by indicator quality from data located in the Irian Jaya 2 stress province. N indicates number weighted and Q indicates quality weighted (A = 4, B = 3, C =2, D = 1).

	A	A-B N	A-B Q	A-C N	A-C Q	A-D N	A-D Q
Mean	-	047	047	044	045	044	045
Std	-	31	31	27	28	27	28
$\overline{R}$	-	0.561	0.561	0.641	0.621	0.641	0.621
Number	0	8	8	13	13	13	13
% Pass	-	90	90	99	99	99	99

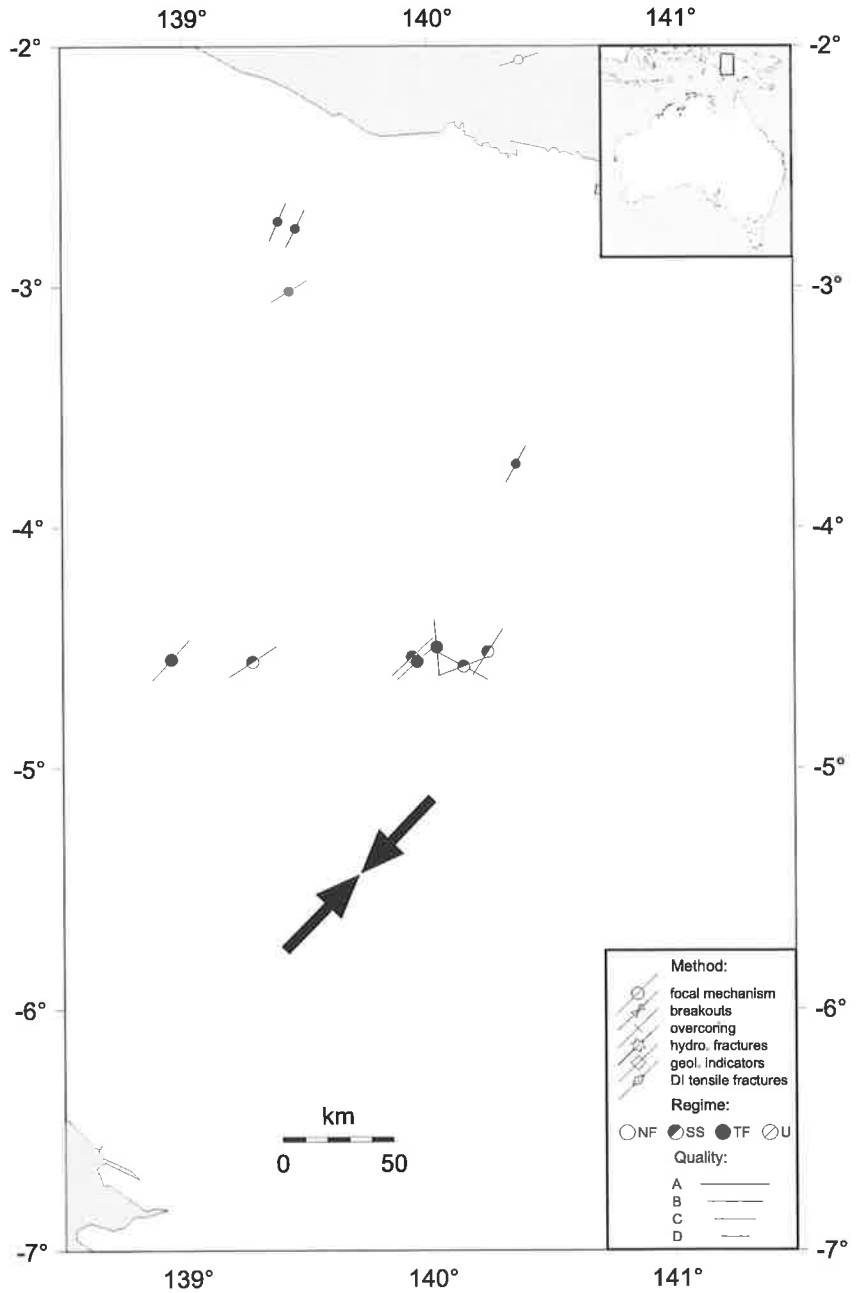

Figure F.12 Stress field of the Irian Jaya 2 stress province with the large arrow defining the average σ_{Hmax} orientation of the A-C quality data used in the analysis of the regional stress field.

New Guinea 1

The New Guinea 1 stress province is a sub-section of data from the ASM database bound by latitude –2.5° to –5° and longitude 141.5° to 148°.

Table F.12 Statistical analysis by indicator quality from data located in the New Guinea 1 stress province. N indicates number weighted and Q indicates quality weighted (A = 4, B = 3, C =2, D = 1).

	A	A-B N	A-B Q	A-C N	A-C Q	A-D N	A-D Q
Mean	-	-	-	049	049	049	049
Std	-	-	-	7	7	7	7
$\overline{R}$	-	-	-	0.973	0.973	0.973	0.973
Number	0	0	0	4	4	4	4
% Pass	-	-	-	99	99	99	99

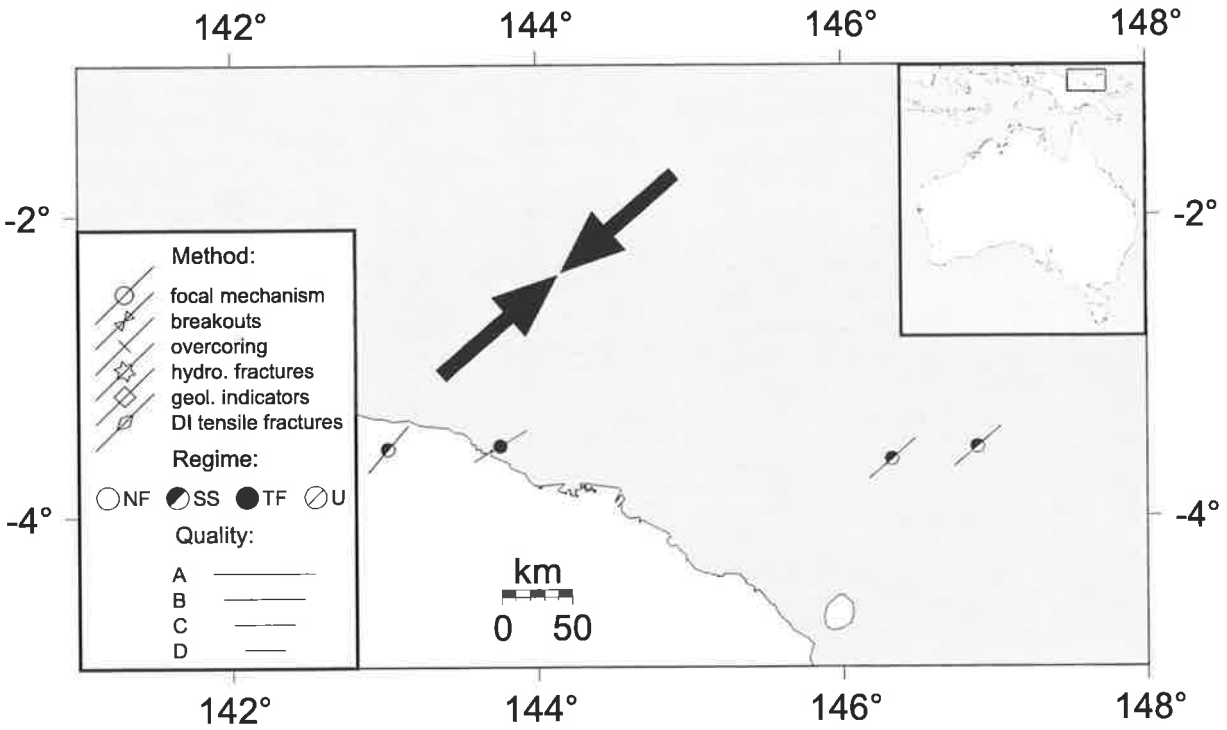

Figure F.13 Stress field of the New Guinea 1 stress province with the large arrow defining the average σ_{Hmax} orientation of the A-C quality data used in the analysis of the regional stress field.

New Guinea 2

The New Guinea 2 stress province is a sub-section of data from the ASM database bound by latitude –5° to –8° and longitude 141.5° to 149°.

Table F.13 Statistical analysis by indicator quality from data located in the New Guinea 2 stress province. N indicates number weighted and Q indicates quality weighted (A = 4, B = 3, C =2, D = 1).

	A	A-B N	A-B Q	A-C N	A-C Q	A-D N	A-D Q
Mean	-	005	005	016	014	016	014
Std	-	34	34	24	26	24	26
$\overline{R}$	-	0.504	0.504	0.698	0.653	0.698	0.653
Number	0	4	4	8	8	8	8
% Pass	-	fail	fail	97.5	95	97.5	95

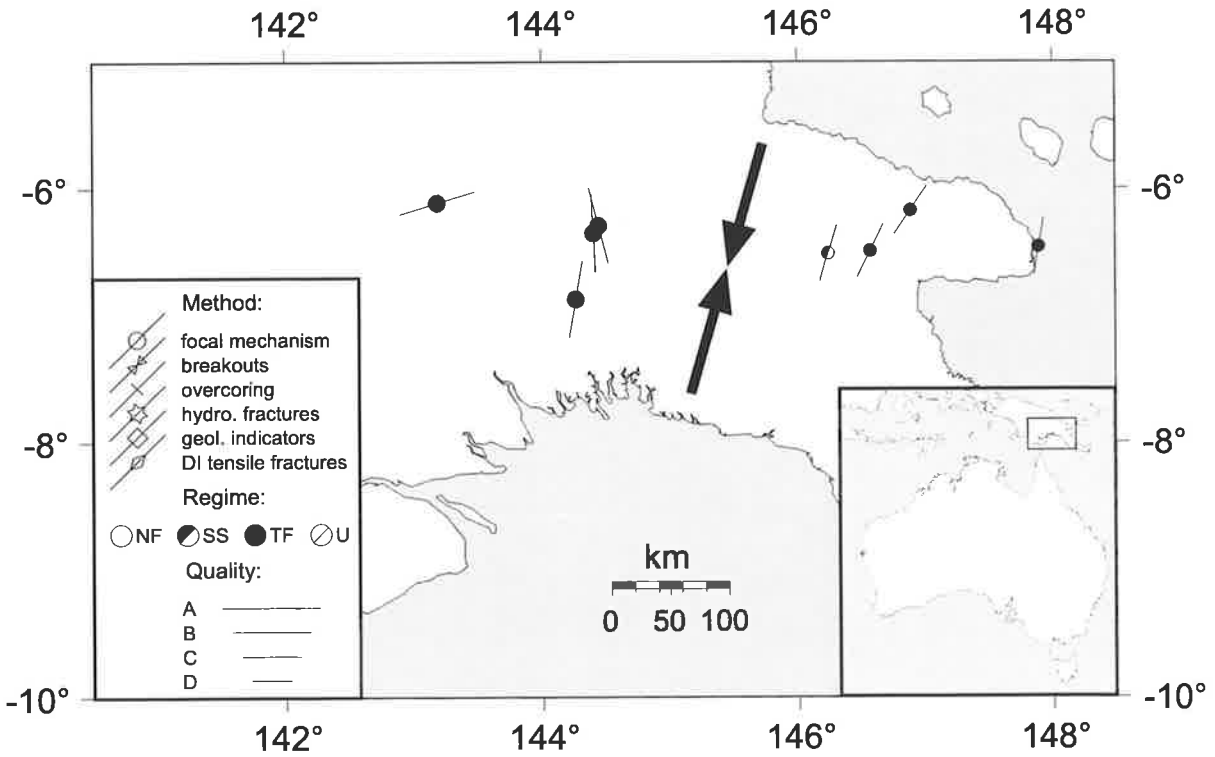

Figure F.14 Stress field of the New Guinea 2 stress province with the large arrow defining the average σ_{Hmax} orientation of the A-C quality data used in the analysis of the regional stress field.

Otway Basin

The Otway Basin stress province is a sub-section of data from the ASM database bound by latitude –36.5° to –39° and longitude 138° to 141.5°.

Table F.14 Statistical analysis by indicator quality from data located in the Otway Basin stress province. N indicates number weighted and Q indicates quality weighted (A = 4, B = 3, C =2, D = 1).

	A	A-B N	A-B Q	A-C N	A-C Q	A-D N	A-D Q
Mean	142	142	142	134	137	134	136
Std	13	13	13	14	15	15	15
$\overline{R}$	0.898	0.898	0.898	0.882	0.879	0.867	0.870
Number	3	3	3	6	6	15	15
% Pass	-	-	-	99	99	99.9	99.9

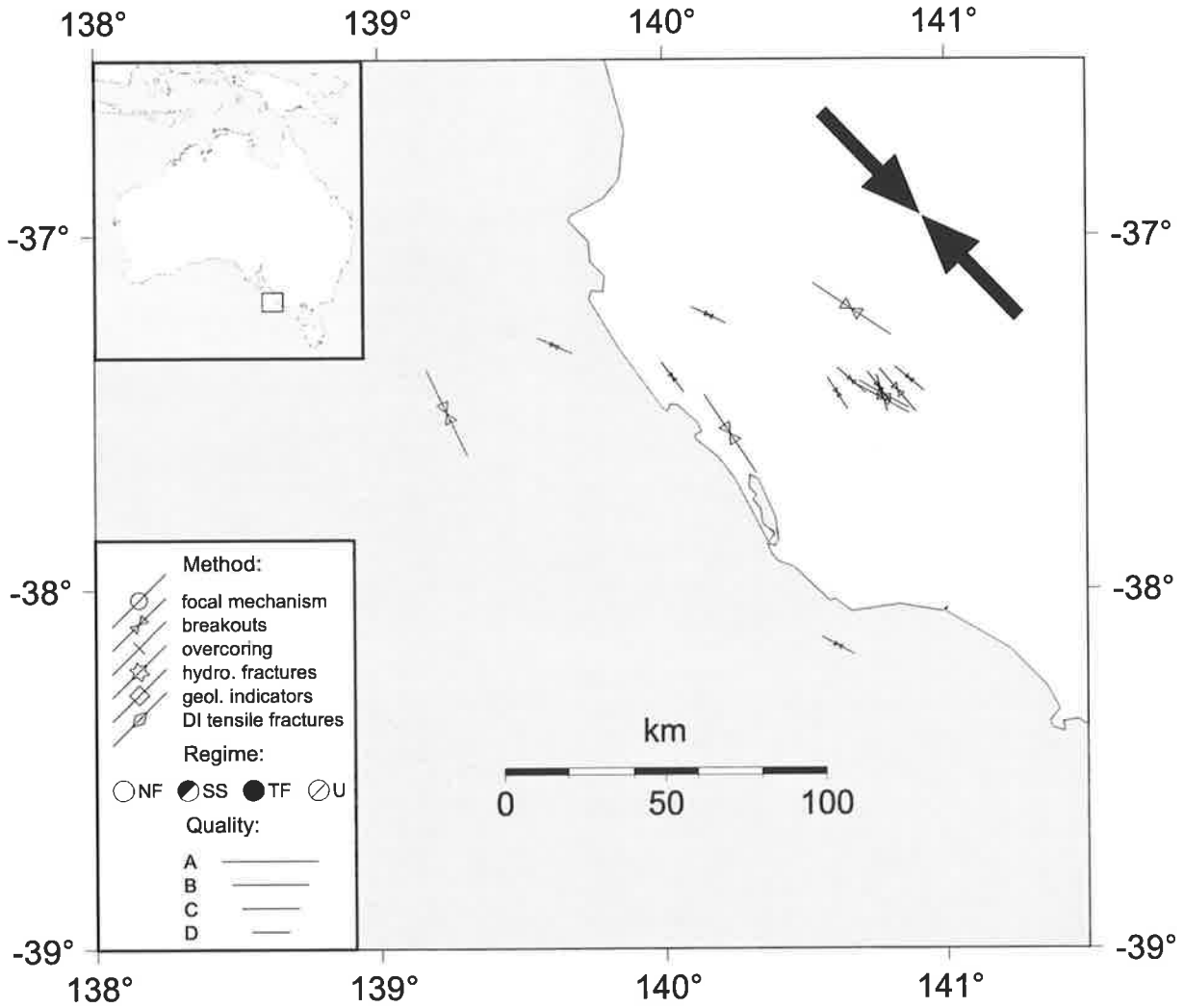

Figure F.15 Stress field of the Otway Basin stress province with the large arrow defining the average σ_{Hmax} orientation of the A-C quality data used in the analysis of the regional stress field.

Perth

The Perth stress province is a sub-section of data from the ASM database bound by latitude –28° to –34° and longitude 113° to 118°.

Table F.15 Statistical analysis by indicator quality from data located in the Perth stress province. N indicates number weighted and Q indicates quality weighted (A = 4, B = 3, C =2, D = 1).

	A	A-B N	A-B Q	A-C N	A-C Q	A-D N	A-D Q
Mean	093	093	093	096	095	100	097
Std	0	24	24	26	26	38	32
$\overline{R}$	1.000	0.695	0.706	0.658	0.670	0.411	0.537
Number	1	9	9	22	22	35	35
% Pass	-	99	99	99.9	99.9	99	99.9

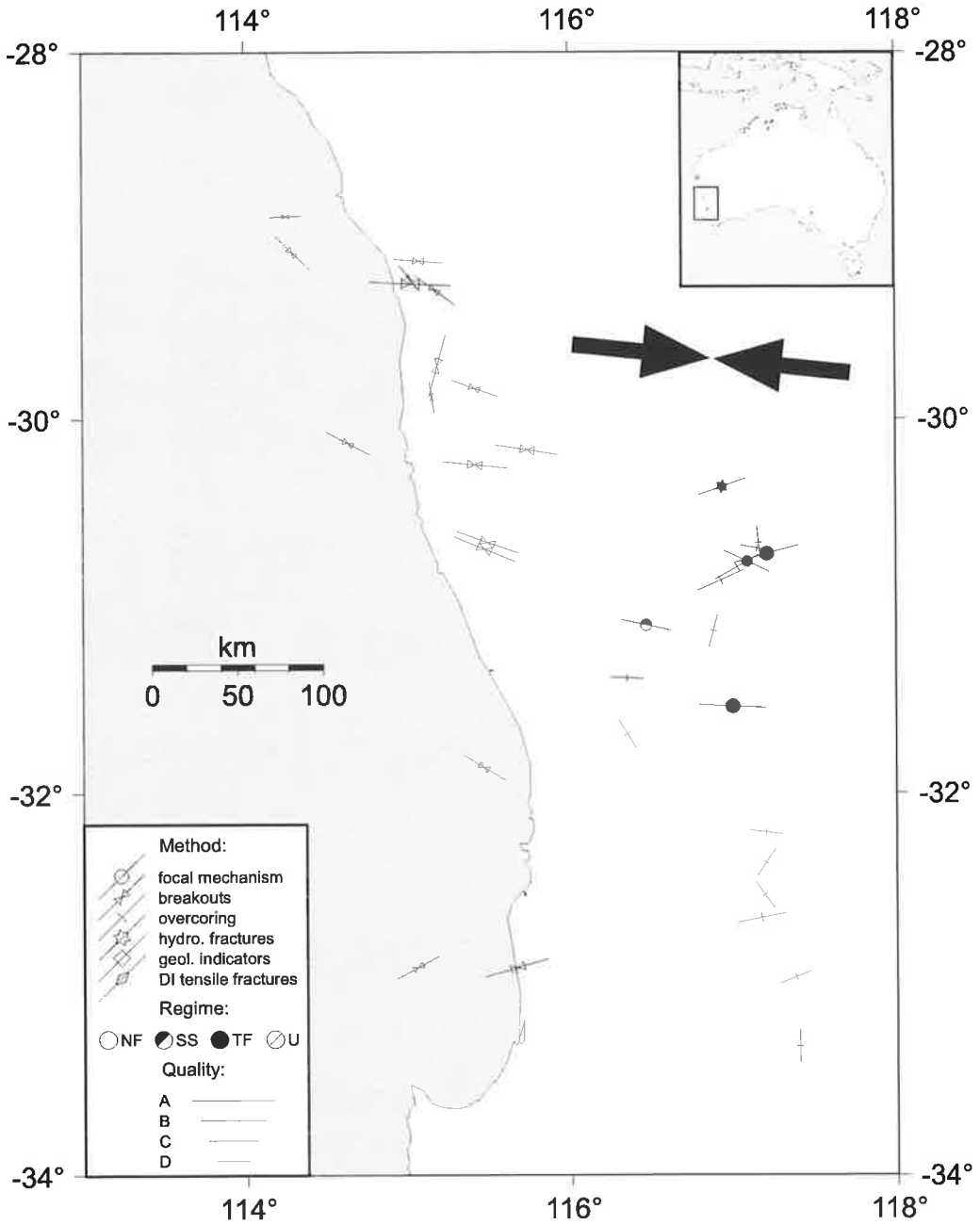

Figure F.16 Stress field of the Perth stress province with the large arrow defining the average σ_{Hmax} orientation of the A-C quality data used in the analysis of the regional stress field.

Sydney Basin

The Sydney Basin stress province is a sub-section of data from the ASM database bound by latitude –31.5° to –35° and longitude 149.5° to 153°.

Table F.16 Statistical analysis by indicator quality from data located in the Sydney Basin stress province. N indicates number weighted and Q indicates quality weighted (A = 4, B = 3, C =2, D = 1).

	A	A-B N	A-B Q	A-C N	A-C Q	A-D N	A-D Q
Mean	043	053	052	054	053	054	053
Std	27	28	28	41	38	46	42
$\overline{R}$	0.643	0.624	0.623	0.356	0.414	0.271	0.344
Number	3	13	13	28	28	64	64
% Pass	-	99	99	95	99	97.5	99.9

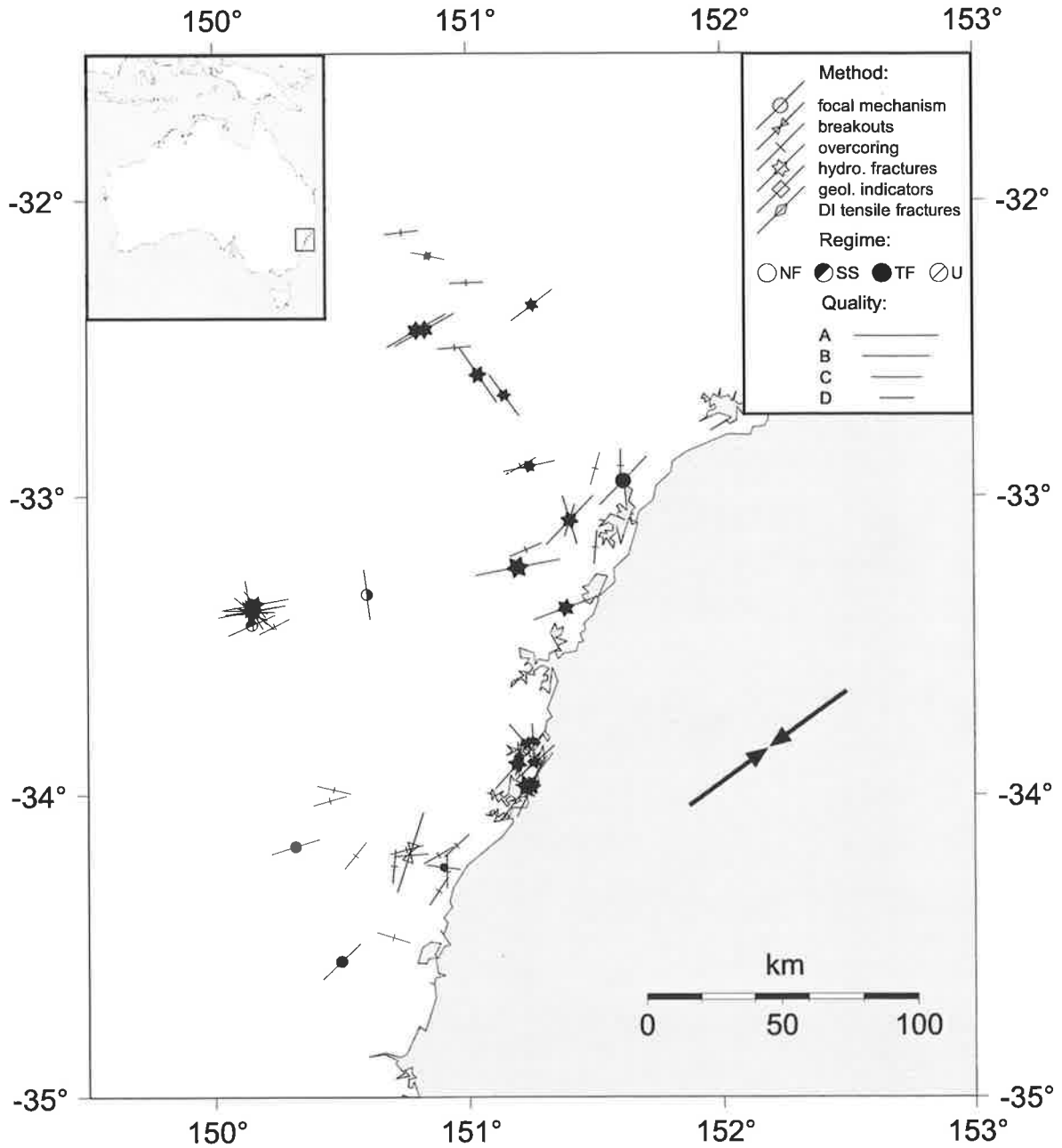

Figure F.17 Stress field of the Sydney Basin stress province with the large arrow defining the average σ_{Hmax} orientation of the A-C quality data used in the analysis of the regional stress field

Appendix G

Stress Trajectory Mapping Code

Listed below is the MATLAB code for creating the stress trajectory maps. All code can be found in digital form under the stress trajectory directory on the accompanying CDROM. The code consists of the main program, stress_trajectory_map_Australia.m, and two subprograms, weights.m and weights4.m, for calculating the weights. The data file with the stress measurements should be in the following form: latitude, longitude, σ_{Hmax} orientation and quality. The quality ranges from four corresponding to A, three to B, two to C and one to D. The input variables are listed in the comments of the main program.

FILE: stress_trajectory_map_Australia.m

```
function a=Stress_maps(obs,f,l,M)

%  Main routine used to calculate stress trajectory maps.
%
%  function a=stress_maps(obs,f,l,M)
%
%  obs is the observed data made up of lats, longs and azimuth.
%  f = the amount of fidelity.
%  l = landa which is the amount of smoothing.
%  M = the number of iterations the procedure goes through.

m=1;
count=length(obs);
for i=1:count;
   delta(i)=1;
end;

for i=1:count;
   Y(1,i)=cos(pi*obs(i,3)/180);
   Y(2,i)=sin(pi*obs(i,3)/180);
end;

F=Y;

% Calculate the Local Weights

Wbar = weights(obs,f);

% Calculate fitted orientations by recalculating M number of times

for n=1:M
   for i=1:count;
      G=0;
      sum=0;
      sum2=0;
      for j=1:count;
         sum = sum + (Y(:,i)*Y(:,i)')*Wbar(i,j)*delta(i);
      end;
```

```
   for j=1:count;
         if j == i
            sum2=sum2+0;
         else
            sum2 = sum2 + (F(:,i)*F(:,j)')*Wbar(i,j)*delta(i);
         end
      end;
      sum2=sum2*l;
      G=sum+sum2;
      [V,D]=eig(G);
      G=V;

      if G(1,1)<0 & G(2,1)<0
         G(1,1)=-G(1,1);
         G(2,1)=-G(2,1);
      elseif G(1,2)<0 & G(2,2)<0
         G(1,2)=-G(1,2);
         G(2,2)=-G(2,2);
      else
         G=G;
      end

      md=max(D);
      md2=max(md);
      if D(1,1) == md2
           F(1,i)=G(1,1);
           F(2,i)=G(2,1);
      elseif D(2,1) == md2
           F(1,i)=G(1,1);
           F(2,i)=G(2,1);
      else
           F(1,i)=G(1,2);
           F(2,i)=G(2,2);
      end
   end;

   % Compute updated robustness weights

   for i=1:count;
      T(:,i)=Y(:,i)-F(:,i);
   end
   for i=1:count;
      A(i)=(T(1,i)^2+T(2,i)^2)^0.5;
   end
   s=median(A);

   for i=1:count;
      x=((Y(1,i)-F(1,i))^2+(Y(2,i)-F(2,i))^2)^(0.5)/6*s;
      if x<1
         delta(i)=(1-x^2)^2;
      else delta(i)=0;
      end
   end
end

for i=1:count
   Final(i,1)=obs(i,1);
   Final(i,2)=obs(i,2);
   Final(i,3)=acos(F(1,i))*180/pi;
end

Final=(Final)

% Create contours of SHmax value at each location
```

```
ma1=max(obs(:,1))+5;
ma2=max(obs(:,2))+5;
mi1=min(obs(:,1))-5;
mi2=min(obs(:,2))-5;

% Contours moving up in x direction y constant
t0 = clock;
k=0;
d=0;
for u=mi1:5:ma1
   d=d+1;
   x(1)=u;
   y(1)=mi2;
   for i=1:5000
      if x(i)<=ma1 & y(i)<=ma2 & x(i)>=mi1 & y(i)>=mi2
         t(1)=x(i);
         t(2)=y(i);
         W = weights4(obs,t,f);
         sum=0;
         for j=1:count;
            sum = sum + (F(:,j)*F(:,j)')*W(1,j)*delta(j);
         end;
         G=sum;
         [V,D]=eig(G);
         G=V;
         if G(1,1)<0 & G(2,1)<0
               G(1,1)=-G(1,1);
               G(2,1)=-G(2,1);
         elseif G(1,2)<0 & G(2,2)<0
               G(1,2)=-G(1,2);
               G(2,2)=-G(2,2);
         else
               G=G;
         end
         md=max(D);
         md2=max(md);
         if D(1,1) == md2
               gridfn(1,i)=G(1,1);
               gridfn(2,i)=G(2,1);
         elseif D(2,1) == md2
               gridfn(1,i)=G(1,1);
               gridfn(2,i)=G(2,1);
         else
               gridfn(1,i)=G(1,2);
               gridfn(2,i)=G(2,2);
         end
         angle(i)=acos(gridfn(1,i));

         % Make angle between 0 and 360 degrees
         if angle(i)>2*pi;
            b=angle(i)/(2*pi);
            angle(i)=angle(i)-floor(b)*2*pi;
         end;
         if angle(i)<0;
            b=angle(i)/(2*pi);
            angle(i)=angle(i)-floor(b)*2*pi;
         end;

         % make smooth trajectory
         if i==1
            if angle(i)>pi/2 & angle(i)<pi;
               angle(i)=angle(i)+pi;
            elseif angle(i)>=pi & angle(i)<3*pi/2;
```

```
            angle(i)=angle(i)-pi;
         end
      else
         if angle(i)>pi;
            angletemp=angle(i)-pi;
         else
            angletemp=angle(i)+pi;
         end
         if abs(angle(i-1)-angle(i))>abs(angle(i-1)-angletemp);
            angle(i)=angletemp;
         end
      end

      r=0.05;
      x(i+1)=x(i)+(r*sin(angle(i)));
      y(i+1)=y(i)+(r*cos(angle(i)));
      k=k+1;
      contoura(k,:)=[1000+d,x(i+1),y(i+1)];
   else break
   end
end
plot(x,y);
hold on;
x=0;
y=0;
end
save outputa.dat contoura -ascii
etime(clock,t0)

% Contours moving up in y direction x constant
t0 = clock;
k=0;
x=0;
y=0;
for u=mi2:5:ma2
   d=d+1;
   x(1)=mi1;
   y(1)=u;
   for i=1:5000
      if x(i)<=ma1 & y(i)<=ma2 & x(i)>=mi1 & y(i)>=mi2
         t(1)=x(i);
         t(2)=y(i);
         W = weights4(obs,t,f);
         sum=0;
         for j=1:count;
            sum = sum + (F(:,j)*F(:,j)')*W(1,j)*delta(j);
         end;
         G=sum;
         [V,D]=eig(G);
         G=V;
         if G(1,1)<0 & G(2,1)<0
               G(1,1)=-G(1,1);
               G(2,1)=-G(2,1);
         elseif G(1,2)<0 & G(2,2)<0
               G(1,2)=-G(1,2);
               G(2,2)=-G(2,2);
         else
               G=G;
         end
         md=max(D);
         md2=max(md);
         if D(1,1) == md2
               gridfn(1,i)=G(1,1);
               gridfn(2,i)=G(2,1);
```

```
        elseif D(2,1) == md2
              gridfn(1,i)=G(1,1);
              gridfn(2,i)=G(2,1);
        else
              gridfn(1,i)=G(1,2);
              gridfn(2,i)=G(2,2);
        end
        angle(i)=acos(gridfn(1,i));

        % Make angle between 0 and 360 degrees
        if angle(i)>2*pi;
           b=angle(i)/(2*pi);
           angle(i)=angle(i)-floor(b)*2*pi;
        end;
        if angle(i)<0;
           b=angle(i)/(2*pi);
           angle(i)=angle(i)-floor(b)*2*pi;
        end;

        % make smooth trajectory
        if i==1
           if angle(i)>pi & angle(i)<2*pi;
              angle(i)=angle(i)-pi;
        end
        else
           if angle(i)>pi;
              angletemp=angle(i)-pi;
           else
              angletemp=angle(i)+pi;
           end
           if abs(angle(i-1)-angle(i))>abs(angle(i-1)-angletemp);
              angle(i)=angletemp;
           end
        end

        r=0.05;
        x(i+1)=x(i)+(r*sin(angle(i)));
        y(i+1)=y(i)+(r*cos(angle(i)));
        k=k+1;
        contourb(k,:)=[1000+d,x(i+1),y(i+1)];
      else break
      end
   end
   plot(x,y);
   hold on;
   x=0;
   y=0;
end
save outputb.dat contourb -ascii
etime(clock,t0)

% Contours moving up in x direction y constant
t0 = clock;
k=0;
x=0;
y=0;
for u=mi1:5:ma1
   d=d+1;
   x(1)=u;
   y(1)=ma2;
   for i=1:5000
      if x(i)<=ma1 & y(i)<=ma2 & x(i)>=mi1 & y(i)>=mi2
         t(1)=x(i);
         t(2)=y(i);
```

```
W = weights4(obs,t,f);
sum=0;
for j=1:count;
   sum = sum + (F(:,j)*F(:,j)')*W(1,j)*delta(j);
end;
G=sum;
[V,D]=eig(G);
G=V;
if G(1,1)<0 & G(2,1)<0
      G(1,1)=-G(1,1);
      G(2,1)=-G(2,1);
elseif G(1,2)<0 & G(2,2)<0
      G(1,2)=-G(1,2);
      G(2,2)=-G(2,2);
else
      G=G;
end
md=max(D);
md2=max(md);
if D(1,1) == md2
      gridfn(1,i)=G(1,1);
      gridfn(2,i)=G(2,1);
elseif D(2,1) == md2
      gridfn(1,i)=G(1,1);
      gridfn(2,i)=G(2,1);
else
      gridfn(1,i)=G(1,2);
      gridfn(2,i)=G(2,2);
end
angle(i)=acos(gridfn(1,i));

% Make angle between 0 and 360 degrees
if angle(i)>2*pi;
   b=angle(i)/(2*pi);
   angle(i)=angle(i)-floor(b)*2*pi;
end;
if angle(i)<0;
   b=angle(i)/(2*pi);
   angle(i)=angle(i)-floor(b)*2*pi;
end;

% make smooth trajectory
if i==1
   if angle(i)<pi/2
      angle(i)=angle(i)+pi;
   elseif angle(i)>3*pi/2;
      angle(i)=angle(i)-pi;
   end
else
   if angle(i)>pi;
      angletemp=angle(i)-pi;
   else
      angletemp=angle(i)+pi;
   end
   if abs(angle(i-1)-angle(i))>abs(angle(i-1)-angletemp);
      angle(i)=angletemp;
   end
end

r=0.05;
x(i+1)=x(i)+(r*sin(angle(i)));
y(i+1)=y(i)+(r*cos(angle(i)));
k=k+1;
contourc(k,:)=[1000+d,x(i+1),y(i+1)];
```

```
        else break
      end
   end
   plot(x,y);
   hold on;
   x=0;
   y=0;
end
save outputc.dat contourc -ascii
etime(clock,t0)

% Contours moving up in y direction x constant
t0 = clock;
k=0;
x=0;
y=0;
for u=mi2:5:ma2
   d=d+1;
   x(1)=ma1;
   y(1)=u;
   for i=1:5000
      if x(i)<=ma1 & y(i)<=ma2 & x(i)>=mi1 & y(i)>=mi2
         t(1)=x(i);
         t(2)=y(i);
         W = weights4(obs,t,f);
         sum=0;
         for j=1:count;
            sum = sum + (F(:,j)*F(:,j)')*W(1,j)*delta(j);
         end;
         G=sum;
         [V,D]=eig(G);
         G=V;
         if G(1,1)<0 & G(2,1)<0
               G(1,1)=-G(1,1);
               G(2,1)=-G(2,1);
         elseif G(1,2)<0 & G(2,2)<0
               G(1,2)=-G(1,2);
               G(2,2)=-G(2,2);
         else
               G=G;
         end
         md=max(D);
         md2=max(md);
         if D(1,1) == md2
               gridfn(1,i)=G(1,1);
               gridfn(2,i)=G(2,1);
         elseif D(2,1) == md2
               gridfn(1,i)=G(1,1);
               gridfn(2,i)=G(2,1);
         else
               gridfn(1,i)=G(1,2);
               gridfn(2,i)=G(2,2);
         end
         angle(i)=acos(gridfn(1,i));

         % Make angle between 0 and 360 degrees
         if angle(i)>2*pi;
            b=angle(i)/(2*pi);
            angle(i)=angle(i)-floor(b)*2*pi;
         end;
         if angle(i)<0;
            b=angle(i)/(2*pi);
            angle(i)=angle(i)-floor(b)*2*pi;
         end;
```

```
        % make smooth trajectory
        if i==1
           if angle(i)>0 & angle(i)<pi;
              angle(i)=angle(i)+pi;
           end
        else
           if angle(i)>pi;
              angletemp=angle(i)-pi;
           else
              angletemp=angle(i)+pi;
           end
           if abs(angle(i-1)-angle(i))>abs(angle(i-1)-angletemp);
              angle(i)=angletemp;
           end
        end

        r=0.05;
        x(i+1)=x(i)+(r*sin(angle(i)));
        y(i+1)=y(i)+(r*cos(angle(i)));
        k=k+1;
        contourd(k,:)=[1000+d,x(i+1),y(i+1)];
     else break
     end
  end
  plot(x,y);
  hold on;
  x=0;
  y=0;
end
save outputd.dat contourd -ascii
etime(clock,t0)

contour=[contoura;contourb;contourc;contourd];
save output.dat contour -ascii

%   Add observed data to grid
for i=1:count;
   raw(i,1)=obs(i,1);
   raw(i,2)=obs(i,2);
   raw(i,3)=(obs(i,3)*pi/180);
end

r=0.2;
for i=1:count
   p1(1)=raw(i,1)+r*sin(raw(i,3));
   p2(1)=raw(i,2)+r*cos(raw(i,3));
   p1(2)=raw(i,1)-r*sin(raw(i,3));
   p2(2)=raw(i,2)-r*cos(raw(i,3));
   plot(p1,p2);
   hold on;
end
axis([mi1 ma1 mi2 ma2])
```

FILE: weights.m

```
function y=weights(obs,f)
%  Sub program to calculate the weights given to the
%  surrounding stress measurements

count=length(obs);
```

```
r=f*count;
r=round(r);

for i=1:count;
   for j=1:2;
      X(i,j)=obs(i,j);
   end;
end;

for i=1:count;
    X(i,3)=obs(i,4);
end;

for i=1:count;
   for j=1:count;
      distance(i,j)=((X(i,1)-X(j,1))^2+(X(i,2)-X(j,2))^2)^(0.5);
   end;
end;

k=sort(distance,2);
for i=1:count;
   h(i)=k(i,r+1);
end;

for i=1:count;
   for j=1:count;
      if ((X(i,1)-X(j,1))^2+(X(i,2)-X(j,2))^2)^(0.5)/h(i) < 1
         W(i,j)=((1-(((X(i,1)-X(j,1))^2+(X(i,2)-
X(j,2))^2)^(0.5)/h(i))^3)^3)*X(i,3);
      else W(i,j)=0;
      end;
   end;
end;

sum=0;
for i=1:count;
   for j=1:count;
      if i ~= j
         sum=sum + W(i,j);
      else sum=sum;
      end
   end;
   G(i)=sum;
end;

for i=1:count;
   for j=1:count;
      if  i == j
         Wbar(i,j)=W(i,j);
      else Wbar(i,j)= W(i,j)/G(i);
      end;
   end;
end;

for i=1:count;
   for j=1:count;
      if i == j
         Wbar(i,j)=1;
      else Wbar(i,j)=Wbar(i,j);
      end
   end;
end;

y=Wbar;
```

FILE: weights4.m

```
function y=weights2(obs,t,f)
%  Sub program to calculate the weights given to the
%  surrounding stress measurements

grid=t;

count=length(obs);
r=f*count;
r=round(r);

for i=1:count;
   for j=1:2;
      X(i,j)=obs(i,j);
   end;
end;

%for i=1:count;
%    X(i,3)=obs(i,4);
%end;

for j=1:count;
   distance(j,1)=X(j,1);
   distance(j,2)=X(j,2);
   distance(j,3)=((grid(1,1)-X(j,1))^2+(grid(1,2)-X(j,2))^2)^(0.5);
end;

[k,index]=sort(distance(:,3));
index=index(1:r);
h(1)=k(r,1);

for j=1:count;
   swtch=find(index(:)==j);
   if(swtch>0)
      W(1,j)=((1-(((grid(1,1)-X(j,1))^2+(grid(1,2)-
X(j,2))^2)^(0.5)/h(1))^3)^3); %*X(i,3);
   else W(1,j)=0;
   end;
end;

y=W;
```

Appendix H

Published Papers

This appendix contains three published papers to which the author contributed in the course of his PhD thesis work. The paper on which Chapter 6 is based (Reynolds and Hillis, 2000) is also included. The papers included in this appendix are listed below.

Hillis, R. R., Meyer, J. J. & Reynolds, S. D. 1998. The Australian stress map. *Exploration Geophysics* **29**, 420-427.

Hillis, R. R., Enever, J. R. & Reynolds, S. D. 1999. In situ field of eastern Australia. *Australian Journal of Earth Sciences* **46**, 813-825.

Hillis, R. R. & Reynolds, S. D. 2000. The Australian Stress Map. *Journal of the Geological Society, London* **157**, 915-921.

Reynolds, S. D. & Hillis, R. R. 2000. The in situ stress field of the Perth Basin, Australia. *Geophysical Research Letters* **27**, 3421-3424.

Hillis, R.R., Meyer, J.J., and Reynolds, S.D., (1998) The Australian stress map. *Exploration Geophysics, v. 29 (4), pp. 420-427.*

Hillis, R.R., Enever, J.R., and Reynolds, S.D., (1999) In situ stress field of eastern Australia.
Australian Journal of Earth Sciences, v. 46 (5), pp. 813-825.

Hillis, R.R., and Reynolds, S.D., (2000) The Australian stress map.
Journal of the Geological Society, London, v. 157 (5), pp. 915-921, September 2000

GEOPHYSICAL RESEARCH LETTERS, VOL. 27, NO. 20, PAGES 3421-3424, OCTOBER 15, 2000

The *in situ* stress field of the Perth Basin, Australia

S.D. Reynolds and R.R. Hillis

National Centre for Petroleum Geology and Geophysics, Thebarton Campus, University of Adelaide, Australia

Abstract. A total of 17 wells in the Perth Basin were interpreted to have 114 breakouts covering a combined length of 3.2 km and a mean σ_{Hmax} orientation of 108°N. The inferred mean orientation of σ_{Hmax} in the Perth Basin is broadly consistent with that in the adjacent basement, Yilgarn Block. The new data confirm that σ_{Hmax} orientation in the region is consistent with other stress indicators, different depths and different geological provinces. The new data also confirm that the orientation of σ_{Hmax} does not parallel the NNE direction of absolute plate velocity. Anomalous north-south σ_{Hmax} orientations identified in a number of wells in the Perth Basin can be attributed to local structural effects.

Introduction

In most continental areas the maximum *in situ* horizontal stress (σ_{Hmax}) orientation parallels the direction of absolute plate velocity e.g. stable North America, western Europe and South America [*Richardson,* 1992]. The Australian continent is unique in that σ_{Hmax} is not parallel to the direction of absolute plate velocity. The variation of σ_{Hmax} orientation within the Indo-Australian plate as a whole has been explained in terms of the complex plate boundary forces acting on it, especially along its northeastern convergent boundary [*Coblentz et al.*, 1998].

Previous data suggested a regional east-west σ_{Hmax} orientation in the Perth area [*Hillis et al.*, 1998], almost orthogonal to the NNE direction of absolute plate velocity. Hence the Perth area is an important location with which to test whether σ_{Hmax} parallels absolute plate velocity. Previous *in situ* stress data in the Perth area were restricted to the Yilgarn Block, a major Precambrian basement province separated from the Perth Basin by the Darling Fault (Figure 1). Further more, all but 4 out of 18 stress indicators in the Yilgarn Block were based on poor quality (C and D), shallow overcoring and hydraulic fracturing data. In addition, 4 earthquake focal mechanisms were available in the Yilgarn Block. These data indicated a broadly east-west σ_{Hmax}. In this paper we present borehole breakout data from the Perth Basin (Figure 1).

Geological Setting

The Perth Basin is a deep linear trough located in the southwest of Western Australia. The basin extends in a north-south direction for approximately 1000 km covering both onshore and offshore. Sedimentation commenced in the northern Perth Basin in the Ordovician and had initiated throughout most of the basin by the Carboniferous to early Permian [*Harris*, 1994]. Up to 15 km of Phanerozoic sedimentary rocks may have been deposited in parts of the basin [*Playford et al.*, 1976]. The basin has a half graben configuration and is situated along a passive continental margin bounded on the east side by the Darling Fault [*Harris*, 1994]. The Darling Fault is the major structural feature of the basin separating the Phanerozoic sedimentary rocks from Archaean rocks of the Yilgarn Block to the east. The Darling Fault extends in a north-south direction for about 1000 km with a maximum throw possibly exceeding 15 km [*Playford et al.*, 1976]. The prominent fault direction throughout the basin is north to north-northwest [*Dentith et al.*, 1994] with most faults moderately to steeply dipping [*Playford et al.*, 1976].

Methodology

Borehole breakout occurs when the concentrated stress around a wellbore exceeds the compressive strength of the rock [*Zoback et al.*, 1985]. When this arises conjugate shear fractures form in the side of the wellbore causing the rock to break off [*Gough and Bell*, 1982]. This results in the wellbore being elongated in the direction perpendicular to σ_{Hmax}. The

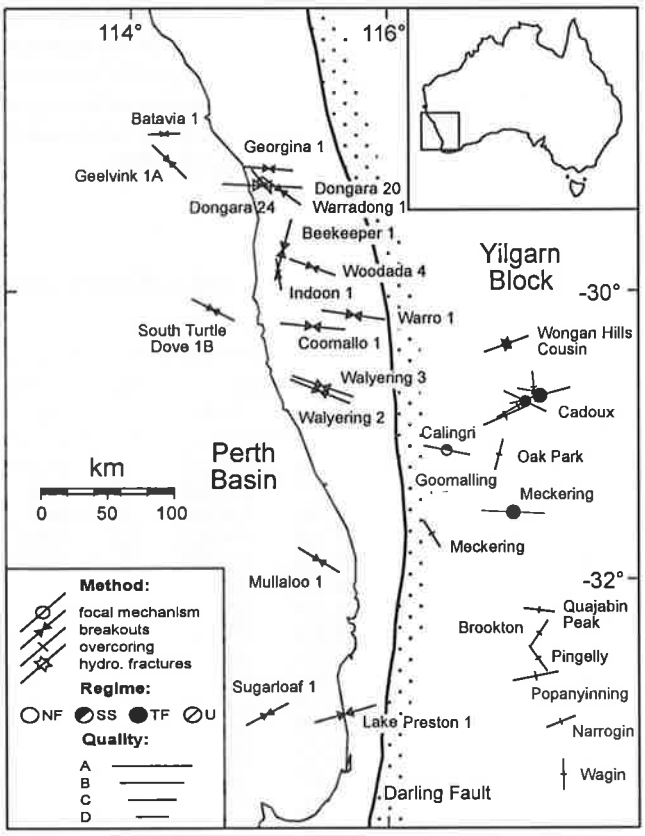

Figure 1. Stress map of the Perth region showing A-D quality stress indicators with location map as insert.

Paper number 2000GL011538
0094-8276/00/2000GL011538$05.00

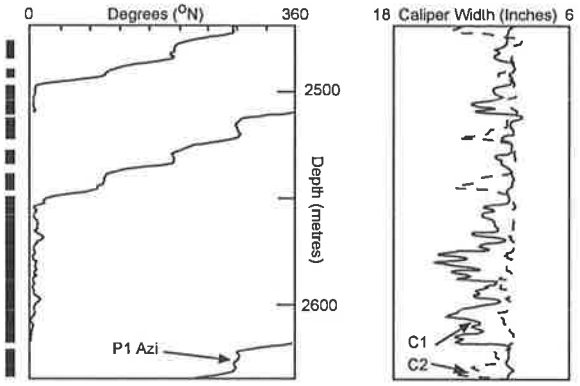

Figure 2. Section of 4 arm dipmeter data from Walyering 3 showing consistent breakout in a north-south direction (indicated by the black vertical bars at the extreme left), thus the σ_{Hmax} orientation is east-west. C1 and C2 are the two orthogonal borehole diameters. P1Azi is the azimuth of caliper pad 1 with respect to north.

four-arm dipmeter tool can be used to identify and orient these elongate zones. All breakout interpretation in the Perth Basin was done using the caliper data on paper logs from Schlumberger's high-resolution dipmeter tool (HDT). It is assumed that one of the principle stresses is parallel with the axis of the borehole.

Identification of the breakouts was done using rules based on the criteria set out by *Plumb and Hickman*, [1985]. Only wells with deviations less than 10° were used in the study. Wells with deviations greater than 5° were checked for key seating. Breakout orientations were corrected for magnetic declination of either 2 or 3 degrees depending on the location. Figure 2 shows a section from Walyering 3 with breakouts consistently oriented in the north-south direction indicating an east-west direction for σ_{Hmax}. Each of the wells were ranked using the World Stress Map scheme [*Zoback*, 1992].

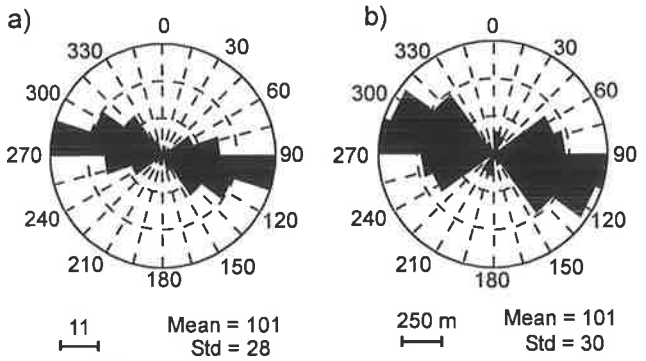

Figure 3. Rose diagram showing individual breakouts from the Perth Basin, a) unweighted and b) length weighted.

Results

A total of 114 breakouts with a combined length of 3.2 km were interpreted in 17 wells throughout the Perth Basin. The breakouts covered a depth range from 720 m to 4150 m. The average σ_{Hmax} orientation inferred from the individual breakouts is 101N (Table 1). This compares to a σ_{Hmax} direction of 108°N when all 17 wells from the basin are averaged (Table 2). Figure 1 shows the stress map (A-D quality indicators) for the Perth Basin and the Yilgarn Block. Much of the scatter present in the stress orientations across the Perth region is a result of the less reliable D quality indicators. The unweighted rose diagram for σ_{Hmax} orientations inferred from individual breakouts in the Perth Basin clearly displays the east-west trend (Figure 3a), while the length weighted plot has slightly more scatter but still exhibits the east-west trend (Figure 3b). A few individual wells show a more north-south trend (Figure 1). However, at the basin scale the north-south trend is not significant (Figure 3). A substantial decrease in the standard deviation of mean σ_{Hmax} orientations in the region is observed if the poorer, D-quality data are omitted (Table 2).

Table 1. Summary of breakouts in each well. Depth and lengths are all in metres. Azi: azimuth of σ_{Hmax}, S.D.: circular standard deviation.

Well	Location		No.	Depth		Unweighted			Length Weighted			
	Lat.	Long.		Top	Bot	Azi	S.D.	Q	Σlength	Azi	S.D.	Q
Batavia 1	-28.900	114.260	1	2320	2349	088	-	D	29	088	-	D
Beekeeper 1	-29.715	115.185	4	2590	3000	016	9	B	264	015	8	B
Coomallo 1	-30.249	115.416	3	2941	3185	096	2	B	105	098	1	B
Dongara 20	-29.268	115.022	13	738	1781	093	9	A	150	093	9	A
Dongara 24	-29.237	115.017	2	1142	1198	142	7	D	29	138	5	D
Geelvink 1A	-29.096	114.298	3	2919	3095	134	5	C	37	135	5	C
Georgina 1	-29.145	115.074	4	1109	1549	100	12	C	45	095	11	C
Indoon 1	-29.884	115.151	2	1377	2136	171	13	D	29	161	8	D
Lake Preston	-32.920	115.661	17	2941	4150	074	20	B	864	080	17	B
Mullaloo 1	-31.867	115.462	7	940	1995	108	33	D	413	122	23	C
Sth. Turtle Dove 1B	-30.130	114.636	3	1151	1242	112	24	C	94	118	21	C
Sugarloaf	-32.915	115.052	5	3371	3524	062	8	C	27	061	8	C
Walyering 2	-30.702	115.473	8	3108	3710	113	3	B	152	113	2	B
Walyering 3	-30.667	115.493	28	1880	2980	110	17	B	641	106	16	B
Warradong 1	-29.301	115.171	4	3213	3587	127	14	C	54	131	6	C
Warro 1	-30.168	115.736	7	1156	1214	099	11	B	52	105	15	B
Woodada 4	-29.835	115.141	3	1740	1935	115	18	C	90	110	17	C
Perth Basin			114	738	4150	101	28		3193	101	30	

Table 2. Summary of breakout data for the Perth Basin and Yilgarn Block

Region	Quality	Mean	Std
Perth Basin Wells	A-D	108°N	30°
Yilgarn Block Data (FMS/OC/HF)	A-D	085°N	43°
Perth Basin + Yilgarn Block	A-D	100°N	38°
Perth Basin Wells	A-C	105°N	26°
Yilgarn Block Data (FMS/OC/HF)	A-C	082°N	18°
Perth Basin + Yilgarn Block	A-C	096°N	26°

Discussion

Plate Boundary Effects

Stress orientations in the Perth Basin and Yilgarn Block cover two distinct geological provinces and are inferred from a variety of different stress determination techniques. Shallow (0-100 m) overcoring and hydraulic fracturing experiments along with deeper (1-5 km) earthquake focal mechanism solutions are available in the Yilgarn Block, whereas in the Perth Basin stress indicators have been inferred from borehole breakouts at depths of 700 m to 4 km (Figure 4). Thus the new breakout data provides a large number of observations over a considerable depth range. There is a broadly consistent east-west σ_{Hmax} orientation in both the Yilgarn Block and Perth Basin. This east-west σ_{Hmax} orientation, which is consistent over approximately 300500 km and across different stress indicators, depths and geological provinces, is likely to be a first order stress trend *sensu* [*Zoback*, 1992].

The South American plate, western Europe and stable North America have σ_{Hmax} orientations, which are parallel to the direction of absolute plate velocity [*Richardson*, 1992]. Thus, Plate boundary forces appear to have a first order control on the stress field in those areas [*Richardson*, 1992]. In contrast the variable stress field throughout the Australian continent does not coincide with the NNE direction of absolute plate velocity for the Indo-Australian plate [*Richardson*, 1992]. Stress orientations in Australia vary from east-west in the western side of the continent (Perth region, Carnarvon Basin) to northeast-southwest across the northern margin (New Guinea, Bonaparte Basin, Canning Basin), to northwest-southeast through south-eastern Australia (Otway Basin, Gippsland Basin), and to NNE-SSW in central and north-eastern Australia [*Hillis et al.*, 1998].

The Perth region, which includes both the Perth Basin and the Yilgarn Block, is an important location in highlighting the misfit between the direction of absolute plate velocity and σ_{Hmax} orientations in Australia. The mean σ_{Hmax} orientation for the Perth region, when only considering the more reliable A-C data, is 096°N. This orientation is approximately perpendicular to the direction of absolute plate velocity.

Cloetingh and Wortel, [1996] and *Coblentz et al.*, [1995] showed that the variable orientations of the Australian stress field can be modelled as originating from plate boundary forces if the heterogenous nature of the north-eastern convergent plate boundary is recognised. In continental areas where σ_{Hmax} parallels the direction of absolute plate motion, plate boundary configurations, and the associated forces, are relatively simple [*Gölke and Coblentz*, 1996]. The Indo-Australian plate has an extremely complex convergent north-eastern boundary comprising segments of continent-continent collision, continent-island arc collision, oceanic-island arc subduction and oceanic-oceanic subduction. Stresses are focussed by the collisional segments of the boundary (i.e. Himalaya, New Guinea and New Zealand), being normal to

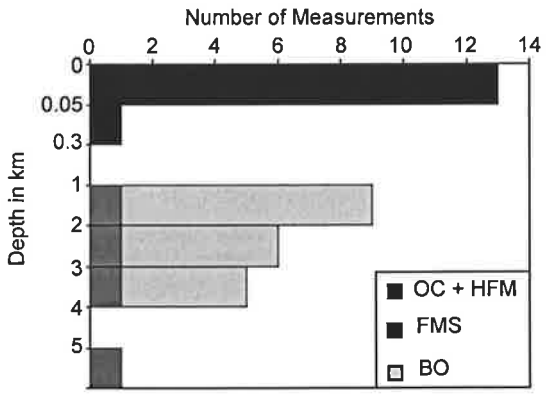

Figure 4. Distribution of all stress data from the Perth region divided by type and depth. Breakout depths represent an averaged value for each well. OC: overcoring, HFM: hydraulic fracture measurement, FMS: Focal Mechanism, BO: Breakout.

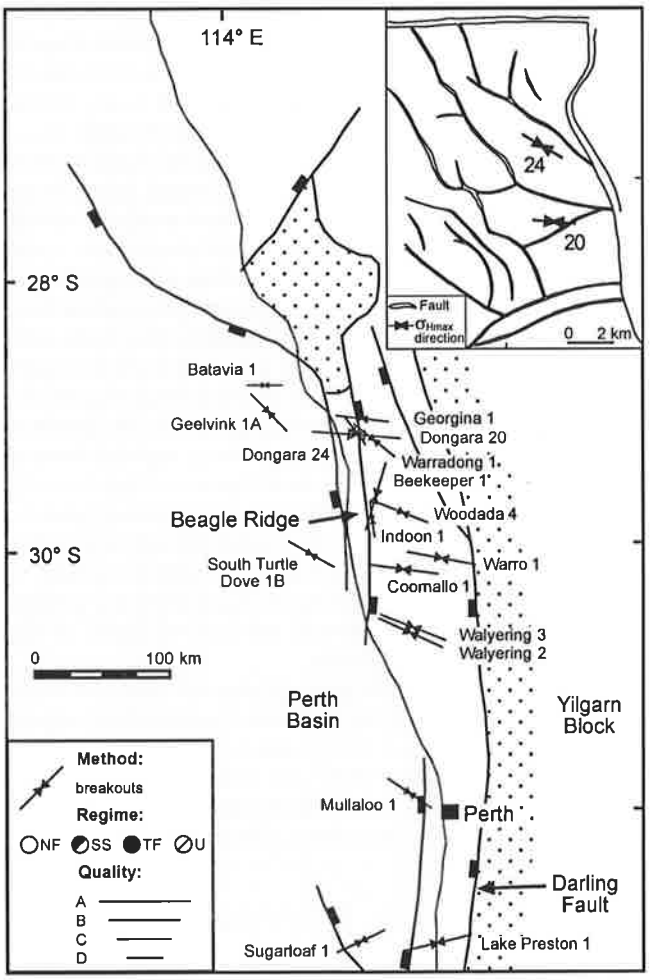

Figure 5. Regional structural map of the Perth Basin adapted from *Ellis and Bruce*, [1998] overlain by the new stress data for the Perth Basin. Insert showing the local structural map of the Dongara oil field [*Ellis and Bruce*, 1998] with the maximum horizontal stress orientation for wells 20 and 24.

those segments and rotating between them. The broad rotation between σ_{Hmax} normal to the Himalayan and normal to New Guinea results in the east-west σ_{Hmax} orientation seen in the western part of Australia in general and the Perth Basin/Yilgarn Block in particular [*Coblentz et al.*, 1998].

Local Structural Effects

Numerous regional stress studies have identified local variations in stress orientations that differ substantially from the regional stress trend. A number of authors have attributed this variation from the regional as being due to local structures [*Aleksandroski et al.*, 1992; *Ask*, 1997]. Local deflections from the regional stress trend are often hard to assign to specific structures due to the lack of detail in the stress and/or structural data. Nonetheless, perturbations of the stress field due to local structures should not be unexpected as most petroleum exploration wells are drilled on anomalous structures [*Aleksandroski et al.*, 1992].

Bell et al., [1992] described how non-sealing faults and open fractures may act as free surfaces within the rock body. These free surfaces deflect stress trajectories such that the minimum principal stress is rotated perpendicular to the free surface. Sealed fractures with no strong rheological contrast with the surrounding rock do not deflect stress trajectories.

The regional east-west σ_{Hmax} orientation has clearly been established throughout the Perth region. However, a number of wells exhibit a more north-south σ_{Hmax} orientation (Figure 5). The dominant structural grain throughout the Perth Basin is north-south to northwest-southeast [*Dentith et al.*, 1994]. Thus, it is suggested that the observed north-south σ_{Hmax} orientations result from the reorientation of the regional east-west σ_{Hmax} orientation by north-south oriented fractures as described by *Bell et al.*, [1992]. The two wells in which stresses are most clearly locally reoriented are Indoon 1 and Beekeeper 1. These wells are located in close proximity to the Beagle Ridge, a north-south trending horst. The breakouts in Beekeeper 1 are extensive throughout the well and consistently oriented approximately east-west (well is ranked B quality in WSM scheme). This consistent stress orientation, at right angles to the regional trend, suggest that the structure perturbing the stress field is likely to be a regional feature adjacent to the well rather than a local feature cutting the well. A number of wells, namely Dongara 20 and Georgina 1, display the regional east-west stress trend but are at a similar proximity to the Beagle Ridge as Indoon 1 and Beekeeper 1. This highlights the problematic nature in determining sources of local stress deflection due to the lack of detail in the regional stress/structural datasets.

Figure 5 insert shows the stress orientation from two wells in the Dongara oil field along with a detailed structural map of the field at approximately 2000 m depth. One well shows the regional east-west trend while the other has a northwest-southeast trend, parallel to an adjacent fault. We interpret this as a stress re-orientation associated with the nearby fault.

Conclusion

Breakouts from 17 wells in the Perth Basin produce an average σ_{Hmax} orientation of 108°N. The east-west σ_{Hmax} orientation inferred here for the Perth Basin is consistent with that from the adjacent Yilgarn Block based on hydraulic fracturing, overcoring and focal mechanism solution data. Thus, the east-west σ_{Hmax} orientation is consistent with other stress indicators, different depths and different geological provinces. The broadly east-west σ_H orientation in the Perth region is orthogonal to the direction of absolute plate velocity. However, this orientation can be modelled as resulting from plate boundary forces if the heterogenous nature of the north-eastern convergent boundary of the Indo-Australian plate is recognised [*Coblentz et al.*, 1995]. Some local stress rotations are observed in the Perth Basin breakout data. These are interpreted as being due to stress re-orientation around faults.

References

Aleksandroski, P., O.H. Inderhaug, and B. Knapstad, Tectonic structures and wellbore breakout orientation, in *33rd US Symposium on Rock Mechanics*, pp. 29-37, Santa Fe, Balkema, Rotterdam, 1992.

Ask, M.V.S., In situ stress from breakouts in the Danish Sector of the North Sea, *Mar. Pet. Geol.*, *14*, 0-13, 1997.

Bell, J.S., G. Caillet, and J. Adams, Attempts to detect open fractures and non-sealing faults with dipmeter logs, in *Geological Applications of Wireline Logs II*, edited by A. Hurst, C.M. Griffiths, and P.F. Worthington, pp. 211-220, Geological Society Special Publications, 1992.

Cloetingh, S., and R. Wortel, Stress in the Indo-Australia plate, *Tectonophysics*, *132*, 49-67, 1986.

Coblentz, D.D., M. Sandiford, R.M. Richardson, S. Zhou, and R.R. Hillis, The origins of the intraplate stress field in continental Australia, *Earth Planet. Sci. Lett.*, *133*, 299-309, 1995.

Coblentz, D.D., S. Zhou, R.R. Hillis, R.M. Richardson, and M. Sandiford, Topography, boundary forces, and the Indo-Australian intraplate stress field, *J. Geophys Res.*, *103* (B1), 919-931, 1998.

Dentith, M.C., A. Long, J. Scott, L.B. Harris, and S.A. Wilde, The influence of basement on faulting within the Perth Basin, Western Australia, in *The Sedimentary Basins of Western Australia: Proceedings of Petroleum Exploration Society of Australia Symposium*, edited by P.G. Purcell, and R.R. Purcell, pp. 791-799, Perth, Western Australia, 1994.

Ellis, G.K., and R.H. Bruce, Dongara oil and gas field, Perth Basin, in *The Sedimentary Basins of Western Australia 2: Proceedings of Petroleum Exploration Society of Australia Symposium*, edited by P.G. Purcell, and R.R. Purcell, pp. 625-635, Perth, Western Australia, 1998.

Gölke, M., and D. Coblentz, Origins of the European regional stress field, *Tectonophysics*, *266*, 11-24, 1996.

Gough, D.I., and J.S. Bell, Stress orientations from borehole wall fractures with examples from Colorado, east Texas, and northern Canada, *Can. J. Earth Sci.*, *19*, 1358-1370, 1982.

Harris, L.B., Structural and tectonic synthesis for the Perth Basin, Western Australia, *J. Pet. Geol.*, *17* (2), 129-156, 1994.

Hillis, R.R., J.J. Meyer, and S.D. Reynolds, The Australian stress map, *Explor. Geophys.*, *29*, 420-427, 1998.

Playford, P.E., A.E. Cockbain, and G.H. Low, Geology of the Perth Basin, Westren Australia, *Bull. Geol. Surv. West. Aust.*, *124*, 1976.

Plumb, R.A., and S.H. Hickman, Stress-induced borehole elongation: A comparison between the Four-Arm Dipmeter and the Borehole Televiewer in the Auburn Geothermal Well, *J. Geophys Res.*, *90* (B7), 5513-5521, 1985.

Richardson, R.M., Ridge forces, absolute plate motions, and the intraplate stress field, *J. Geophys Res.*, *97* (B8), 11739-11748, 1992.

Zoback, M.D., D. Moos, L. Mastin, and R.N. Anderson, Well bore breakouts and in situ stress, *J. Geophys Res.*, *90* (B7), 5523-5530, 1985.

Zoback, M.L., First- and second-order patterns of stress in the lithosphere: the world stress map project, *J. Geophys Res.*, *97* (B8), 11703-11728, 1992.

S.D. Reynolds and R.R. Hillis, NCPGG, Thebarton Campus, University of Adelaide, S.A. 5005, Australia. (e-mail: reynolds@ncpgg.adelaide.edu.au, rhillis@ncpgg.adelaide.edu.au)

(Received February 25, 2000; revised August 15, 2000; accepted August 17, 2000.)